Transition Metal Doped Colloidal Semiconductor Nanocrystals: From Functionality to Device Development

Von der Fakultät für Ingenieurwissenschaften
Abteilung Elektrotechnik und Informationstechnik
der Universität Duisburg-Essen

zur Erlangung des akademischen Grades

Doktor der Naturwissenschaften

genehmigte Dissertation

von

Franziska Elisabeth Muckel, M.Sc.
aus
Solingen

Gutachter: Prof. Dr. Gerd Bacher
Gutachter: Prof. Dr. Paul Koenraad
Datum der mündlichen Prüfung: 14. März 2018

Parts of this thesis have already been published:

- F. Muckel, S. Delikanli, P. L. Hernández-Martínez, T. Priesner, S. Lorenz, J. Ackermann, M. Sharma, H. V. Demir and G. Bacher
  "sp-d Exchange Interactions in Wave Function Engineered Colloidal CdSe/Mn:CdS Hetero-Nanoplatelets"
  Nano Letters 18(3), 2047-2053 (**2018**)

- F. Muckel, C. J. Barrows, A. Graf, A. Schmitz, C. S. Erickson, D. R. Gamelin and G. Bacher
  "Current-Induced Magnetic Polarons in a Colloidal Quantum-Dot Device"
  Nano Letters 17(8), 4768-4773 (**2017**)

- J. Yang, F. Muckel, W. B, R. Fainblat, H. Chang, G. Bacher and T Hyeon
  "Chemical Synthesis, Doping, and Transformation of Magic-Sized Semiconductor Alloy Nanocluster"
  Journal of the American Chemical Society 139(19), 6761-6770 (**2017**)

- F. Muckel, J. Yang, S. Lorenz, W. Baek, H. Chang, T. Hyeon, G. Bacher and R. Fainblat
  "Digital Doping in Magic-Sized CdSe Clusters"
  ACS Nano 10(7), 7135-7141 (**2016**)

Some contents of this thesis have been presented on international conferences:
Presenters are underlined.

- F. Muckel, S. Delikanli, T. Priesner, J. Ackermann, P. L. Hernández-Martínez, H. V. Demir and G. Bacher
  "Tailoring sp-d exchange coupling in CdSe/Mn:CdS core-shell nanoplatelets"
  Nanoscience with Nanocrystals (NaNaX 8), 3th - 8th July 2017, Braga, Portugal

- F. Muckel, S. Lorenz, J. Yang, R. Fainblat, T. Hyeon and G. Bacher
  "Giant magneto-optical response in single-atom doped $(CdSe)_{13}$ nanocluster at room temperature"
  Nanoscience with Nanocrystals (NaNaX 8), 3th - 8th July 2017, Braga, Portugal

- F. Muckel, J. Yang, R. Fainblat, S. Lorenz, T. Hyeon and G. Bacher
  "Manganese doped $(CdSe)_{13}$ magic sized clusters"
  9th International Conference on Physics and Applications of Spin-Related Phenomena in Solids (PASPS 9), 8th - 11th August 2016, Kobe, Japan

- F. Muckel, C. J. Barrows, A. Schmitz, A. Graf, D. R. Gamelin and G. Bacher
  "Electrically induced excitonic magnetic polaron in a colloidal quantum dot device"
  The 9th International Conference on Quantum Dots (QD2016), 22th - 27th May 2016, Jeju, Korea

- F. Muckel, R. Fainblat, V. Vlaskin, C. J. Barrows, D. R. Gamelin and G. Bacher
  "Magneto-optical study of excited states in chemically prepared Mn^{2+}-doped CdSe quantum dots"
  20 Years of Quantum Dots at Los Alamos, 12th - 16th April 2015, Los Alamos, USA

- F. Muckel, R. Fainblat, J. Frohleiks, G. Bacher, J. H. Yu and T. Hyeon
  "Magnetic dopant-carrier exchange coupling in Mn^{2+}-doped CdSe-Nanoribbons"
  DPG Spring Meeting of the Condensed Matter Section, Deutsche Physikalische Gesellschaft, 10^{th} - 15^{th} March 2013, Regensburg, Germany

Further publications in peer reviewed journals:

- J. Yang, R. Fainblat, S. G. Kwon, F. Muckel, J. H. Yu, H. Terlinden, B. H. Kim, D. Iavarone, M. K. Choi, I. Y. Kim, I. Park, H.K. Hong, J. Lee, J. S. Son, Z. Lee, K. Kang, S.-J. Hwang, G. Bacher and T. Hyeon
  "Route to the Smallest Doped Semiconductor: Mn^{2+}-Doped $(CdSe)_{13}$ Cluster"
  Journal of the American Chemical Society 137(40), 12776-12779 (**2015**)

- R. Fainblat, F. Muckel, C. J. Barrows, V. A. Vlaskin, D. R. Gamelin and G. Bacher
  "Valance-Band Mixing Effects in Upper-Excited-State Magento-Optical Responses of Colloidal Mn^{2+}-Doped CdSe Quantum Dots"
  ACS Nano 8(12), 12669-12675 (**2014**)

- C. Punckt, F. Muckel, S. Wolff, I. A. Aksay, C. A. Chavarin, G. Bacher and W. Mertin
  "The effect of degree of reduction on the electrical properties of functionalized graphene sheets"
  Applied Physics Letters 102(2), 023114 (**2013**)

- R. Fainblat, J. Frohleiks, F. Muckel, J. H. Yo, J. Yang, T. Hyeon and G. Bacher
  "Quantum Confinement-Controlled Exchange Coupling in Manganese(II)-Doped CdSe Two-Dimensional Quantum Well Nanoribbons"
  Nano Letters 12(10), 5311-5317 (**2012**)

Contents

List of Symbols

A_0	maximum absorption value
A_{σ^-/σ^+}	absorption of σ^-/σ^+ light
A	absorption
$B_{13,\mathrm{x}^{\mathrm{cor}}}(n)$	binomial distribution
$B_\mathrm{R}/C_\mathrm{R}$	Racah parameter
B_S	Brillouin function describing the magnetization of a paramagnet with spin S
$B_\mathrm{exc}^\mathrm{loc}$	local magnetic exchange field
B_exc	magnetic exchange field
B	magnitude of the magnetic field
E_0	central peak energy
$E_\mathrm{EMP}^\mathrm{sat}$	polaron energy in case of saturation
E_EMP	polaron energy
E_Stokes	Stokes shift
E_abs	absorption peak energy
E_emission	emission peak energy
$E_\mathrm{exc}^\mathrm{0D/2D}$	exciton binding energy in a zero-/two-dimensionally confined system
$E_\mathrm{exc}^\mathrm{bulk}$	bulk exciton binding energy
E_exc	exciton binding energy
F_m	projection quantum number of the total angular momentum of an exciton along an observation axis
F	total angular momentum quantum number of an exciton
I_0	initial light intensity
$I_\mathrm{MCD}^\mathrm{0T}$	MCD signal at zero external magnetic field
I_MCD	MCD signal
I_{σ^-/σ^+}	transmitted intensity of σ^-/σ^+ light
$I_\mathrm{reference}$	transmitted intensity of the reference light path

I_{sample}	transmitted intensity of the sample light path
J	total angular momentum quantum number of an atom/ion
L	total orbital momentum quantum number of an atom/ion
M	magnetization
$N_0\alpha$	exchange coupling constant of the conduction band
$N_0\beta$	exchange coupling constant of the valence band
N_{b}	number of bonds
N_{co}	coordination number of neighboring atoms
N_{m}	projection quantum number of the total angular momentum of an electron/a hole
N	total angular momentum quantum number of an electron/a hole
$P_{0/1/2}$	probability of undoped/monodoped/bidoped clusters in an ensemble
P_{iso}	probability of isolated Mn^{2+} ions in a DMS material
R_{a}	distance to neighboring atoms
S_{eff}	effective spin, empirical parameter in the modified Brillouin function
S_{fit}	dimensionless coupling constant
S	total spin of an atom/ion
T_{AF}	antiferromagnetic temperature
T_{eff}	effective temperature of the Mn spins as included in the Brillouin function
T_{heat}	temperature correction considering spin heating
T	temperature
V_{AC}	AC voltage
V_{DC}	DC voltage
V_{ex}	charge carrier volume
Z_{LF}	effective charge of the ligand atoms
Z_{b}	effective bond charge
Z	atomic number of an element
ΔA_{max}	maximum in the absorption difference between σ^- and σ^+ light
ΔA	absorption difference between σ^- and σ^+ light
$\Delta E\,(T)$	energy difference between the bandgap at a certain temperature T and the bandgap at 0 K (or 5 K)
ΔE_{Z}	giant Zeeman splitting
ΔE_{tran}	energy spacing between two transitions
$\Delta S_{\mathrm{e-h}}$	formation entropy of an electron - hole pair

ΔT	temperature offset in the Brillouin function
$\Delta U_{\mathrm{VB/CB}}$	valence/conduction band offset
$\Delta\mu_0$	edge step of the X-ray absorption
Δ_{LF}	ligand field strength
Δ_{cf}	crystal field energy separating the heavy and light hole subband in a wurtzite semiconductor
Δ_{so}	spin-orbit split-off energy
α_{V}	parameter in the Varshni fit
β_{V}	parameter in the Varshni fit
χ	EXAFS signal
δ_{scat}	phase shift for the scattering of photo-electrons
$\gamma_{\mathrm{e/h}}$	overlap of the charge carrier (electron/hole) wave function with the TM^{2+} ions
$\hat{\mathscr{A}}/\hat{\mathscr{B}}$	fit parameter describing the maximum contribution of the $\mathscr{A}$- and $\mathscr{B}$- term for MCD
$\hbar\omega$	phonon energy
λ_{so}	spin-orbit coupling parameter of a ligand field term
$\langle\hbar\omega\rangle$	average phonon energy
$\langle S_{\mathrm{z}}\rangle$	mean spin moment along a predefined z-axis
$\mathscr{A}_1/\mathscr{B}_0/\mathscr{C}_0$	MCD parameter of the $\mathscr{A}$, $\mathscr{B}$, $\mathscr{C}$- term
μ_0	bare atom background of the X-ray absorption
μ	X-ray absorption
$\overline{r^4}$	mean fourth power radius of the transition metal d electron orbitals
$\vec{s}_{\mathrm{e/h}}$	spin operator of a band carrier (electron or hole)
$\vec{S}$	spin operator of an atom/ion
σ^2_{N}	mean-square disorder of the distance to neighboring atoms
σ	half Gaussian bandwidth
τ_{EMP}	polaron formation time
τ_{exc}	exciton life time
φ	phase signal
ξ	argument of the Brillouin function
ζ_{so}	single-electron spin-orbit coupling parameter
a_{B}	excitonic Bohr radius
a_{QD}	quantum dot radius
a	bond length

b	bowing parameter to describe the composition dependent shift of the bandgap
d_{ML}	thickness of a monolayer
e	elementary charge
$f(E)$	peak-normalized Gaussian function in energy
f_{scat}	scattering amplitude of photo-electrons
g_{TM}	gyromagnetic factor of a transition metal (Mn or Co)
j	total angular momentum quantum number of an electron/a hole in a subband
k_{B}	Boltzmann constant
k_{PE}	photo-electron wave number
l_{env}	orbital quantum number of an envelope function
l	orbital momentum quantum number of an electron/a hole in a subband
$m_{\mathrm{e/hh/lh/so}}$	effective mass of the electron/heavy hole/light hole/split-off hole
m_{j}	projection quantum number of the total angular momentum of an electron/a hole in a subband along an observation axis
n_{env}	principal quantum number of the envelope function
n_{exc}	quantum number of a hydrogenic exciton state
n	principal quantum number
$s_{\mathrm{z,e/h/exc}}$	spin projection of an electron, hole or an exciton along a predefined z-axis
s_{z}	spin projection along a predominant axis for band carriers (electron or hole)
s	spin quantum number of a charge carrier in a band/subband
$x_{\mathrm{Mn/Co}}$	nominal concentration including all Mn^{2+}/Co^{2+} ions incorporated in the host crystal
x_{Zn}	overall Zn concentration among all magnetically inactive cations
x_{cor}	corrected concentration used in the binomial coefficients to estimate the portion of undoped, monodoped and bidoped clusters
x_{eff}	effective concentration describing the magneto-optically active TM^{2+} ions
x	concentration of a foreign atom in a host material
$\lvert\chi(R)\rvert$	magnitude of the Fourier-transformed EXAFS signal
$E_{\mathrm{g}}^{\mathrm{CdSe,ZnSe}}$	fundamental bandgap of CdSe, ZnSe

E_{g}	fundamental bandgap
$E_{\mathrm{c/v}}$	energy of the conduction or valence band
ϵ_0	vacuum permittivity
ϵ_{r}	dielectric constant
g_{int}	intrinsic g-factor
$g_{\mathrm{sp-d}}$	g-factor of the *sp-d* exchange interaction
g_{eff}	effective g-factor of an exciton
$g_{\mathrm{e/h}}$	intrinsic g-factor of the electron/hole
$\mathcal{H}_{\mathrm{dd}}$	Heisenberg Hamiltonian describing the *d-d* exchange interaction between neighboring dopants
$\mathcal{H}_{\mathrm{int,c/v}}$	Hamiltonian of the intrinsic Zeeman splitting for the conduction/valence band
$\mathcal{H}_{\mathrm{s/p-d}}$	Heisenberg Hamiltonian describing the *s-d* or *p-d* exchange interaction
J^{dd}	exchange integral for the *d-d* exchange
$J_{\mathrm{s/p-d}}$	exchange integral for the *s-d* or *p-d* exchange
$\vec{k}$	wave vector
A_{MCD}	contribution of the *sp-d* exchange interaction to the MCD signal
$A_{\mathrm{MCD}}^{\mathrm{int}}$	intrinsic contribution to the MCD signal
$\widehat{A_{\mathrm{MCD}}^{\mathrm{sp-d}}}$	maximal contribution of the *sp-d* exchange interaction to the MCD signal
$A_{\mathrm{MCD}}^{\mathrm{sp-d}}$	contribution of the *sp-d* exchange interaction to the MCD signal
$\vec{B}$	external magnetic field
E_{q}	quantization energy
L_{x}	thickness of a quantum well
μ_{B}	Bohr magneton
V	potential applied to a Schrödinger equation
$\mathcal{S}$	representation of the *s*-like state of the conduction band
$u_{\mathrm{ke/hh/lh/so}}$	Bloch function of the electron/heavy/light or split off hole
$\downarrow$ / $\uparrow$	representation of the spin state
$\mathcal{X}$, $\mathcal{Y}$, $\mathcal{Z}$	representation of the p_x, p_y and p_z states in the valence band
$\vec{R}$	position vector of a TM^{2+} ion
R	position of a TM^{2+} ion
$\alpha_{\mathrm{n,l}}$	n^{th} zero of the l^{th} order spherical Bessel function
k	wave number

$\vec{q}$	predominant axis
$\vec{T}$	lattice vector
$\vec{r}$	position vector
r	position
$\Psi_{\mathrm{e/h}}$	wave function of an electron/a hole
$\psi_{\mathrm{e/h}}$	envelope function of an electron/a hole

Acronyms

π	linearly polarized light
$(CdSe)_{13}$	cluster consisting of 13 cadmium and 13 selenium ions
$(ZnSe)_{13}$	cluster consisting of 13 zinc and 13 selenium ions
$(Zn_xCd_{1-x}Se)_{13}$	alloy clusters containing 13 cations and anions with a total Zn concentration x
σ^+	circularly right polarized light
σ^-	circularly left polarized light
hh	heavy hole
lh	light hole
so	spin-orbit split-off hole
AC	alternating current/voltage
AcO	acetate (CH_3COO)
APD	avalanche photodiode
Ar	argon
c-ALD	colloidal atomic layer deposition
CCD	charge-coupled device
Cd	cadmium
CdSe	cadmium selenide
Cl	clorine
Co	cobalt
DC	direct current/voltage
DFT	density functional theory
DMS	diluted magnetic semiconductor
EDT	1,2-ethanedithiol
EL	electroluminescence
EMP	excitonic magnetic polaron

EQE	external quantum efficiency
EXAFS	extendend X-ray absorption fine structure
I	iodine
ICP-AES	inductively coupled plasma - atomic emission spectroscopy
ITO	indium tin oxide
LDI-TOF MS	light desorption/ionization time-of-flight mass spectrometry
LED	light emitting diode
MCD	magnetic circular dichroism
ML	monolayer
Mn	manganese
$Mn_2Cd_{11}Se_{13}$	bidoped clusters consisting of 2 manganese, 11 cadmium and 13 selenium ions
$MnCd_{12}Se_{13}$	monodoped clusters consisting of 1 manganese, 12 cadmium and 13 selenium ions
MSC	magic sized cluster
NMF	N-methylformamide
NN	nearest neighbors
NNN	next-nearest neighbors
NP	nanoplatelet
octylamine	unbranched chain organic compound with the formula $C_8H_{17}NH_2$
oleylamine	unbranched chain organic compound with the formula $C_{18}H_{35}NH_2$
PEDOT:PSS	poly(3,4-ethylenedioxythiophene)-poly(styrenesulfonate)
PEM	photoelastic modulator
PL	photoluminescence
PLE	photoluminescence excitation
poly-TPD	poly[N,N'-bis(4-butylphenyl)-N,N'-bis(phenyl)-benzidine]
QCSE	Quantum-confined Stark effect
QD	quantum dot
RKKY	Rudermann-Kittel-Kasuya-Yosida interaction
S	sulphur
Se	selenium
SEM	scanning electron microscope
SLR	spin-lattice relaxation
TBP	tributylphosphine

Te	tellurium
TEM	transmission electron microscope
TM	transition metal
TOP	trioctylphosphine
TRPL	time resolved photoluminescence
Zn	zinc

Chapter 1

Introduction

The dawn of the *Digital Age*, which was based on the invention and continuous improvement of integrated circuit technologies, has fundamentally altered peoples lives during the last three decades in nearly every single aspect: Computers, smart phones and the availability of information provided through the internet change the way people work and communicate, revolutionize their healthcare and enable contact to foreign cultures across the world, shaping modern societies. While Moore's law [1] successfully described the evolution of the integrated circuit density since the 1970s, the miniaturization of transistor sizes now reaches an intrinsic limit due to the appearance of quantum effects, which creates demand for alternative approaches. In addition to the charge, which represents the information carrier in virtually all transistor based electronics, electrons carry a spin as an additional degree of freedom, whose manipulation in solid state systems is addressed in the field of *spintronics* (spin transport electronics) [2–4]. Due to the expected decreased energy needed for spin manipulation compared to charge manipulation, implementation of the spin as information carrier in addition to or instead of the charge promises advanced device concepts enabling higher information processing rates, increased integration densities and decreased energy consumption. With the giant magneto resistance effect [5, 6], awarded with the Physics Nobel Price in 2007, this concept has already been successfully implemented into commercial hard disks, where data storage is realized through the manipulation of spins in metallic materials.

However, the central vision of spintronics is the idea to combine both data storage and data processing in a single device, which avoids time and energy losses due to the necessary exchange of information between both systems. This requires furnishing a semiconductor with magnetic properties, as can be achieved by doping with transition metal (TM) atoms in diluted magnetic semiconductor (DMS) materials [7]. Herein, so-called *sp-d* exchange interactions between the electrons and holes in the *s*-like conduction and

the *p*-like valence band with the *3d* electrons of the TM^{2+} ions enable a combination of the electronic and optical advantages of semiconductors with magnetic functionality [8, 9]. More recently, the adaptation of the DMS concept to colloidally synthesized nanostructures has renewed the interest in this material class [10–14]. In contrast to epitaxial semiconductors, which are prepared with the use of cost-intensive high-vacuum technologies, solution-synthesized nanostructures benefit from reduced manufacturing costs. In addition, they combine a high flexibility of available sizes, shapes and morphologies with the ease and versatility of subsequent solution processability [15, 16]. The latter, including thin layer preparation methods like spin-coating, printing and spraying from dispersion, highlights colloidal nanostructures as a promising material class for the implementation as active materials in next-generation printable or wearable low-cost electronic devices e.g., for tomorrows' lifestyle or healthcare applications [17, 18].

Ever since the first demonstration of TM doping in colloidal semiconductor quantum dots (QDs) [19–22], increasing research activities revealed a bunch of extraordinary magnetic and magneto-optical properties, which mainly arise from the increased *sp-d* exchange interactions due to the strong charge carrier quantization in these materials [23–29]. However, quite recently, considerable progress in colloidal chemistry [29–32] expands the family of DMS nanocrystals from magnetically doped, spherical QDs to various, fundamentally different shapes. From undoped nanostructures it is known that the precise shape of a quantum confined object crucially defines their electronic structure and optical properties [33–36]. Thus, the novel degree of freedom achieved for the architecture of DMS nanostructures enables an insight into the specific exchange interactions with different types of electronic transitions [37]. By introducing transition metal dopants into either colloidal quantum wells [32] or highly confined magic sized clusters (MSCs) [31], the exchange interactions of two-dimensionally or zero-dimensionally confined states can be accessed. On the other hand, the possibilities provided by the solution processability of colloidally synthesized materials facilitate the integration of DMS nanocrystals into solution-processed devices. These two advantages of colloidally synthesized DMS structures - the flexibility in shape and composition as well as the solution processability - are exploited within this thesis with the intention to elaborate the functionality affected by individual monolayers (MLs) or even single atoms, and to demonstrate the feasibility of electrical devices based on DMS nanocrystals.

In zero-dimensional DMS QDs, which have been studied for almost two decades [12], the spherical confinement is known to introduce a mixing between the different valence subbands [33, 34]. The *sp-d* exchange interactions of the resulting states are quite well understood [38], including their tunability through wave function engineering in complex, partly-doped core/shell QDs [24, 39]. In contrast to this, a two-dimensional confinement

separates the valence subbands, enabling access to transitions with well defined hole states [35, 36]. In particular, the lately developed material class of higly-anisotropic colloidal nanoplatelets (NPs) [40–44], which can be produced with thicknesses of a few nm combined with lateral dimensions of several tens of nm, enable precise synthetic control of thickness and composition, including core/shell [45, 46] or core/crown [47, 48] architectures. In combination with transition metal doping [32], this material system allows the analysis of the impact of thickness variation on the *sp-d* exchange interactions with atomic layer precision. Up to now, literature on the magneto-optical properties of colloidal DMS NPs is rare and restricted to the emissive states [32, 49]. Especially, clear evidence of *sp-d* exchange interactions for the band carriers in thickness-tunable colloidal NPs is lacking.

If the nanostructure size is minimized to a few MLs for all three dimensions, doping becomes challenging [11, 12, 50, 51], as due to the excess mixing enthalpy impurities are excluded from QD nuclei and thus no doping in particles with diameters below 2 nm is feasible with conventional methods like hot injection [50] or diffusion doping [30]. However, via low temperature Lewis acid-base synthesis [31] transition metal doping has been demonstrated in MSCs [52–56]. These fascinating colloidal QDs, which appear as building blocks during the synthesis of higher order nanostructures [56–59], exist only with strictly defined numbers of atoms [52], representing the boundary between semiconductors and molecules. In these strongly confined systems, the zero-dimensional band edge transition is split into single fine structure components, as has been shown in manganese (Mn^{2+}) doped cadmium-selenid (CdSe) MSCs consisting of 26 atoms (Mn:$(CdSe)_{13}$) [31]. The high confinement thus enables investigation of the *sp-d* exchange interactions with individual fine structure states.

Due to their well defined, countable number of atoms, the replacement of a single atom corresponds to a change in composition of about 7 %. Thus, both magnetic doping as well as alloying with a nonmagnetic equivalent is expected to distinctly influence the (magneto-)optical properties of the clusters and needs to be considered as a discrete process. While partial replacement of cadmium (Cd) by non-magnetic zinc (Zn) is expected to shift the clusters bandgap in a discrete manner, introducing a dopant may digitally change the giant magneto-optical activity of the $(CdSe)_{13}$ clusters. In bulk DMS materials, Mn^{2+} spins positioned on neighboring lattice sites couple antiferromagnetically [8, 9, 60, 61]. It is not clear, how this might influence the magneto-optical response in magnetically doped MSC, where virtually all cation lattice sites can be considered as nearest neighbors. In case the magnetic moments of the Mn^{2+} ions in clusters doped with two or more dopants partly nullify each other, DMS MSCs might represent a promising material for the application in solotronic applications [62, 63], a novel research field concentrating on the manipulation of solitary atoms or dopants in a solid state matrix.

Due to their minimal size, MSCs contain a drastically reduced number of bonds as compared to conventional colloidal QDs and are characterized by a distinct lattice structure, which cannot be expressed in terms of a wurtzite or zinc blende unit cell known from bulk. This implies striking consequences for structure related properties: On the one hand, the minimized structure is supposed to increase the clusters' ability to respond to the replacement of a lattice component by an atom of smaller size. On the other hand the influence of optically excited charge carriers on the rigidity of the bonds and the phonon modes might be enhanced. The fact that the precise lattice structure of the $(CdSe)_{13}$ clusters is still controversially discussed [64–69], among other things derives from the restricted applicability of experimental techniques to study the structure. As those techniques are often based on diffraction methods requiring at least medium range of periodicity not available in the small clusters, structure analysis up to now is mainly restricted to atomistic density functional theory (DFT) calculations [64–69]. Studies on DMS QDs doped with cobalt (Co) exploit internal transitions between the different *3d* orbitals of the dopants, whose shape and energy are highly sensitive to the chemical surrounding of the Co^{2+} [70], to gather information about the anionic coordination around the dopant [71–74] and the dopant-anion bond length [75]. Thus, Co^{2+} doping of MSCs may offer an optical approach to the lattice structure of the clusters.

The crystal structure also determines the phonon dispersion in a material, which on the other hand is decisive for the temperature dependence of the bandgap [76–78], representing an essential fingerprint for any semiconductor. In case of the clusters - and in stark contrast to most semiconductors including conventional QDs still consisting of more than a hundred atoms - almost all atoms can be regarded as located on the surface and the number of bonds is reduced to about 50 or less. Thus, the rigidity of the bonds upon optical excitation, which is discussed to originate the temperature dependence of the bandgap [78, 79], is expected to be distinctly altered in these novel materials.

The circle is closed towards the central motivation behind all interest in DMS nanostructures, i.e., their application in spintronic devices. Despite nearly two decades of research on these materials, electrical control of the magneto-optical properties of DMS nanostructures has not been realized up to date. Few examples demonstrate optical control of the magnetic properties [25, 27], including laser induced spontaneous magnetization in Mn:CdSe QDs up to room temperature [23]. Here, the presence of an optically induced exciton can trigger a magnetic alignment of the embedded dopant spins [8, 80], creating a net magnetization. However, even though optical approaches may have some advantages e.g. for ultrafast-switching, they require additional light sources, while electrical approaches offer compatibility to existing electronics. Although excitonic magnetic polarons (EMPs) have been studied for decades in epitaxial [81–83] as well as colloidal [23,

80, 84] QDs, their electrical control has not been realized up to now.

Within this thesis, the possibilities provided by the colloidal synthesis with respect to control the magneto-optical functionality via size and shape of DMS nanocrystals and to integrate these novel materials into devices are evaluated. Those include the flexibility in nanocrystal architecture to address *sp-d* exchange interactions of two-dimensional and zero-dimensional materials down to the limit of ultrasmall clusters at the border between solids and molecules, and the flexibility of further processing towards devices. These topics are discussed in several chapters, structured as follows:

- The second chapter reviews the theoretical background for the discussed optical and magneto-optical effects in colloidal DMS nanostructures. It starts with an introduction to the bulk crystal and band structure of II-VI semiconductors, followed by a description of quantum confinement in different types of nanocrystals. In addition, the electronic structure of the TM^{2+} dopants is presented. Subsequently, the influence of a magnetic field on the electronic states in undoped as well as in doped materials is elucidated, including the exchange interactions between the dopants themselves, between the dopants and the charge carriers of the host semiconductor and the formation of an EMP.

- In the third chapter, the materials and methods utilized within this thesis are presented. Following a short introduction to the synthesis routes used for the different samples, the further processing for the preparation of thin films for optical characterization and their embedment into electrical devices is described. In addition, the different optical setups used within this thesis are presented.

- The fourth chapter describes how the optical and magneto-optical properties of $(CdSe)_{13}$ can be tuned either by doping with Mn^{2+} or by alloying (and additional doping) with Zn (and Mn^{2+}). In the first part the hypothesis of *Digital Doping* is evaluated based on a series of Mn:$(CdSe)_{13}$ clusters with different doping concentrations. Via light desorption/ionization time-of-flight mass spectrometry (LDI-TOF MS), the relative ratios of clusters doped with zero, one or two Mn^{2+} dopants are determined and correlated with the giant Zeeman splitting. In the second part, the optical and magneto-optical properties of alloy DMS clusters are presented, evidencing the combination of three different cations in one cluster. In addition, the temperature dependence of the giant Zeeman splitting is investigated.

- The structure related properties of MSCs are discussed in chapter five. First, an optical approach for the structure analysis in Co^{2+}-doped $(CdSe)_{13}$ is presented. Following a discussion of the band-edge magneto-optical response, the magneto-optical features related to the Co^{2+} internal ligand field transition are evaluated in

order to investigate the Co^{2+} environment, i.e., its coordination by anions and the Co^{2+}-anion bond length. Complementary extendend X-ray absorption fine structure (EXAFS) measurements are presented, allowing an additional approach to the Co-Se bond length. Subsequently, the influence of the small structure on the phonon modes and the temperature dependence of the bandgap is discussed. The bandgap shift is monitored with various optical techniques in undoped as well as Mn^{2+}-doped $(CdSe)_{13}$ clusters, and interpreted within a thermodynamic model.

- The sixth chapter presents the magneto-optical properties of shell-doped colloidal multilayer NPs. After proving the existence of *sp-d* exchange interactions in these materials, the electronic structure of excited states is analysed with the aid of the magneto-optical response. The probability to tune the *s-d* and *p-d* exchange interactions for the various ground and excited states via wave function engineering is evaluated by variation of the core and shell thickness in CdSe/Mn:CdS core/shell and CdSe/MnS/Mn:CdS core/multishell NPs.

- Chapter seven describes the development of an electrical device based on Mn:CdSe/CdS core/shell QDs, with the purpose to enable current-induced magnetism. Following a presentation of the relevant optical properties of the QDs and the room temperature performance of the device, temperature dependent electroluminescence measurements are conducted to evidence the existence and evaluate the strength of the electrically induced EMP.

- In chapter eight the different findings of this thesis are summarized.

Chapter 2

Theoretical Background

In this chapter the theoretical framework for the physical properties of colloidal DMS nanostructures is laid, providing the basis for the discussion and classification of the observed optical and magneto-optical effects. Based on the introduction of the crystal lattice and the resulting band structure of bulk II-VI semiconductors, the particularities originated by charge carrier confinement are discussed. In addition, the electronic states introduced by the transition metal (TM^{2+}) dopants are reviewed. Following a short discussion of the intrinsic Zeeman effect present in any semiconductor, the interactions between a magnetic field and the electronic structure of DMS nanostructures are presented. Finally, the formation of excitonic magnetic polarons (EMPs) in magnetically doped quantum dots (QDs) is presented.

2.1 Crystal Lattice and Electronic Structure of Bulk II-VI Semiconductors

All DMS nanostructures examined within this thesis belong to the family of II-VI compound semiconductors. In their undoped form, II-VI materials consist of an one-to-one combination of a metal element from the groups 2 or 12 (i.e., the second main or subgroup, formally denominated as IIA and IIB) and a non-metal from the chalcogens (i.e., group 16 or group VI). In order to establish an understanding of the electronic structure of the nanocrystals, the corresponding bulk properties are discussed first.

2.1.1 Crystal and Band Structure

The crystal structure of a solid material, which is decisive for its band structure as it provides the potential for the charge carriers, results from the combination of the included elements determining the bonding types. In II-VI materials, the group II metals contribute to the bonding with their *s*-type outer electrons ($4s^2$ and $5s^2$ for zinc (Zn) and cadmium (Cd), respectively), while the group VI chalcogenides offer the six electrons in their valence orbitals ($3s^2 3p^4$ and $4s^2 4p^4$ for sulphur (S) and selenium (Se), respectively). These orbitals form so-called sp^3 hybrid orbitals, which trigger a tetrahedral arrangement of the atoms around each other. Due to the strong differences in the electronegativities, the covalent tetrahedral bonds possess a high ionic character (62 % to 70 % for the various combinations of Cd, Zn, Se and S) [85], for which reason the atoms in the lattice are also denominated as cations or anions, respectively.

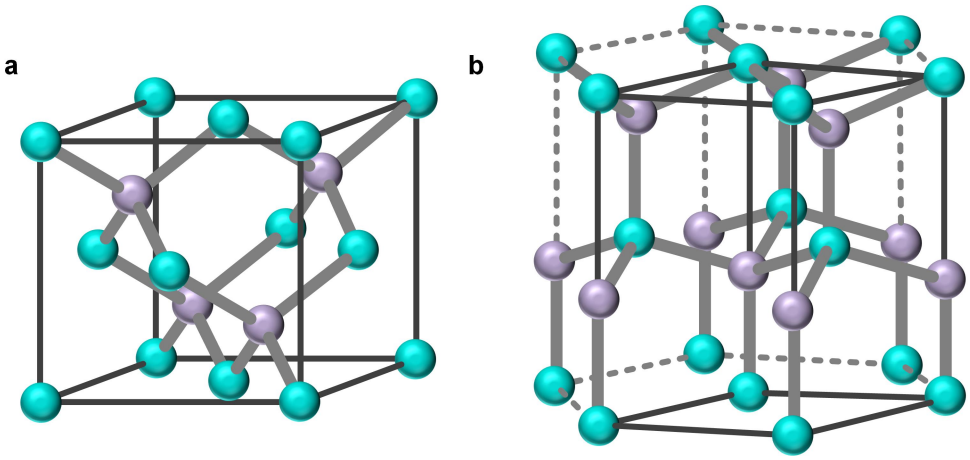

Figure 2.1: Crystal structure of the zinc blende (a) and the wurtzite lattice (b). Cations are illustrated in turquoise and anions in violet. From [86].

The tetrahedral bonding results, depending on pressure, temperature [87] and composition (i.e. concentration of TM^{2+}-doping [88]), in two closely-related crystal structures, the zinc blende and the wurtzite lattice, as illustrated in Figure 2.1. The former consists of two (one for each element) cubic face-centered sublattices, which are shifted by one-fourth of the unit cell diagonal. In the wurtzite structure, the two hexagonal close-packed lattices for the cations and anions are shifted by $\frac{3}{8}$ of the lattice constant along the c-axis. Both lattice structures differ in the stacking sequence along the cation-anion bound, which is ABCABC for zinc blende and ABAB for wurtzite [87]. In contrast to the zinc blende lattice, wurtzite structures exhibit a reduced symmetry, which has a crucial impact on the band structure.

In both lattice types the sp^3 orbitals of the constituent atoms in the crystal form the optically relevant electronic bands, i.e. the mainly bonding, occupied valence band and the

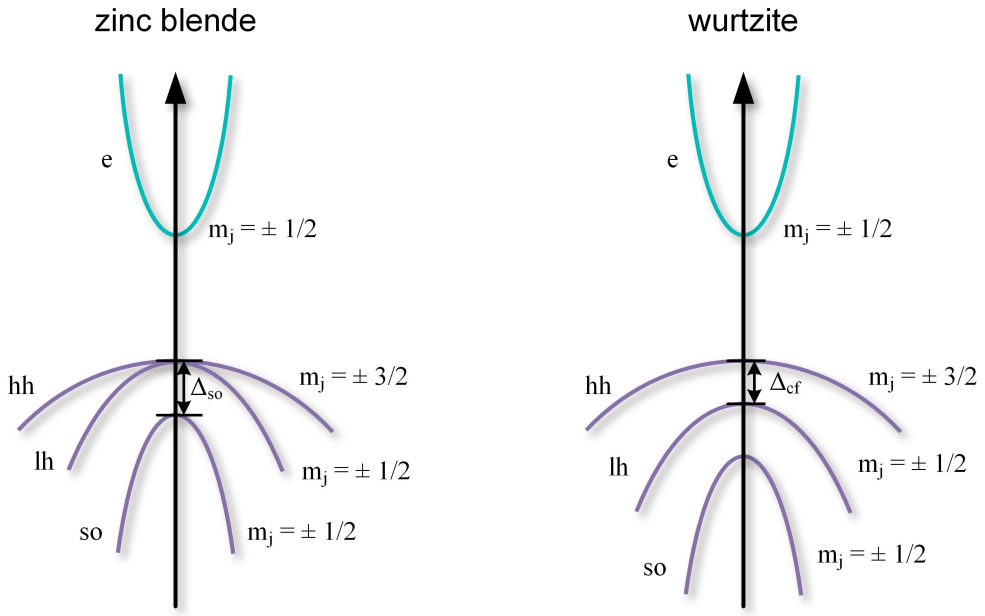

Figure 2.2: Schematic band structure of zinc blende (a) and wurtzite (b) structured materials. The conduction and valence bands are shown in turquoise and violet, respectively.

mainly anti-bonding, unoccupied conduction band, which are separated by the bandgap E_g. In II-VI semiconductors the valence band states are essentially provided by the *p*-type orbitals of the chalcogens, while the conduction band is mainly *s*-type and originates from the unoccupied outer orbitals of the metal cations.

Figure 2.2 depicts the schematic band structure of zinc blende and wurtzite type II-VI materials, respectively. In both types the conduction and valence bands exhibit their minima and maxima at the center of the Brillouin zone (Γ-point), forming a direct semiconductor. The electrons in the *s*-type conduction band exhibit zero orbital momentum ($l = 0$) and their total angular momentum ($j = l + s$) accounts for $j = \frac{1}{2}$. As the valence band is of *p*-type symmetry, all subbands possess an orbital angular momentum of $l = 1$. Due to the spin-orbit coupling the otherwise sixfold (including spin) degenerated valence band is split into a twofold degenerated spin-orbit split-off hole (*so*) band with a total angular momentum of $j = \frac{1}{2}$ and a four-fold state with $j = \frac{3}{2}$ at the Γ-point. The splitting is denominated as split-off energy Δ_{so}. For $k \neq 0$ the $j = \frac{3}{2}$ states are further split according to the projection of their total angular momentum along an observation axis (which might be a predominant axis due to lattice anisotropies or strain or the direction of an intrinsic or external magnetic field), indicated by the quantum number m_j. In accordance with their curvature in the energy dispersion determining the effective mass, the two subbands are called heavy hole (*hh*) for the $m_j = \pm\frac{3}{2}$ band and light hole (*lh*) for the $m_j = \pm\frac{1}{2}$ band. In a wurtzite type semiconductor the *hh* and *lh* subbands are already split at the

Γ-point due to the anisotropy in the crystal structure, as illustrated in Figure 2.2b. This splitting separating the *hh* and *lh* subbands is denominated as crystal field energy Δ_{cf}.

2.1.2 Doping and Alloying in II-VI Semiconductors

Both, the lattice and electronic structure are modified when impurity atoms are incorporated into a semiconductor host lattice, either in case of TM^{2+}-doping or for alloying. In order to differentiate between the two, alloying can be understood as a mixture in composition between two (or even more) equivalent end point elements or compounds, whose weights can be ideally tuned between 0 % to 100 % without phase segregation, like it is the case for most II-VI ternary alloys [89]. In contrast to this, doping may be interpreted as the admixture of one element, e.g., a transition metal into a dominant host material - which may be a binary II-VI compound semiconductor - by partial replacement of some atoms in the lattice. Typically the maximum doping concentrations are small.

The solubility of Mn^{2+} in CdSe, CdS or ZnS can reach up to 50 %, while at higher concentrations mixed phases occur in epitaxially grown crystals [9]. The main difference between both types of so-called pseudo-binary mixtures (combining two binary compounds sharing one element) is that in case of e.g., CdSe - ZnSe alloying, two cations with isovalent electronic structure (i.e. *(n-1)$d^{10}ns^2$* with completely filled *d* orbitals) are admixed, while in case of Mn^{2+} doping the *3d* shell is only half filled. Due to this, Mn^{2+} can either form bonds based on the tetragonal *sp^3* hybridization or an octahedral *spd* orbital configuration involving the free *d* orbitals, the latter representing the condition found in the stable rocksalt structured modifications of pure Mn chalcogenides (MnS and MnSe) [90]. This limits the incorporation of Mn^{2+} in zinc blende or wurtzite structured host semiconductors to below ≈ 50 % in bulk.

The lattice parameter as well as any material property originating from a significant volume in the lattice like e.g., the mechanical properties, are known to change linearly with the composition of the alloy between the two values for the pure components [91]. The lattice constant $a(x)$ of a II-VI pseudo-binary alloy $A_xB_{1-x}C$ follows Vegard's law [92]:

$$a(x) = x \cdot a_{\mathrm{AC}} + (1 - x) \cdot a_{\mathrm{BC}} \tag{2.1}$$

In contrast to this, the electronic structure and the optical properties do not simply scale with the composition. Figure 2.3 depicts the bandgaps of several II-VI pseudo-binary alloys (from [91]). The bandgap is found to follow a quadratic dependence on the composition [89]:

$$E_{\mathrm{g}}(x) = x \cdot E_{\mathrm{g}}^{\mathrm{AC}} + (1 - x)E_{\mathrm{g}}^{\mathrm{BC}} - x(1 - x)b \tag{2.2}$$

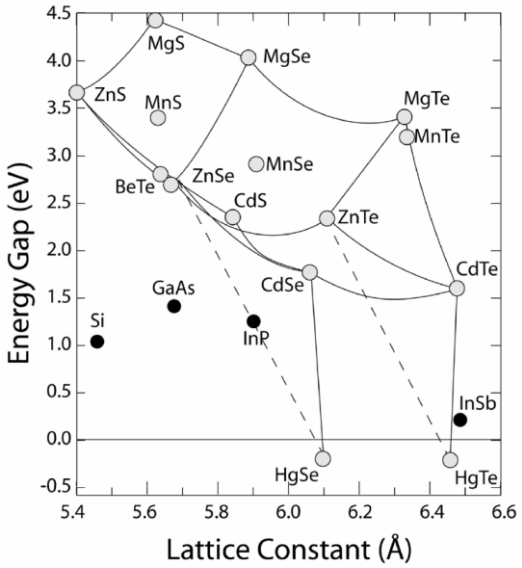

Figure 2.3: Energy gap as a function of the lattice constant for various II-VI pseudo-binary alloys (from [91]).

Herein $E_g^{AC/BC}$ denominates the bandgap of the pure components AC and BC and b is the bowing parameter, which usually has a positive value, so that the bandgap for alloys may even be reduced compared to the values of the pure components. This deviation from a linear dependence has been attributed to a combination of various influences.

$$b = b_{\text{intr}} + b_{\text{fluct}} \tag{2.3}$$

The first part b_{intr} represents an intrinsic contribution to the bowing. Describing the band structure of a random alloy with a *virtual crystal approximation*, the use of a linearly averaged atomic core potential in the Schrödinger equation leads to a quadratic dependence of the bandgap on the composition [91, 93]. Thus, even in a perfectly mixed alloy, bowing would be present. The second part originates from deviations from the averaged potential caused by e.g., local alloy fluctuations or local strain etc. [89, 91].

2.1.3 Temperature Effects on the Electronic Structure

The temperature dependence of the fundamental bandgap is a characteristic similarity among most semiconductors. With increasing temperature, the bandgap im most group IV, III-V or II-VI materials is observed to decrease monotonically, exhibiting weak quadratic or cubic dependencies at low temperatures, which changes to a nearly linear decay above the Debye temperature. Here, lead salts (e. g., PbS or PbSe), which exhibit a positive $\frac{dE_g}{dT}$, represent an exception. In most other semiconductors, the bandgap decay between cryogenic and room temperature accounts for $\approx$ 50 meV to 100 meV

[89], as can be seen in Figure 2.4 (plots are based on the fitting parameters given in [94]).

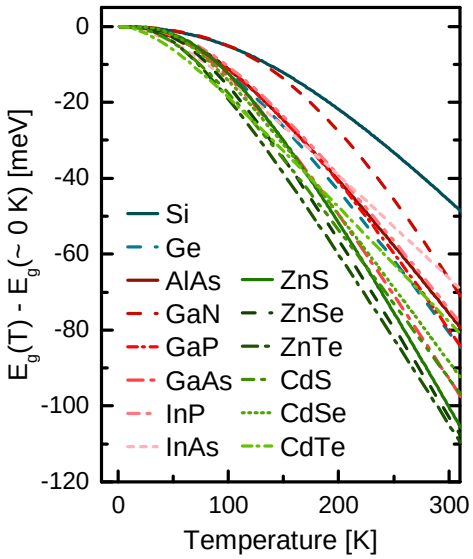

Figure 2.4: Temperature dependence of the bandgap for several group IV, III-V and II-VI semiconductors. Data sets plotted after [94].

The negative thermal coefficient of the bandgap is commonly attributed to a superposition of two effects, (i) the thermal lattice expansion and (ii) the electron phonon coupling - the latter representing the major contribution ($\approx 75\,\%$) [76, 77, 95]. The most common expression traditionally used to describe the temperature dependence of the bandgap in semiconductors is an empirical equation proposed by Varshni [76, 77]:

$$E_\mathrm{g}(T) = E_\mathrm{g}(0\,\mathrm{K}) - \frac{\alpha_\mathrm{V} T^2}{T + \beta_\mathrm{V}} \tag{2.4}$$

Herein $E_\mathrm{g}(0\,\mathrm{K})$ denotes the bandgap at $0\,\mathrm{K}$ and α_V and β_V are known as Varshni parameters, the latter being loosely related to the Debye temperature. At high temperatures ($T \gg \beta_\mathrm{V}$) the slope with temperature equals α_V.

Although most experimental results are sufficiently described with this equation, its parameters (α_V and β_V) do not exhibit a physical meaning; especially β_V exhibits only poor agreement with the Debye temperature in most cases [87]. As both factors contributing to the temperature dependent bandgap shift - the lattice dilation as well as the electron phonon interaction - scale with the occupation number of the involved phonons [77, 95], the temperature dependence can in general be described using expressions based on Bose-Einstein terms (describing the occupation factors of phonons). A semi-empirical model neglecting any phonon dispersion, which provides fitting parameters exhibiting a higher physical significance than the Varshni parameters, has been proposed by O'Donnel

and Chen [77]:

$$E_{\mathrm{g}}(T) = E_{\mathrm{g}}(0\,\mathrm{K}) - S_{\mathrm{fit}}\langle\hbar\omega\rangle\left[\coth\left(\frac{\langle\hbar\omega\rangle}{2k_{\mathrm{B}}T}\right) - 1\right] \tag{2.5}$$

Herein $\langle\hbar\omega\rangle$ denotes the average phonon energy and S_{fit} represents a dimensionless coupling constant. By a simple algebraic manipulation, it can easily be transformed to Equation 2.6, in which form it will be used later on.

$$E_{\mathrm{g}}(T) = E_{\mathrm{g}}(0\,\mathrm{K}) - \frac{2S_{\mathrm{fit}}\langle\hbar\omega\rangle}{\exp(\langle\hbar\omega\rangle/k_{\mathrm{B}}T) - 1} \tag{2.6}$$

At high temperatures $\frac{dE_{\mathrm{g}}}{dT}$ accounts for $-2S_{\mathrm{fit}}k_{\mathrm{B}}T$.

Table 2.1 lists Varshni parameters as well as S_{fit} and $\langle\hbar\omega\rangle$ for various II-VI semiconductors. Among these, the bandgap slope at high temperatures is minimal for zinc blende structured CdSe or hexagonal CdS and maximal for ZnSe.

Table 2.1: Varshni parameters and parameters for Equation 2.6 of O'Donnel & Chen for modeling the temperature dependence of the bandgap in II-VI semiconductors (from [89]).

Compound	Varshni's Equation			O'Donnel & Chen		
	$E_{\mathrm{g}}(0\,\mathrm{K})$ [eV]	α_{V} [meV K^{-1}]	β_{V} [K]	$E_{\mathrm{g}}(0\,\mathrm{K})$[eV]	S_{fit}	$\langle\hbar\omega\rangle$ [meV]
c-CdSe	1.772	0.37	150	1.765	2.83	18.9
h-CdSe	1.834	0.424	118	1.849	2.94	25.4
h-CdS	2.558	0.386	103	2.568	1.54	13.9
c-ZnSe	2.825	0.67	270	2.818	3.12	15.1

2.1.4 Excitons in Bulk Semiconductors

Due to their opposite charges, a free electron and a hole in a semiconductor can bind to each other through their Coulomb attraction, forming a so-called exciton, which is not captured in the single-particle picture drawn above. In most semiconductors, including the II-VI materials, the Coulomb interaction is shielded by the remaining electrons (as described by the dielectric constant ϵ_{r}), so that electron and hole are delocalized over many unit cells with a binding energy in the order of several tens of meV. This so-called Wannier exciton can be described as a quasi particle with an exciton center-of-mass-motion and a relative movement of the electron around the hole in analogy to the hydrogen atom, which gives rise to an exciton binding energy $E_{\mathrm{exc}}^{\mathrm{bulk}}$ as well as an exciton Bohr radius a_{B}

[96, 97]:

$$E_{\mathrm{exc}}^{\mathrm{bulk}} = -\frac{m_{\mathrm{r}} e^4}{2\hbar^2 \left(4\pi\epsilon_0\epsilon_{\mathrm{r}}\right)^2} \frac{1}{n_{\mathrm{exc}}^2}$$
$$a_{\mathrm{B}} = \frac{\hbar^2 4\pi\epsilon_0\epsilon_{\mathrm{r}}}{m_{\mathrm{r}} e^2} \tag{2.7}$$

Here m_{r} denotes the reduced effective mass of the exciton, which is defined as:

$$\frac{1}{m_{\mathrm{r}}} = \frac{1}{m_{\mathrm{e}}} + \frac{1}{m_{\mathrm{h}}} \tag{2.8}$$

This leads to several hydrogen-like excitonic levels ($n_{\mathrm{exc}} = 1, 2, ...$), where usually the $n_{\mathrm{exc}} = 1$ ground state is observed in experiment. In most cases, the exciton formation can be treated as a second order perturbation, slightly reducing the transition energies, which result from the single-particle conduction and valence band states. Due to their nature, the electron-hole wave function overlap integral of excitons and thus their oscillator strength is strongly enhanced, and therefore excitonic transitions often dominate the absorption of a material.

2.2 Influence of Quantum Confinement on the Electronic Structure

In case that at least one dimension of a structure approaches the length scale of the exciton Bohr radius, the wave functions of the electrons and holes are confined, so that their allowed energy states are no longer continuous, but semi-discrete or discrete, depending on the type of confinement. Due to the confinement energy of the electron and the hole the bandgap increases with decreasing dimension, introducing a size dependence of the bandgap.

In a three dimensional bulk material, the electron or hole wave functions may be described as plain wave terms within the frame of so-called Bloch functions [96]:

$$\Psi\left(\vec{r}\right) = u_{\mathrm{k}}\left(\vec{r}\right) \exp\left(i\vec{k} \cdot \vec{r}\right) \tag{2.9}$$

Herein $u_{\mathrm{k}}(\vec{r}) = u_{\mathrm{k}}(\vec{r} + \vec{T})$ describes the local variation of the wave function on a lattice site with the periodicity of the lattice vector $\vec{T}$, $\vec{r}$ denotes the position in the crystal and $\vec{k}$ is the wave vector. The wave function of an electron or a hole in a confining potential is given by a linear combination of Bloch functions with different k. In case the size of the nanostructure exceeds the dimension of a lattice cell, the Bloch functions are only weakly dependent on the wave vector ($u_{\mathrm{k}} \approx u_{\mathrm{k}=0}$) and the wave function can be simplified in

form of a product of the Bloch function and an envelope function $\psi(\vec{r})$ [96]:

$$\Psi\left(\vec{r}\right) = u_{\mathrm{k}=0}\left(\vec{r}\right)\psi\left(\vec{r}\right) \tag{2.10}$$

Within this so-called *envelope function approximation*, the confinement effects affect only on the envelope function, and the Schrödinger equation used to calculate energy states of quantum confined systems can be directly applied to the envelope function rather than to the whole wave function $\Psi\left(\vec{r}\right)$.

The confinement barrier may either be realized by a surrounding semiconductor with a higher bandgap like in epitaxial quantum dots or quantum wells, or by vacuum (or the ligands in most cases) in free-standing structures like colloidal nanocrystals. Depending on the shape of a structure, the electron and hole wave functions are either confined in one, two or three directions, like it is the case in quantum wells, quantum wires or quantum dots, respectively. In contrast to the conduction band, the three subbands of the valence band may be either separated or mixed by the confining potential, as elaborated below. In strongly confined systems, the electron-hole exchange interactions between both types of charge carriers have to be considered additionally, often causing a fine structure of the observed excitonic pattern.

Below, the electronic structure of two dimensional quantum wells like colloidal nanoplatelets are discussed with the help of the well-known "particle-in-a-box" model. Subsequently, the influence of a spherical confinement on the conduction and valence band states is presented and finally, the fine structure of the band edge excitonic transition in a strongly confined spherical system as apparent in MSCs is outlined.

2.2.1 Electronic Structure of Two-Dimensional Quantum Wells

The electronic states in a two-dimensional quantum well can be described with the "particle-in-a-box" model, considering the movement of an electron in an one-dimensional potential with infinitely high barriers (compare Figure 2.5). This approximation well describes colloidal two-dimensional structures like NPs or nanoribbons [35, 37], which are surrounded by organic ligands, but fails to describe epitaxial quantum wells embedded in cladding layers made of semiconductors with higher bandgaps. Here the finite potential height of the cladding layers has to be considered. The energies of the quantized states as well as the wave functions can be calculated based on the stationary Schrödinger equation:

$$-\frac{\hbar^2}{2m}\frac{d^2\psi_{n_{\mathrm{env}}}(x)}{dx^2} + V(x)\psi_{n_{\mathrm{env}}}(x) = E_{\mathrm{q}_{n_{\mathrm{env}}}}\psi_{n_{\mathrm{env}}}(x) \tag{2.11}$$

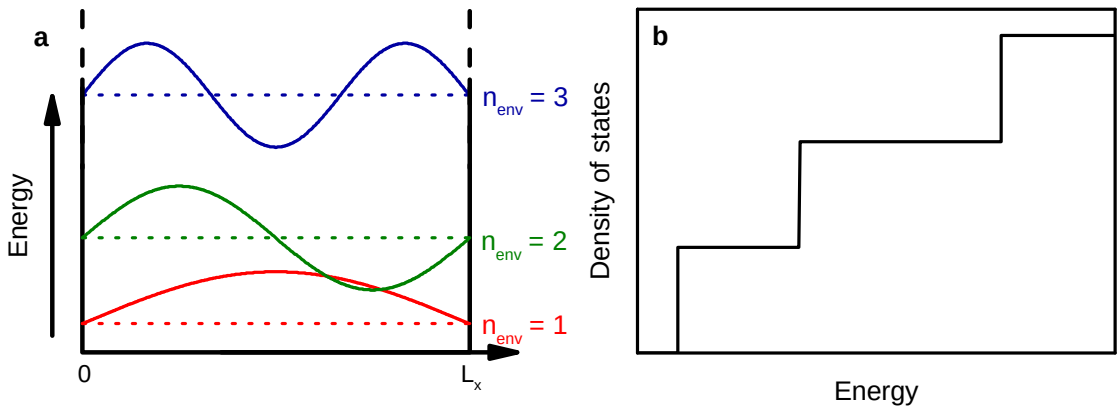

Figure 2.5: "Particle-in-a-box" model. (a) depicts the potential well and the energies and wave functions of the $n = 1, 2, 3$ states. (b) illustrates the density of states in a two-dimensional system.

Here, $V(x)$ represents the one-dimensional potential, m is the effective mass and $E_{\mathrm{q}_{n_{\mathrm{env}}}}$ and $\psi_{n_{\mathrm{env}}}$ denote the quantization energy and the envelope wave function of the state with the principle envelope quantum number n_{env}. Applying continuity conditions for the edges of the well, where the wave function vanishes ($\psi(0) = \psi(L_{\mathrm{x}}) = 0$), the energy states and wave functions can be calculated as:

$$E_{\mathrm{q}_{n_{\mathrm{env}}}} = \frac{\hbar^2 \pi^2}{2m} \frac{n_{\mathrm{env}}^2}{L_{\mathrm{x}}^2} \tag{2.12}$$

$$\psi_{n_{\mathrm{env}}}(x) = \sqrt{\frac{2}{L_{\mathrm{x}}}} \sin\left(\frac{n_{\mathrm{env}} \pi x}{L_{\mathrm{x}}}\right) \tag{2.13}$$

Herein, L_{x} is the quantum well width and $n_{\mathrm{env}} = 1, 2, 3, ...$ represents the envelope principal quantum number. Figure 2.5a depicts the energies and wave functions of the three energetically lowest states. The energy values, which refer to the energy of the bottom of the well, increase quadratically with n_{env}, while the wave functions possess the form of sine waves. Note that the first allowed energy is above the bottom of the quantum well, so that the bandgap increases in case of carrier confinement. The electrons and holes are confined solely in the quantization direction and are free to move in the plane of the quantum well, leading to a step-wise function of the density of states, compare Figure 2.5b (neglecting excitonic effects).

In general, the oscillator strength of a transition involving a hole state and an electron state is proportional to the overlap integral of the conduction and valence band wave functions. In a quantum well, the envelope functions are relevant. As in case of infinite barrier heights all envelope functions are sine waves, which represent a system of orthogonal functions, the overlap integral is zero for $\Delta n_{\mathrm{env}} = |n_{\mathrm{env,e}} - n_{\mathrm{env,h}}| \neq 0$ and all interband transitions with unequal n_{env} are forbidden. However, this selection rule is only

valid for infinite quantum wells. In finite quantum wells, which describe the common case in real systems, the wave functions decline exponentially outside the well, which softens the selection rules, so that transitions with $\Delta n = 0, \pm 2, \pm 4, ...$ become allowed.

The two-dimensional confinement in quantum wells also leads to a reduction of the exciton Bohr radius as compared to three dimensional semiconductors, which induces an increase of the exciton binding energy. Two-dimensional excitons can be described based on a product of the quantum well states (Equation 2.13) and a two-dimensional wave function [98], which leads to exciton binding energies given by [99]:

$$E_{\mathrm{exc}}^{\mathrm{2D}} = -\frac{m_{\mathrm{r}} e^4}{2\hbar^2 \left(4\pi\epsilon_0\epsilon_{\mathrm{r}}\right)^2} \frac{1}{\left(n_{\mathrm{exc}} - \frac{1}{2}\right)^2} \underset{n_{\mathrm{exc}}=1}{=} 4E_{\mathrm{exc}}^{\mathrm{bulk}} \tag{2.14}$$

For the ground state exciton ($n_{\mathrm{exc}} = 1$), this accounts for an increase of the exciton binding energy by a factor of four compared to the bulk value.

As evident from Equation 2.12, the confinement energy scales inversely with the effective mass of a charge carrier. Due to the different effective masses of the *hh* and *lh*, the one-dimensional quantum confinement in two-dimensional materials lifts the degeneracy at the top of the valence band and separates the *hh* and *lh* subbands. This enables the observation of excitonic transitions with well defined hole characters, as depicted in Figure 2.6 for colloidal nanoplatelets, which represent an ideal model system for a quantum well. Three distinct absorption peaks can be attributed to the *hh*, *lh* and *so* excitonic transitions (*hh*-X, *lh*-X and *so*-X).

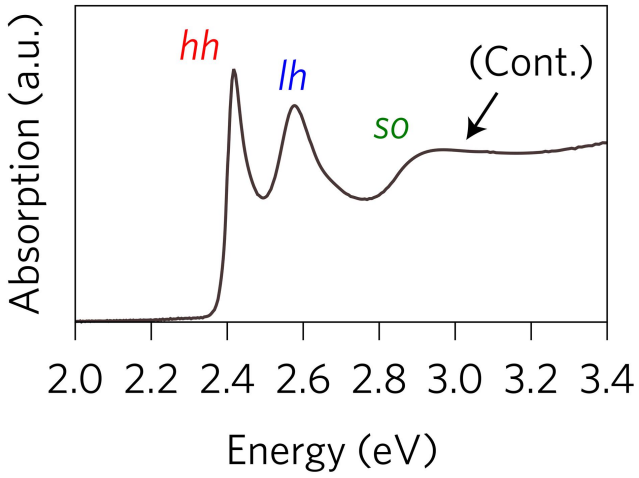

Figure 2.6: Absorption spectrum of colloidal CdSe nanoplatelets exhibiting distinct resonances for the *hh*-X, *lh*-X and *so*-X excitonic transitions. From [100].

The very fundamental "particle-in-a-box" model is quite sufficient to describe the basic optical features of colloidal nanoplatelets. However, systematic studies show that

the non-parabolicities of the electron and *lh* bands have to be considered in order to describe the *lh*-X transition energy quantitatively [35]. In highly confined regimes the lowest allowed k value increases ($k \propto \frac{1}{L_x^2}$), and due to the non-parabolicities the *lh* effective mass approaches the *hh* value, and thus the energy spacing between the *hh*-X and *lh*-X transition is found to be independent on the NP thickness.

Beyond this simple model, quantum wells do exhibit a fine structure caused by the electron-hole exchange interaction [101–104] - similar to the one described below for strongly confined quantum dots. The exchange interactions split the fourfold-degenerated *hh*-X state corresponding to different spin constellations (different combinations of $m_{\mathrm{j_{hh}}} = \pm\frac{3}{2}$ and $m_{\mathrm{j_e}} = \pm\frac{1}{2}$) into a bright and a dark doublet, defined by the total angular momentum projection $F_{\mathrm{m}} = m_{\mathrm{j_e}} + m_{\mathrm{j_{hh}}} = \pm 2$ or ± 1, respectively. While bright excitons ($F_{\mathrm{m}} = \pm 1$) can couple with the light field directly, dark excitons ($F_{\mathrm{m}} = \pm 2$) cannot recombine without e.g., a phonon carrying the redundant angular momentum.

2.2.2 Spherical Confinement in a Zero-Dimensional Quantum Dot

In spherically confined QDs like the giant shell nanoparticles or the MSCs, the two-dimensional confinement is replaced by a spherical confinement, leading to the model of a "particle-in-a-sphere" with an infinite barrier well at $r = a_{\mathrm{QD}}$, with a_{QD} respresenting the quantum dot radius. Solving the Schrödinger equation for such a potential yields spherical envelope wave functions similar to the atomic orbitals (analogously labeled with the quantum numbers $n_{\mathrm{env}} = 1, 2, 3, ...$ and $l_{\mathrm{env}} = 0, 1, 2, ... \equiv S, P, D, ...$) [12] with energies given by:

$$E_{\mathrm{q}n_{\mathrm{env}},\mathrm{l}_{\mathrm{env}}} = \frac{\hbar^2 \alpha^2_{\mathrm{n_{env}},\mathrm{l_{env}}}}{2ma^2_{\mathrm{QD}}} \tag{2.15}$$

Here $\alpha_{\mathrm{n_{env}},\mathrm{l_{env}}}$ represents the $n_{\mathrm{env}}{}^{\mathrm{th}}$ zero of the $l_{\mathrm{env}}{}^{\mathrm{th}}$ order spherical Bessel function. As the wave functions are based on a product of spherical harmonics and spherical Bessel functions, the selection rules for transitions between "particle-in-a-sphere" states follow from the orthogonality as $\Delta n_{\mathrm{env}} = \Delta l_{\mathrm{env}} = 0$.

In a spherical confinement, the Coulomb correction for the band edge excitonic transition accounts for [105]:

$$E^{\mathrm{0D}}_{\mathrm{exc}} = -\frac{1.8e^2}{4\pi\epsilon_{\mathrm{r}}\epsilon_0 a_{\mathrm{QD}}} \tag{2.16}$$

The "particle-in-a-sphere" model correctly describes the dependencies of the quantization energy on the dimensionality a_{QD} and is able to picture the electron wave functions and energy states in the conduction band [106], but fails to describe the holes states of the

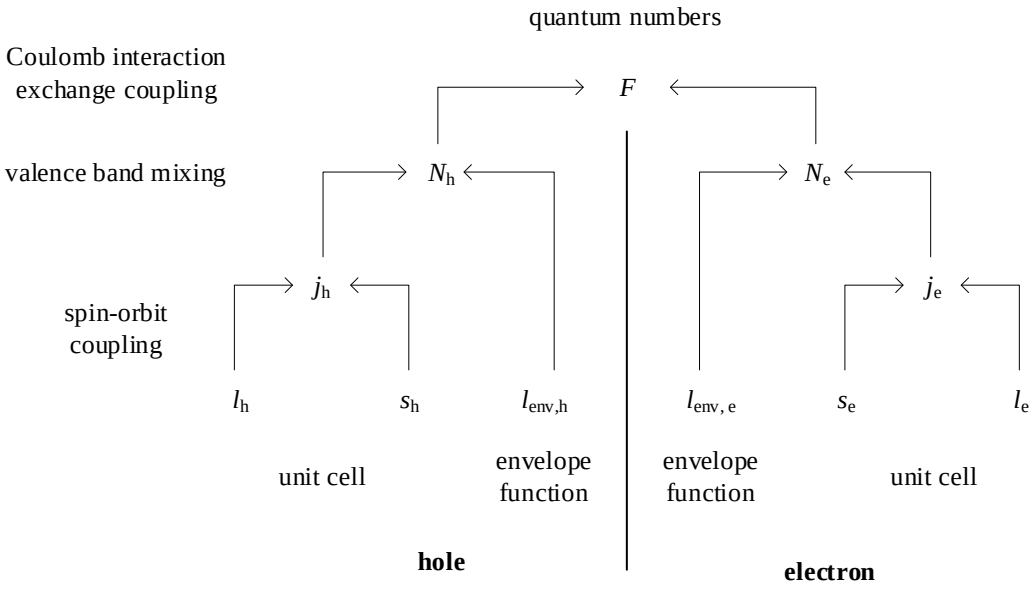

Figure 2.7: Relevant quantum numbers for the wave functions in the spherical confinement of colloidal QDs (after [12]). Both the unit cell total angular momentum ($j = l+s$) as well as the envelope orbital momentum l_{env} do not persist as good quantum numbers. A state with a given total angular momentum N represents a linear combination of various pairs of j and l_{env}. Note that for an electron in the twofold degenerated conduction band no mixing occurs. After [12].

inherently degenerated valence band [12]. In contrast to the two dimensional confinement in quantum wells, where each hole subband produces its own independent ladder of quantized states, the different valence subbands are mixed in the spherical confinement of the quantum dots [33, 34]. As a result, both the total angular momentum j_{h} resulting from the unit cell of the bulk as well as the envelope function orbital momentum $l_{\mathrm{env,h}}$ are no longer good quantum numbers. Instead, the sum of both components, which is given by the total angular momentum N_{h}, together with the parity remain the only good quantum numbers (compare Figure 2.7). Valence band hole states in colloidal nanocrystals include contributions from envelope functions with $l_{\mathrm{env,h}}$ and $l_{\mathrm{env,h}} + 2$, which is denominated as "*S-D* mixing", and represent admixtures of subbands with different j_{h}, i.e., different hole characters.

The valence band states are labeled according to $n_{\mathrm{env}} l_{\mathrm{env,h}}{}_{N_{\mathrm{h}}}$ with $l_{\mathrm{env,h}}$ representing the lowest involved envelope function. As the conduction band is not affected by band mixing, the electron states are denominated solely by their envelope function quantum numbers as $n_{\mathrm{env,e}} l_{\mathrm{env,ee}}$. Calculated conduction and valence band states are depicted in Figure 2.8 for varying nanocrystal radii, together with the energies of several transitions [34]. Note that for both theoretical calculations the conduction band non-parabolicities have been considered, while the Coulomb interaction has been integrated as a first-order

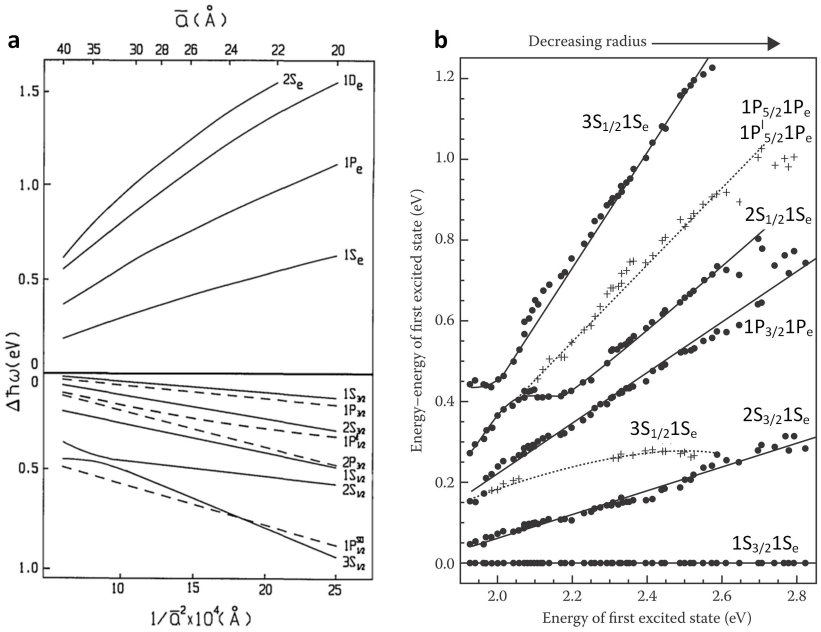

Figure 2.8: Valence band mixing in colloidal QDs. (a) Conduction and valence band energy states calculated based on an *effective mass approximation*. From [33]. (b) depicts a comparison of theoretically calculated (line) and experimentally determined (dots) energies for various transitions. Calculated energies include the Coulomb interaction as a first-order energy correction. After [34].

energy correction.

The energetically lowest band edge transition involves the $1S_{3/2}$ hole state and the $1S_e$ electron state ($1S_{3/2}1S_e$) and commonly evokes the dominating absorption peak of colloidal QDs. In order to describe the absorption pattern of colloidal quantum dots, the valence band mixing due to a spherical confinement acting on the hole subbands is sufficient [34]. Nevertheless, each line drawn in Figure 2.8 represents a highly manifold multiplet, whose degeneracy is partly lifted in reality due to additional effects not considered in the model above, like the electron-hole exchange interaction or uniaxial pertubations like shape anisotropies or a wurtzite lattice structure. These effects give rise to the so-called fine structure splitting for each transition, which becomes relevant for the dynamics of the photoluminescence [106, 107] or the Stokes shift between absorption and emission [108, 109] of colloidal QDs. In very small nanocrystals like the MSCs, the fine structure may even be visible in the ensemble absorption [31]. The fine structure as well as its observation in MSCs is thus discussed in the next subbsection.

2.2.3 Band Edge Transition in Strongly Confined Quantum Dots

While the electron state exhibits twofold degeneracy, the hole state of the $1S_{3/2}1S_e$ band edge transition is fourfold degenerated with respect to the projection of its total angular

momentum $N_{\mathrm{m,h}} = \pm\frac{3}{2}, \pm\frac{1}{2}$ ($N_{\mathrm{m,h}} = \pm N_{\mathrm{h}}, \pm(N_{\mathrm{h}} - 1)$). This leads to an eightfold degenerated band edge excitonic transition, which is split into a maximum of five fine structure states due to two, fundamentally different perturbations: (i) The influence of an uniaxial pertubation, which might either be represented by a lattice asymmetry in wurtzite structured materials or a shape anisotropy due to oblate or prolate geometry. (ii) The influence of the exchange interactions between the electron and the hole, which appear negligible in bulk but increase strongly upon reduction of the nanocrystal dimensions.

Analog to the uniaxial anisotropy present in bulk wurtzite semicondcutors or quantum wells splitting the hh and lh components with different m_{j}, the nanocrystal anisotropy splits the quantized hole states according to their projection of the total angular momentum $N_{\mathrm{m,h}}$ of $\pm\frac{3}{2}$ and $\pm\frac{1}{2}$ to two (twofold) Kramer-doublets (compare Figure 2.9, left side). While the splitting due to the intrinsic lattice anisotropy scales with the ratio of the hh to lh effective masses, the splitting due to shape anisotropy increases with the confinement energy and may change its sign depending on whether the crystals are oblate or prolate. Thus, the net splitting, resulting from a superposition of both anisotropies, can even be negative, inverting the order of the hole states.

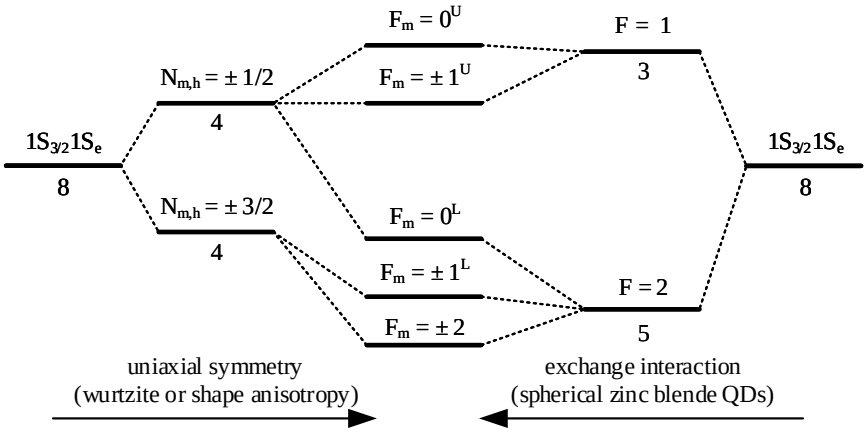

Figure 2.9: Fine structure splitting in strongly confined spherical QDs. While the nanocrystal asymmetry (either lattice or shape anisotropy) lifts the hole state degeneracy according to the projection of the hole total angular momentum, the exchange interaction in small nanocrystals splits the band edge exciton into an optically passive $F = 2$ and an optically active $F = 1$ state. After [12].

The electron-hole exchange interaction on the other hand splits the eightfold degenerated $1\mathrm{S}_{3/2}1\mathrm{S}_{\mathrm{e}}$ transition according to the electron and hole spin states, which are described by the excitonic (i.e. electron + hole) total angular momentum F. In zinc blende bulk crystals the band edge transition is split into an optically passive $F = 2$ and an optically active $F = 1$ state. According to their angular momentum projections the former is fivefold and the latter threefold degenerate (compare right side of Figure 2.9).

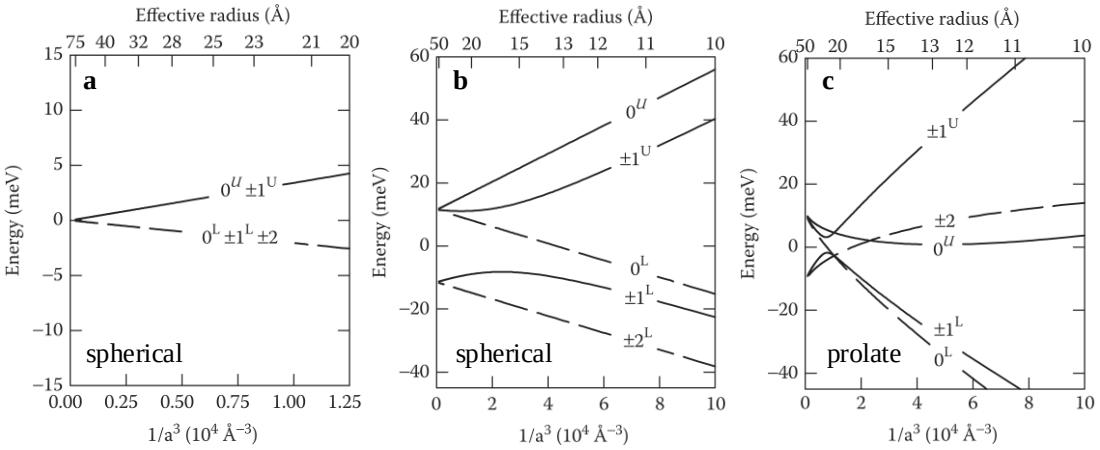

Figure 2.10: Calculated fine structure pattern of spherical QDs with zinc blende (a, CdTe) or wurtzite (b, CdSe) lattice structure compared to the splitting in prolate nanocrystals with wurtzite structure (c, CdSe). From [106]. Dashed/solid lines indicate optically passive/active states.

Together, the nanocrystal anisotropy and the exchange interaction split the band edge transition into one twofold degenerated state with exciton angular momentum projection $F_\mathrm{m} = \pm 2$, two twofold degenerated states with $F_\mathrm{m} = \pm 1$ and two non-degenerated states with $F_\mathrm{m} = 0$. In order to differentiate between fine structure states with the same F_m, they are labeled with $^\mathrm{L}/_\mathrm{U}$ for the lower and the upper state, respectively. Calculated fine structure patterns for spherical nanocrystals with zinc blende (solely exchange interaction) and wurtzite structure (exchange interactions + lattice anisotropy) are compared to prolate, wurtzite structured QDs in Figure 2.10. Optically allowed transitions are indicated with solid lines, while dashed lines indicate optically forbidden transitions. Similarly to the dark state in quantum wells, the ± 2 transition is optically inactive, as photons cannot carry an angular moment of 2. The optical inactivity of the 0^L state results from a destructive interference of the two indistinguishable excitonic states contributing to $F = 0$ (i.e., the two combinations of $N_\mathrm{m,h} = \pm\frac{1}{2}$ and $m_\mathrm{j,e} = \mp\frac{1}{2}$).

Yang *et al.* used the fine structure theory developed for colloidal QDs to explain band edge transitions of $(CdSe)_{13}$ MSCs [31]. These clusters represent the boundary between molecules and nanocrystals, containing only 26 atoms. Comparing absorption and MCD spectra, they were able to identify several magneto-optically active and inactive transitions, which were attributed to the fine structure peaks of the $1S_{3/2}1S_e$ band edge transition. The assignment of the different peaks are shown in Figure 2.11a.

Obviously, the fine structure theory by Efros, Al. L. *et al.* represents a rough approximation for the electronic structure of the $(CdSe)_{13}$ MSCs [106]. In particular, the basic assumption for the *envelope function approximation*, requiring that the dimensions of the structure considerably exceed the size of the unit cell, is not fulfilled for the clusters.

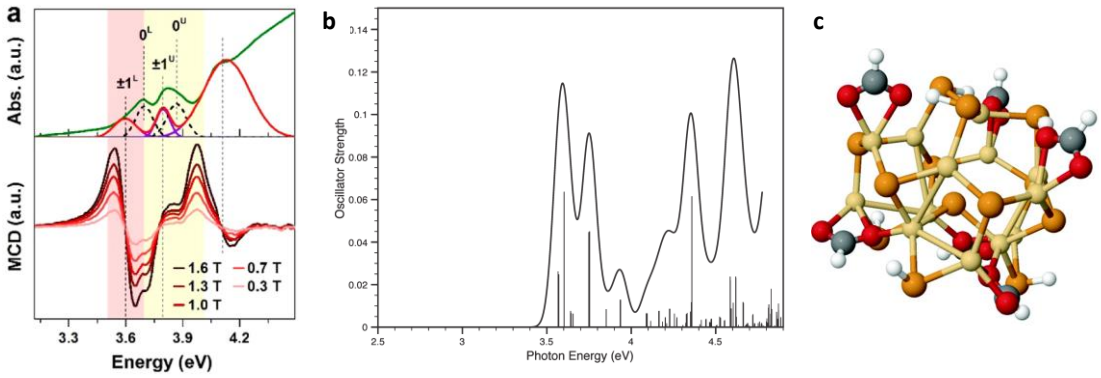

Figure 2.11: Fine structure splitting in strongly confined MSC. (a) depicts an absorption (top) and magnetic circular dichroism (MCD) (bottom) spectrum of Mn^{2+}-doped $(CdSe)_{13}$ MSCs at 5 K. Dashed lines indicate the different fine structure peaks. From [31]. In (b) calculated transition energies as well as a simulated absorption spectrum achieved via time-dependent DFT are shown. (c) depicts the corresponding crystal structure of the $(CdSe)_{13}$ clusters. (b) and (c) from [64].

As the charge carrier wave functions in $(CdSe)_{13}$ can obviously not be described with the envelope function used in conventional QDs, any effective mass approximation can be regarded as a crude simplification for the clusters representing the boundary towards molecules. Thus, it is conceivable that the selection rules determining the optical activities are partly lifted, allowing e.g., the observation of the formally forbidden transitions. The assignment of the various fine structure states as known from [106] to the observed transitions in $(CdSe)_{13}$ MSCs can thus only be interpreted as symbolic equivalents. However, the fine structure theory provides a theoretical access for the understanding of the optical and magneto-optical behaviour of the observed absorption pattern in the $(CdSe)_{13}$ clusters.

The common way to describe the optical properties of such small clusters is their atomistic calculation via DFT [64, 66, 68, 110, 111]. Here in a first step, the lattice structure of the MSCs is obtained minimizing the clusters overall energy. Subsequently, access to the electronic structure can be gained. Figure 2.11b depicts a theoretical absorption spectrum obtained as a Gaussian convolution of the transition energies calculated via time-dependent DFT for the $(CdSe)_{13}$ cluster shown in Figure 2.11c. Note that the specific structure of the $(CdSe)_{13}$ MSCs, which is still controversially discussed [64–69] (compare 5.1.3), determines the absorption shape. The spectrum is calculated for a so-called core-cage cluster, which is considered as one of the most stable structures of $(CdSe)_{13}$, additionally capped with formate hydrogen pairs (red, grey and white atoms in Figure 2.11c). The calculated spectrum reveals the two dominant absorption peaks above 3.5 eV, which are evident in the experimental data (compare Figure 2.11a). Particularly, the two absorption peaks include at least eight individual transitions up to 3.8 eV, indicated by

the black lines in Figure 2.11b. Accordingly, the picture of the electronic structure drawn by DFT calculations is not significantly different from the fine structure pattern proposed based on the *effective-mass approximation* by Efros, Al. L. *et al.* It can thus be assumed that the two peaks dominating the bandgap absorption of MSCs originate from the fine structure of the $1S_{3/2}1S_e$ transition.

2.3 Electronic Structure of Transition Metal Ions in a Tetrahedral Crystal Field

First row transition metals ions - as used for magnetic doping in DMS materials - are characterized by their partly filled *3d* subshell combined with a filled *4s* valence orbital. In analogy to Cd^{2+}, these outer electrons are released in case the dopants are embedded as TM^{2+} cations into a II-VI host semicondcutor, so that the *4s* and *4p* orbitals (hybridized to $4sp^3$) can be regarded developing the covalent bonds, while the inner *3d* orbitals of the transition metals are considered as nonbonding orbitals [112] (note that this may be different in other material systems). Due to the partly filled *d*-shell, the TM^{2+} dopants exhibit a nonzero spin moment S, in strong contrast to the atoms/ions of the host material in the $3d^{10}$ configuration with $S = L = 0$. For the TM^{2+} used as dopants within the scope of this thesis, the spin moments equal $S = \frac{5}{2}$, $L = 0$ for Mn^{2+} and $S = \frac{3}{2}$, $L = 3$ for Co^{2+}, exhibiting electron configurations of $[Ar]3d^5$ and $[Ar]3d^7$, respectively.

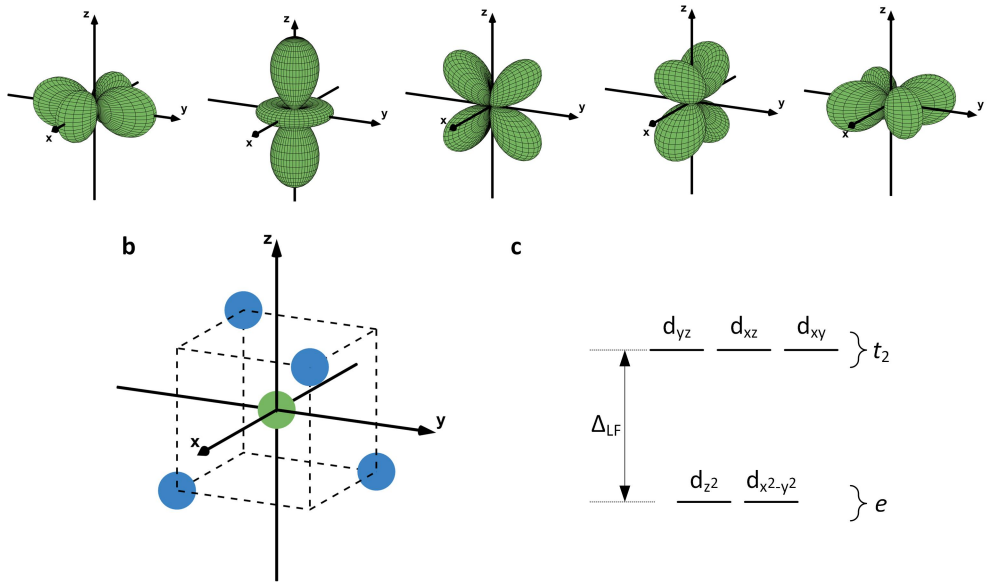

Figure 2.12: Electronic structure of the TM^{2+} *3d* orbitals. (a) depicts the five different *3d* orbitals. In (b) the tetrahedral arrangement of the four anions around a TM^{2+} cation is illustrated. Both from [113]. (c) represents the splitting of the *3d* orbitals in a crystal field.

In addition to the magnetic exchange interactions between the dopant spins and the charge carriers of the host semiconductor (discussed in detail below), TM^{2+}-doping also introduces additional electronic transitions between the (not completely filled) orbitals located essentially on the TM^{2+} ions. The energetic pattern of the *3d* orbitals can be qualitatively described within the crystal field theory, in which the nearest anions (Se or Zn) surrounding the TM^{2+} cation are treated as point charges creating a potential, which interacts with the TM^{2+} *d* orbitals [70, 114]. The relative coordination of the anions (denominated as ligands in this context) around the TM^{2+} ions is crucial for the *3d* orbital energy splitting. Figure 2.12a depicts the orbital part of the five *d* orbitals, derived as a real representation of the the hydrogen-like wave functions of a free ion [113, 115]. While the d_{z^2} and $d_{x^2-y^2}$ orbitals have their electron density maxima directed along the Cartesian axes, the remaining d_{yz}, d_{xz} and d_{xy} orbitals point towards the region between the axes. Comparison with the tetrahedral coordination of the four ligand atoms around the central ion (representing a T_d point group, compare Figure 2.12b) evidences, that the *d* orbitals are not equally affected by the ligands: As the repulsion between the latter and the ligands depends on the degree in which the orbitals venture into the vicinity of the point charges, it is obvious that the d_{yz}, d_{xz} and d_{xy} orbitals are energetically less favorable than the d_{z^2} and $d_{x^2-y^2}$ orbitals. The electrostatic potential of the ligands introduces a splitting in a doubly degenerate *e* and a triple degenerated t_2 set (the numerical subset denotes the behavior with respect to rotation or reflection), as depicted in Figure 2.12c.

In order to quantitatively describe the so-called ligand field electronic transitions in TM^{2+} ions containing more than one electron in the *3d* shell, the crystal field theory must be expanded to the ligand field theory, which in addition includes the *d*-*d* inter-electronic repulsion between the electrons occupying the *d* shell and the spin-orbit coupling between the spin and orbital momentum of these electrons [70]. The former depends on the distribution of *3d* electrons among the different orbitals and determines that it is energetically more favorable for two electrons to occupy differed orbitals with parallel spin than one with paired spins. It also dictates the order, in which different orbitals are occupied (known as Hund's rule for the ground state). For first-raw TM elements like Co^{2+} or Mn^{2+}, where the *d* orbitals are not shielded by electrons in higher *s* or *p* orbitals, the influence of the ligand field is of the same magnitude or smaller than the inter-electron repulsion, while the spin-orbit interaction can be regarded as a small perturbation.

Inter-electronic repulsion between the electrons in the *3d* orbitals gives rise to the free ion terms, i.e. the various energy levels resulting from the different assignments of electrons to a certain set of orbitals (denominated as ^{2S+1}X, with $2S+1$ as the spin multiplicity and X specifying L with $S = 0$, $P = 1$, $D = 2$, ...) [115]. For Mn^{2+} ions the most stable

free ion configuration ^{6}S corresponds to five unpaired electrons ($S = \frac{5}{2}$ and $L = 0$), while the Co^{2+} ground state ^{4}F denotes a configuration with three unpaired spins and a total angular momentum of $L = 3$. Influenced by a ligand field, these free ion terms split or convert into either one- (A), two- (E) or threefold (T) orbitally degenerated terms, while maintaining their spin multiplicity $2S + 1$.; e.g, $^4T_1$ denotes a 12-fold degenerated term with an orbital multiplicity of 3 and a spin multiplicity of 4.

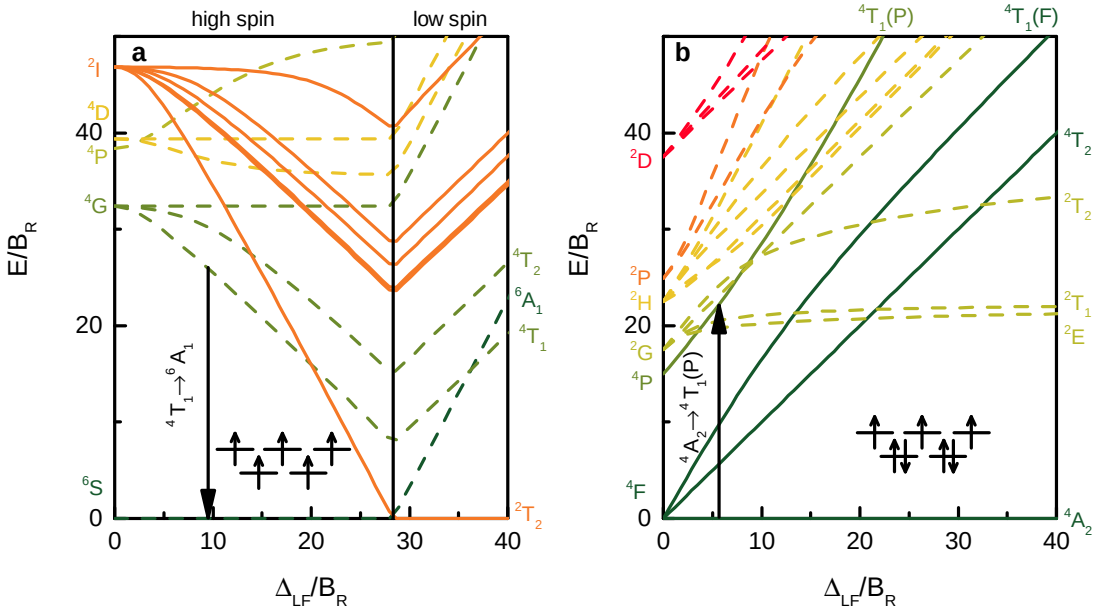

Figure 2.13: Tanabe-Sugano diagram for Mn^{2+} (a) and Co^{2+} (b). Transitions are depicted for C_R/B_R ratios typically found in II-VI materials ($C_R/B_R = 4.48$ for Mn^{2+} and $C_R/B_R = 4.5$ for Co^{2+}. The nomenclature for the free ion terms can be found at the left axis, while the denomination of the ligand field terms is given at the right and upper axes. After [116].

The energy levels of the ligand field terms can be calculated quantitatively including both ligand fields and inter-electronic repulsion (described with the cation-specific Racah parameters B_R and C_R [117]), and are commonly presented in form of Tanabe-Sugano diagrams [70, 118], in which the energies of the excited states are plotted against the ground state energy as a function of the ligand field strength Δ_{LF}. As both axes are scaled in multiples of the Racah parameter B_R, one diagram can be used for a specific ion in any crystal field. Δ_{LF} and B_R values for Mn^{2+} and Co^{2+} in several II-VI hosts can be found in Table 2.2.

Figure 2.13 depicts Tanabe-Sugano diagrams for Mn^{2+} and Co^{2+} in T_d geometry. Insets represent the spin configuration in the ligand field ground terms with maximum spin projection, while black arrows indicate the most important transitions for both ions in II-VI semiconductors, respectively. The energies of transitions between states with different S also depend on the Racah parameter C_R, and are indicated in Figure 2.13

Table 2.2: Ligand field energy and Racah parameter B_R for Mn^{2+} and Co^{2+}.

ion	host	$\Delta_{LF}/10$ [cm^{-1}]	B_R [cm^{-1}]	C_R [cm^{-1}]	reference
Mn^{2+}	ZnSe	405	740	2740	[119]
Mn^{2+}	ZnS	440	762	2736	[119]
Co^{2+}	CdSe	320–323	598–610	-	[120, 121]
Co^{2+}	CdS	315–316	664–665	-	[120, 122]
Co^{2+}	ZnSe	361	584	2670	[120]
Co^{2+}	ZnS	375–385	610–611	2831	[120, 123]

for C_R/B_R values most likely for Mn^{2+} and Co^{2+} in II-VI materials ($C_R/B_R = 4.48$ and 4.5 for Mn^{2+} and Co^{2+}, respectively). For Mn^{2+} a discontinuity in the diagram marks the crystal field strength at which the transition from high spin to low spin species occurs, as the increasing crystal field splitting forces the spins to pair in the lower e subset. The oscillator strengths of the various transitions (reflected with solid and dashed lines in Figure 2.13 for allowed and less-allowed transitions, respectively), defining whether a specific peak is observed in absorption, are determined by two selections rules: (i) the spin selection rule requiring maintenance of the spin quantum number S and (ii) the parity selection rule (often known as Laporte rule), demanding different parities for the ground and excited state wave function. As tetrahedral complexes do not exhibit an inversion center, all ligand field transitions are formally Laporte allowed.

In case of Mn^{2+} with five unpaired spins in the ground state, all *d-d* ligand field transitions are formally spin-forbidden, but gain some intensity due to spin-orbit coupling between the spin and orbital momentum of the TM^{2+} cations as well as the surrounding anions [11, 124], weakening the well defined spin quantum numbers. However, the energetically lowest $^4T_1 \rightarrow {}^6A_1$ transition, which is hardly observed in absorption in Mn^{2+}-doped DMS materials [121], generates a characteristic feature in photoluminescence (PL). This transition in particular dominates the emission behavior of many II-VI QDs doped with Mn^{2+}, as it often lies energetically below the host semicondcutor bandgap, allowing an energy transfer from excitonic states into the Mn^{2+} ligand field levels.

In contrast to Mn^{2+}, Co^{2+} has several low-energy ligand field transitions, which are spin-allowed and provide an optical approach to the chemical environment of Co^{2+} dopants in II-VI materials. While the two energetically lowest transitions to the $^4T_2$ and $^4T_1(F)$ states are in the infrared and near-infrared region of the spectrum, the $^4A_2 \rightarrow {}^4T_1(P)$ transition is frequently observed even at low Co^{2+} concentrations in absorption. Upon application of an external magnetic field, the spin degeneracy is partly removed allowing for the observation of pronounced features of the $^4A_2 \rightarrow {}^4T_1(P)$ transition also in MCD spectroscopy [71, 125–127]. In strong contrast to Mn^{2+}, the PL of Co^{2+}-doped DMS

materials is strongly quenched in most cases, as the cascade of Co^{2+} internal ligand field transitions, in particular the $^4T_1(P)$ and $^4T_1(F)$ levels, provide efficient nonradiative relaxation pathways.

2.4 Zeeman Effect and Exchange Interactions

The extraordinary functionalities of DMS materials originate from the exchange coupling between the *3d* electrons of the TM^{2+} dopants and the *s*- and *p*-like electrons and holes of the host material, respectively. These functionalities gain importance in case the TM^{2+} spins exhibit an intrinsic order and thus an overall magnetization, either due to alignment along an external magnetic field or an internal exchange field provided by charge carriers. The impact of a magnetic field on the intrinsic electronic structure of the host semiconductor and the magneto-optical characteristics of DMS materials are presented below.

2.4.1 Intrinsic Zeeman Effect

In the presence of an external magnetic field, the electronic structure and likewise the optical properties of a semiconductor are changed due to a coupling of the magnetic moments of the charge carriers to the magnetic field. Depending on the orientation between the magnetic field and the magnetic moments, the energy levels are shifted introducing a splitting of the optical transitions. This is called the intrinsic Zeeman effect.

For a charge carrier in the conduction or valence band, the Hamiltonian describing the linear magnetic field effects (neglecting the diamagnetic shift) can be written as [12]:

$$\mathcal{H}_{\mathrm{int,c/v}} = g_{\mathrm{e/h}}\,\mu_{\mathrm{B}}\,\vec{s}_{\mathrm{e/h}} \cdot \vec{B} \tag{2.17}$$

Herein, $g_{\mathrm{e/h}}$ and $\vec{s}_{\mathrm{e/h}}$ denote the Landé g-factor and the spin operator of the electron and the hole, respectively, μ_{B} is the Bohr magneton and $\vec{B}$ an external magnetic field with amplitude B. The Zeeman shift of a specific band depends on its total angular momentum projection m_{j} along the magnetic field ($\propto g_{\mathrm{e/h}}\,\mu_{\mathrm{B}}\,m_{\mathrm{j}}B$).

The energy of an electron in the conduction band or a hole in the valence band at the

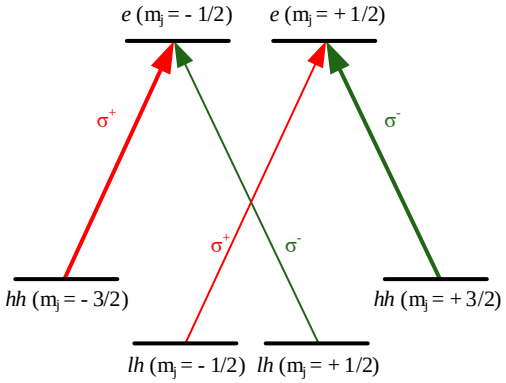

Figure 2.14: Selection rules for the $e - hh$ and $e - lh$ transitions according to the Bloch function quantum numbers.

Γ-point can then be described as [128]:

$$\begin{aligned} E_c =& E_\mathrm{g} \pm \frac{1}{2}\, g_\mathrm{e}\, \mu_\mathrm{B} B \quad \text{for} \quad m_\mathrm{j} = \pm\frac{1}{2} \\ E_v =& \begin{cases} \pm\frac{3}{2}\, g_\mathrm{h}\, \mu_\mathrm{B}\, B & \text{for the } hh \ (m_\mathrm{j} = \pm\frac{3}{2}) \\ \pm\frac{1}{2}\, g_\mathrm{h}\, \mu_\mathrm{B}\, B & \text{for the } lh \ (m_\mathrm{j} = \pm\frac{1}{2}) \end{cases} \end{aligned} \tag{2.18}$$

According to the optical selection rules, the corresponding energy splitting of the optical transitions results in a superposition of the electron and hole splitting. As photons carry an angular momentum of $\pm\hbar$, transitions are allowed in case of $\Delta l = 1$, which is satisfied for a transition involving a s-type conduction and a p-type valence band states. A spinflip is forbidden by the spin selection rule ($\Delta s = 0$). The change in the projection of the total angular momentum Δm_j defines whether a transition is optically allowed for circularly left polarized (σ^-) ($\Delta m_\mathrm{j} = -1$), circularly right polarized (σ^+) ($\Delta m_\mathrm{j} = +1$) or linear (π) polarized ($\Delta m_\mathrm{j} = 0$) light. For a bulk semiconductor, the optical allowed transitions for σ^- and σ^+ light are indicated in Figure 2.14.

The Zeeman splitting is defined as the difference in the transition energies between the σ^+ and σ^- light, following the convention in [12]:

$$\Delta E_\mathrm{Z} = E_{\sigma^+} - E_{\sigma^-} \tag{2.19}$$

The intrinsic Zeeman splitting can also be expressed using an excitonic g-factor g_int:

$$\Delta E_{\mathrm{Z}_\mathrm{int}} = g_\mathrm{int} \mu_\mathrm{B} B \tag{2.20}$$

The magnitude of the intrinsic Zeeman effect is usually rather small ($|g_\mathrm{int}| \approx 1$) and can

Table 2.3: Intrinsic g-factor g_{int} for relevant II-VI semiconductors.

host	g_{int}	
CdSe	1 to 1.4	[129, 130]
CdS	-1 to -1.3	estimated from [131]
ZnSe	1.1 to 2.5	[22, 24]

often be neglected compared to the giant Zeeman splitting induced by the *sp-d* exchange interactions [8, 9]. It is temperature independent [129], but changes slightly with the crystal size [130, 131]. The intrinsic g-factors for several II-VI hosts relevant for this thesis are listed in Table 2.3.

2.4.2 Orientation of a TM^{2+} Sublattice along a Magnetic Field

The magneto-optical functionalities of DMS materials scale with the overall magnetization of the TM^{2+} spin sublattice. In order to minimize their energy, the magnetic moments of the TM^{2+} dopants align along an (external) magnetic field, creating a net magnetic moment. This is antagonized by the thermal energy. On the other hand, the TM^{2+} ions exhibit so-called *d-d* spin-spin exchange interactions, which may influence their orientation towards each other. Both influences have to be considered - depending on temperature and dopant concentration - in order to describe the behavior of the TM^{2+} sublattice.

In the dilute limit below a concentration of 1 %, the TM^{2+} ions can be regarded as isolated magnetic moments and any interaction between neighboring TM^{2+} ions can be neglected [88]. In this case, the magnetic moments behave like ideal paramagnets, tending to align along the external magnetic field. This orienting force is opposed by the thermal energy, which impedes the TM^{2+} spins from orienting in the direction of the external field. Neglecting any anisotropies, the magnetization originated by their magnetic moments can be described with the Brillouin function $B_{\mathrm{S}}(\xi)$, giving respect to the fact that the magnetic moments of a paramagnetic atom or ion in a lattice can only adopt quantized states defined by $\pm S, \pm(S-1), ...$, which are occupied following a Boltzmann distribution.

$$B_{\mathrm{S}}(\xi) = \frac{2S+1}{2S} \coth\left(\frac{2S+1}{2S}\xi\right) - \frac{1}{2S} \coth\left(\frac{1}{2S}\xi\right) \tag{2.21}$$

with

$$\xi = \frac{g_{\mathrm{TM}}\mu_{\mathrm{B}} S B}{k_{\mathrm{B}} T} \tag{2.22}$$

Herein, g_{TM} denotes the gyromagnetic factor (g-factor). The g_{TM} of Mn^{2+} and Co^{2+} are $g_{\mathrm{Mn}} = 2.0041$ (2.0029, 2.0051) in CdSe (CdS, ZnSe) [12] and $g_{\mathrm{Co}} = 2.3$ (2.26) in CdSe (CdS) [132]. μ_{B} represents the Bohr magneton, k_{B} the Boltzmann constant and T the

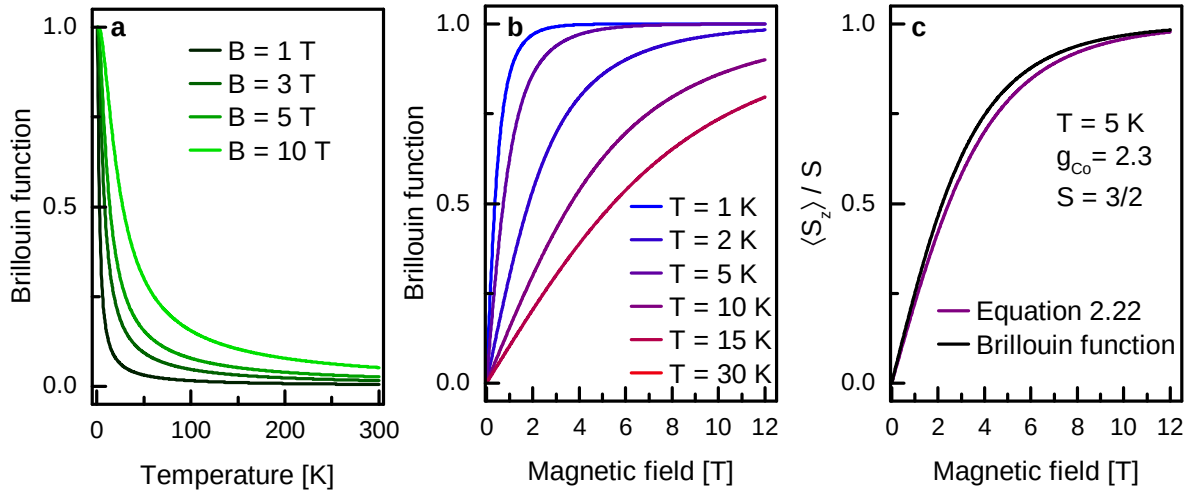

Figure 2.15: Temperature and magnetic field dependence of the Brillouin function. (a) illustrates the decrease of the Brillouin function with temperature at different magnetic fields, while (b) compares its increase with magnetic field at different temperatures. Both depict the Brillouin function for Mn^{2+} ions with $g_{Mn} = 2$ and $S = \frac{5}{2}$. In (c), the Brillouin function is compared to Equation 2.25 for Co^{2+} in CdSe (with $S = \frac{3}{2}$, $g_{Co} = 2.3$ and $D = 0.062\,\text{meV}$) at 5 K.

temperature.

Figure 2.15 depicts the temperature and magnetic field dependencies of the Brillouin function. At zero magnetic field the magnetic moments are distributed isotropically cancelling out each other, so that no net magnetization is present. With increasing magnetic field the spins align along the predominant direction, while with increasing temperature the thermal energy decreases the degree of orientation among the TM^{2+} sublattice. At high magnetic fields and/or low temperatures, the magnetization saturates in case that all TM^{2+} magnetic moments are aligned. The magnetization originating from the TM^{2+} spins can be described by:

$$M = N_0 x g_{\text{TM}} \mu_{\text{B}} S B_{\text{S}}(\xi) \tag{2.23}$$

The mean projection of the spin S along the direction of the magnetic field is given by:

$$\langle S_{\text{z}} \rangle = S B_{\text{S}}(\xi) \tag{2.24}$$

In the strict sense, the Brillouin function is only appropriate for systems with negligible anisotropy, i.e. DMS materials with zinc blende structure. In anisotropic systems like wurtzite structured materials, the spin-orbit interaction together with the crystal field may generate magnetic anisotropy causing a deviation from the Brillouin function. However, magnetic dopants with zero orbital momentum like Mn^{2+} do not exhibit spin-orbit coupling, for which reason the magnetization of Mn^{2+} can be well described with the

Brillouin function even in anisotropic systems. TM^{2+} dopants with orbital momentum like Co^{2+} exhibit a zero field splitting D (favoring orientation along a predefined axis even without external magnetic field) and an anisotropic g-factor. The correct analytic expression describing the mean spin for a paramagnet with $S = \frac{3}{2}$ in a magnetic field parallel to the anisotropic axis is given in Equation 2.25 [8].

$$\langle S_z \rangle = \frac{\frac{1}{2}\sinh\left(\frac{1}{2}\frac{g_{TM}\mu_B B}{k_B T}\right) + \frac{3}{2}e^{-2\frac{D}{k_B T}}\sinh\left(\frac{3}{2}\frac{g_{TM}\mu_B B}{k_B T}\right)}{\cosh\left(\frac{1}{2}\frac{g_{TM}\mu_B B}{k_B T}\right) + e^{-2\frac{D}{k_B T}}\cosh\left(\frac{3}{2}\frac{g_{TM}\mu_B B}{k_B T}\right)} \tag{2.25}$$

For Co^{2+} in CdSe these effects are rather small, as can be seen in Figure 2.15c. The zero splitting $2D$ ($D = 0.062\,\text{meV}$ for Co:CdSe [8]) does not exceed $k_B T$ even at low temperatures, allowing application of the Brillouin function for Co^{2+} in wurtzite materials [125–127, 132].

2.4.3 *d-d* Exchange Interaction between Magnetic Ions

Upon increase of the TM^{2+} content, the mean dopant-dopant distance in the DMS lattice decreases, which gives rise to the impact of the so-called *d-d* exchange interactions between the not completely filled *3d* orbitals of neighboring TM^{2+} dopants. As these exchange interactions decline rapidly through space, their impact is limited to nearest neighbors (NN) and (quite weakly) next-nearest neighbors (NNN), apparent in so-called magnetic clusters, which do not interact magnetically with other clusters. The exchange interactions between two interacting spins $\vec{S}_1$ and $\vec{S}_2$ can be captured with a Heisenberg Hamiltonian [8, 9]:

$$\mathcal{H}_{dd} = -J^{dd}\vec{S}_1 \cdot \vec{S}_2 \tag{2.26}$$

Herein, J^{dd} denotes the exchange integral, indicating whether the coupling is ferromagnetic ($J^{dd} > 0$) or antiferromagnetic ($J^{dd} < 0$).

The underlying mechanism of the exchange coupling described by J^{dd} can either be direct through a spacial overlap between involved orbitals or indirectly mediated by orbitals of a bridging atom between the two coupled spins. Exhibiting an elongated range compared to the direct one, the indirect, so-called superexchange, has been shown to represent the dominant exchange channel in most II-VI DMSs [133]. Due to the strong hybridization between the TM^{2+} *3d* orbitals and the valence band carried by the *3p* or *4p* orbitals of the anions (S or Se, respectively), the TM^{2+} spins on neighboring cation lattice sites couple antiferromagnetically, as the electrons in the bridging orbital of the non-magnetic anion develop antiparallel order to the *3d* electrons of both TM^{2+} according to the Pauli principle. Corresponding to Larson *et al.* the antiferromagnetic superexchange accounts

for roughly 95 % of $J_{\mathrm{NN}}^{\mathrm{dd}}$ and $J_{\mathrm{NNN}}^{\mathrm{dd}}$ (the former exceeding the latter 5 to 10 times) [133]. Besides this, the TM^{2+} ions are also coupled via the Bloembergen-Rowland interaction, which is partly carried by the conduction band states. Similarly to the Rudermann-Kittel-Kasuya-Yosida interaction (RKKY) in metals, a spatial oscillating spin polarization of the electrons around one TM^{2+} interacts with another TM^{2+} ion. Depending on the TM^{2+}-TM^{2+} distance this interaction can contribute positively or negatively to J^{dd}. For Mn^{2+} the Bloembergen-Rowland interaction is antiferromagnetic and contributes with $\approx 5\,\%$ to J^{dd} [61, 133].

Independent of the underlying mechanism, an antiferromagnetic coupling between neighboring TM^{2+} ions lowers the overall magnetization of the dopant sublattice and thus influences the magnitude of the observable *sp-d* exchange interactions. The influence of the antiferromagnetically coupled TM^{2+} clusters can be successfully described by the introduction of two empirical parameters S_{eff} and T_{AF} to the Brillouin function [60]:

$$M = N_0 x g_{\mathrm{TM}} \mu_{\mathrm{B}} S_{\mathrm{eff}} B_{\mathrm{S}} \left(\frac{g_{\mathrm{TM}} \mu_{\mathrm{B}} S B}{k_{\mathrm{B}} \left(T + T_{\mathrm{AF}} \right)} \right) \tag{2.27}$$

Herein, T_{AF} denotes the antiferromagnetic temperature and S_{eff} the effective spin momentum. Alternatively, S_{eff} can be expressed via an effective concentration x_{eff}:

$$\frac{x_{\mathrm{eff}}}{x} = \frac{S_{\mathrm{eff}}}{S} \tag{2.28}$$

with

$$M = N_0 x_{\mathrm{eff}} g_{\mathrm{TM}} \mu_{\mathrm{B}} S B_{\mathrm{S}} \left(\frac{g_{\mathrm{TM}} \mu_{\mathrm{B}} S B}{k_{\mathrm{B}} \left(T + T_{\mathrm{AF}} \right)} \right) \tag{2.29}$$

Although both parameters (T_{AF} and x_{eff}) are empirical and do not own a physical derivation, they exhibit an intuitive meaning [8]. The effective concentration x_{eff} accounts for the fact that not all TM^{2+} ions embedded in the host lattice contribute to the magnetization, as those coupled in antiferromagnetic pairs nullify each other. On the other hand, the antiferromagnetic temperature T_{AF} reflects the influence of further TM^{2+} dopants on those dopants, which are not antiferromagnetically coupled with TM^{2+} ions on a NN position. As this influence is quite small, T_{AF} develops proportional to the overall concentration x_{TM} of embedded TM^{2+} ions [134].

2.4.4 *sp-d* Exchange Interactions in Diluted Magnetic Semiconductors

In this section the influence of a magnetic field on the band states of a DMS semiconductor mediated through the coupling between the dopants' *d*-shell electrons and the charge carriers of the *s*- or *p*- shell band states is discussed. Together, the *sp-d* exchange interactions provide the basis for the observation of characteristic giant magneto-optical effects of DMS materials, like the giant Zeeman splitting or the EMP formation.

In analogy to the *d-d* exchange, the *s-d* and *p-d* exchange can be described with a Heisenberg Hamiltonian, summing up over all TM^{2+} spins interacting with an electron or a hole:

$$\mathcal{H}_{\mathrm{s/p-d}} = -\sum_i J_{\mathrm{s/p-d}} \left(\vec{r} - \vec{R}_{\mathrm{i}}\right) \vec{s}_{\mathrm{e/h}} \cdot \vec{S}_{\mathrm{i}} \tag{2.30}$$

Here $J_{\mathrm{s/p-d}}$ denotes the exchange integral for a TM^{2+} ion i placed at a lattice position $\vec{R}_{\mathrm{i}}$ and the electron or hole, respectively, and $\vec{s}_{\mathrm{e/h}}$ and $\vec{S}$ represent the spin operators of the charge carrier and the TM^{2+} dopant, respectively. The sign of $J_{\mathrm{s/p-d}}$ denotes whether a ferromagnetic or antiferromagnetic coupling between the charge carriers and the dopant spins is energetically favorable. The contributions to the magnetic exchange integral $J_{\mathrm{s/p-d}}$ can be classified in two groups, the potential exchange J_{pot} and the indirect kinetic exchange J_{kin} [88, 135].

$$J_{\mathrm{s/p-d}} = J_{\mathrm{kine/h}} + J_{\mathrm{pot_{e/h}}} \tag{2.31}$$

The potential contribution refers to the Coulomb exchange between two charge carriers described by the Pauli principle and decreases as r^{-1}. It is always positive favoring a ferromagnetic alignment and is usually distinctly smaller than the kinetic contribution. The latter arises due to the hybridization of the *3d* orbitals with the orbitals of the conduction and valence bands allowing a transfer of the spin density, and can be either positive or negative. If apparent, it usually dominates $J_{\mathrm{s/p-d}}$. In bulk, hybridization of *s*- and *d*-orbitals is symmetry forbidden at the Γ-point, and therefore the rather small, ferromagnetic potential contribution J_{pot} determines the conduction band exchange integral $J_{\mathrm{s-d}}$ [88]. Recently, this interaction has been described as being mediated by a kinetic *s-s* exchange between the conduction band and the spin split *4s* orbitals of the Mn^{2+} ions in Mn:CdSe [136]. As the TM^{2+} dopants are incorporated on the lattice sites of the cations (Cd or Zn), the TM^{2+} *3d* orbitals exhibit a hybridization with the *p* electrons of the anions providing the valence band. This *p-d* hybridization results in a strong antiferromagnetic kinetic contribution J_{kin} to $J_{\mathrm{p-d}}$.

Table 2.4: *sp-d* exchange coupling constants for various bulk DMS systems. [8]

Compound	$N_0\alpha$ [eV]	$N_0\beta$ [eV]
Mn:CdSe	0.23	−1.27
Mn:CdS	0.22	−1.8
Mn:ZnSe	0.26	−1.31
Co:CdSe	0.28	−1.87

In a semiconductor, the charge carriers in the valence and conduction band states are localized over a large amount of unit cells, so that a great number of TM^{2+} ions interact with each charge carrier. This justifies application of the so-called *mean field approximation*, where the vectorial TM^{2+} spins $\vec{S}$ are replaced by their thermally averaged spin projection along a predefined axis $\langle S_z \rangle$. In addition, the *virtual crystal approximation* allows substituting the random distribution of the TM^{2+} ions on the cation lattice sites by the cation density N_0 weighted with the probability to find a TM^{2+} ion on a cation lattice site, which is usually given by the doping concentration x. With these approximations the conduction and valence band Hamiltonians convert into:

$$\begin{aligned} \mathcal{H}_{\mathrm{s-d}} &= -N_0\alpha x s_{\mathrm{ze}} \langle S_z \rangle \\ \mathcal{H}_{\mathrm{p-d}} &= -N_0\beta x s_{\mathrm{zh}} \langle S_z \rangle \end{aligned} \tag{2.32}$$

Here $N_0\alpha$ and $N_0\beta$ represent the exchange coupling constants given by $\frac{N_0\alpha}{N_0} = \langle \mathcal{S}|J_{\mathrm{s-d}}|\mathcal{S}\rangle$ and $\frac{N_0\beta}{N_0} = \langle \mathcal{X}|J_{\mathrm{p-d}}|\mathcal{X}\rangle$ [134]. $\mathcal{S}$ represents the *s*-like state of the conduction band, while the p_x, p_y and p_z states of the valence band are described by $\mathcal{X}$, $\mathcal{Y}$ and $\mathcal{Z}$. Relevant exchange coupling constants are given in Table 2.4.

Based on these representations, the subband Bloch functions of the conduction and valence band can be parametrized with the following basis vectors, with ↑/↓ representing the spin. The conduction band basis vectors are given by [9, 134]:

$$u_{\mathrm{k\,e},\frac{1}{2}} = \mathcal{S}\uparrow \quad u_{\mathrm{k\,e},-\frac{1}{2}} = \mathcal{S}\downarrow \tag{2.33}$$

The six fold degenerated valence band can be described with [9, 134]:

$$\begin{aligned} u_{\mathrm{k\,hh},\mathrm{m_j}=\frac{3}{2}} &= \frac{1}{\sqrt{2}}(\mathcal{X}+i\mathcal{Y})\uparrow \quad u_{\mathrm{k\,hh},\mathrm{m_j}=-\frac{3}{2}} = \frac{i}{\sqrt{2}}(\mathcal{X}-i\mathcal{Y})\downarrow \\ u_{\mathrm{k\,lh},\mathrm{m_j}=\frac{1}{2}} &= \frac{i}{\sqrt{6}}[(\mathcal{X}+i\mathcal{Y})\downarrow -2\mathcal{Z}\uparrow] \quad u_{\mathrm{k\,lh},\mathrm{m_j}=-\frac{1}{2}} = \frac{1}{\sqrt{6}}[(\mathcal{X}-i\mathcal{Y})\uparrow +2\mathcal{Z}\downarrow] \\ u_{\mathrm{k\,so},\mathrm{m_j}=\frac{1}{2}} &= \frac{1}{\sqrt{3}}[(\mathcal{X}+i\mathcal{Y})\downarrow +\mathcal{Z}\uparrow] \quad u_{\mathrm{k\,so},\mathrm{m_j}=-\frac{1}{2}} = -\frac{i}{\sqrt{3}}[(\mathcal{X}-i\mathcal{Y})\uparrow -\mathcal{Z}\downarrow] \end{aligned} \tag{2.34}$$

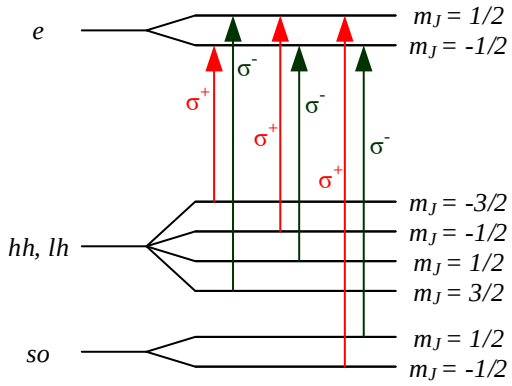

Figure 2.16: Band splittings in zinc blende DMS semiconductors. The red and green arrows indicate the optically allowed σ^+ and σ^- transitions, respectively.

With this basis vectors, the Hamiltonians take the form of diagonalized matrices [9, 134].

$$\begin{aligned}
\mathcal{H}_{\mathrm{s-d}} &= \frac{1}{2} x \langle S_\mathrm{z} \rangle \begin{Bmatrix} N_0\alpha & 0 \\ 0 & -N_0\alpha \end{Bmatrix} \\
\mathcal{H}_{\mathrm{p-d_{hh,\,lh}}} &= \frac{1}{2} x \langle S_\mathrm{z} \rangle \begin{Bmatrix} N_0\beta & 0 & 0 & 0 \\ 0 & \frac{N_0\beta}{3} & 0 & 0 \\ 0 & 0 & -\frac{N_0\beta}{3} & 0 \\ 0 & 0 & 0 & N_0\beta \end{Bmatrix} \\
\mathcal{H}_{\mathrm{p-d_{so}}} &= \frac{1}{2} x \langle S_\mathrm{z} \rangle \begin{Bmatrix} -\frac{N_0\beta}{3} & 0 \\ 0 & \frac{N_0\beta}{3} \end{Bmatrix}
\end{aligned} \tag{2.35}$$

The resulting energy pattern in an external magnetic field generating a nonzero $\langle S_\mathrm{z} \rangle$ is depicted in Figure 2.16 for a ferromagnetic coupling between the *3d* electrons and the conduction band electrons and an antiferromagnetic coupling to the valence band ($N_0\alpha > 0$ and $N_0\beta < 0$). The circularly polarized transitions, allowed according to the Bloch function selection rules presented in Section 2.4.1 (compare Figure 2.14), are indicated. While for the *hh* and *lh* the spin states with negative angular momentum projection are higher in energy compared to their positive counterparts, this splitting is inverted for the electron and the *so*.

The Zeeman splitting observed in DMS materials in general represents a superposition of the intrisic Zeeman term and the so-called giant Zeeman splitting originated by the *sp-d* exchange interaction. The latter exceeds the intrinsic contribution by magnitudes even at low TM^{2+} concentrations. Based on the definition of the Zeeman splitting (Equation 2.19), the giant Zeeman splittings of the excitonic transitions corresponding to the three valence subbands exhibit different magnitudes as given in Equation 2.36.

$$\begin{aligned}\Delta E_{\mathrm{Zhh}} &= x\left(N_0\beta - N_0\alpha\right)\langle S_{\mathrm{z}}\rangle \\ \Delta E_{\mathrm{Zlh}} &= x\left(\frac{N_0\beta}{3} + N_0\alpha\right)\langle S_{\mathrm{z}}\rangle \\ \Delta E_{\mathrm{Zso}} &= x\left(-\frac{N_0\beta}{3} + N_0\alpha\right)\langle S_{\mathrm{z}}\rangle\end{aligned} \tag{2.36}$$

While for the *hh*-X (*so*-X) transition, both exchange integrals tend to a negative (positive) giant Zeeman splitting (considering the signs of $N_0\alpha$ and $N_0\beta$), for the *lh*-X transition, the electron and hole contributions partly counterbalance each other, resulting in a small negative Zeeman splitting. In zinc blende structured, bulk DMS materials, the *hh*-X and *lh*-X transitions are both known to exhibit a negative giant Zeeman splitting [137–139], while the *so*-X transition exhibits a positive ΔE_{Z} [9, 140]. At elevated TM^{2+} concentrations, $\langle S_{\mathrm{z}}\rangle$ has to be described with the modified Brillouin function including the replacement of x by x_{eff}.

With increasing magnetic field the giant Zeeman splitting follows the Brillouin function, exhibiting saturation at high magnetic fields and/or low temperatures. In the low field limit the splitting can be described with an effective g-factor g_{eff}:

$$\Delta E_{\mathrm{Z}} = g_{\mathrm{eff}}\mu_{\mathrm{B}}B \quad \text{with} \quad g_{\mathrm{eff}} = g_{\mathrm{sp-d}} + g_{\mathrm{int}} \tag{2.37}$$

Modification of the *sp-d* Exchange Splitting in Quantum Confined Systems

In analogy to the electronic structure, the magneto-optical properties, i.e. the *sp-d* exchange interaction, is altered in a quantum confined system. On the one hand the confinement of the charge carriers in one or more dimensions introduces new or additional anisotropic axes, which may influence the coupling of the charge carrier spins to the magnetic moments of the dopants [141, 142]. On the other hand the quantization of the wave vector k directly determines the ion-carrier interaction, which may lead to a modification of the exchange coupling constants $N_0\alpha$ and $N_0\beta$ [136, 143, 144].

In zero dimensional colloidal QDs of medium size (i.e. $a_{\mathrm{QD}} > \frac{a_{\mathrm{B}}}{2}$), the magnitude and sign of the giant Zeeman splitting for the $1S_{3/2}1S_{\mathrm{e}}$ band edge transition, exhibiting a hole with angular momentum $N_{\mathrm{h}} = \frac{3}{2}$, can be well described approximating a *hh*-X bulk transition [11, 30, 127]. In case of a reduced carrier dopant overlap due to either an extension of the wave functions beyond the doped volume or a synthesis dependent non-uniform dopant distribution, a scaling factor is introduced - either an excitonic one, γ, or two separate values $\gamma_{\mathrm{e/h}}$ for the electron and hole dopant overlap [11, 24, 80, 145]:

$$\Delta E_{\mathrm{Z1S_{3/2}1Se}} = x_{\mathrm{eff}}\left(\gamma_{\mathrm{h}}N_0\beta - \gamma_{\mathrm{e}}N_0\alpha\right)\langle S_{\mathrm{z}}\rangle \approx x_{\mathrm{eff}}\gamma\left(N_0\beta - N_0\alpha\right)\langle S_{\mathrm{z}}\rangle \tag{2.38}$$

For strongly confined QDs a reduction of the observed giant Zeeman splitting is predicted due to (i) an increasing hh/lh mixing for the $1S_{3/2}1S_e$ transition [143] and (ii) a reduction of the exchange coupling constants due to additional kinetic contributions arising from the quantized k values [8, 143, 146]. However, more recent DFT calculations suggest that the bulk approximation is valid even for QDs with $2a_{QD} \approx 1.5\,\mathrm{nm}$ [136]. In wurtzite structured QDs, the uniaxial anisotropy may reduce the average giant Zeeman splitting of a QD ensemble, as it introduces a preferred axis, which is randomly distributed with respect to the magnetic field direction and represents a competitive projection axis for the valence band total angular momentum N_h.

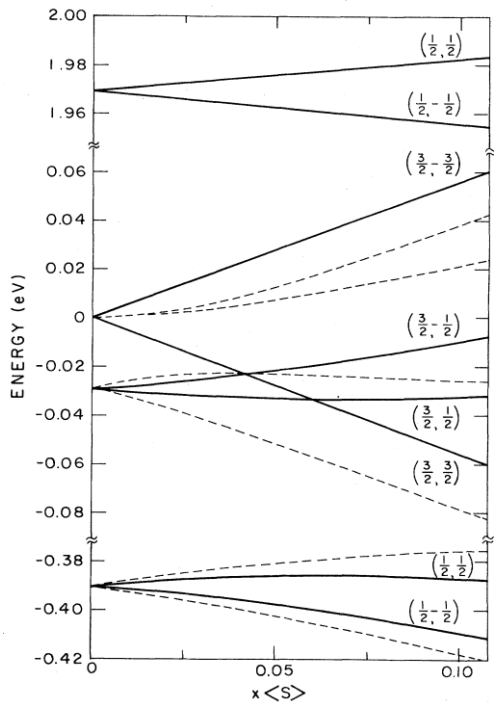

Figure 2.17: Energy levels of the conduction and valence band in a DMS with uniaxial pertubation. Solid lines represent the case of $\vec{B} \parallel \vec{q}$, while dashed lines visualize $\vec{B} \perp \vec{q}$. The subbands are labeled with (j, m_j) given in parenthesis. Note that m_j is not a good quantum number for $\vec{B} \perp \vec{q}$. From [147], calculated for wurtzite structured Mn:CdSe.

In two dimensional quantum wells, the quantization axis represents a similar predominant direction in the lattice, on which the hole total angular momentum J may be projected [141, 142]. Note that any uniaxial perturbation like the wurtzite lattice ansiotropy [147, 148] or strain [149], which partly lifts the valence band degeneracy introducing a splitting of the hh and lh subbands, in principle has the same impact on the DMS energy states in a magnetic field [141, 142]. Figure 2.17 depicts the field dependent conduction and valence band states in a magnetic field parallel ($\vec{B} \parallel \vec{q}$, solid lines) and perpendicular ($\vec{B} \perp \vec{q}$, dashed lines) to an anisotropic axis [147]. For $\vec{B} \parallel \vec{q}$, both preferred directions are parallel and the hh-X giant Zeeman splitting equals the bulk Equation 2.36 [142, 147,

148]. However, the zero-field *hh*-*lh* splitting together with the magnetic interaction mixes the $m_j = \frac{1}{2}$ states (*lh* and *so*), which introduces an asymmetric reduction in the corresponding *lh* and *so* subband Zeeman effect (compare Figure 2.17, solid lines). Both the *lh* as well as the *so* band splittings are smaller compared to their zinc blende counterparts. While this only slightly reduces the *so*-X excitonic Zeeman splitting, the *lh*-X splitting may invert in sign, in case the positive conduction band contribution $N_0\alpha$ becomes dominant (compare Equation 2.36). An opposite splitting for the *hh*-X and *lh*-X has been observed in strained [149] or wurtzite structured [148] bulk DMS and in quantum confined two-dimensional colloidal nanoribbons [37]. For $\vec{B} \perp \vec{q}$, the two predominant axes, i.e. the quantization axis and the direction of the magnetic field, are competitive leading to the represented complex energy pattern.

2.4.5 Excitonic Magnetic Polarons

The *sp*-*d* exchange interactions between the charge carriers and localized magnetic dopants in DMS can lead to the formation of a so-called excitonic magnetic polaron (EMP). Here, the magnetic coupling causes a ferromagnetic alignment of the localized spins in the vicinity of an optically excited charge carrier or an exciton (electron-hole pair). This results in a cloud of polarized spins, which exhibit a net magnetization within the volume of the exciton.

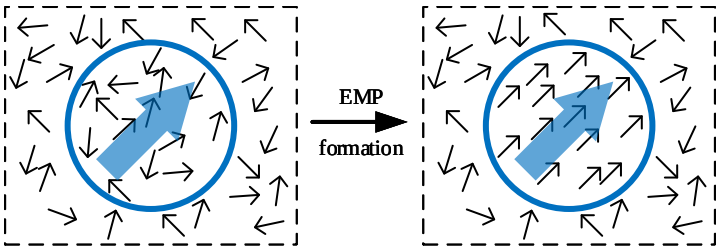

Figure 2.18: Process of excitonic magnetic polaron formation. The spins of the TM^{2+} dopants and the predominant direction provided by the exciton are shown as big and small arrows, respectively, for the initial state after the exciton excitation (left) and the final state of magnetic saturation (right).

Figure 2.18 depicts the initial and final state of the polaron formation. After excitation of an electron-hole pair, its energy relaxation to the bottom and top of the conduction and valence band, respectively, and the exciton formation, it is assumed that the exciton adjusts its spin to the direction of the initial mean magnetization, determined by the randomly fluctuating TM^{2+} spins [8, 80]. During the polaron formation time τ_{EMP}, the TM^{2+} spins within the exciton volume align with the exciton spin, which generates an increasing magnetic moment and the so-called polaron energy E_{EMP}. If the exciton lifetime

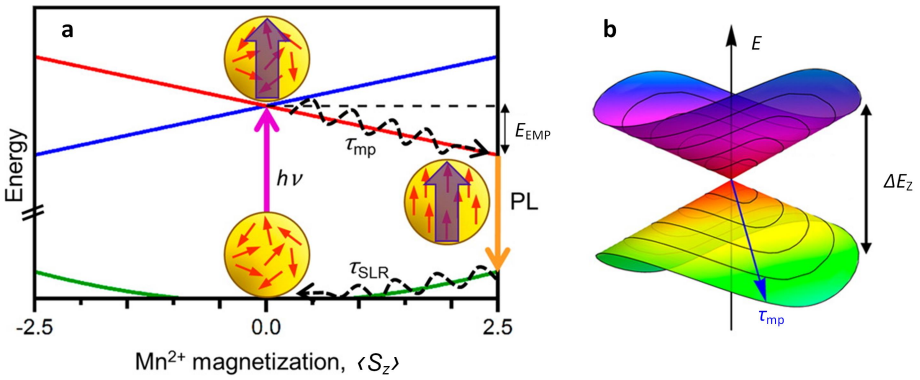

Figure 2.19: Energy diagram of the EMP formation in a colloidal DMS QD. (a) depicts a single-coordinate diagram with $\langle S_z \rangle$ projected along the polaron axis. (b) represents a multidimensional energy diagram including anisotropic effects wrapping the potential energy surface. Both from [80].

τ_{exc} exceeds the polaron formation time (usually in the order of 100 ps to 200 ps [8, 23, 80]), the EMP reaches saturation in case of low temperatures with all TM^{2+} spins aligned parallel to each other, or an equilibrium state balanced by the thermal energy at elevated temperatures. Otherwise this process is interrupted by the exciton recombination.

The driving force behind the polaron formation is the magnetic exchange coupling between the exciton and the dopants. It can be expressed by means of a magnetic exchange field $B_{exc}^{loc}(\vec{r})$ proportional to the local carrier density at the dopant lattice sites. As the hole exchange coupling exceeds the electron contribution by a factor of 4 to 6, B_{exc} is often assumed to originate exclusively from the valence band exchange coupling [150].

$$B_{exc}^{loc}(\vec{r}) = \frac{N_0\beta}{2g_{TM}\mu_B N_0}|\psi_h(\vec{r})|^2 \tag{2.39}$$

The inhomogeneous $B_{exc}^{loc}(\vec{r})$ is replaced by a homogeneous B_{exc} inside the exciton or hole localization volume V_{ex}:

$$B_{exc} = \frac{|N_0\beta|}{2g_{TM}\mu_B N_0}\frac{1}{V_{ex}} \tag{2.40}$$

Scaling with the inverse wave function volume, B_{exc} is strongly enhanced in colloidal DMS QDs [80, 84], where EMP formation has been observed up to room temperature [23]. In Figure 2.19a the influence of the EMP formation on the exciton energy in DMS QDs is illustrated. In the stationary equilibrium the exciton energy is reduced by the polaron energy E_{EMP}, matching half the giant Zeeman splitting originated by an external magnetic field of strength B_{exc}.

$$E_{EMP} = \frac{1}{2}x\,(N_0\beta - N_0\alpha)\,SB_S\left(\frac{g_{TM}\mu_B S B_{exc}}{k_B T}\right) \tag{2.41}$$

The maximal polaron energy $E_{\mathrm{EMP}}^{\mathrm{sat}}$ in case that all Mn^{2+} spins are aligned parallel to the magnetic exchange field is given by:

$$E_{\mathrm{EMP}}^{\mathrm{sat}} = \frac{1}{2} x \left(N_0\beta - N_0\alpha\right) S \tag{2.42}$$

In colloidal QDs exhibiting a predominant axis either through a wurtzite structure or shape anisotropy, a certain orientation of the polaron within the QD is energetically favorable (compare Figure 2.19b). Evoking a slow reorientation process towards the preferred direction, this causes an additional redshift of the emission energy with a time constant of several ns [23, 80]. In colloidal DMS QDs the polaron energy as well as the magnetic

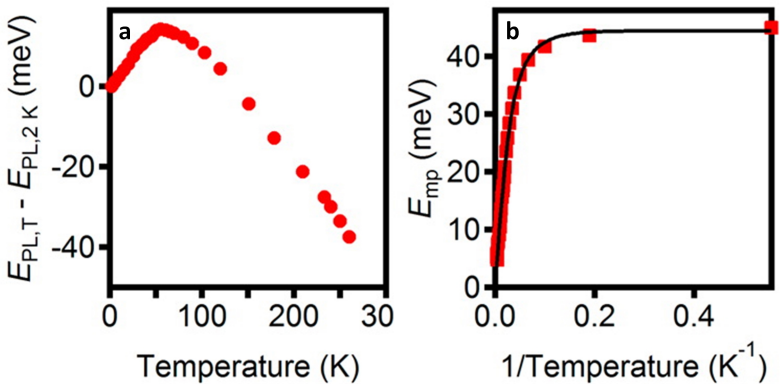

Figure 2.20: Anomalous temperature dependence in emission due to EMP formation. (a) depicts the temperature dependence of the PL emission energy for Mn:CdSe QDs. In (b) the extracted polaron energy E_{EMP} is depicted. Both from [80]

exchange field can be extracted by means of PL characterization. Besides the transient redshift of the emission energy during the polaron formation time τ_{EMP} in time-resolved PL [23, 82], the time-integrated PL exhibits a complex temperature dependence in case of polaron formation. As in colloidal QDs the excitonic lifetime τ_{exc} typically exceeds τ_{EMP} by orders of magnitude, the time-integrated PL monitors the EMP energy in the stationary equilibrium. At cryogenic temperatures the excitonic emission of the $1S_{3/2}1S_e$ band edge transition is lowered by the polaron energy E_{EMP}. With increasing temperature the thermal energy impedes polaron formation and E_{EMP} decreases corresponding to Equation 2.41, which induces a shift of the emission towards higher energies with increasing T. This energy shift exhibits the opposite sign as the commonly observed decrease of the bandgap described by Varshni's equation (compare Section 2.1.3), and is thus referred to as an anomalous temperature dependence - representing a characteristic fingerprint for EMP formation. At elevated temperatures E_{EMP} becomes negligible and the emission energy follows the temperature dependent decrease of the bandgap, exhibiting the commonly observed redshift. Figure 2.20 depicts an anomalous temperature dependence in the emission energy of colloidal Mn:CdSe QDs evidencing EMP formation [80]. E_{EMP}(T)

can be extracted as the temperature dependent Stokes shift (compare Figure 2.20), i.e. the difference between emission and absorption (reduced by a temperature independent shift of about 30 meV to 40 meV [23, 80]). Fitting $E_{\mathrm{EMP}}(T)$ to Equation 2.41 allows extraction of the magnetic exchange field B_{exc} and the saturation polaron energy $E_{\mathrm{EMP}}^{\mathrm{sat}}$.

Chapter 3

Materials and Methods

This chapter presents the preparation and further processing of the DMS nanostructures, as well as the applied characterization techniques and setups used during this thesis. Following a short description of the different nanoparticle synthesis methods, the sample processing for optical characterization as well as the preparation of QD light emitting diodes (LEDs) is described Subsequently, the different characterization methods are presented.

3.1 Nanocrystal Synthesis

Within this thesis, three different types of DMS nanocrystals are utilized: Mn^{2+}- and Co^{2+}-doped magic sized clusters (MCSs), magnetically doped giant shell QDs and shell-doped colloidal nanoplatelets (NPs). All sample synthesis has been conducted by international partners, and thus the different synthesis routes will only be briefly discussed below.

3.1.1 Diffusion Doped Mn:CdSe/CdS Core/Shell Quantum Dots

For the preparation of DMS QD devices, magnetically doped giant shell QDs with a doped Mn:CdSe core and an undoped CdS shell are used. CdSe/CdS giant shell structures are known to exhibit excellent photoluminescence (PL) quantum yields [151–153], which can distinctly improve the performance of QD based LEDs [154, 155]. Mn:CdSe/CdS particles synthesis as well as their characterization with transmission electron microscope (TEM) have been conducted by Dr. Charles Barrows at the Group of Prof. Daniel Gamelin at the University of Washington in Seattle, USA. Undoped reference particles were prepared by Christian Erickson in the same group

Although undoped CdSe colloidal QDs represent the most thoroughly studied and best understood material system throughout the maturation of nanocrystal science, magnetic doping of this material appeared challenging in the beginning, with doping concentrations in QDs far behind the dopant content in the growth solution [11, 12, 50, 51]. Hot injection approaches to form Mn:CdSe QDs suffer from the fact that (i) due to the excess enthalpy of mixing no dopants are embedded in the central QDs cores and (ii) incorporation of impurities during the QD growth is very inefficient. The former prohibits doping in QDs with diameters below 2 nm via hot injection approaches [50]. In contrast to this, diffusion doping of predefined CdSe cores has been shown to achieve a homogeneous dopant distribution within the nanocrystal volume [30, 156]. Here, stochiometric addition of both, Mn^{2+} cations and Se^{2-} anions to the surface of undoped CdSe cores is followed by subsequent diffusion of the dopants into the QD volume towards a thermodynamically favored randomization at relatively high temperatures (300 °C). Oswald rippening, i.e. mass transfer from smaller to larger nanocrystals, which usually appears at those temperatures destroying the QDs size distribution, is successfully suppressed by high Mn^{2+} and Se^{2-} concentrations limiting the Cd^{2+} diffusion length in the solution. The diffusion doping synthesis yields homogeneously doped QDs with slightly increased sizes compared to the initially undoped CdSe QDs.

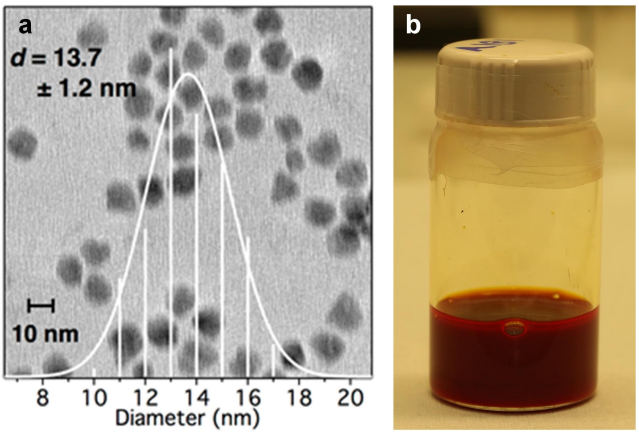

Figure 3.1: Colloidal DMS core/shell QDs. (a) TEM image and size histogram of magnetically doped Mn:CdSe/CdS giant shell QDs [157]. (b) depicts a photograph of the undoped reference CdSe/CdS QDs.

The Mn^{2+}-doped CdSe cores of the giant shell particles used in this thesis are based on undoped CdSe QDs prepared via the hot injection method described in [158] and capped with oleate. For diffusion doping, the QDs are dried and mixed with selenium powder and tributylphosphine (TBP) in octadecen under nitrogen atmosphere Separately, hexadecylamine and stearic acid are heated in octadecen to 100 °C for 30 min and then manganese acetate is added. After degassing, the mixture is heated to 300 °C and the QDs/Se mixture is added. After several hours at 300 °C, the solution is cooled down with

a toluene injection at ≈ 120 °C to prevent stearic acid from solidification. The magnetically doped cores are cleaned via precipitation with ethanol and redispersed in toluene.

For the CdS shell growth [159], the as prepared cores are mixed with oleylamine and octadecen and then degassed for 1 h at room temperature and 5 min at 100 °C. While the temperature is raised to 310 °C, at 200 °C two solutions with cadmium oleate and octanthiol, both in octadecen, are injected. During the growth process oleic acid is added. After precipitation with acetone, the final particles are redispersed in hexanol.

Figure 7.2a depicts a TEM image of the magnetically doped Mn:CdSe/CdS QDs together with a size histogram. The core/shell QDs exhibit a diameter of 13.7 ± 1.2 nm, including 13 ML of CdS shell. Based on a CdS lattice constant of 0.582 nm [35], the core can be estimated to have a diameter of ≈ 6 nm. For reference purposes, undoped QDs with similar core and shell thicknesses (4 nm CdSe core and 4.5 nm CdS shell) are prepared, as depicted in Figure 3.1b.

3.1.2 Colloidal Synthesis of Undoped and Transition Metal Doped (II-VI)$_{13}$ Clusters

A part of this thesis discusses the impact of strong quantization on the optical and magneto-optical properties of undoped as well as doped MSCs consisting of 26 atoms. The MSCs can be classified as II-VI semiconductors composed of 13 Se and 13 Cd atoms, the latter being substituted partly by Zn in case of alloy clusters or by Mn^{2+} or Co^{2+} in case of magnetic doping. The particle synthesis was conducted by Dr. Jiwoong Yang in the group of Prof. Taeghwan Hyeon at the Seoul National University in Seoul, Korea.

Frequently observed during the synthesis of large 2D nanostructures, MSCs are regarded as important prenucleation intermediates in the colloidal synthesis [56–59]. Following the first evidence of $(CdSe)_{13}$, $(CdSe)_{19}$, $(CdSe)_{33}$ and $(CdSe)_{34}$ via mass spectrometry in a solution derived synthetic mixture [52], the synthesis of batches with single-sized MSCs has raised increasing attention. In general, single-sized MSCs can be achieved in a Lewis acid-based reaction between CdX_2, with X being either halide (clorine (Cl)) or acetate (CH_3COO)), and a Se precursor (either selenocarbamate or selenourea) in a primary-amine solution (oleylamine, octylamine, propylamine or pentylamine) [31, 56, 160]. In this process the CdX_2 in combination with the amines forms a laminar mesophase consisting of CdX_2 layers separated by amine bilayers [160, 161]. On addition of the selenium precursor at low temperatures (0 °C to 25 °C), $(CdSe)_{13}$ clusters grow within the primary-amine templates [29, 54, 160]. During the synthesis, metastable $(CdSe)_{34}$ clusters (as well as $(CdSe)_{19}$ and $(CdSe)_{33}$ in some cases) are formed, which convert exclusively

into $(CdSe)_{13}$ in a few hours up to a few weeks, dependent on the amine solvent [58]. Sonication enhanced by ligand exchange breaks the lamelar bilayer templates achieving isolated MSCs surrounded by amines with one ligand bound to each Cd atom [111]. At elevated temperatures (>40 °C) the $(CdSe)_{13}$ and $(CdSe)_{34}$ clusters embedded in the lamelar amine bilayer templates coalescence and convert into 2D wurtzite structures like nanoribbons or NPs [29, 58, 59, 162].

The MSCs used in this work are consistently synthesized with the usage of a standard Schlenk technique providing an argon (Ar) atmosphere. For the synthesis of undoped $(CdSe)_{13}$, $CdCl_2$ in octylamine is heated to 120 °C for 2 h to achieve the lamelar $CdCl_2(octylamine)_2$ complex. Octylammonium selenocarbamate representing the Se precursor is prepared by bubbling carbon monoxide gas into a mixture of Se powder and octylamine for 1 h at room temperature. After injecting the octylamonium selenocarbamate solution into the metal precursor at room temperature, the complete conversion into $(CdSe)_{13}$ clusters is achieved within 40 h. In order to remove excess elemental Se, trioctylphosphine (TOP) in ethanol is added followed by additional washing steps in pure ethanol to purify the $[(CdSe)_{13}$ $(octylamine)_{13}]$ products. Due to the short-chained octylamine ligands, as prepared $(CdSe)_{13}$ MSCs are aggregated in 2D bilayer complexes causing light scattering in transmission based optical characterization techniques (absorption and MCD). Thus, the clusters are surface modified substituting octylamine with longer-chained oleylamine by mixing as synthesized clusters with excess oleylamine and subsequent ultrasonic treatment for 2 h. After precipitating and washing with ethanol, the clusters are redispersed in chloroform.

In order to achieve magnetic doping the $CdCl_2$ precursor is combined with $MnCl_2$ (or $CoCl_2$ in case of Co^{2+}-doping) prior to the formation of metal amine complexes. Further reaction steps including purification and ligand exchange did not differ from the synthesis of undoped $(CdSe)_{13}$. The final doping concentration can be precisely adjusted by the initial amount of $MnCl_2$ between 0 % and 10 %, even though the final concentration of Mn^{2+} ions in the $(CdSe)_{13}$ does not fully achieve the initial concentration [31]. LDI-TOF MS on Mn:$(CdSe)_{13}$ revealed that during the synthesis undoped as well as doped clusters containing one or two Mn ions are formed (denominated as mono- and bidoped species). Evidence of clusters containing three or even more dopants has not been found [31].

To obtain alloy clusters, the $CdCl_2$ precursor is mixed with $ZnCl_2$ initially [59]. In contrast to $(CdSe)_{13}$ clusters, alloy and $(ZnSe)_{13}$ clusters are not stable with an oleylamine passivation and the ligand exchange is omitted here. For alloy clusters the initial Cd/Zn ratio directly corresponds to the final concentrations in the reaction product. In order to achieve magnetic doping, $MnCd_2$ is admixed to the $CdCl_2/ZnCl_2$ precursor mixture.

Figure 3.2: Colloidal DMS clusters. Photograph of Co:$(CdSe)_{13}$ (left), undoped $(ZnSe)_{13}$ (center) and Mn:$(CdSe)_{13}$ (right) dispersions in a mixture of oleylamine and chloroform.

A photograph of as prepared MSC samples of different compositions in dispersion is shown in Figure 3.2. Due to the cluster agglomeration in 2D bilayer complexes the dispersions exhibit strong scattering, which causes a mainly white color of the dispersions.

3.1.3 Synthesis of CdSe/Mn:CdS Nanoplatelets via Colloidal Atomic Layer Deposition

Besides zero-dimensional DMS materials, the magneto-optical properties as well as the electronic structure of Mn^{2+}-doped multi-shell NPs are studied within this thesis. In contrast to the MSCs or colloidal core/shell QDs, two-dimensional NPs exhibit highly anisotropic shapes with thicknesses of a few MLs compared to lateral dimensions of a few up to several tens of nm, usually larger than the exciton Bohr radius. The NPs characterized in this thesis have been synthesized by Dr. Savas Delikanli in the groups of Prof. Volkan Demir at the Bilkent University in Ankara, Turkey, and the Nanyang Technological University in Singapore.

As mentioned above, anisotropic two-dimensional colloidal nanostructures can be ob-

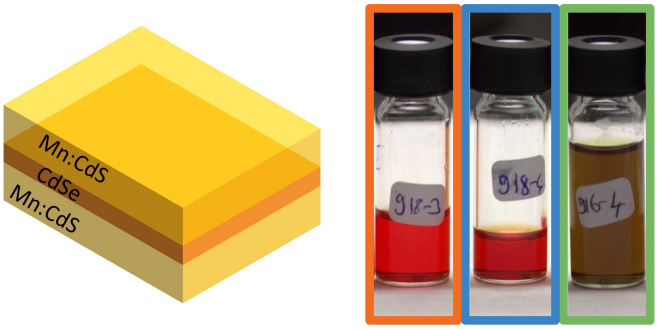

Figure 3.3: Colloidal NPs from Set I: The samples are based on a 2 or 3 ML thick CdSe core surrounded by a 6 or 8 ML Mn:CdS shell (3 or 4 ML on each side). The photographs show (2) CdSe/ (6) Mn:CdS (orange box), (2) CdSe/(8) Mn:CdS (blue box) and (3) CdSe/(8) Mn:CdS (green box) NPs in N-methylformamide (NMF).

tained from MSCs (either $(CdSe)_{13}$ [29, 58, 59] or $(CdSe)_{34}$ [162]) embedded in the lamellar amine-bilayer mesophase by annealing at moderate temperatures. This so-called templated-growth synthesis yields wurtzite structured nanoribbons or quantum wells, whose thicknesses are dictated by the MSC size. In contrast to that, the thicknesses of zinc blende structured NPs can be controlled on the atomic scale between 2 to 5 ML for CdSe [43]. Here an anisotropic growth of the NP seeds, which determines the final thickness, is evoked by hindering the growth for specific crystallographic directions through modification of the growth kinetics by passivation with organic ligands [43]. In a typical synthesis protocol, a long-chained $Cd(carboxylate)_2$ precursor together with Se powder is heated in a non-coordinating solvent like octadecen. At temperatures between 180 °C to 240 °C, the addition of a short-chained $Cd(caboxylate)_2$ salt (acetate or propionate) to the preformed, isotropic nanocrystal seeds evokes an anisotropic lateral expansion forming the NPs. To obtain thin NPs (2 ML to 3 ML), the initial step allowing growth of the seed crystals may be omitted [163].

For the samples used in this thesis, the undoped CdSe core platelets with 2 ML thickness are obtained based on a mixture of cadmium acetate and oleic acid in octadecen. After degassing for 1 h, the mixture is heated under nitrogen to 120 °C and a TOP-selenium solution is added. The synthesis is finished after 6 h. Addition of ethanol allowed precipitation of the NP to remove synthetic by-products, followed by redispersion in hexanol. For the NPs with 3 ML core thickness, the initial mixture included selenium dissolved in octadecen as an additional component. This mixture is degassed for 1 h and heated to 240 °C for 3 min. After quickly cooling to room temperature, the NPs are precipitated by the addition of ethanol and redispersed in hexanol.

From spherical QDs it is known that an inorganic shell can be used to increase the PL quantum efficiency by confining the charge carrier wave functions in the core and minimizing the overlap with surface defects [16, 164]. Besides this, combination of different

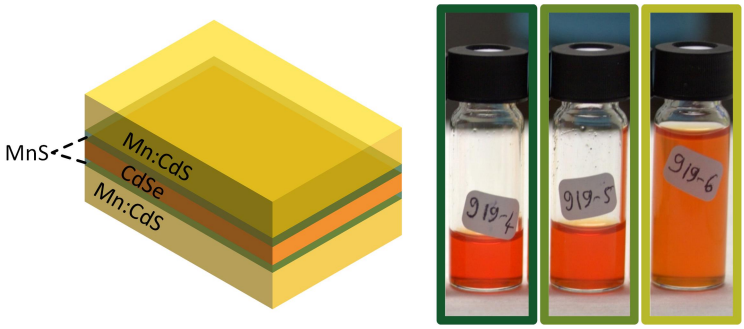

Figure 3.4: Colloidal NPs from Set II: The samples are based on a 2 ML thick CdSe core surrounded by a 2 ML MnS interlayer and a 6, 8 or 10 ML Mn:CdS shell. The photographs show (2) CdSe/ (2) MnS/(6) Mn:CdS, (2) CdSe/ (2) MnS/(8) Mn:CdS and (2) CdSe/(2) MnS/(10) Mn:CdS NPs in NMF (from left to right).

materials in core/shell structured hetero-NPs allows for the manipulation of the electron and hole wave functions and their overlap with the core and shell, respectively [43, 44]. As NPs are not very stable against high-temperature processes, shell growth is more challenging here compared to the case of spherical QDs. An elegant way to add a shell of well defined thickness and composition to predefined core platelets is the so-called colloidal atomic layer deposition (c-ALD) technique [45]. The outer Cd facets are initially passivated by oleate chains, which are removed upon transfer to a polar solvent. Through a complete exchange of the precursor solution, the NPs' cores are subsequently covered by anionic and cationic layers. By adding a manganese acetate complex to the cationic precursor, magnetic dopants can be incorporated into the shell [32].

For this thesis, core/shell and core/interlayer/shell NPs are synthesized with shells made of Mn:CdS (pure MnS). For the deposition of those layers, the CdSe NPs are cleaned three times with ethanol to avoid reaction of remaining precursors from the core synthesis. The CdSe NPs in hexane are added to ammonium sulphide in N-methylformamide (NMF) to obtain a first sulphide layer. After 3 to 5 min, the NPs are cleaned with a mixture of acetonitrile and toluene and redispersed in NMF. Cleaning is repeated for three times. After the last washing step, they are dispersed in NMF containing a mixture of cadmium and manganese acetate for 30 min to form a cationic layer. Subsequently the NPs are cleaned with acetonitril and redispersed in NMF three times. The steps described above are repeated to obtain the desired thicknesses. Pure MnS interlayers are obtained using pure manganese acetate instead of a mixture with cadmium acetate.

Two different sets of samples are used. In sample set I, the cores consist of either 2 or 3 ML CdSe, surrounded by 6 or 8 ML (three or four on each side) Mn:CdS. The samples of set II are based on a 2 ML CdSe core, surrounded with a 2 ML MnS interlayer (one on each side) and a Mn:CdS shell of 6 to 10 ML thickness (3 to 5 ML on each side). The Mn^{2+} concentration in all Mn:CdS layers accounts for 1.2 %, as determined via inductively coupled plasma mass spectrometry. A list of all doped samples can be found in Table 3.1 (undoped references are not listed).

Table 3.1: Magnetically doped NPs used in this study.

	Sample	Composition		
		CdSe core	MnS interlayer	Mn:CdS
set I	(2) CdSe/(8) Mn:CdS	2 ML	–	2×4 ML
	(2) CdSe/(6) Mn:CdS	2 ML	–	2×3 ML
	(3) CdSe/(8) Mn:CdS	3 ML	–	2×4 ML
set II	(2) CdSe/(2) MnS/(6) Mn:CdS	2 ML	2×1 ML	2×3 ML
	(2) CdSe/(2) MnS/(8) Mn:CdS	2 ML	2×1 ML	2×4 ML
	(2) CdSe/(2) MnS/(10) Mn:CdS	2 ML	2×1 ML	2×5 ML

3.2 Sample Preparation

As the as-prepared colloidal nanostructures are dispersed in volatile solvents, further processing is necessary prior to the different characterization techniques. While for optical and magneto-optical characterization the nanostructures are usually transferred onto a solid substrate as a thin layer, the DMS QDs are embedded as active material in a solid state device allowing generation of electroluminescence (EL).

3.2.1 Thin Film Sample Preparation for Optical and Magneto-Optical Characterization

Even though transmission based measurements on dispersions often exhibit optimized signal-to-noise ratios due to reduced agglomeration, sample preparation into a solid layer is required for measurements at cryogenic temperatures inside a cryostat, where the sample is thermally isolated by a vacuum. For other characterization techniques like PL or photoluminescence excitation (PLE) spectroscopy, a higher signal is expected in case the nanostructures are more concentrated. Those require the preparation of the colloidal DMS materials as a thin layer on an optically inactive substrate like quartz glass or silicon.

Figure 3.5: Cold finger of the ST-300 cryostat from Janis with sample holder.

In order to investigate either the absorption or the magneto-optical response via MCD, the sample, usually dispersed in a volatile solvent with the usage of stabilizing organic ligands, has to be transferred into a transparent thin film layer suitable for transmission measurements. All samples investigated during this thesis are prepared on 5 mm × 5 mm quarz glass substrates polished on both sides. They fit into a sample holder, which can be screwed on the cold finger of the cryostate (compare Figure 3.5). The specific sample preparation varies between different samples depending on the solvent, the nanoparticle concentration in the dispersion and the type and amount of organic ligands. In purpose to achieve clear MCD and absorption signals, it is important to minimize particle agglomeration, as bigger agglomerates cause light scattering superimposing the absorption signal.

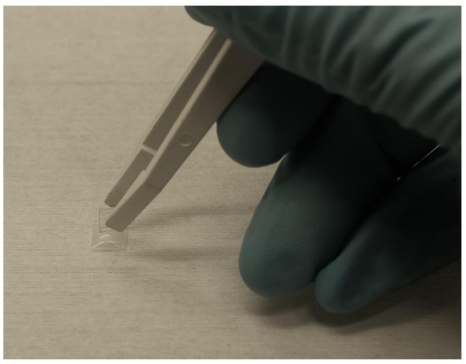

Figure 3.6: Preparation of transparent thin films between a quartz glass sandwich.

On the other hand the amount of sample (layer thickness), or the optical density caused by the sample, respectively, has to be adjusted so that enough light is transmitted to the photomultiplier, while reasonable high absorption and MCD values are generated in order to achieve a good signal-to-noise-ratio.

Magnetically Doped Magic Sized Cluster

MSCs are usually dispersed in a mixture of chloroform and oleylamine (or octylamine in case of the alloy MSC), which serves as both solvent as well as stabilizing ligands. As the melting point of oleylamine is little below room temperature, excess oleylamine in the dispersion tends to form a whitish precipitation causing extensive scattering when dried under air, which can be avoided by placing the dispersion between two quartz glass substrates, as has been shown in preliminary studies [165]. For this purpose, usually $\approx 10\,\mu$L to $15\,\mu$L of MSCs dispersed in a mixture of chloroform and oleylamine with a oleylamine:chloroform ratio of about 1:3 to 1:6 are dropcasted onto one quarz glass substrate. The solution is let dried for $\approx 1\,$min to $3\,$min, and then covered with a second quarz glass substrate (compare Figure 3.6), which causes a leakage of excess dispersion from this so-called sandwich. The amount of nanocrystals remaining between the quarz glass substrates and thus the thickness of the prepared nanocrystal layer is determined by both the MSC concentration in the dispersion as well as the contact pressure onto the second substrate applied during the preparation. The sandwich samples are let dried for at least 20 min before transferring them to the sample holder. For Mn^{2+}-doped alloy and $(ZnSe)_{13}$ MSCs passivated with octylamine, the thin film preparation needs to be adjusted. The shorter-chained ligand exhibits a lower melting temperature compared to oleylamine ($-1\,$°C compared to $18\,$°C to $26\,$°C [166]) and tends to crystallize even if prepared between two quartz glass substrates. This crystallization, which causes light scattering and impedes any MCD measurement at cryogenic temperatures, can be avoided by adding a small amount of oleylamine to the dispersion just prior to sample preparation.

Shell-Doped Colloidal Nanoplatelets

Exhibiting a highly anisotropic shape, the NPs are known to possess strong tendencies for agglomeration or stacking [167–169]. In order to enable thin film formation on the quarz glass without stacking, (i) the solvent is changed from NMF exhibiting a high evaporation point of about 200 °C [166] to chloroform (evaporation temperature 61 °C [166]) to reduce the solvent evaporation time, and (ii) the NPs are passivated with additional excess oleylamine as ligands. The NPs are separated from NMF by centrifugation and decantation (compare Figure 3.7), and redispersed in a 10:1 mixture of chloroform and oleylamine. To ensure a homogeneous inter-mixture the solution is treated with ultrasonification for 5 to 10 min. The following preparation between a quartz glass sandwich is similiar to the procedure for MSCs.

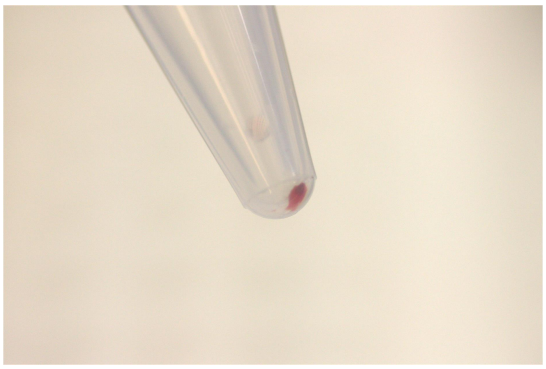

Figure 3.7: Isolated colloidal NPs after centrifugation and decantation.

For characterization methods relying on emission like PL or PLE spectroscopy, the layer morphology of the nanocrystals is not as decisive as for absorption or MCD. In order to avoid background luminescence from the cold finger, the nanocrystals are usually transferred onto a non-transparent substrate like silicon (or silicon covered with silicon oxide) via drop-casting and evaporation of the solvent. The substrate is affixed to the cryostat cold finger either with a transparent removable glue (Fixogum von Marabu) or with conductive silver paint. In case of the MSCs the high content of oleylamine in the dispersion, which crystallizes on an uncovered substrate, occasionally causes scattering of the exciting laser and can thus impede PL measurements. This is avoided either by dilution of the dispersion with chloroform reducing the amount of oleylamine on the substrate, or by covering the silicon substrate with a transparent quartz glass plate. The latter is applied for PLE measurements, as they are conducted in the same cryostat as used for MCD (compare Figure 3.5).

3.2.2 Preparation of Light Emitting Devices Based on Colloidal Quantum Dots

The design of the colloidal QD device for temperature dependent EL measurements is inspired by state-of-the-art QD-LEDs [170–172] and includes a hole-injection and a hole transport-layer, but lacks an electron transport layer like ZnO for the sake of convenience. The device is based on a 1 cm × 1 cm glass substrate covered with an indium tin oxide (ITO) layer. This transparent anode allows light emission during the operation. The substrate is treated with a standard cleaning process to prepare the surface: After 2 min boiling and ultrasonification in both acetone and ethanol, consecutively, the substrate is rinsed with isopropanol and treated with an oxygen plasma for about 10 min. The substrate is covered with poly(3,4-ethylenedioxythiophene)-poly(styrenesulfonate) (PEDOT:PSS) (Sigma Aldrich, 0.8 % in H_2O conductive inkjet, filtered through a 0.45 μm polypropylene filter) as hole injection layer via spin coating at 2000 rpm for 60 s and annealed for 20 min at 150 °C. Subsequently, poly[N,N'-bis(4-butylphenyl)-N,N'-bis(phenyl)-benzidine] (poly-TPD) (Plasmachem) as hole transport layer is spin coated on top (2000 rpm for 30 s) and let dried under atmosphere for ≈ 1 h.

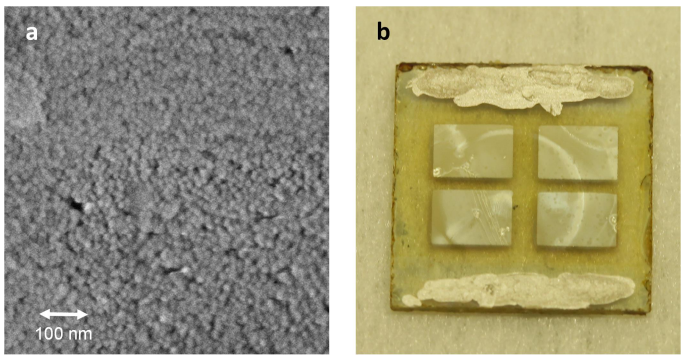

Figure 3.8: Preparation of the EMP device. (a) depicts a scanning electron microscope (SEM) image of the QD layer treated with 1,2-ethanedithiol (EDT). In (b) an as prepared device is shown. The organic layers as well as the QD are removed along two edges of the substrate and replaced by a layer of conductive silver to ensure good electric contact to the ITO.

During the temperature dependent EL measurements, the QD device experiences high thermal stress and extensive operation times. In order to increase the robustness and stability of the active layer, the QDs are treated with the cross linker EDT [173]. This short-chained ligand with active groups at both ends is able to link the QDs, forming a dense layer. The active layer is prepared by sequential spin coating. Following the application of the Mn:CdSe/CdS QDs in hexane, the EDT solution (Sigma-Aldrich, 0.1 mol l^{-1} in acetonitrile) is dropcasted on top and left there for 30 s prior to spin-coating to allow the ligand exchange happen. Pure acetonitrile and pure hexane are consecutively spin

coated to remove excess free-standing EDT and the ligand exchanged organic molecules. All spin coating is done for 60 s at 2000 rpm. As the increase of the layer density during the cross-linking process is known to create cracks in the layer [173], the spin coating sequence described above is repeated three times to achieve a closed layer (compare Figure 3.8a).

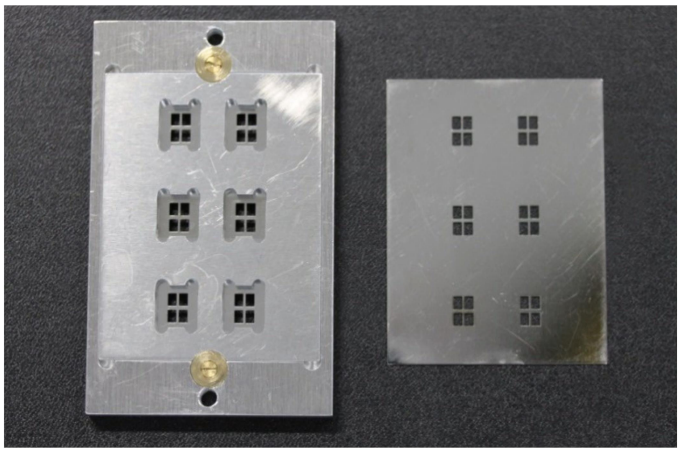

Figure 3.9: Shadow mask and sample holder for the high vacuum coating plant.

Finally 200 nm of silver is evaporated (Oerlikon Univex 350) to form the top electrode on top of the layer assembly through a shadow mask. The shadow mask (compare Figure 3.9) is embedded in a self-made sample holder allowing for the processing of six QD devices with four 2 mm × 3 mm contact pads on each substrate. An as prepared QD devices is depicted in Figure 3.8b.

3.3 Basic Non-Magnetic Optical Characterization

Within this thesis, various characterization methods are applied to investigate the optical and magneto-optical functionalities of the DMS nanostructures. The basic optical methods, which do not make use of an externally applied magnetic field and provide an insight into the electronic structure of the materials, are described below. While absorption and PLE measurements are conducted with commercially available systems, the PL measurements used here are collected with two different, home-build setups. Note that a few absorption spectra are obtained with the MCD setup, compare Section 3.4.2.

3.3.1 Absorption Spectroscopy

Absorption spectroscopy allows an excellent insight into the electronic structure of a material, as all possible optical transitions can be observed according to their oscillator

strength, including excited state transitions. The absorption spectra, which are not detected with the MCD setup, are obtained with an UV-2550 UV-Vis spectrophotometer from Shimadzu. A detailed drawing of the optical path is depicted in Figure 3.10a. The UV-2550 is equipped with two light sources (a deuterium and a halogen lamp), allowing measurements between 190 nm and 900 nm. A double monochromator enables a spectral resolution of 0.1 nm. The beam is modulated and split by a partly reflecting optical chopper into a sample and a reference beam. Both signals are detected with a photomultiplier and a lock-in amplifier. A liquid helium cryostat (Janis: ST-300) can be incorporated in the UV-2550 to obtain temperature dependent absorption spectra.

As common in molecular spectroscopy, the absorption A is defined to the base 10 instead of the natural logarithm, with I_0 and I_{sample} representing the light intensity before and after the sample, respectively.

$$A = \lg \frac{I_0}{I_{\text{sample}}} \tag{3.1}$$

With the intensity of the sample beam behind the sample I_{sample} and the reference beam $I_{\text{reference}}$, the absorption in the UV-2550 is determined as:

$$A = \lg \frac{I_{\text{reference}}}{I_{\text{sample}}} \tag{3.2}$$

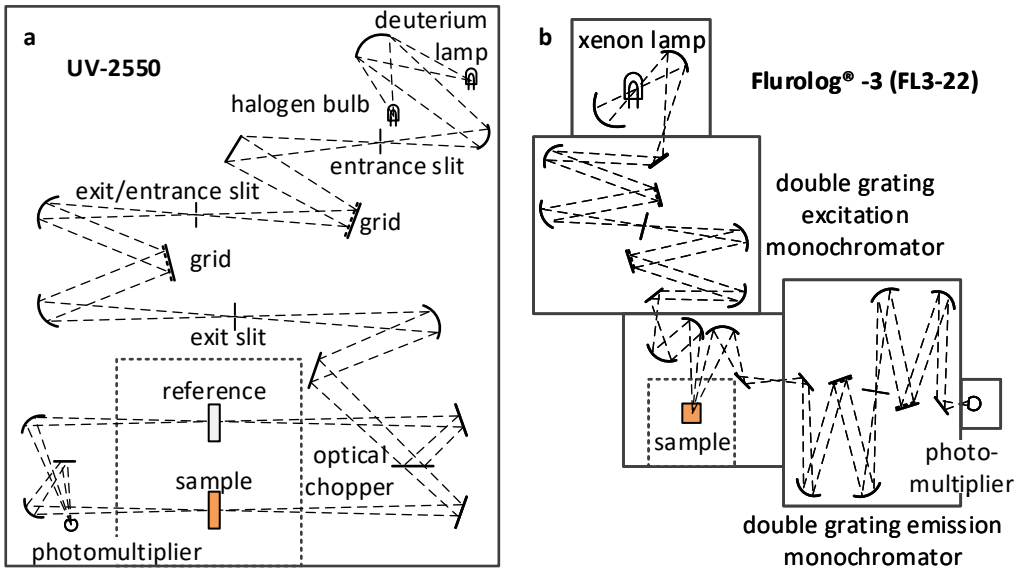

Figure 3.10: Commercial setups for absorption (a) and PLE (b) spectroscopy.

3.3.2 Photoluminescence Excitation Spectroscopy

In PLE spectroscopy the PL emission intensity at a specific spectral position is detected, while the wavelength of the excitation light is varied. After absorption of the exciting light, the energy is transferred to the luminescent state and detected. Thus, the PLE spectra often resemble the absorption spectra of a material. In addition, PLE spectroscopy also includes information about the efficiency of the energy transfer between an absorbing and the monitored emitting state.

The temperature dependent PLE spectra of Mn:$(CdSe)_{13}$ are determined with a Flurolog®-3 (FL3-22) from Horiba (compare Figure 3.10b). The light source is represented by a 450 W xenon lamp. The FL3-22 is equipped with a double grating monochromator with gratings of 1200 mm^{-1} in both the emission and the excitation path. The sample is placed in a so-called T-box. For temperature dependent studies a liquid helium cryostat (Janis, ST-300) can be incorporated in the Flurolog®-3. In PLE mode, the excitation energy is varied by the excitation monochromator, while the PL intensity at a defined wavelength is detected with a photomultiplier. In addition to PLE spectroscopy, the Flurolog®-3 also allows PL measurements by passing through the emission monochromator.

3.3.3 Time-Integrated and Time-Resolved Photoluminescence Spectroscopy

In contrast to absorption or PLE measurements, in PL spectroscopy, the light emission of a semiconductor is characterized. Often restricted to the energetically lowest transition, PL spectroscopy enables an insight into the dynamics of the charge carriers after an absorption process. The PL spectra in this thesis are obtained with different setups. While the PL signal of Mn:CdSe/CdS particles in the device are obtained with an extension of the EL setup described below and the PL of the NPs are characterized with the Flurolog®-3, most time-integrated measurements on MSCs and all time-resolved PL signals are recorded with the self-build setup depicted in Figure 3.11.

A Ti:Sapphire laser (Mira 900 from Coherent) with a repetition rate of 76 MHz and 100 fs pulse width, optically pumped by a frequency doubled Nd:YAG laser (Verdi V10 from Coherent), serves as excitation source. The infrared light can either be frequency trippled or doubled to wavelengths of 270 nm or 405 nm, respectively. The desired wavelength is selected with a prism. The laser beam is expanded to improve the focusing capability and focused on the sample, which is placed in a liquid heluim cryostat (Janis, ST-300). The luminescence is collimated and guided to the detection unit.

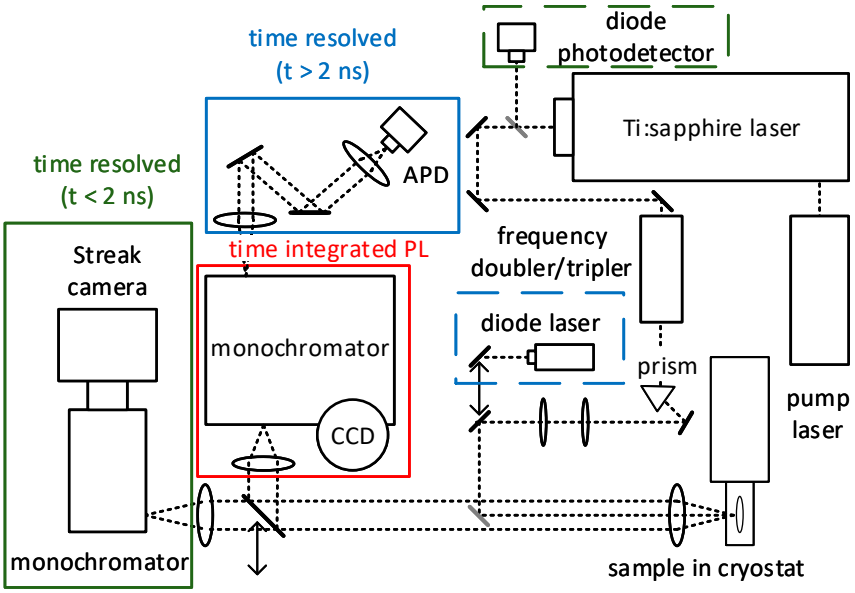

Figure 3.11: Experimental setup for time-integrated and time-resolved PL spectroscopy.

Time integrated spectra are detected with a monochromator (iHR320, Horiba Jobin Yvon with gratings of 150 mm^{-1}, 600 mm^{-1} and 1200 mm^{-1}) combined with a charge-coupled device (CCD) (Symphony, Horiba Jobin Yvon), to which the luminescence is guided via a movable mirror. Two different detection units are available to obtain time traces of the PL signal. For emissions with short lifetimes, a streak camera equipped with an additional monochromator (from Hamamatsu, with 100 mm^{-1}, 300 mm^{-1} and 600 mm^{-1} gratings) allows recording of spectrally- and time-resolved PL signals up to 2 ns. The streak camera is synchronized with the Ti:sapphire laser via a diode photodetector. To allow characterization of samples exhibiting longer lifetimes, an avalanche photodiode (APD) setup (Becker & Hickl GmbH) is placed at the second exit of the monochromator used for time-integrated PL spectroscopy, enabling time traces up to μs. For this purpose, a picosecond pulsed laser diode can be introduced as excitation source via a movable mirror. Its repetition frequency can be tuned between 5 MHz and 31 kHz, and serves as reference for the APD.

3.4 Magnetic Circular Dichroism Spectroscopy

Magnetic circular dichroism is based on the determination of the difference in absorption between σ^- and σ^+ polarized light and represents a powerful tool for the investigation of the influence of a magnetic field on the electronic structure of a DMS material. In contrast to emission based spectroscopic methods like magnetic circularly polarized photolumines-

cence, MCD provides an experimental access to both the ground state as well as excited state transitions, as it is based on absorption spectroscopy. Whereas absorption spectra of colloidal nanostructures often consist of a superposition of excitonic transitions with the absorption bands of free carriers as well as background signals caused by Rayleigh scattering, the MCD signal is extremely sensitive to excitonic transitions. In addition, the MCD signal reveals a sign and amplitude for the splitting of a certain electronic transition in a magnetic field, which represents an additional information to the absorption. This makes MCD a versatile interpretative tool for the magnetic field induced splitting of optically active electronic states.

3.4.1 Theory of Magnetic Circular Dichroism

Following the convention of Piepho *et al.,* the difference absorption signal is defined as the difference in the absorption of σ^- and σ^+ polarized light according to Equation 3.3 [174].

$$\Delta A = A_{\sigma^+} - A_{\sigma^-} = \frac{I_{\mathrm{MCD}}}{1.1515} \tag{3.3}$$

Assuming a twofold degenerated transition probed with circularly polarized light (with non-degenerated ground state), the MCD signal equals zero in the absence of an external magnetic field, as the absorption features of σ^- and σ^+ polarized light coincide energetically. In the presence of an external magnetic field the degeneracy of this transition is lifted and the two absorption bands are separated by the Zeeman splitting ΔE_{Z}, generating the MCD signal. Figure 3.12 depicts the absorption signal $A = (A_{\sigma^-} + A_{\sigma^-})/2$ as well as the two absorption bands split by ΔE_{Z} in comparison to the resulting, derivative-shaped MCD signal. The amplitude of this so-called $\mathscr{A}$-term signal (denoting the derivative-shaped contribution to the MCD signal) is proportional to the Zeeman splitting, while the shape of the feature directly reflects the sign of the splitting. In case the σ^- transition is higher in energy than its σ^+ counterpart ($\Delta E_{\mathrm{Z}} < 0$, compare Equation 2.19), ΔA is positive on the low-energy side of the crossing-point representing a negative $\mathscr{A}$-term as shown in Figure 3.12. The zero-crossing of the MCD signal coincides with the peak position of the zero-field absorption. Besides the derivative-shaped $\mathscr{A}$-term, two other possible contributions to MCD signals are known. E.g. for molecules, a temperature dependent $\mathscr{C}$-term arises in case of a thermally occupied, degenerated ground state. An absorption-band-shaped $\mathscr{B}$-term may originate due to field induced mixing between excited states lying close to each other. Both terms usually play a marginal role for excitonic transition in DMS nanostructures, as due to the giant Zeeman splitting the $\mathscr{A}$-term contribution dominates [174, 175].

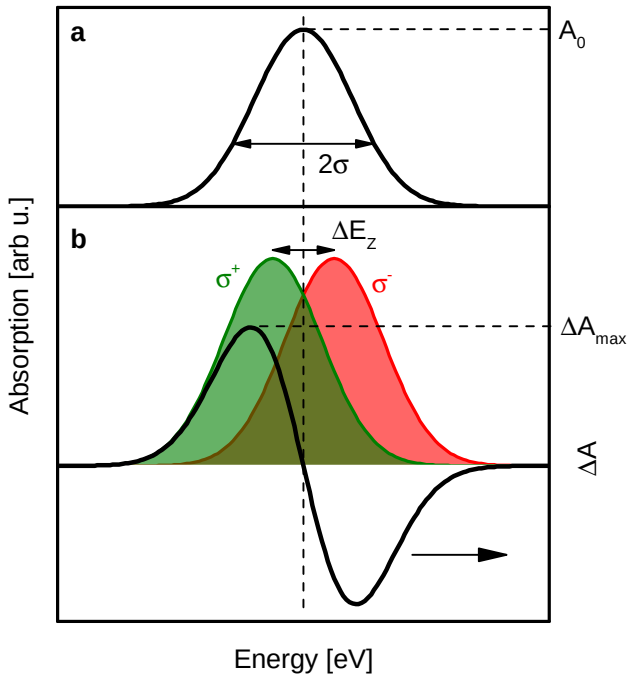

Figure 3.12: Principles of MCD spectroscopy. (a) depicts the Gaussian-shaped absorption peak, while in (b) the absorption peaks corresponding to σ^+ and σ^- polarized light separated by the Zeeman energy ΔE_Z are depicted in comparison to the absorption difference ΔA.

Application of the rigid shift approximation, which assumes that only the energetic positions of the absorption bands shift while the band shape does not change with magnetic field, allows extraction of quantitative values for ΔE_Z. This requires knowledge of the absorption band shape of the corresponding transition. ΔE_Z can be obtained either by fitting the MCD spectrum with two Gaussian peaks of opposite signs having the same band shape as the zero-field absorption or, provided that the Zeeman splitting is small compared to the bandwidth 2σ of the absorption peak ($\sigma > \Delta E_Z$), directly calculated from equation 3.4.

$$|\Delta E_Z| = \frac{\sqrt{2e}}{2}\sigma\frac{\Delta A_{\max}}{A_0} \tag{3.4}$$

Herein, 2σ denotes the Gaussian bandwidth (according to a peak-normalized Gaussian of $f(E) = \exp(-\frac{(E-E_0)^2}{\sigma^2})$), A_0 the maximum absorption value and $\Delta A_{\max}$ the maximum MCD amplitude (compare Figure 3.12).

The MCD signal is often determined as the ratio between transmitted intensities of σ^- and σ^+ polarized light. This signal, further referred to as MCD signal and denoted as I_{MCD}, is directly proportional to ΔA for $\Delta A < 0.1$. [12, 175]

$$I_{\mathrm{MCD}} = \frac{I_{\sigma^-} - I_{\sigma^+}}{I_{\sigma^+} + I_{\sigma^-}} = 1.1515 \cdot \Delta A \tag{3.5}$$

3.4.2 Experimental Setup for Magnetic Circular Dichroism

Figure 3.13 depicts the MCD setup used for the determination of the MCD spectra. A 75 W xenon lamp combined with a monochromator provides a color tunable light source, which allows the serial collection of spectra via tuning of the wavelength. The lamp (LOT-Oriel, LSB510 (xenon lamp), LSH102 (adapter) and LSN151 (power supply)) generates white light with a nearly constant intensity between 250 nm and 700 nm, which is focused onto the entrance slit of the computerized monochromator (LOT-Oriel, Omni-λ 150), equipped with two gratings with 1200 mm^{-1}, optimized for 300 nm (MSG32-1200-300) and 500 nm (MSG32-1200-500), respectively.

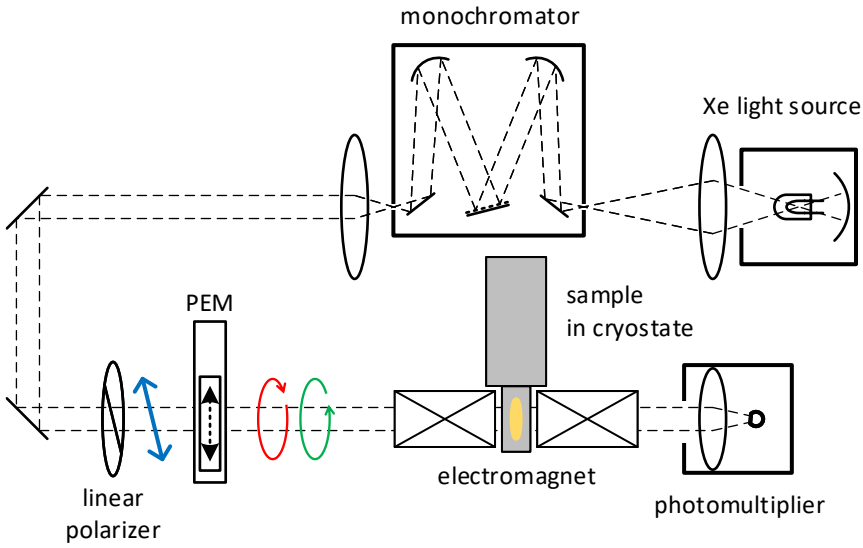

Figure 3.13: Experimental setup for magnetic circular dichroism measurements.

The monochromatic light (bandwidth of $\approx$ 1 nm) is collimated and directed towards the sample with mirrors. Before reaching the sample, the light passes a linear polarizer, which blocks light components perpendicular to its predominant direction creating linear polarized light and a photoelastic modulator (PEM) converting it alternately into σ^- and σ^+ polarized light, with π polarized light in the changeover [176]. The PEM (Hinds Instruments, I/FS50 with PEM-90 (controller)) consist of a quarz glass plate, which is periodically deformed via a piezo element with a frequency of 50 kHz modulating the refractive indexes for light of different polarization introducing a tunable phase shift between the two polarization components.

The sample is placed between two quarz glass windows in a liquid heluim crysostate (ST-300 from Janis), which allows one to tune the temperature between 5 K and 300 K. The cryostat is positioned in between the two pole shoes of an electromagnet providing a magnetic field parallel to the light propagation axis (Faraday geometry), which can be adjusted up to 1.6 T. The transmitted light is focused onto a photomuliplier tube

(Hamamatsu, R928 (tube) with C9525 (power supply)).

The output signal, which is determined as the voltage drop of the photomultiplier anode current across a 50 Ω resistance, consists of a DC as well as an AC contribution. The DC voltage, reflecting the mean transmission of σ^- and σ^+ polarized light, is detected with a multimeter (Hewlett Packard: 34401A). The AC contribution, orders of magnitudes smaller in amplitude, is amplified with a voltage amplifier (Femto: DLPVA-100-BLN-A) and filtered with a dual-phase lock-in amplifier (Signal Recovery: 7225 DSP), which determines the amplitude as well as the phase component φ of the AC signal using the PEM output frequency as reference signal. In case the difference between σ^- and σ^+ polarized light exhibits a sign reversal, a phase shift is detected. The MCD signal is calculated according to Equation 3.6. The spectrum is corrected by the signal measured without an external field ($I^{0\mathrm{T}}_{\mathrm{MCD}}$), which includes any sample or setup related phase perturbations caused e.g., by reflections in the pole shoes or scattering artifacts.

$$I_{\mathrm{MCD}} = \frac{2\sqrt{2}}{2}\frac{V_{\mathrm{AC}} \cdot \cos\varphi}{V_{\mathrm{DC}}} - I^{0\mathrm{T}}_{\mathrm{MCD}} \tag{3.6}$$

The correction by a constant factor is due to the fact that the lock-in amplifier detects the effective rather than the peak-to-peak value of the AC component, while the DC value equals the mean transmitted intensity of σ^- and σ^+ polarized light instead of the sum, as defined in equation 3.5.

In order to determine absorption spectra, the sample must be replaced by a bare quarz glass substrate allowing to record a lamp spectrum, so that the absorption spectrum can be calculated according to 3.7

$$A = \lg \frac{V^{lamp}_{\mathrm{DC}}}{V^{sample}_{\mathrm{DC}}} \tag{3.7}$$

Herein $V^{sample}_{\mathrm{DC}}/V^{lamp}_{\mathrm{DC}}$ denotes the DC voltage measured with a sample/bare substrate placed in the optical path. The combination of both MCD and absorption spectrum allows for the extraction of quantitative values for the Zeeman splitting of an excitonic transition according to Equation 3.4 by fitting the absorption peak with a Gaussian profile.

3.5 Temperature Dependent Electroluminescence of Colloidal Quantum Dot Light Emitting Devices

With the purpose to demonstrate an electrically induced EMP, a characterization technology allowing temperature dependent EL measurements of colloidal QD devices between cryogenic and room temperature is developed within this thesis. Due to the reduced

robustness of both the active layer consisting of colloidal QDs as well as the solution-processed organic layers, temperature-stable electrical contacting is challenging. As wire-bonding on top of a metal-coated QD layer is not possible, the contacts are realized with spring-loaded contact pins, which are able to counterbalance thermal expansion during a temperature series.

The QD devices are integrated into a self-made sample holder (compare Figure 3.14), which allows integration of the contacted QD device into a cryostat, enabling optical approach to the active areas. Thermal conductivity to the cold finger is ensured by preparing the sample side of the sample holder with copper. Electrical contacts are realized by gold-coated copper-beryllium contact pins from Feinmetal. Prior to the integration of the QD device into the cryostat, the organic layers as well as the QDs are removed along the edges of the substrate and replaced by a layer of conductive silver paint to ensure contact between the ITO and the contact pins. The sample holder can be integrated into a closed-cycle helium cryostat, as visualized in Figure 3.14c-e (OptistatAC from Oxford Instruments).

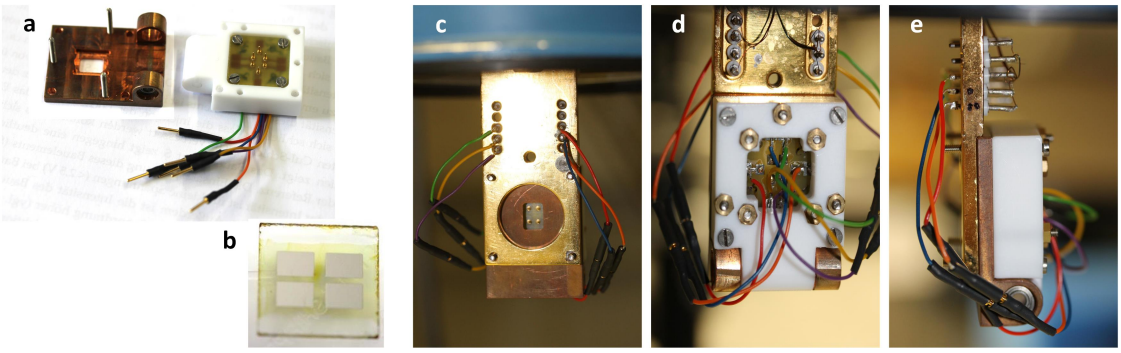

Figure 3.14: Incorporation of the QD devices into a closed cycle cryostat. (a) depicts the two parts of the sample holder, while (b) shows an as-prepared device. In (c-e) the sample holder affixed to the cold finger of the cryostat is shown.

Figure 3.15 depicts the optical setup for the temperature dependent EL measurements. The cryostate is placed on a translation stage allowing movement perpendicular to the optical path, but parallel to the optical table. The QD-LEDs are operated with a sourcemeter (Keithley 2601), cable-connected to the cryostate. It can be either used as voltage or as current source. Furthermore the Keithley can be connected to a computer allowing fully-automated IV characterization. The EL signal is collimated with a lens, which is adjustable in height in order to selectively address each of the four active areas on the device. The EL signal is then focused into a monochromator (iHR320, Horiba Jobin Yvon with a 150 mm^{-1} and two 600 mm^{-1} gratings) equipped with a CCD (Symphony, Horiba Jobin Yvon), allowing detection of EL spectra.

Simultaneous detection of PL spectra is enabled by incorporation of a He-Cd laser in

the optical path via a beam splitter. The laser beam is enlarged to improve the focussing capability and guided onto the devices incorporated in the cryostat.

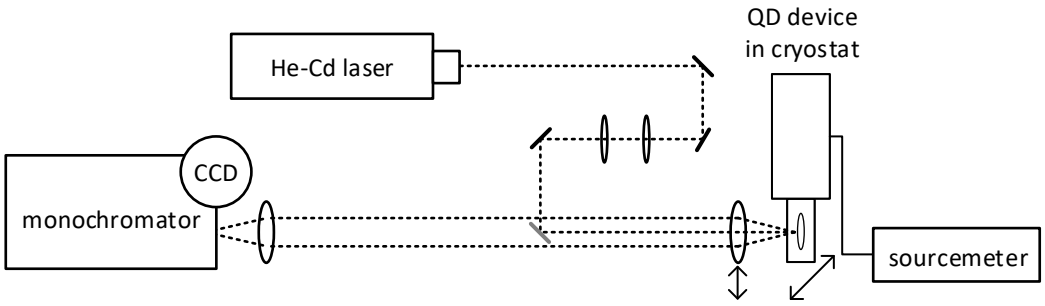

Figure 3.15: Temperature dependent EL setup, allowing simultaneous PL characterization of the devices.

Chapter 4

Tuning the (Magneto-)Optical Properties of $(CdSe)_{13}$ Clusters by Discrete Replacement of Individual Atoms

Magic sized clusters (MSCs) consisting of a predefined number of 26 atoms are considered to carry an essential part during the synthesis of different nanostructures and are thus of high interest regarding their chemical properties [52–56]. Beyond that, their specific structure also reveals unique aspects, which distinguish MSCs from conventional nanostructures. First, placed at the border between molecules and QDs, MSCs represent the case of ultimate quantum confinement in a semiconductor nanocrystal, which e.g. results in the observation of magneto-optically active and inactive transitions of the fine structure of the $1S_{3/2}1S_e$ transition [31]. The dimension of one cluster barely exceeds the size of one unit cell, with the result that almost all atoms can be considered sitting on the surface, while atom-atom interactions are mostly restricted to nearest neighbors. Due to their small, countable number of atoms any change in the composition, like e. g., doping or alloying, must be considered as a discrete replacement of a few out of 13 anions or cations in the lattice rather than a continuous shift of the composition between 0 % to 100 % concentration. The consequences of these peculiarities on the optical and magneto-optical properties of undoped, Mn^{2+} and Co^{2+}-doped as well as ZnCdSe alloyed clusters are objective of this thesis.

The first subsection concentrates on the magneto-optical properties of Mn^{2+}-doped $(CdSe)_{13}$ clusters, mainly on the consequences of the Mn^{2+}-Mn^{2+} interactions on the magneto-optical activity of different cluster species formed during the synthesis. The

second part describes how the bandgap as well as the magneto-optical response can be digitally shifted in energy by alloying Mn^{2+}-doped clusters between $(CdSe)_{13}$ and $(ZnSe)_{13}$.

4.1 *Digital Doping* in Mn:$(CdSe)_{13}$ Clusters

Magnetic doping in colloidal QDs is known to enable a combination of the unique optical and electrical properties of confined semiconductor systems with magnetic functionalities, allowing for the observation of strongly enhanced exchange interactions between the dopant spins and the confined charge carriers as compared to their bulk counterparts [12, 23, 29]. Due to limitations in the capability of CdSe crystal nuclei to incorporate impurity atoms [12], doping in conventional QDs can either be achieved kinetically by adsorption of impurities on the nanocrystal surface and coverage by further material [50, 51] or via diffusion doping of preformed cores, which grow slightly during the impurity incorporation process [30, 156]. Hence, conventional magnetically doped QDs usually exhibit diameters $> 2.5\,\mathrm{nm}$, in which charge carriers are quantum confined, whereas the Mn^{2+} ions, still embedded in hundreds to thousand atoms of the host lattice, experience the same direct environment as compared to bulk DMS materials with similar dopant concentrations. This is completely altered in case of Mn^{2+} incorporation into $(CdSe)_{13}$, where due to the restricted number of available lattice sites several Mn^{2+} ions incorporated in the same cluster are most probably forced to be on nearest-neighbor positions, implying striking consequences for their magnetic behavior.

4.1.1 Idea of *Digital Doping*

From bulk DMS materials it is well known that the interactions between the dopants themselves gain importance with increasing doping concentration. Mn^{2+} ions incorporated on nearest neighbor sites form anitferromagnetically coupled Mn^{2+}-Mn^{2+} pairs nullifying their overall magnetic moment, and do not contribute to the *sp-d* exchange interaction. The presence of this antiferromagnetic coupling can be accurately described with the empirically modified Brillouin function (Equation 2.29)[60], introducing an effective doping concentration x_{eff} smaller than the actual concentration x_{Mn} and an antiferromagnetic temperature T_{AF}, reflecting the influence of distant Mn^{2+} ions. In bulk DMS the Mn^{2+} ions can be assumed to be randomly distributed within the host lattice and for small Mn^{2+} contents $< 5\,\%$ the effective concentration equals the portion P_{iso} of isolated Mn^{2+} ions ($x_{\mathrm{eff}} = P_{\mathrm{iso}}(x_{\mathrm{Mn}}) = x_{\mathrm{Mn}} \cdot (1 - x_{\mathrm{Mn}})^{12}$). With increasing dopant concentration the fraction of small clusters like triplets or quartets [177], contributing to the overall magnetization with a nonzero spin moment, has to be taken into account and x_{eff} follows an

empirical expression [178] ($x_{\text{eff}} = x_{\text{Mn}} \cdot (0.265\ \exp(-43.34 \cdot x_{\text{Mn}}) + 0.735\ \exp(-6.19 \cdot x_{\text{Mn}}))$, solid line in Figure 4.1). Note that the antiferromagnetic interactions between neighboring ions severely limit the magnetic properties of bulk DMS, as x_{eff} never reaches 0.05 in its maximum.

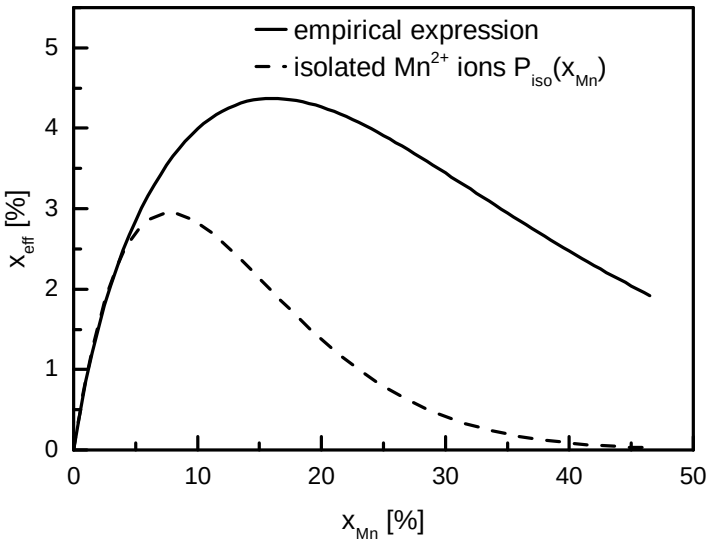

Figure 4.1: x_{eff} at different nominal concentrations x_{Mn} in comparison to the portion of isolated Mn^{2+} ions P_{iso} (dashed line) in bulk DMS. Depicted solid line show fits for Mn^{2+}-doped CdTe [178], but is valid in general for Mn^{2+} in II-VI hosts [179].

This situation might be completely different in Mn^{2+}-doped $(CdSe)_{13}$, in which the replacement of a single ion equals a discrete step in the doping concentration of 7.7 %. This suggests a particularly strong magneto-optical response in clusters doped with a single Mn^{2+} ion. With nearly all 26 atoms in one cluster representing nearest neighbor atoms, it is on the other hand very likely that the Mn^{2+} ions in clusters containing two dopants couple antiferromagnetically, and in this case no magneto-optical response would be expected. According to that, $(CdSe)_{13}$ MSCs would offer the possibility to turn the magneto-optical activity *on* from undoped clusters by replacing a single Cd atom by Mn in monodoped $Cd_{12}MnSe_{13}$ and *off* by the replacement of two dopants in bidoped $Cd_{11}Mn_2Se_{13}$. Due to our synthesis route all three species are prepared as a mixed batch containing undoped as well as mono- and bidoped clusters, with their portions being dependent on the overall Mn^{2+} concentration x_{Mn}. Nevertheless, even in the case of a mixed ensemble the only species exhibiting magneto-optical functionality exceeding the intrinsic Zeeman splitting would be monodoped clusters, and thus all giant magneto-optical response in the ensemble would be generated by isolated dopants. The *Digital Doping* behavior makes Mn^{2+}-doped MSCs an interesting candidate for solotronics [62, 63]. This recently emerging research field concentrates on the creation, observation and manipulation of solitary dopants in semiconductors and their electrical, optical and magneto(-optical) properties [62, 63, 180, 181].

4.1.2 Mass Spectrometry on Doped Clusters

To probe the hypothesis of *Digital Doping* in Mn^{2+}-doped $(CdSe)_{13}$, a concentration series with overall Mn^{2+} contents between $x_{Mn} = 0\,\%$ and $x_{Mn} = 10\,\%$ are prepared via variation of the $MnCl_2$ concentration in the precursor solution. Exact doping concentrations as extracted from inductively coupled plasma - atomic emission spectroscopy (ICP-AES) measurements are listed in Table 4.1. Sample synthesis as well as LDI-TOF MS and ICP-AES have been conducted by Dr. Jiwoong Yang at the Seoul National University in Seoul, Korea.

In order to determine how these overall concentrations are distributed among the different species obtained during the synthesis (i.e. undoped, monodoped and bidoped clusters), the actual composition of the ensemble is extracted via LDI-TOF MS. Figure 4.2 depicts mass spectra of samples with varying x_{Mn}, with m/z given in multiples of the unified atomic mass unit. All spectra contain three main peaks, which can be unambiguously related to the different species according to their masses: With atomic weights of 112.41 u, 78.96 u, 54.94 u and 35.45 u for Cd, Se, Mn and Cl [182], respectively, the different species should exhibit masses of 2523.26 u, 2465.79 u and 2408.32 u for $(CdSe)_{13}$, $MnCd_{12}Se_{13}$ and $Mn_2Cd_{11}Se_{13}$, respectively (note that each species is ionized with one Cl^- ion). The fine structure and the width of the three peaks derive from the contribution of isotopes, which can be precisely simulated as visible in Figure 4.2.

All three peaks exhibit a clear change in intensity with x_{Mn}. At low concentrations the portion of undoped clusters dominates, while with increasing x_{Mn} the percentage of mono- and bidoped clusters increases. Independent of the doping concentration, no evidence of clusters containing three or more dopants is present at m/z values below 2390. As all three species are very similar in their structure and composition, they can be considered to share the same ionization processes, which means that they exhibit related probabilities of getting ionized or fragmented. This enables the extraction of the relative amounts of undoped, monodoped and bidoped species in the ensemble based on the

Table 4.1: Exact doping concentrations of the samples used in this section as extracted via ICP-AES.

integers used in the text	LDI-TOF MS samples	MCD samples
2 %	$2.20 \pm 0.02\,\%$	$2.30 \pm 0.07\,\%$
4 %	$4.00 \pm 0.05\,\%$	$4.00 \pm 0.25\,\%$
6 %	–	$6.32 \pm 0.36\,\%$
7 %	$7.40 \pm 0.15\,\%$	–
8 %	–	$8.14 \pm 0.53\,\%$
10 %	$9.9 \pm 0.2\,\%$	$10.16 \pm 0.63\,\%$

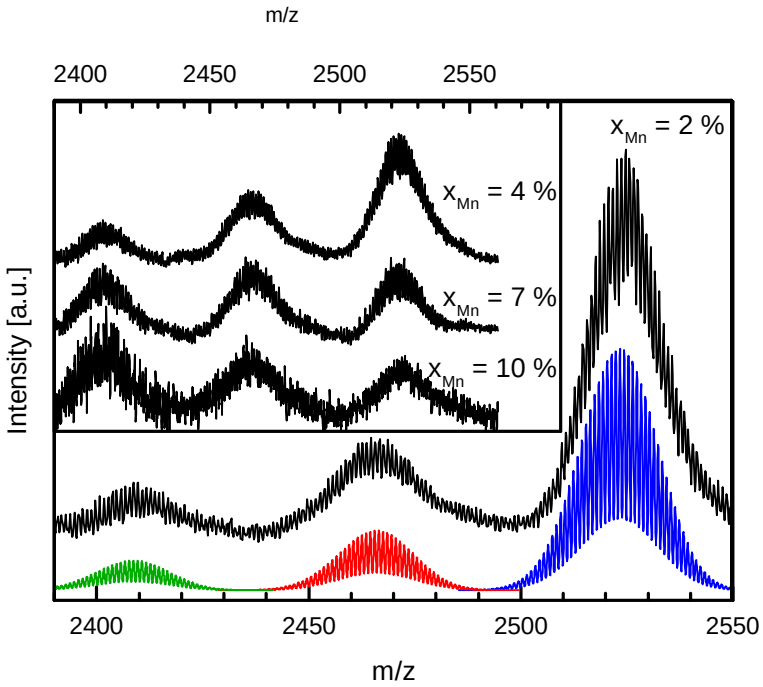

Figure 4.2: Mass spectra of Mn^{2+}-doped $(CdSe)_{13}$. For $(CdSe)_{13}$ with a Mn^{2+} concentration of $x_{Mn} = 2\,\%$ the LDI-TOF MS data (black) is compared to simulated isotropic distributions ($Mn_2Cd_{11}Se_{13}$ in green, $MnCd_{12}Se_{13}$ in red and $(CdSe)_{13}$ in blue). The inset depicts LDI-TOF MS data for samples with different doping concentrations.

intensities of the corresponding peaks in the LDI-TOF MS spectra, although quantitative analysis of MS data is usually not trivial [183, 184]. The extracted relative amounts of the three species are depicted in Figure 4.3. With increasing overall Mn^{2+} concentration x_{Mn} the percentage of undoped clusters decreases, while the ratio of bidoped clusters increases. A maximum of monodoped clusters is found at a doping concentration of 7.4 %.

The probabilities $P_0(x_{Mn})$, $P_1(x_{Mn})$ and $P_2(x_{Mn})$ for un-, mono- and bidoped clusters are in addition simulated on the basis of a binomial distribution. As no evidence of clusters doped with three or more Mn^{2+} ions is found in experiment, only undoped, mono- and bidoped clusters are considered. The simulation ensures that at any given overall concentration x_{Mn}, the probabilities of the three different species add up to unity, while the total number of Mn^{2+} ions in the ensemble accounts for x_{Mn} (compare Equations 4.1 and 4.2).

$$P_0(x_{Mn}) + P_1(x_{Mn}) + P_2(x_{Mn}) = 1 \tag{4.1}$$

$$x_{Mn} = \frac{1}{13} \cdot P_1(x_{Mn}) + \frac{2}{13} \cdot P_2(x_{Mn}) \tag{4.2}$$

Assuming the same probabilities for embedding one Mn^{2+} in any of the different species, the probability that an undoped, monodoped or bidoped cluster is built exhibit the same

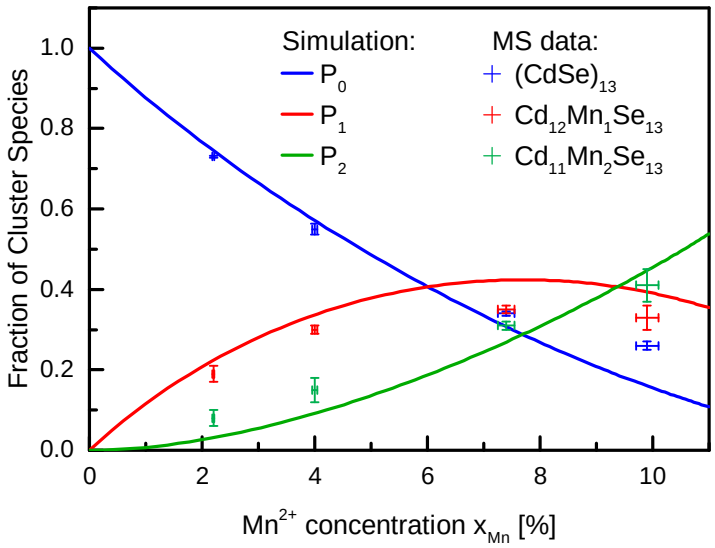

Figure 4.3: Ratios of different cluster species as extracted from MS spectra (symbols) compared to simulated dopant distributions (solid lines) at a given overall concentration x_{Mn}.

ratios as the corresponding values of the binomial probability mass function:

$$\begin{aligned} &P_0(x_{\mathrm{Mn}}) : P_1(x_{\mathrm{Mn}}) : P_2(x_{\mathrm{Mn}}) \\ &\qquad = B_{13,\mathrm{x_{cor}}}(0) : B_{13,\mathrm{x_{cor}}}(1) : B_{13,\mathrm{x_{cor}}}(2) \\ &\text{with} \quad B_{13,\mathrm{x_{cor}}}(i) = \binom{13}{i} {x_{\mathrm{cor}}}^{i} \left(1 - x_{\mathrm{cor}}\right)^{13-i} \end{aligned} \tag{4.3}$$

In the binomial probability mass function the corrected concentration x_{cor} reflects the absence of clusters doped with more than two Mn^{2+} ions. The probabilities for the different species are then given by:

$$\begin{aligned} P_0(x_{\mathrm{Mn}}) &= \frac{B_{13,\mathrm{x_{cor}}}(0)}{B_{13,\mathrm{x_{cor}}}(0) + B_{13,\mathrm{x_{cor}}}(1) + B_{13,\mathrm{x_{cor}}}(2)} \\ P_1(x_{\mathrm{Mn}}) &= \frac{B_{13,\mathrm{x_{cor}}}(1)}{B_{13,\mathrm{x_{cor}}}(0) + B_{13,\mathrm{x_{cor}}}(1) + B_{13,\mathrm{x_{cor}}}(2)} \\ P_2(x_{\mathrm{Mn}}) &= \frac{B_{13,\mathrm{x_{cor}}}(2)}{B_{13,\mathrm{x_{cor}}}(0) + B_{13,\mathrm{x_{cor}}}(1) + B_{13,\mathrm{x_{cor}}}(2)} \end{aligned} \tag{4.4}$$

The correlation between x_{Mn} and x_{cor} can be expressed as:

$$\begin{aligned} x_{\mathrm{Mn}} = &\frac{1}{13} \frac{B_{13,\mathrm{x_{cor}}}(1)}{B_{13,\mathrm{x_{cor}}}(0) + B_{13,\mathrm{x_{cor}}}(1) + B_{13,\mathrm{x_{cor}}}(2)} \\ &+ \frac{2}{13} \frac{B_{13,\mathrm{x_{cor}}}(2)}{B_{13,\mathrm{x_{cor}}}(0) + B_{13,\mathrm{x_{cor}}}(1) + B_{13,\mathrm{x_{cor}}}(2)} \end{aligned} \tag{4.5}$$

Simulated ratios of the different cluster species are depicted in Figure 4.3 as solid lines,

exhibiting very good agreement with the values extracted from the MS data. The small deviations between the experimentally determined and the calculated values might be explained by the difference in formation entropies for mono- and bidoped clusters [29], not considered in the binomial approximation. Together, LDI-TOF MS measurements and the simulated ratios represent a strong evidence that no clusters with three or more dopants are formed. Furthermore the good agreement between both proves that the dopants are statistically distributed among the cluster ensemble.

4.1.3 Evidence of *Digital Doping* in Mn^{2+}-Doped Clusters

The magneto-optical response, representing an evidence of effective *sp-d* exchange interactions, was examined for samples with varying overall Mn^{2+} concentrations using MCD spectroscopy. Figure 4.4 depicts absorption and MCD signals of MSCs containing a Mn^{2+} concentration of $x_{\mathrm{Mn}} = 2\,\%$. Both spectra contain a superposition of various peaks, which were identified as the fine structure of the $1S_{3/2}1S_e$ band edge transition [31]. The mismatch between the MCD zero crossing (approx. 3.65 eV) and the dominant peak in absorption (approx. 3.7 eV) reveals the existence of the magneto-optically active $\pm 1^{\mathrm{L}}$ transition (shown in red), contributing to both the absorption and MCD signal, and the magneto-optically inactive 0^{L} peak, which is not present in MCD, but strongly contributes to the absorption signal. The two peaks between 3.8 eV and 4.0 eV are assigned to the magneto-optically active $\pm 1^{U}$ transition (red) and the magneto-optically inactive 0^{U} peak (blue), following the argumentation in [31].

As the MCD signal represents a superposition of various contributions, only the Zeeman splitting of the energetically lowest $\pm 1^{\mathrm{L}}$ transition is evaluated here, as the low energy tail of the corresponding MCD feature does not exhibit any overlap with other transitions. To determine the width and height of the $\pm 1^{\mathrm{L}}$ absorption peaks necessary for the extraction of the corresponding Zeeman splitting (compare Equation 3.4), the absorption spectrum up to 3.95 eV is fitted with four peaks, with the first one being fixed to the position of the MCD zero crossing. This procedure allows the extraction of the Zeeman splitting ΔE_{Z} as -2.0 meV, which corresponds to an effective g-factor of $g_{\mathrm{eff}} = -25$.

Figure 4.5a shows the extracted Zeeman splittings for MSC samples with different doping concentrations up to $x_{\mathrm{Mn}} = 10\,\%$ (exact concentration values can be found in Table 4.1). The error bars result from uncertainties in the fitting procedure leading to inaccuracy in the extracted Zeeman splittings. The splitting increases with increasing Mn^{2+} concentration up to a maximal giant Zeeman splitting of -13.5 meV for $x_{\mathrm{Mn}} = 6\,\%$.

The Zeeman splitting in DMS in general is proportional to the concentration of magneto-optically active ions x_{eff} and their mean spin moment along the magnetic axis

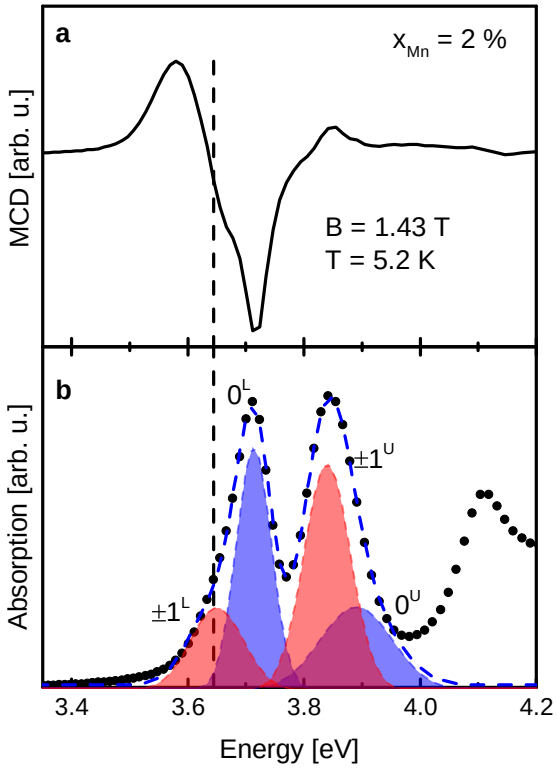

Figure 4.4: Magneto-optical characterization of Mn^{2+}-doped MSCs with $x_{Mn} = 2\,\%$ at 5 K and 1.43 T: (a) MCD and (b) absorption spectrum. Red (blue) peaks in (b) represent fits to the magneto-optically active (inactive) transitions, while the sum of the fits is depicted in a blue dashed line. Experimental data is shown as black dots. The energetic position of the $\pm1^L$ transition is highlighted with a dashed black line.

$\langle S_z \rangle$, which is determined by the magnetic field and the temperature via the Brillouin function (compare also Figure 2.4.4):

$$\Delta E_Z \propto x_{\text{eff}} \langle S_z \rangle \tag{4.6}$$

The proportionality is determined by the overlap γ of the wave function of the involved charge carriers with the Mn^{2+} ions, as well as the strength of the exchange coupling, which is described by the exchange coupling constants $N_0\alpha$ and $N_0\beta$, both being independent on the Mn^{2+} concentration. If MSCs are considered as borderline case of a spherical quantum dot, the proportionality constant accounts for $\gamma(-N_0\alpha + N_0\beta)$, assuming a pure *hh*-X transition. Nevertheless, the comparison to conventional quantum dots with similar doping concentrations exhibits substantially smaller Zeeman splittings measured in case of the MSCs [30]. This might be either due to a quantum confinement induced modification of the exchange coupling constants [37, 143, 146] or the admixture of different valence band subbands due to the spherical confinement [38, 106]. On the other hand, most of the 13 cation lattice sites can be considered as surface atoms and thus the overlap γ of a Mn^{2+}-dopant with the charge carriers' envelope functions may be significantly reduced.

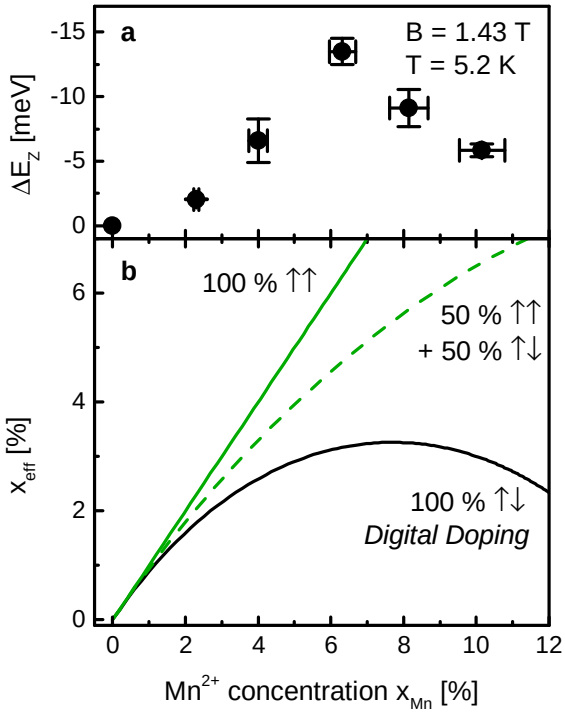

Figure 4.5: (a) Extracted Zeeman splittings of the $\pm 1^L$ transitions for cluster samples with different overall concentration x_{Mn}. Data is listed in Table 4.2. (b) depicts the expectations for the concentration of magneto-optically active ions in Mn^{2+}-doped MSCs with (black line) and without (straight green line) *Digital Doping*. The case of 50 % antiferromagnetical coupling in bidoped clusters is depicted as dashed green line.

However, neither the overlap γ nor the strength of the exchange coupling itself is expected to depend on the overall Mn^{2+} concentration. The Brillouin function determining $\langle S_z \rangle$ usually contains the - concentration dependent - antiferromagnetic temperature T_{AF}, describing the influence of distant Mn^{2+} ions (more than a unit cell apart). Those interactions can be neglected in case of the clusters, as the lattice does not contain much more than a unit cell and neighboring clusters are separated by oleylamine ligands impeding any antiferromagnetic interactions. Hence the Zeeman splitting should be directly proportional to the concentration of magneto-optically active Mn^{2+} ions x_{eff}. It is thus instructive to compare the Zeeman splitting dependence on the overall concentration x_{Mn} with theoretical expectations for x_{eff} in different cases.

For the clusters two limiting situations can be considered. In case that the Mn^{2+} ions embedded in bidoped clusters do not interact and behave completely paramagnetic, all doped clusters (mono- and bidoped) would contribute to the magneto-optical response and thus the effective concentration would equal the nominal concentration ($x_{\mathrm{eff}} = x_{\mathrm{Mn}}$, straight green line in Figure 4.5b). In the opposite situation the Mn^{2+} ions in bidoped clusters are completely aligned antiferromagnetically and do not contribute at all to the magneto-optical response. Thus x_{eff} would follow the ratio of monodoped clusters

($x_{\mathrm{eff}} = P_1(x_{\mathrm{Mn}})$, black line). This represents the case of *Digital Doping*. Partial coupling would lead to an expectation between those limiting cases, as illustrated for an antiferromagnetic coupling in 50 % of the bidoped clusters in Figure 4.5. Comparison of the experimentally extracted data with the theoretical expectations reveals that the picture of *Digital Doping* quite nicely describes the measured dependence. Especially, the predicted concentration with maximal magneto-optical response of 7.7 % agrees well with the experimental concentration with the maximum Zeeman splitting at 6 %. These findings also directly imply that the magneto-optical response derives from solitary dopants in monodoped clusters, while bidoped clusters are almost completely inactive in MCD (except the small intrinsic contribution). By replacing one atom in the $(CdSe)_{13}$ clusters with Mn^{2+}, the giant magneto-optical response can be turned *on*, while by addition of a second dopant, it is turned *off* again.

Table 4.2: Extracted Zeeman splittings and the corresponding g-factors for Mn^{2+}-doped $(CdSe)_{13}$ with different doping concentrations at 5 K and 1.43 T.

doping concentration [%]	ΔE_{Z} [meV]	g_{eff}
2.30 ± 0.07	2.0	−25
4.00 ± 0.25	6.6	−81
6.32 ± 0.36	13.5	−166
8.14 ± 0.53	9.13	−112
10.16 ± 0.63	5.9	−72

4.1.4 Magneto-Optical Response up to Room Temperature

The temperature dependence of the magneto-optical response offers the possibility to trace the influence of thermal energy on the Mn^{2+} magnetization. Figure 4.6 depicts MCD spectra at different temperatures for three different samples with $x_{\mathrm{Mn}} = 2\,\%, 6\,\%$ and $10\,\%$, respectively. All samples exhibit a strong decrease in amplitude combined with a shift towards lower energies with increasing temperatures, the latter being originated by the characteristic temperature dependence of the bandgap common for most semiconductors.

Remarkably, the magneto-optical response persists up to room temperature (spectra in the insets) without any inversion in the sign of the MCD. This evidences that even at room temperature the giant Zeeman splitting exceeds the intrinsic contribution, which is expected to exhibit a positive sign in bulk CdSe [88]. Note that the intrinsic contribution is influenced by quantization in small QDs, but remains positive even at diameters of 38 Å [130]. Stemming exclusively from solitary dopants in monodoped clusters, this magnetic functionality at room temperature distinguishes Mn^{2+}-doped MSCs as promising material for future spintronic applications.

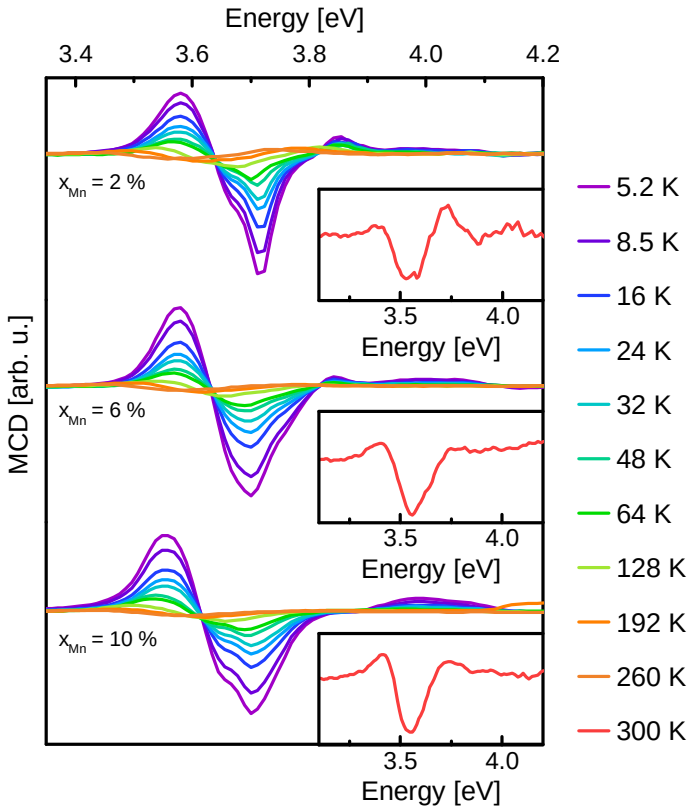

Figure 4.6: MCD spectra of Mn^{2+}-doped $(CdSe)_{13}$ with different doping concentrations at 1.43 T and varying temperatures between 5 K and 300 K. Room temperature spectra are shown in the insets.

Figure 4.7a compares the decrease in amplitude for the first MCD maximum with the extracted Zeeman splittings up to a temperature of 64 K (values at higher temperatures have not been extracted with respect to enlarged uncertainties due to the increasing line widths with temperature), revealing that the MCD amplitude evolves proportional to ΔE_Z. This allows deduction of the decline in Zeeman splitting from the trend in the MCD amplitude. The decrease stems from the thermal energy impeding the alignment of the Mn^{2+} ions along the external magnetic field, which is described by the Brillouin function:

$$\langle S_z \rangle = x_{\text{eff}} S \cdot B_S \left(\frac{g_{Mn} \mu_B S B}{k_B T_{\text{eff}}} \right) \quad \text{with} \quad T_{\text{eff}} = T + \Delta T \tag{4.7}$$

The Mn^{2+} spin temperature determining the Brillouin function is composed of the actual bath temperature T and a small correction ΔT. In bulk DMS this corresponds to the coupling of more distant Mn^{2+} ions and is thus denominated as the antiferromagnetic temperature T_{AF} in the conventional theory of Gaj *et al.* [60]. In common DMS materials such as Mn^{2+}-doped CdSe or CdTe, T_{AF} does not exceed 2.6 K [60, 178, 185]. As outlined above, the interactions with further Mn^{2+} ions can be neglected in Mn^{2+}-doped $(CdSe)_{13}$ and therefore T_{AF} is expected to equal zero in this material.

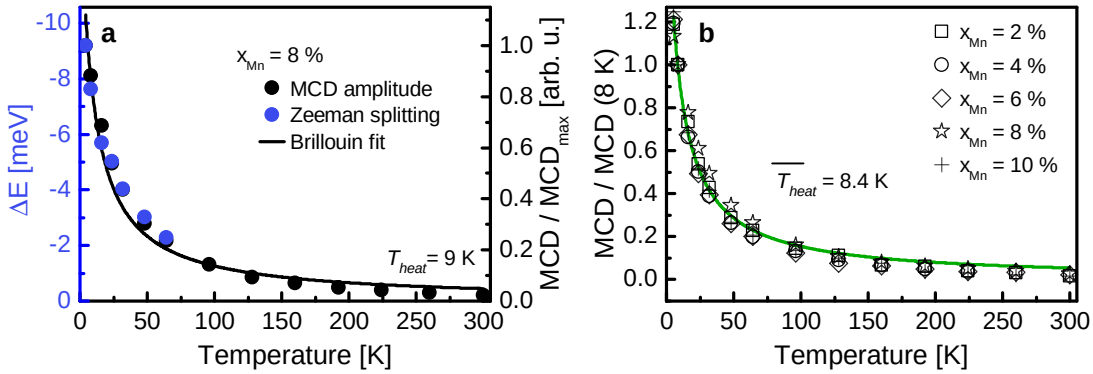

Figure 4.7: (a) Temperature dependence of the Zeeman splitting ΔE_Z (blue, left axis) compared to the decrease in MCD amplitude (black, right axis). The black line indicates a Brillouin fit. (b) compares the temperature dependent decrease of the MCD amplitude for different Mn^{2+} concentrations, normalized to the value at 8 K. A Brillouin fit is indicated with a black/green line.

Interestingly, fitting the temperature dependent decay of the MCD amplitude in Figure 4.7 with Equation 4.7 yields a nonzero ΔT of $\approx$ 9 K for Mn^{2+}-doped $(CdSe)_{13}$ with $x_{Mn} = 8\,\%$. Similarly enhanced so-called Mn^{2+} temperatures T_{heat} have also been observed in other DMS materials related to an energy transfer from free carriers to the Mn^{2+} ensemble. This so-called spin heating results from a fast and efficient energy transfer into the Mn^{2+} spin system from either photogenerated [186–189] or electrically induced [190] carriers, while on the other hand the cooling down of the Mn^{2+} system to the bath temperature T is restricted by the spin-lattice relaxation (SLR) times. As isolated Mn^{2+} ions exhibit a zero orbital momentum, they do not directly interact with the phonon system [8], and therefore SLR occurs with the aid of Mn^{2+} clusters in bulk DMS. Thus, the SLR times critically depend on the Mn^{2+} concentration [186, 188], leading to the observation of enhanced temperatures T_{heat} of a few up to several tens of Kelvins above the bath temperature at low doping concentrations. The excess energy of free carriers can either be transfered *directly* to the spin system by spin exchange scattering, providing simultaneous spin and energy transfer, or *indirectly* via acoustical phonons emitted by the carriers, which increases the bath temperature. The *direct* transfer can also include the excitation of the internal $^6A_1 \rightarrow {}^4T_1$ transition from excitonic states, as observed in Mn^{2+}-doped $(CdSe)_{13}$ (compare [31]). In single-Mn^{2+}-doped epitaxial QDs, enhanced spin temperatures of up to 60 K have been observed [191]. Thus, the enhanced spin temperature might be attributed to the effect of spin heating in the monodoped clusters, e. g., induced by the excess energy released during the excitation of the internal $^6A_1 \rightarrow {}^4T_1$ transition. Note that the band edge in our clusters strongly exceeds the internal Mn^{2+} transition in energy (3.6 eV compared to $\approx$ 2.1 eV).

This hypothesis is affirmed by the comparison between the temperature dependent

decays of the MCD amplitude for several samples with different doping concentrations. Figure 4.7b reveals that regardless of the Mn^{2+} concentration the MCD signal follows the same Brillouin trend. All decays can be fitted with one mean $\overline{T_{\mathrm{heat}}} = 8.4\,\mathrm{K}$, which is in contrast to the antiferromagntic temperature T_{AF} in conventional DMS materials increasing proportionally to the overall Mn^{2+} concentration. The observation of a similiar T_{heat} among different concentrations furthermore is consistent with the conclusion that only monodoped clusters cause the magneto-optical response throughout the whole concentration range between 0 % and 10 %.

4.2 Mn^{2+}-Doped Alloy $(Zn_xCd_{1-x}Se)_{13}$ Clusters

The previous chapter deals with the possibility to activate and deactivate the giant magneto-optical response in $(CdSe)_{13}$ clusters in a digital manner through Mn^{2+} incorporation. By varying the concentration of the $MnCl_2$ precursor, concentrations up to 10 % can be reached experimentally. This Mn^{2+} content introduces a small bandgap shift of about ≈ 30 meV, as visible in Figure 4.6 between the 5 K MCD responses of Mn^{2+}-doped samples with $x_{Mn} = 2\,\%$ and 10 %, respectively.

In bulk and colloidal semiconductors QDs, alloying, i.e. the continuous tuning of the composition between two materials, represents a common tool to adjust the optical and electrical properties, particularly the fundamental bandgap [192–197]. By changing the concentration x from 0 % to 100 % in pseudo-binary alloys of type $A_xB_{1-x}C$, the bandgap can be continuously tuned between the bandgap of AC and BC, as has been shown for various II-VI material combinations. In case of MSCs containing only 26 atoms, alloying is only possible discretely changing the concentration in steps of 7.7 %. Even more interesting, simultaneous alloying and doping would offer the possibility to precisely tune the energetic region of the magneto-optical response of a colloidal DMS material. This vision requires the combination of four different elements (namely Cd, Zn, Mn and Se in our case) in one stable crystal containing a defined number of 26 lattice sites. Furthermore the combination of CdSe and ZnSe along with the high confinement due to the very small size in the MSCs pushes the spectral region of the magneto-optical activity towards the high UV, which is not easily achieved in colloidal DMS nanostructures, as those are restricted in their minimum size.

4.2.1 Undoped $(Zn_xCd_{1-x}Se)_{13}$ Clusters

Figure 4.8 depicts mass spectra and room temperature absorption of undoped $(Zn_xCd_{1-x}Se)_{13}$ clusters, proving the successful variation of the Zn content in the clusters between 0 % and 100 %. The sample preparation as well as LDI-TOF MS and room-temperature optical characterization have been conducted by Dr. Jiwoong Yang at the Seoul National University. The LDI-TOF MS spectrum shown in Figure 4.8b exhibits multiple peaks equally seperated in m/z. Comparison to simulated isotropic distributions (colored peaks) reveals that each peak can be assigned to a specific cluster species with a well defined number of Zn and Cd cations between 0 and 13, with their spacing corresponding to the difference in atomic masses between Cd and Zn (112.41 u and 65.39 u for Cd and Zn, respectively). The possibility to variably substitute all 13 cations stands in distinct contrast to transition metal doping, where a maximum number of two cation

lattice sites can be replaced with Mn^{2+} ions, as elaborated above. This difference most likely originates from the fact that Zn represents an isovalent substituent to Cd, while the TM^{2+} exhibit partly unpaired *3d* electrons. The absorption spectra shown in Figure 4.8c reflect the properties of ensembles containing a mixture of different species in case of alloying, as visible in the enhanced line widths for samples containing both Zn and Cd in comparison to samples with pure $(CdSe)_{13}$ or $(ZnSe)_{13}$ clusters. With increasing overall Zn content the absorption peaks corresponding to the $1S_{3/2}1S_e$ band edge transition continuously shift towards higher energies, evidencing the expected tunability of the bandgap.

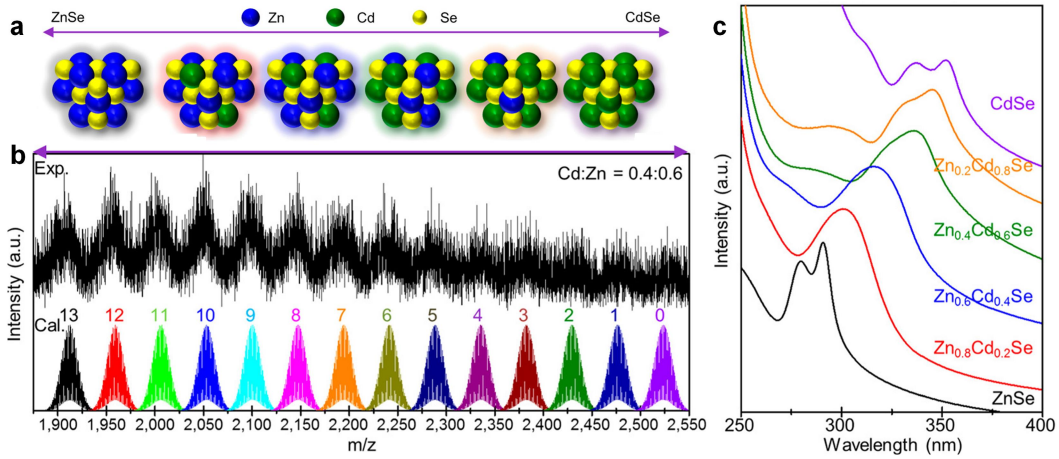

Figure 4.8: (a) depicts a sketch visualizing the idea of alloying in $(Zn_xCd_{1-x}Se)_{13}$ clusters. In (b), LDI-TOF MS spectra of an as prepared ensemble with an overall Zn content of $x_{Zn} = 0.6$ is shown. The colored peaks depict simulated isotropic distributions for the different cluster species, with the number of comprised Zn atoms given above. (c) depicts room temperature absorption spectra of cluster dispersions with different overall Zn contents. From [59].

4.2.2 Magneto-Optical Properties of Mn^{2+}-Doped Alloy Clusters

In order to furnish the alloy clusters with an additional magneto-optical functionality, $MnCl_2$ is added to the precursor solution to obtain Mn^{2+}-doping. All doped samples examined during this study contain $x_{Mn} = 6\,\%$ Mn^{2+} concentration among the total amount of cations. The Zn contents given represent the percentage compared to the overall amount of non-magnetic cations, i.e., merely Zn and Cd cations.

First evidences of successful Mn^{2+} incorporation can be found in the room temperature absorption, PL and PLE spectra. Mn^{2+}-doped clusters exhibit absorption peaks with similar energetic positions as their undoped counterparts, indicating that the clusters

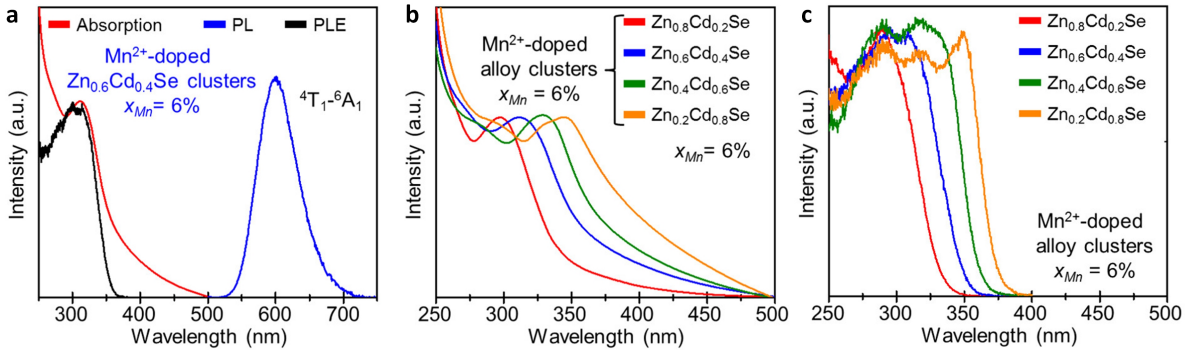

Figure 4.9: Room temperature optical characterization of Mn^{2+}-doped alloy clusters. (a) Room temperature absorption (red), PL (blue) and PLE (black) spectra of Mn^{2+}-doped $(Zn_{0.6}Cd_{0.4}Se)_{13}$ with $x_{Mn} = 6\,\%$. Absorption (b) and PLE (c) spectra of Mn^{2+}-doped alloy clusters with $x_{Mn} = 6\,\%$ doping concentration and varying Zn content.

maintain their structure even after Mn^{2+} incorporation. The Mn^{2+}-doped alloy clusters exhibit the characteristic Mn^{2+} ligand field transition at $\approx 2.1\,eV$ in PL (compare Figure 4.9a) and PLE spectra of this transition closely resemble the absorption spectra of the same samples (compare Figure 4.9b and c).

The challenge of incorporating four different atoms in one single cluster opens up the question of the feasibility of magneto-optically active doping of the alloy clusters and their function as diluted magnetic semiconductors. To finally proof the magneto-optical activity of the embedded Mn^{2+} ions, MCD spectroscopy was conducted. In contrast to Mn^{2+}-doped $(CdSe)_{13}$ clusters, which are surface-modified with oleylamine to improve the dispersibility and reduce light scattering [198], Mn^{2+}-doped alloy and $(ZnSe)_{13}$ clusters are not stable after ligand exchange and are thus dispersed in octylamine. For the magneto-optical characterization, a small amount of oleylamine was added just prior sample preparation to avoid scattering through oleylamine crystallization.

Figure 4.10 depicts the normalized magneto-optical responses at cryogenic temperature for Mn^{2+}-doped alloy cluster samples exhibiting different Zn contents between 0 to 1. With increasing Zn content the whole MCD feature shifts towards higher energies. Although the MCD spectra of alloy clusters exhibit larger line widths, the characteristic shape of the MCD feature is still maintained. This proves that the Mn^{2+} ions are successfully incorporated developing a magneto-optical activity, and documents that alloy clusters can be regarded as a member of the family of DMS materials. It also unambiguously demonstrates the successful combination of four different cations in a single cluster. Furthermore, due to the extraordinary high quantization energies in these small clusters, the measured energy range of the magneto-optical response lay in the high UV regime for samples with high Zn contents, expanding the spectral range for future spintronic and solotronic applications.

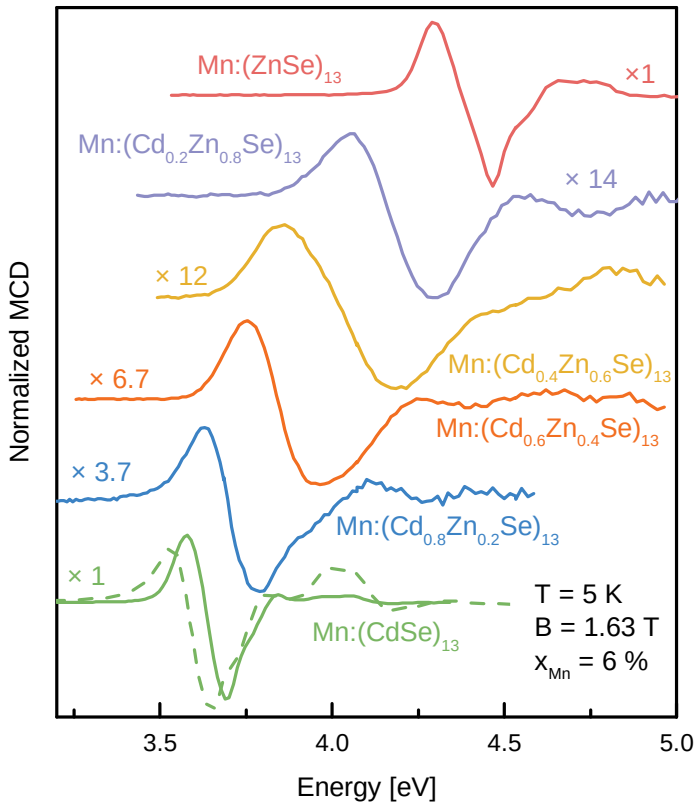

Figure 4.10: Normalized MCD spectra of Mn^{2+}-doped alloy clusters with different Zn contents and $x_{Mn} = 6\,\%$ doping concentration. All spectra are detected at 5 K and 1.63 T. For pure Mn:$(CdSe)_{13}$, measurements on samples passivated with oleylamine (solid line) and octylamine (dashed line) are depicted. Relative normalizing factors are indicated for each spectrum.

Note that while all samples containing Zn are stable, when passivated with octylamine, octylamine covered $(CdSe)_{13}$ degenerate within a few weeks, which becomes apparent in a color change of the dispersion from whitish to red. As prepared octylamine capped $(CdSe)_{13}$ clusters (dashed green line) are slightly shifted in energy as compared to samples passivated with oleylamine (solid green line, data from Figure 4.4), respectively. A possible explanation for this energy shift might be a slightly different lattice structure favored by either oleylamine or octylamine ligands.

The energetic position of the zero crossings (depicted in Figure 4.11) mark the $\pm 1^{\mathrm{L}}$ state of the band edge $1S_{3/2}1S_e$ transition, representing a good indicator for the bandgap shift depending on the Zn content. Considering only stable cluster samples (i.e. $(CdSe)_{13}$ capped with oleylamine and all other samples capped with octylamine), the bandgap shift can be well fitted with the quadratic equation used to describe the commonly observed pronounced bowing behavior of the bandgap in bulk alloy $Zn_xCd_{1-x}Se$ (compare Equation 2.2):

$$E_g(x) = xE_g^{\mathrm{ZnSe}} + (1-x)E_g^{\mathrm{CdSe}} - x(1-x)b \tag{4.8}$$

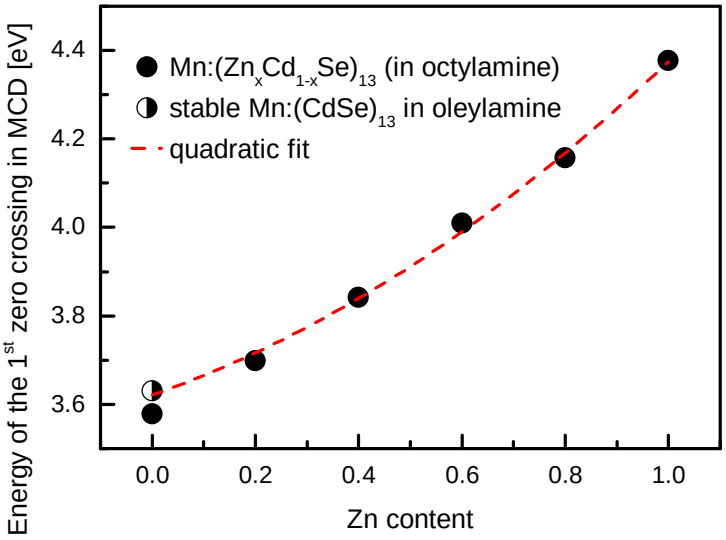

Figure 4.11: Band edge in Mn^{2+}-doped alloy clusters. The energetic position of the first zero crossing in MCD is compared as taken from measurements in Figure 4.10. The values represent the energies of the $\pm 1^{L}$ transition belonging to the fine structure of the $1S_{3/2}1S_e$ band edge. The quadratic fit has been obtained based on Equation 4.8 with $E_g^{ZnSe} = 4.37\,eV$, $E_g^{CdSe} = 3.62\,eV$ and $b = 0.35\,eV$.

Herein $E_g^{CdSe,ZnSe}$ denotes the bandgap of $(CdSe)_{13}$ or $(ZnSe)_{13}$ clusters, respectively, and b is the bowing parameter, which is determined to be 0.35 eV close to reported bulk values (0.30 eV to 0.48 eV [199–201]). The difference between the bandgaps of the pure binary species is slightly smaller compared to the bulk values (0.8 eV compared to $\approx$ 1 eV [202], respectively), which may be related to a decrease of the quantization energy in $(ZnSe)_{13}$ compared to $(CdSe)_{13}$ due to a decreased exciton Bohr radius in ZnSe (4.5 nm in ZnSe and 6 nm in CdSe).

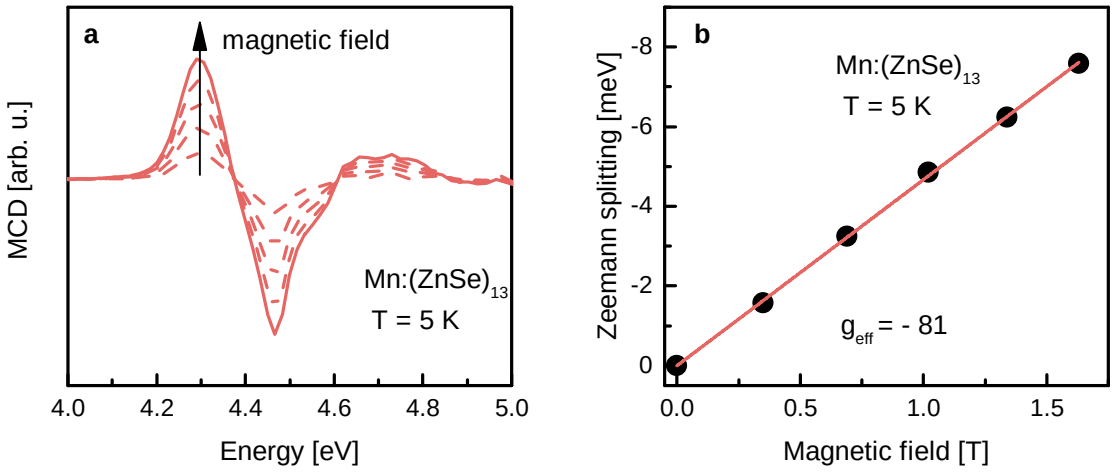

Figure 4.12: Magneto-optical response of Mn^{2+}-doped $(ZnSe)_{13}$. (a) depicts MCD spectra at 5 K and 0.34 T, 0.69 T, 1.02 T, 1.34 T and 1.63 T, respectively. In (b) the corresponding Zeeman splittings are depicted as extracted following the procedure described in Section 4.1.3.

In Figure 4.10, the relative normalization factors, which mirror the different amplitudes of the various MCD spectra, are indicated for each spectrum. While the spectra of pure Mn^{2+}-doped clusters (Mn:$(CdSe)_{13}$ and Mn:$(ZnSe)_{13}$) are of similiar amplitude, alloy clusters exhibit smaller MCD signals. A way to classify the strength of the *sp-d* exchange interactions in these alloy clusters represents the giant Zeeman splitting. For Mn^{2+}-doped $(ZnSe)_{13}$ the magnetic field dependent MCD spectra and the Zeeman splittings of the first transition are depicted in Figure 4.12, the latter extracted following the procedure described in Section 4.1.3. With increasing magnetic field, the MCD amplitude increases linearly, reflecting the magnetization in the spin sublattice due to the alignment along the external magnetic filed. As evident from the non-saturating Zeeman splitting, the magnetic field is not sufficient to completely align all Mn^{2+} ions. The extracted Zeeman splitting corresponds to an effective g-factor of $g_{\text{eff}} = -81$, which is of the same magnitude as in Mn^{2+}-doped $(CdSe)_{13}$ with the same doping concentration. As both materials exhibit similar exchange coupling constants ($N_0\alpha = 0.23\,\text{eV}(0.26\,\text{eV})$ and $N_0\beta = -1.27\,\text{eV}(-1.31\,\text{eV})$ for Mn^{2+} in CdSe (ZnSe)), this suggests that the Mn^{2+} ions share the same magnetic behavior as in Mn^{2+}-doped $(CdSe)_{13}$.

4.2.3 Simulation of the Magneto-Optical Response of Alloy Clusters

For magnetically doped alloy clusters, the giant Zeeman splitting cannot be extracted in a similiar manner as for Mn:$(ZnSe)_{13}$. Here, the absorption spectra represent a superposition of signals from different species with varying number of Zn and Cd cations, which significantly broadens the peaks. The reduction in the MCD amplitude of alloy clusters may either be originated by this broadening, or by a decreased magneto-optical activity of the embedded Mn^{2+} ions as compared to the pure Mn:$(CdSe)_{13}$ and Mn:$(ZnSe)_{13}$ species. In order to enable evaluation of the strength of the *sp-d* exchange coupling in these alloy DMS clusters, the magneto-optical response, i.e., the MCD signals of alloy ensembles with different overall Zn contents are simulated. In the following context, a "species" refers to a subset of particles with exactly the same composition of the host material, i.e. the number of Cd and Zn cations, which may be randomly doped with zero, one or two Mn^{2+} ions. On the other hand a cluster "sample" denotes a mixture of different species resulting in a given overall Zn concentration x_{Zn}.

In order to simulate the MCD spectrum of a cluster ensemble representing a mixture of different Mn^{2+}-doped species, in a first step the theoretical MCD spectra for the

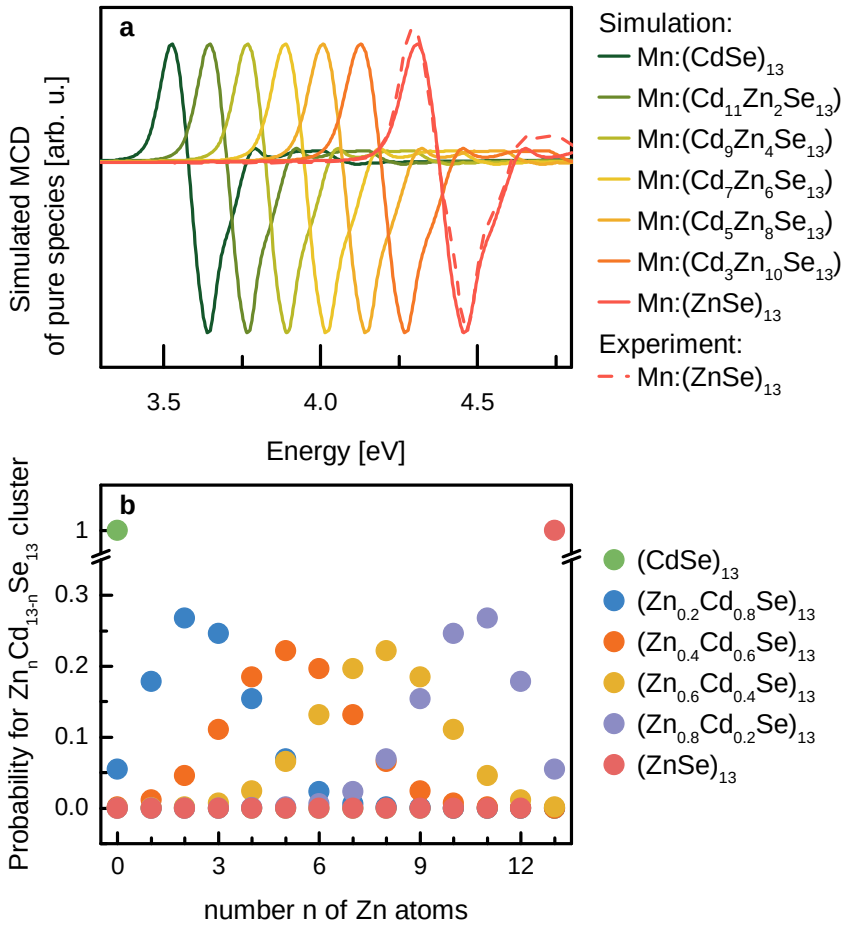

Figure 4.13: Simulation of the MCD spectra for doped alloy clusters. (a) Simulated MCD spectra of selected species. Experimental data for pure Mn^{2+}-doped $(ZnSe)_{13}$ clusters are shown for comparison. In (b) the probabilities for each of the 14 different species containing between zero and 13 Zn atoms are shown for different overall Zn ensemble contents of $x_{Zn} = 0$, 0.2, 0.4, 0.6, 0.8 and 1. For this calculation doping has not been considered.

individual alloy species with defined composition are simulated. For this purpose, the experimentally determined MCD spectrum of Mn:$(CdSe)_{13}$ is shifted in a first approximation linearly in energy between the zero crossings of pure Mn:$(CdSe)_{13}$ and Mn:$(ZnSe)_{13}$. Furthermore the spectra were stretched linearly adjusting the width of the feature (as derived from the first maximum in MCD via fitting to a derivative Gaussian) between 73 meV for Mn:$(CdSe)_{13}$ and 96 meV for Mn:$(ZnSe)_{13}$, to account for the increasing linewidth between $(CdSe)_{13}$ and $(ZnSe)_{13}$ clusters. The simulated spectra for selected species are depicted in Figure 4.13a together with the experimentally determined spectrum of pure Mn:$(ZnSe)_{13}$.

In a second step, the probabilities for the formation of the different species are calculated applying a similar approach as in chapter 4.1.2: As in case of alloying all 13 cations are allowed to be replaced by Zn, the probabilities of the species can be directly derived

from the corresponding binomial distribution:

$$B_{13,x_{Zn}}(i) = \binom{13}{i} {x_{Zn}}^i (1 - x_{Zn})^{13-i} \tag{4.9}$$

Equation 4.9 describes the probability that at a given overall Zn concentration of x_{Zn} a MSC is built containing exactly i Zn and $(13 - i)$ Cd cations. Figure 4.13b depicts the calculated probabilities to find a specific species with $n = 0...13$ Zn atoms for the various overall Zn concentrations used in this study. Note that this approach is basically appropriate for undoped alloys and does not consider the dopants. It is instead assumed that a defined cluster species randomly incorporates zero to two Mn^{2+} ions in case of doping. In a third step, the simulated spectra of the species were weighted with the calculated probabilities to obtain the final simulated spectra of samples with specific overall Zn concentrations.

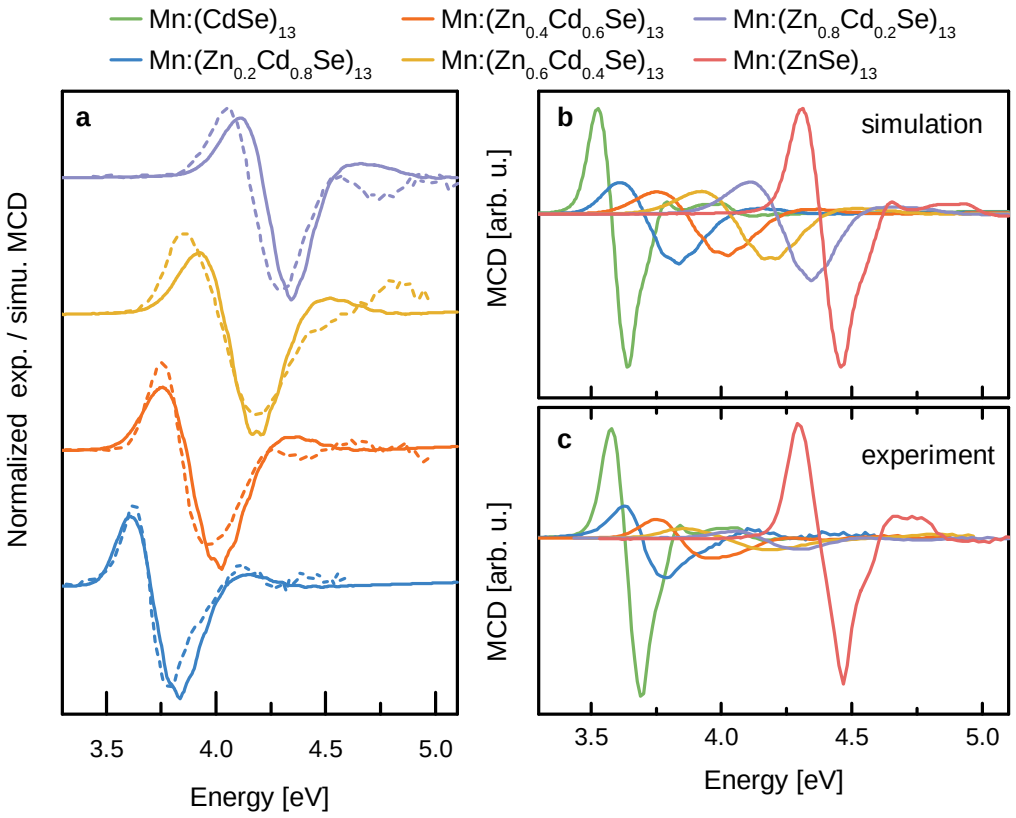

Figure 4.14: Comparison between simulated MCD spectra and experiment. (a) depicts the simulated (solid lines) and experimental (dashed lines) spectra of Mn^{2+}-doped alloy clusters with Zn contents of 0.2, 0.4, 0.6 and 0.8, both normalized peak-to-peak. (b) and (c) compare the - not normalized - MCD spectra for the different samples.

Figure 4.14a depicts the simulated MCD spectra as well as the experimentally determined data for the Mn^{2+}-doped alloy clusters, both normalized peak-to-peak. The simulated spectra quite nicely resemble the experimental data, including both the ener-

getic shift as well as the line widths. Furthermore the simulated spectra reproduce some features of the experiments (i.e. shoulders or kinks, compare in particular the sample with $x_{Zn} = 0.2$). Those features result from the fact, that the energy shift between two species varying in composition by only one Zn atom accounts for ≈ 61 meV. This value is of the same magnitude as the line width of the features originated by a single species (≈ 70 meV to 95 meV).

On the other hand, this similarity in magnitude is expected to result in reduced MCD signals, as the MCD spectra of species differing in composition by one or two Zn cations will partly cancel out each other with the dominant minimum of one species coinciding with the dominant maximum of another species (compare Figure 4.13b). A comparison of the non-normalized MCD amplitudes of experimental and simulated data is shown in Figure 4.14b and c. The alloy DMS clusters experimentally exhibit strongly reduced magneto-optical responses compared to the pure Mn^{2+}-doped $(CdSe)_{13}$ and $(ZnSe)_{13}$. For the simulations, equal MCD amplitudes were assumed among all species, which is equivalent to comparable Zeeman splittings for all species. Nevertheless, the simulated MCD spectra for ensemble samples containing different species exhibit similarly reduced amplitudes as the experimental alloy MSCs. A reduced mean amplitude by a factor four is found for alloys with respect to the binary Mn:$(CdSe)_{13}$ or Mn:$(ZnSe)_{13}$ clusters in simulations, while the experiments exhibit a factor of 6.7. Therefore most of the reduction in the MCD amplitude for alloy clusters can be attributed to the broadening of the spectral resonances due to the mixture of different species. This allows the conclusion that the individual alloy species itself in general exhibit similar MCD amplitudes - and thus *sp-d* exchange interactions - as the binary counterparts.

4.2.4 Temperature Dependence of the Magneto-Optical Response in Mn:$(Zn_xCd_{1-x}Se)_{13}$

Finally, the temperature dependence of the alloy DMS clusters is characterized. Figure 4.15 depicts the temperature dependent MCD spectra up to room temperature for doped alloy clusters ($x_{Zn} = 0.4$) and binary Mn:$(ZnSe)_{13}$. With increasing temperature the spectra of the two samples shift towards lower energies, while the MCD amplitudes rapidly decrease. The absence of a sign reversal evidences that for both samples the magneto-optical response is dominated by the *sp-d* exchange interactions up to room temperature, as for both material systems the intrinsic splitting is expected to exhibit a positive Zeeman splitting ($g_{int} = 1$ to 1.4 for CdSe QDs [28, 129, 130] and 1.1 to 2.5 for ZnSe QDs [22, 24]). Hence, the Mn^{2+}-doped alloy clusters in general enable the usage of *sp-d* exchange interactions with a tunable spectral range of the magneto-optical response in room

temperature spintronic devices.

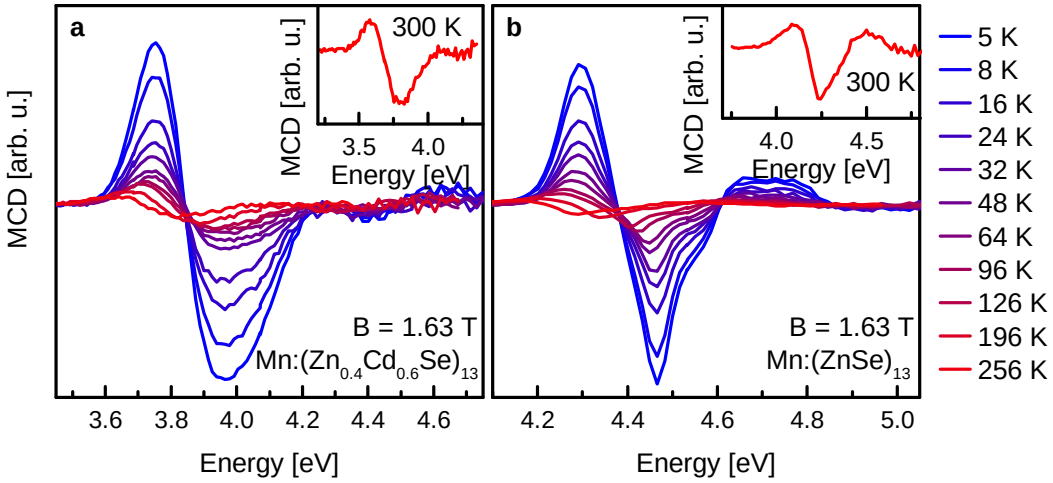

Figure 4.15: Temperature dependence of the magneto-optical response for Mn^{2+}-doped alloy clusters with $x_{Zn} = 0.4$ (a) and pure Mn:$(ZnSe)_{13}$ (b). All spectra are recorded at magnetic fields of 1.63 T. Room temperature spectra are shown in the insets.

Figure 4.16 illustrates the decay of the MCD amplitudes with temperature for different samples. For all samples the MCD amplitude follows a Brillouin decay as characteristic for the giant Zeeman splitting. Analogous to the procedure in Section 4.1.4, a spin temperature T_{heat} can be extracted by describing the decay with Equation 4.7, which yields a value of $\overline{T_{heat}} = 8.7$ K for Mn^{2+}-doped $(ZnSe)_{13}$ exhibiting nice agreement with the Mn^{2+}-doped $(CdSe)_{13}$ cluster samples. This suggests that the Mn^{2+} sublattice in the Mn:$(ZnSe)_{13}$ clusters exhibits similar physics as compared to Mn:$(CdSe)_{13}$. This might include the *Digital Doping* behavior due to the Mn^{2+}-Mn^{2+} exchange interactions as well as the spin heating

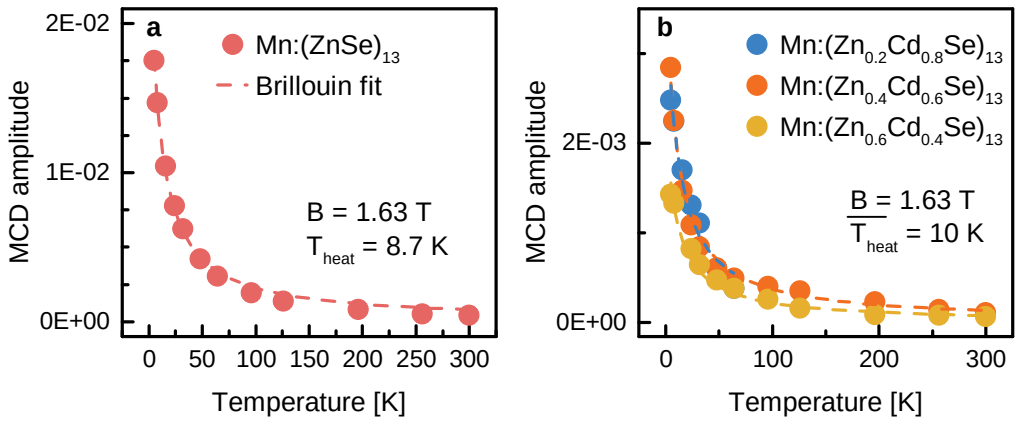

Figure 4.16: Temperature dependence of the MCD amplitude for four different samples. The magneto-optical response could be traced up to 96 K for clusters with $x_{Zn} = 0.2$ and 300 K for samples with $x_{Zn} = 0.4$, 0.6 and 1. Dashed lines indicate Brillouin fits to Equation 4.7.

due to reduced spin-lattice relaxation processes of solely Mn^{2+} ions. Figure 4.16b depicts the temperature dependent MCD amplitudes for three alloy samples with different Zn contents. For samples with $x_{Zn} = 0.4$ and 0.6 the magneto-optical response is traced up to room temperature, while clusters with $x_{Zn} = 0.8$ were monitored up to 96 K. Fitting all samples with an identical mean T_{heat} yields a value of 10 K, comparable to the value extracted for doped binary species.

Chapter 5

Structural Effects in $(CdSe)_{13}$ Clusters Probed by Optical Spectroscopy

In the previous chapter the impact of Mn^{2+}-doping on the magneto-optical properties of $(CdSe)_{13}$ and $(Zn_xCd_{1-x}Se)_{13}$ alloy clusters has been discussed, revealing giant magneto-optical functionalities through the incorporation of TM^{2+} ions. In particular, it has been evaluated how the discrete replacement of a few out of the 13 cations - either by magnetically active or inactive species - influences the clusters optical performance and creates new characteristic properties which directly result from the precisely countable number of atoms in the MSCs.

Besides the small number of atoms, the magic nature of the clusters also implies a minimum size of the crystal, barely exceeding a single unit cell. This reduced crystal size of the $(CdSe)_{13}$ clusters causes several particularities compared to conventional QDs, which are in the scope of this chapter. The small $(CdSe)_{13}$ structure may obviously be more flexible in reacting to the incorporation of a foreign atom, and the lattice structure is decisive for the electronic properties.

The first subsection discusses how the $(CdSe)_{13}$ lattice responds to Co^{2+}-doping, demonstrating how the Co^{2+} ligand field transition can be used to optically probe the Co-Se bond length, which is found to be strongly shortened as compared to conventional Co^{2+}-doped DMS materials. In the second subsection the temperature dependent shift of the bandgap is related to the influence of the reduced lattice size.

5.1 Cobalt-Selenium Bond Lengths in Co:$(CdSe)_{13}$ Nanoclusters

Optical as well as magneto-optical spectroscopy of the band edge transition provides quite limited insights into the influence of doping on the crystal structure of $(CdSe)_{13}$. However, as the relevant transition metal ions are considerably smaller compared to the host Cd^{2+} cations, it is obvious that the $(CdSe)_{13}$ lattice probably responds to the replacement of one ion by an ion with a different size. Considering reported crystal radii of Mn^{2+} and Cd^{2+} in a tetrahedral geometry (80 pm and 92 pm, respectively [203]), Mn^{2+}-doping corresponds to a reduction in size of one of the 13 cations of about 13 %. The Co^{2+} cation is even smaller than the Mn^{2+} (72 pm compared to 80 pm, respectively [203]).

Crystal structure analysis in semiconductor nanostructures is often realized by means of diffraction (mostly electron or X-ray diffraction techniques), which requires at least medium range order among the lattice atoms. In contrast to conventional QDs consisting of several hundreds up to thousands of atoms, medium periodicity does not exist in the clusters, as their structure does not comprise much more than a unit cell. The ligand field transitions of TM^{2+} ions are known to provide an optical approach to the chemical and structural environment around the ion, as their pattern depend on the arrangement of the ligand atoms and their influence on the different *3d* orbitals of the central ion. As Mn^{2+} exhibits high spin $3d^5$ configuration (a half-filled shell), it owns a maximum total spin of $S = \frac{5}{2}$ implying strong exchange coupling interactions. However, all ligand field transitions require a spin flip and are hence forbidden. In contrast to that, Co^{2+} exhibits several low-energy ligand field excited state transitions, which are spin-allowed and visible in absorption even at low concentrations. These transitions have frequently been exploited to investigate the Co^{2+} chemical surrounding, e. g., to probe the Co^{2+} lattice incorporation during synthesis [71, 125, 126] or to measure the bond lengths in alloys DMS QDs [75].

In the samples under study in this chapter Co^{2+} is used as a magnetic dopant in $(CdSe)_{13}$ MSCs to gain access to the structural environment of the dopant ions in the MSCs. After confirmation of the magneto-optical activity of the Co^{2+}-doped $(CdSe)_{13}$ clusters by examination of the band edge excitonic transitions, the ligand field transitions are examined via MCD to extract information about the MSCs lattice structure. Evaluation of the energetic position allows one to estimate the Co^{2+}-Se^{2+} bond length. Finally these findings are correlated with EXAFS analysis. The sample preparation as well as all EXAFS measurements and their evaluation has been conducted by Dr. Jiwoong Yang at the Seoul National University.

5.1.1 *sp-d* Exchange Interactions in Co:$(CdSe)_{13}$ Cluster

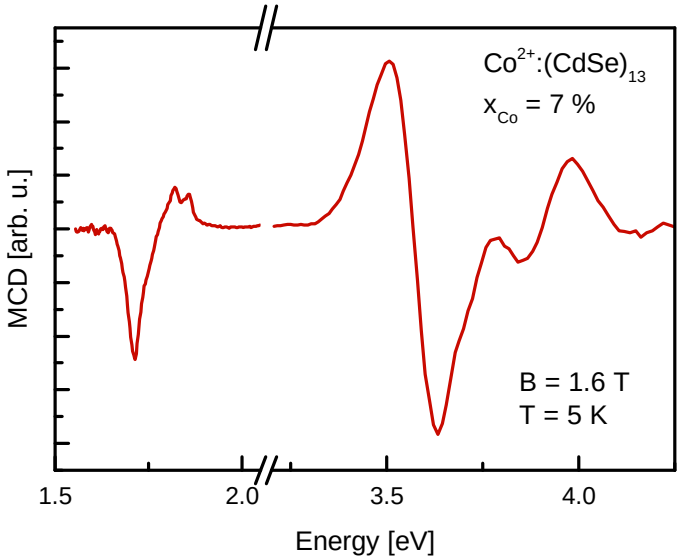

Figure 5.1: Full MCD spectrum of Co^{2+}-doped $(CdSe)_{13}$ clusters $x_{Co} = 7\,\%$. The spectrum measured at 1.6 T and 5 K exhibits the ligand field transition at around 1.7 eV and the excitonic band edge features at 3.6 eV.

As Co^{2+} differ in size from Mn^{2+} cations, Co^{2+}-doped clusters may differ in their lattice structure and may not automatically exhibit the same optical and magneto-optical properties as their Mn^{2+}- doped counterparts. Figure 5.1 summarizes the magneto-otical properties of Co^{2+}-doped $(CdSe)_{13}$ clusters ($x_{Co} = 7\,\%$). The full spectrum contains both the band edge transition at around 3.6 eV as well as a feature related to the Co^{2+} ligand field transition $^4A_2 \rightarrow {}^4T_1(P)$ at about 1.7 eV. While the latter reflects the breaking of the spin degeneracy for internal Co^{2+} ligand field energy terms (discussed in detail below), the band edge splitting directly evidences the *sp-d* exchange interactions between the band charge carriers and the magnetic moments of the Co^{2+}-dopants, proving that the Co^{2+} is incorporated magneto-optically active. Just as their Mn^{2+}-doped counterparts, the band edge of the Co:$(CdSe)_{13}$ consists of a multitude of transitions overlapping each other, with a dominant, energetically lowest peak exhibiting a negative Zeeman splitting (maximum followed by a minimum in energy in MCD). In analogy to Mn:$(CdSe)_{13}$, this peak can be assigned as the $\pm 1^L$ transition of the $1S_{3/2}1S_e$ exciton fine structure.

Magnetic field dependent MCD spectra as well as the corresponding absorption spectra at 5 K are shown in Figure 5.2a and b, respectively, for Co^{2+}-doped $(CdSe)_{13}$ with $x_{Co} = 10\,\%$. The absorption spectrum resembles well the spectrum shown in Figure 4.4 of Mn^{2+}-doped $(CdSe)_{13}$ and can be analogously fit with four peaks, which can be attributed to the fine structure peaks ($\pm 1^L$, 0^L, $\pm 1^U$ and 0^U) of the $1S_{3/2}1S_e$ band edge transition following the procedure described in [31]. The Zeeman splitting for the energetically lowest $\pm 1^L$

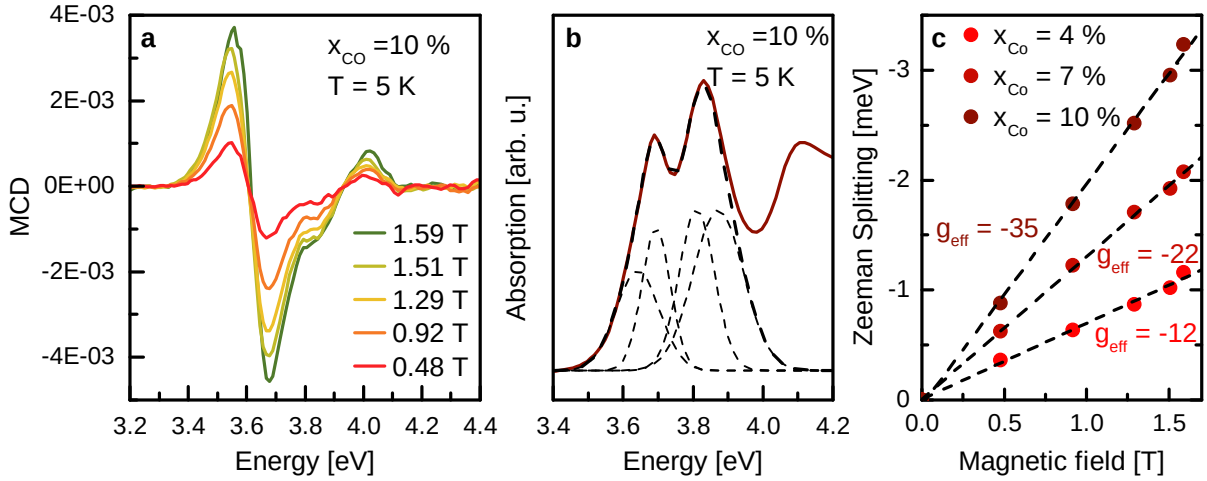

Figure 5.2: (a) MCD spectra of the band edge transition at 5 K and various magnetic fields of a samples with $x_{Co} = 10\,\%$ Co^{2+} concentration. (b) depicts the 5 K absorption spectrum including fits to the fine structure states. A dashed black line represents the sum of the fitted peaks. In (c) the extracted Zeeman splittings of the $\pm 1^L$ transition for the different samples used in this study are compared. Dashed lines represent linear fits to the data, with the effective g factors given aside.

transition, as extracted based on the corresponding absorption peak width and height, is depicted in Figure 5.2c, compared to values for Co^{2+}-doped samples with $x_{Zn} = 4\,\%$ and 7 %, respectively. For all concentrations the Zeeman splitting increases linearly with magnetic field, allowing extraction of effective g-factors (−35, −22 and −12, respectively, for the different doping concentrations, see Figure 5.3c), which are significantly smaller compared to the values obtained for Mn:$(CdSe)_{13}$.

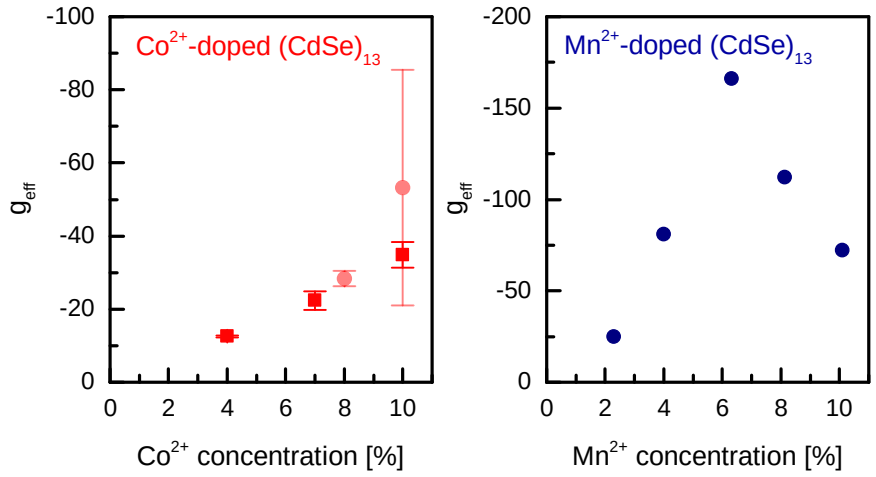

Figure 5.3: Comparison between the concentration dependence of the effective g-factor for Co^{2+}- (red) and Mn^{2+}-doped (blue) $(CdSe)_{13}$, respectively. Supplementary effective g-factors for Co^{2+}-doped samples as determined by M. Sc. Severin Lorenz are depicted in light red [113]. All measurements have been conducted at 5 K and 1.43 T to 1.6 T.

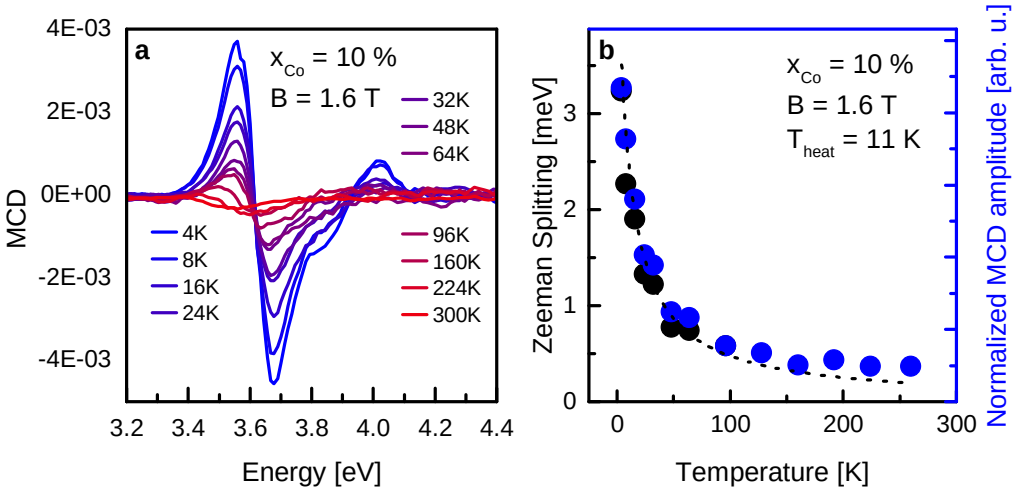

Figure 5.4: (a), Temperature dependence of the MCD signal for Co^{2+}-doped $(CdSe)_{13}$ with $x_{Co} = 10\,\%$ at 1.6 T. (b) depicts the decay of both the extracted Zeeman splitting as well as the MCD amplitude with temperature for the same sample. A dashed black line represents a Brillouin fit for the decay of the MCD amplitude according to Equation 4.7.

As the magnitude of the Zeeman splitting depends on both, the strength of the *sp-d* exchange interaction (parameterized by the exchange coupling constants) as well as the mean spin $\langle S_z \rangle$ of the dopant ensemble, this discrepancy can be partly explained by the difference in the total spin moment between both cations ($S = \frac{3}{2}$ for Co^{2+} compared to $S = \frac{5}{2}$ for Mn^{2+}). While the exchange coupling constants for Mn^{2+} and Co^{2+} in bulk CdSe are quite similar for both TM^{2+} ions (compare Table 2.4), $\langle S_z \rangle$ as estimated by the Brillouin function is expected to decrease by a factor of ≈ 2 assuming $T = 5\,\mathrm{K}$ and $B = 1.6\,\mathrm{T}$ due to the different values of S for Co^{2+} and Mn^{2+}. Note that the gyromagnetic factor also changes from $g_{Mn} \approx 2$ to $g_{Co} \approx 2.3$ [132].

However, the difference in $\langle S_z \rangle$ does not account for the total discrepancy in the Zeeman splittings between both cluster types. In particular, the trend in the Zeeman splitting among samples with different Co^{2+} concentrations does not exhibit a *Digital Doping* behavior, but instead appears to increase monotonously with Co^{2+} concentration. Figure 5.3 for comparison includes additional data for two other samples containing $x_{Co} = 8\,\%$ and $10\,\%$ [113], where especially the latter exhibits quite huge deviations in the extracted Zeeman splittings between different measurements, as indicated by the error bars. This, together with the strongly decreased mean Zeeman splitting compared to Mn^{2+}-doped clusters, might indicate an instability in the crystal lattice in case of Co^{2+}doping, leading to strongly varying magneto-optical activities depending on, e.g., the exact sample synthesis or the technique of thin film preparation for the optical characterization.

Figure 5.4 depicts the temperature dependence of the Co^{2+}-doped sample with $x_{Co} =$

10 %. The magneto-optical response can be traced up to room temperature not exhibiting a sign inversion, which - as the intrinsic component is expected to exhibit a positive splitting (elaborated above) - identifies the *sp-d* exchange interactions as origin of the MCD signal. With increasing temperature the whole signal shifts towards lower energies and decreases in amplitude, as depicted in Figure 5.4b together with the extracted Zeeman splittings up to 64 K. The decay can be described with a Brillouin fit utilizing a spin heating temperature of about 11 K, which is similar to Mn^{2+}-doped clusters.

The temperature depended decays of the MCD amplitude for samples doped with $x_{Co} = 4\,\%$ and $x_{Co} = 7\,\%$ are depicted in Figure 5.5. The MCD signals can be traced up to 160 K and 128 K, respectively, until it vanishes below the signal-to-noise ratio. Both decays can be described with Brillouin fits using similar spin temperatures as for the Mn^{2+}-doped clusters (7 K and 8 K, respectively), suggesting that those Co^{2+} ions which are magneto-optically active behave similiar as the Mn^{2+} cations in $Mn:(CdSe)_{13}$.

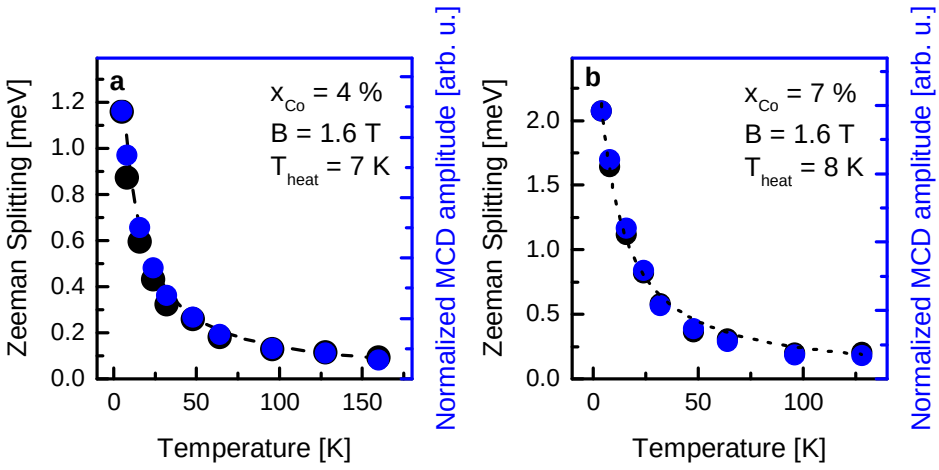

Figure 5.5: Temperature dependent decay of the Zeeman splitting (black) as well as the MCD amplitude (blue) for samples with $x_{Co} = 4\,\%$ and $x_{Co} = 7\,\%$ Co^{2+} concentration, respectively. The dashed lines represents fits according to Equation 4.7.

5.1.2 Ligand Field Transition in Co^{2+}-Doped $(CdSe)_{13}$

Figure 5.6 depicts the room temperature absorption spectrum of $Co:(CdSe)_{13}$ clusters in dispersion. Besides the distinct band edge absorbance (3.6 eV) the spectrum reveals an additional feature at 1.7 eV, related to the $^4A_2 \rightarrow {}^4T_1(P)$ Co^{2+} ligand field transition. The ligand field feature, as enlarged in the inset, is composed of three distinguishable peaks, which are related to the spin-orbit fine structure.

In first approximation, the spin-orbit interaction in TM^{2+} ions can be captured within the Russel-Saunders coupling scheme [70], in which it is described as a small perturbation

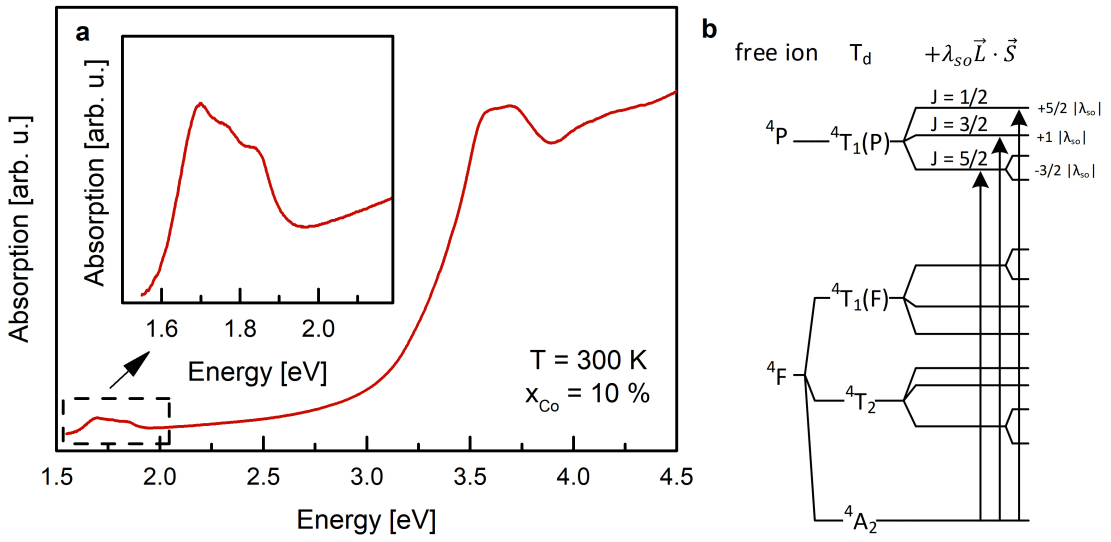

Figure 5.6: Room temperature absorption showing the spin-orbit fine structure of Co:$(CdSe)_{13}$. (a) depicts room temperature absorption of Co^{2+}-coped $(CdSe)_{13}$ with $x_{Co} = 10\,\%$in a chloroform dispersion. The inset displays the spectral region of the $^4A_2 \rightarrow {}^4T_1(P)$ ligand field transition. In (b), the origin of the spin-orbit fine structure is illustrated. After [122, 123].

acting on the terms set up by inter-electron repulsion and the T_d ligand field. In general, the number of states that arise from a spin-orbit split term is equal to either the spin or the orbital multiplicity of the term, whichever is smaller [70]. While the ground term of the observed $^4A_2 \rightarrow {}^4T_1(P)$ transition is not orbitally degenerated and thus does not split, the excited $^4T_1(P)$ term is expected to split threefold (compare Figure 5.6b). The $^4T_1(P)$ term directly derives from the ^4P free ion term of the Co^{2+}. Each energy level may be classified by the spin S, the orbital momentum L and an additional total angular momentum quantum number J, ranging from $|L-S|$ to $|L+S|$, i.e. $J = \frac{5}{2}$, $\frac{3}{2}$ and $\frac{1}{2}$ for the ^4P term ($L = 1$ and $S = \frac{3}{2}$) [122, 123]. The quantity of the splitting is described via the spin-orbit coupling parameters λ_{so} for a term (i.e., a defined combination of several *3d* electrons) and ζ_{so} for a single *3d* electron, related as $\lambda_{so} = -\frac{\zeta_{so}}{2S}$ for more-than-half-filled *d* shells ($\lambda_{so} = -\frac{\zeta_{so}}{3}$ here) [70]. The energy separation between two levels J and $J+1$ equals to $\lambda_{so}(J+1)$, generating the pattern depicted in Figure 5.6 for the so-called inverted spin-orbit multiplet (giving respect to the negative λ_{so}) of the $^4T_1(P)$ term. In case the symmetry is further reduced, i.e. due to lattice anisotropy, the $^4T_1(P)$ ground spin-orbit term (J=5/2) is known to split twofold (compare Figure 5.6b), enabling the observation of four spin-orbit peaks in the fine structure of the $^4A_2 \rightarrow {}^4T_1(P)$ transition, e.g., in Co:ZnO or Co:CdS [122, 123].

A splitting into four spin-orbit peaks cannot be resolved in Figure 5.6. By fitting the $^4T_1(P)$ pattern with three Gaussian transitions, their overall splitting can be determined

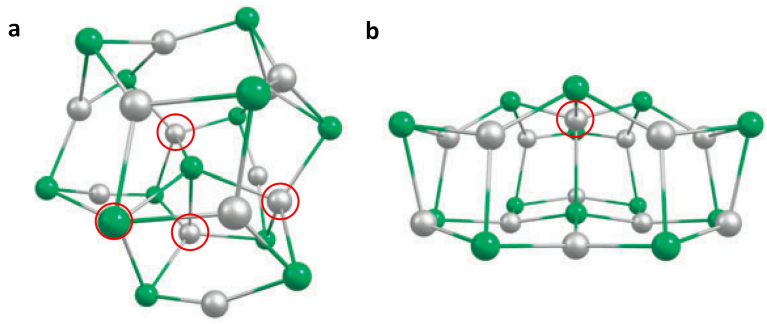

Figure 5.7: Most stable crystal structures of $(CdSe)_{13}$ clusters. Depending on the theoretical approach and the assumed ligands and solvents, either the core-cage-structure (a) or the wurtzite-sliced structure (b) is estimated to be lowest in energy and thus most likely to form [64–69]. Pictures are taken from [66], with the tetrahedral cation lattice sites highlighted with red circles. Note that in (a) one tetrahedral cation site is hidden behind an anion.

as 1161 cm^{-1}, which corresponds to $4\lambda_{so}$ (compare Figure 5.6). For the Co:$(CdSe)_{13}$ clusters the spin-orbit coupling parameters can thus be estimated as $\lambda_{so} \approx -290\,cm^{-1}$ or $\zeta_{so} = 870\,cm^{-1}$, similar to Co^{2+} in bulk CdSe ($\lambda_{so} = -240\,cm^{-1}$ [121]). The overall $^4A_2 \rightarrow {}^4T_1(P)$ splitting is constant ($\approx$1100 cm^{-1}) in most semiconductors like ZnTe, CdTe, ZnSe [204], CdS, ZnS [123] and CdSe [121], where the Co^{2+}-dopants are tetrahedrally coordinated.

Considering the potential crystal structures of stable $(CdSe)_{13}$, which are still controversially discussed in literature [64–69], the number of fourfold coordinated Cd lattice sites is limited. Figure 5.7 depicts the two structures of bare $(CdSe)_{13}$ clusters, which are considered as the most stable configurations based on DFT calculations [66]. While the core-cage configuration exhibits four fourfold coordinated Cd lattice sites, all but one Cd atoms are threefold coordinated in the wurtzite-sliced structure.

In a threefold coordinated configuration the central cation experiences a trigonal planar crystal field, which is known to split the different *3d* orbitals into two, orbitally twofold degenerated subsets (d_{xy}, $d_{x^2-y^2}$ and d_{xz}, d_{yz}) and the d_{z^2} subset. Co^{2+} ions in a trigonal planar crystal field do exhibit a ligand field transition at around 1.7 eV to 2.0 eV in absorption [73, 205]. But this transition is not threefold orbitally degenerated and thus does not exhibit the observed threefold split spin-orbit fine structure. The observation of the $^4T_1(P)$ fine structure thus represents a strong evidence that the Co^{2+} ions are tetrahedrally coordinated.

DFT calculations for methylamine capped $(CdSe)_{13}$ clusters suggest that in clusters prepared in octylamine or oleylamine (which share methylamine as terminal group), the threefold Se coordinated Cd atoms are in addition bond to a nitrogen atom of the organic ligands [66], creating a quite asymmetric pseudo-tetrahedral configuration. However, such

an in-equivalence between the different ligands is expected to strongly increase the splitting between the fine structure of the $^4A_2 \rightarrow {}^4T_1(P)$ transition [206]. In Co:$(CdSe)_{13}$ only a small increase of the $^4A_2 \rightarrow {}^4T_1(P)$ energy splitting is observed ($1161\,cm^{-1}$ compared to $1100\,cm^{-1}$ in bulk Co:CdSe [121]). This may be rather caused by an in-equivalence between the four Se anions surrounding the Co^{2+}, as those may themselves be three or fourfold coordinated [206, 207].

Considering the arguments above, the observed threefold spin-orbit fine structure represents a strong evidence that the Co^{2+} embedded in $(CdSe)_{13}$ experiences a tetrahedral environment. It suggests that the Co^{2+} ions are embedded on fourfold Se-coordinated Cd lattice sites and are not embedded threefold coordinated.

5.1.3 Evidence of Shortened Co-Se Bond Lengths in Co:$(CdSe)_{13}$

Each of the spin-orbit split states classified by L, S and J is $(2J + 1)$-fold degenerate according to the different projections of the total angular momentum along an external magnetic field. This degeneracy is lifted upon the appliance of an external magnetic field, introducing a MCD feature. While absorption spectroscopy is superimposed by scattering, which prohibits investigation of the $^4A_2 \rightarrow {}^4T_1(P)$ transitions at cryogenic temperatures (as those measurements need to be done on thin film samples in a cryostat exhibiting increased scattering), the MCD signal intrinsically does not contain a scattering background. This allows resolving the fine structure of the ligand field transition in MCD, which becomes more distinct at low temperatures due to the decreasing band widths stemming from reduced fluctuations in the ligand-metal distances [70].

Figure 5.8a compares the absorption and MCD spectra of Co:$(CdSe)_{13}$ clusters with $x_{Co} = 10\,\%$. While the spin-orbit fine structure peaks are hardly resolved in absorption, the MCD signal exhibits a pronounced pattern, exhibiting a dominant maximum followed in energy by two clearly separated maxima. As that ligand field transitions in general derive from degenerated ground as well as excited states, they do not exhibit distinct $\mathscr{A}$-terms, but rather represent a superposition of different MCD contributions. Figure 5.8b depicts MCD spectra of the $^4A_2 \rightarrow {}^4T_1(P)$ transition at 5 K and 1.6 T for clusters with $x_{Co} = 4\,\%$, $7\,\%$ and $10\,\%$. The observed feature is completely consistent in shape with low-temperature MCD spectra of Co^{2+} cations embedded in CdSe quantum dots (compare Figure 5.8c) [71]. Note that the ligand field transition of Co^{2+} embedded in DMS QDs generally does not differ from those in bulk DMS, as due to the high number of atoms contained in one nanocrystal (several hundreds up to thousands), most Co^{2+}-dopants experience the same environment as in the bulk

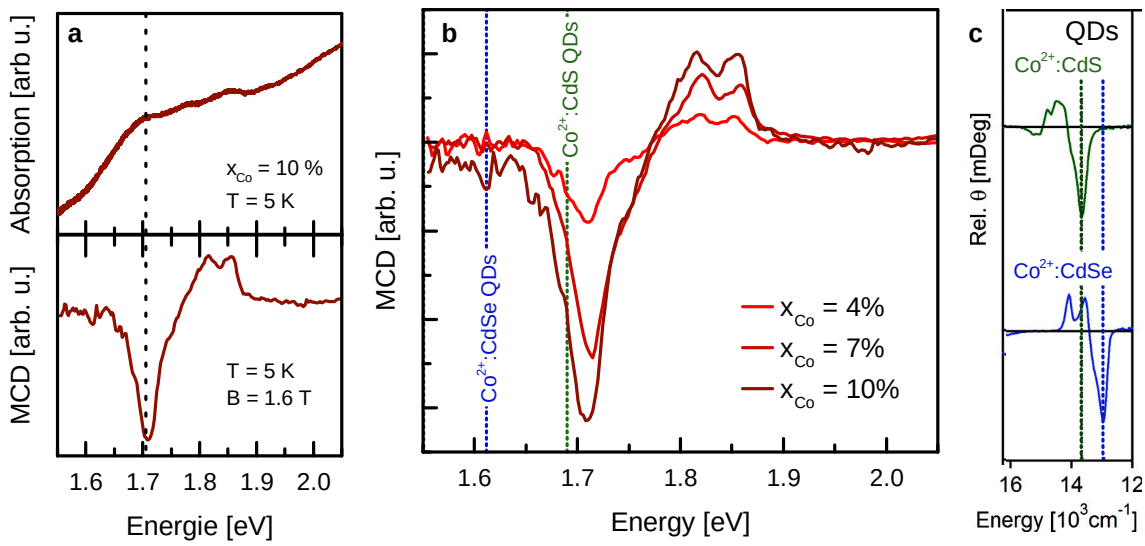

Figure 5.8: Co^{2+} ligand field transition in Co:$(CdSe)_{13}$. (a) MCD and absorption spectra at 5 K and 1.6 T of the $^4A_2 \rightarrow {}^4T_1(P)$ transition in samples doped with $x_{Co} = 10\,\%$. The dashed line highlights the dominant minimum. In (b) MCD spectra at 5 K and 1.6 T of samples with $x_{Co} = 4\,\%$, 7 % and 10 % are compared. (c) depicts reference spectra of the same transition in Co:CdS and Co:CdSe QDs at 5 T and similar temperatures (5 K to 6 K) from [71]. Dashed lines in panels (b) and (c) highlight the energetic positions of the dominant minimum in MCD for Co:CdSe (blue) and Co:CdS (green) QDs, respectively.

material. The fact that the MCD signal of the $^4A_2 \rightarrow {}^4T_1(P)$ transition in Co:$(CdSe)_{13}$ is equivalent in shape to the signal in Co^{2+}-doped CdSe QDs represents a final proof that the Co^{2+} cation experiences a nearly regular tetrahedral environment of ligands. It is striking, that the MCD spectra of samples with different Co^{2+} concentrations do not change in shape or energy, which leads to the suggestion that the Co^{2+} cations in both monodoped as well as bidoped clusters experience similar ligand fields indicating their emplacement on equivalent lattice sites. This observation suggests that the Co:$(CdSe)_{13}$ clusters consist of a core-cage structure rather a than wurzite-sliced one.

Closer comparison of the energetic position of the $^4A_2 \rightarrow {}^4T_1(P)$ transition with literature references (compare the position of the dominant minimum as highlighted with a blue or green dashed line for Co:CdSe and Co:CdS QDs from [71]) reveals a significant shift in energy. As can be deduced from Figure 2.13, the energy of the $^4A_2 \rightarrow {}^4T_1(P)$ transition depends on the ligand field strength Δ_{LF}, suggesting that the Co^{2+} ions in the $(CdSe)_{13}$ clusters experience an enhanced Δ_{LF} as compared to those embedded in conventional QDs. A similar enhanced value for the ligand field energy has been observed in small Co^{2+}-doped CdS clusters, increasing with decreasing cluster size [74].

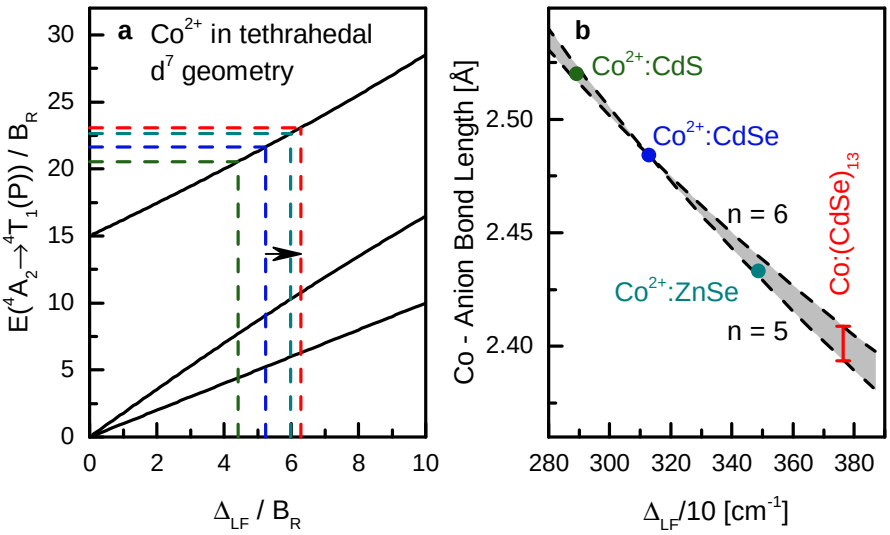

Figure 5.9: Extraction of the Co-Se bond length in Co:$(CdSe)_{13}$. (a) depicts a Tunabe-Sugano diagram for tetrahedral Co^{2+}. The transition energy $E(^4A_2 \rightarrow {}^4T_1(P))$ and Δ_{LF} are indicated for the clusters (red) and Co:CdSe (blue), Co:CdS (green) and Co:ZnSe (turquoise) QDs. After [116]. In (b) the extraction of the Co-anion bond length based on Equation 5.1 is illustrated.

Table 5.1: Racah parameter B_R for Co^{2+} in various II-VI semiconductors

	B_R [cm^{-1}]	reference
CdSe	599	[120]
CdS	610–664	[121, 122]
ZnSe	570–584	[120, 204]

Based on the crystal field theory (treating the ligand atoms as point charges), the crystal field energy in a tetrahedral symmetry can be derived as:

$$\Delta_{LF} = \frac{4}{9}\frac{1}{6}\frac{Z_{LF}e^2\overline{r^4}}{a^5} \tag{5.1}$$

Herein Z_{LF} denotes the charge state of the ligand atoms, e is the elementary charge, $\overline{r^4}$ denotes the mean of the radius to the power of four of the *3d* orbitals and a the TM-anion bond length. Although this zero-th order approximation significantly and systematically underestimates the crystal field splitting, it could be shown empirically that Δ_{LF} indeed varies with a^{-n}, with $5 < n < 6$ [70, 208, 209]. This correlation allows relating a shift in the ligand field strength Δ_{LF} to a change in the bond length between the central transition metal ion and the anions, provided that all of the anions are of the same type [70], as it is the case in the Co:$(CdSe)_{13}$ clusters.

Figure 5.9a illustrates the determination of the ligand field energy Δ_{LF} for the Co:$(CdSe)_{13}$ clusters based on the observed energetic position of the $^4A_2 \rightarrow {}^4T_1(P)$ transi-

Table 5.2: Extraction of the Co-anion bond length. The energy of the $^4A_2 \rightarrow {}^4T_1(P)$ transition as well as extracted Δ_{LF} values for Co^{2+} in CdSe, CdS and ZnSe quantum dots are taken from cryogenic temperature MCD spectra in [71, 126]. Reported Co-Se bond lengths in Co^{2+}-doped CdSe, CdS and ZnSe are listed from literature [75, 123].

	$E(^4A_2 \rightarrow {}^4T_1(P))$ [eV/10^3 cm^{-1}]	$\Delta_{LF}/10$ [cm^{-1}]	a [Å]
Co:$(CdSe)_{13}$	1.71 / 13.8	376	2.393 − 2.409
Co:CdSe QDs	1.61 / 13.0	313	2.484[75]
Co:CdS QDs	1.69 / 13.7	290	2.52[123]
Co:ZnSe QDs	1.64 / 13.2	349	2.433[75]

tion. As the $^4A_2 \rightarrow {}^4T_1(P)$ transition is normally spread over a width of ≈1100 cm^{-1} due to spin-orbit coupling, the energy position $E(^4A_2 \rightarrow {}^4T_1(P))$ of the transition is commonly deduced either as the maximum [75] or the center of gravity [70] of the 300 K absorption spectrum. In Co:$(CdSe)_{13}$ the energetically lowest absorption peak of the spin-orbit split $^4A_2 \rightarrow {}^4T_1(P)$ transition at cryogenic temperatures in a first approximation coincides with the dominant minimum in MCD (compare Figure 5.8a). This peak represents the maximum in the room temperature absorption (compare Figure 5.6), and thus the dominant maximum in MCD - being clearly pronounced in the spectrum - is taken as the transition energy $E(^4A_2 \rightarrow {}^4T_1(P))$ of the $^4A_2 \rightarrow {}^4T_1(P)$ transition. Considering the Tunabe-Sugano diagram for Co^{2+} in a tetrahedral ligand field the corresponding ligand field energy Δ_{LF} can be extracted (compare Figure 5.9a), provided that the Racah parameter B_R for the material system is known. Those can be taken from literature (compare Table 5.1). For Co:$(CdSe)_{13}$ a Δ_{LF} of 3760 cm^{-1} can be extracted.

In order to verify this optical approach to extract quantitative values for the Co-Se bond length, the same approach was applied to Co^{2+}-doped CdS and ZnSe DMS QDs. Values for $E(^4A_2 \rightarrow {}^4T_1(P))$ were extracted in an analogous manner based on ligand field transition MCD spectra from literature [71, 126]. The extracted energetic positions of the $^4A_2 \rightarrow {}^4T_1(P)$ transition in eV and cm^{-1}, as well as the extracted Δ_{LF} are listed in Table 5.2.

Based on the determination of Δ_{LF}, the values of the bond lengths can be extrapolated starting from the Co-Se bond length in Co:CdSe QDs, as known from literature ($a^{\text{Co:CdSe QDs}} = 2.484$ Å [75]), using Equation 5.2.

$$a = a^{\text{Co:CdSe QDs}} \sqrt[n]{\Delta_{LF}^{\text{Co:CdSe QDs}}/\Delta_{LF}} = 2.484\,\text{Å} \sqrt[n]{\frac{313\,\text{cm}^{-1}}{\Delta_{LF}/10}} \tag{5.2}$$

Figure 5.9b plots the range (grey region), which is extrapolated for the Co-anion bond lengths assuming $n = 5$ to 6. Green and turquoise dots indicate experimentally determined

Co-anion bond length from literature for Co:CdS and Co:ZnSe QDs (data is listed in Table 5.2). They exhibit quite nice agreement with the estimated dimensions of the bond lengths. This proves that the approach presented here to extract Co-anion bond lengths from the $^4A_2 \rightarrow {}^4T_1(P)$ transition energy provides reliable values.

Based on this, the Co-Se bond length in Co:$(CdSe)_{13}$ clusters can be extrapolated to lie between 2.393 Å and 2.409 Å (red line in Figure 5.9b). This is about 3.0 % to 3.6 % smaller as compared to Co^{2+}-doped QDs or bulk DMS. This shortening in the bond length mirrors how the small $(CdSe)_{13}$ cluster, with mostly all atoms being placed on the surface, is able to respond to a difference in size for one of the 26 atoms. To compare this shortening to the situation in undoped as well as Mn^{2+}-doped clusters, extendend X-ray absorption fine structure (EXAFS) measurements on those three types of clusters are discussed in the following.

5.1.4 Validation of the Co-Se Bond Length via EXAFS

For EXAFS measurements the modulation of the X-ray absorption right above the K-edge is examined, enabling characterization of the local atomic coordination of a specific element. In case of the Mn^{2+}- and Co^{2+}-doped $(CdSe)_{13}$ clusters, the Cd, Mn and Co K-edges were examine to determine the Cd-Se, Mn-Se and Co-Se bond lengths. All EXAFS measurements and data analysis outlined in this chapter have been conducted in the group of Prof. Taeghwan Hyeon at the Seoul National University.

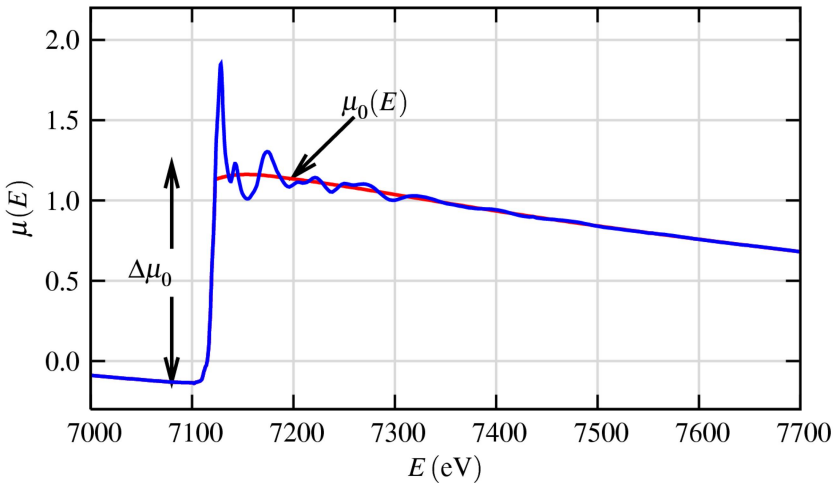

Figure 5.10: X-ray absorption raw signal at a characteristic absorption edge. $\Delta\mu_0$ and μ_0 are indicated. From [210].

X-ray absoption at the K-edge occurs through the photo-electric effect, as soon as the X-ray energy is large enough to lift an electron from the K-shell to continuum. In this case the absorption $\Delta\mu_0$ increases sharply, corresponding to the characteristic K-absorption

edge. The energy needed for this absorption process depends on the element under study, i.e. whether the Cd, Mn or Co K-edge is evaluated. The ejected photoelectron, whose kinetic energy is provided by the excess energy of the absorption process, is scattered at the neighboring Se atoms, returns back to the absorbing atom (Cd, Mn or Co) and interferes with itself. The amplitude of the backscattered photoelectron at the absorbing atom, variing with energy, causes small oscillations in the absorption coefficient, which represent the EXAFS signal χ. In order to extract χ [210], a bare-atom background μ_0 is subtracted from the raw absorption data μ and the signal is normalized by the edge step $\Delta\mu_0$ (compare Figure 5.10):

$$\chi(E) = \frac{\mu(E) - \mu_0(E)}{\Delta\mu_0} \tag{5.3}$$

As EXAFS represents an interference effect of the photo-electron, it is convenient to scale the energy axis in terms of the photo-electron wavenumber k_{PE}. In addition χ is often weighted by k_{PE}^2 or k_{PE}^3 to enhance the visibility of more distant oscillations. Figure 5.11 depicts k_{PE}^3-weighted EXAFS spectra of Mn^{2+}-doped $(CdSe)_{13}$ clusters with different doping concentrations at both the Cd K-edge, giving insights into the structural environment of the Cd atoms in the clusters, as well as the Mn K-edge, which exclusively probes the environment of the dopants.

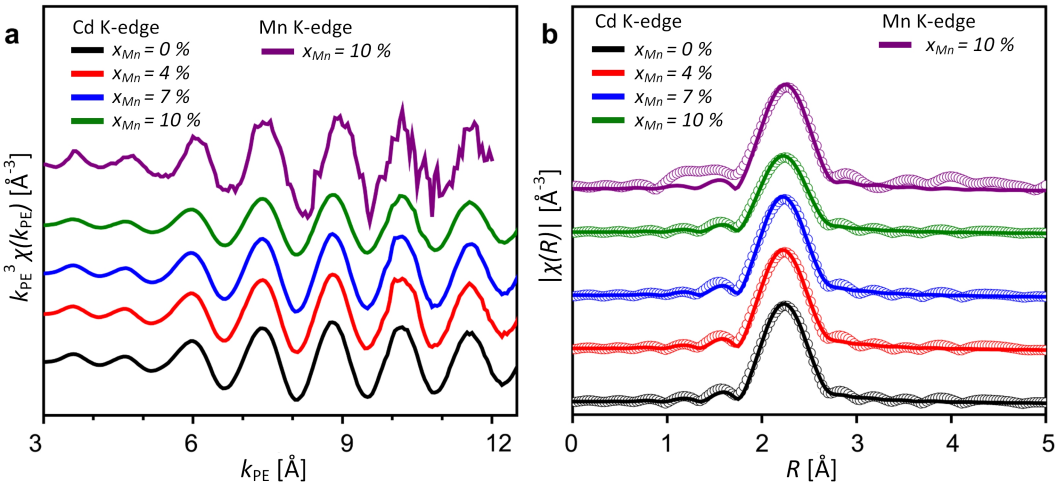

Figure 5.11: (a), k_{PE}^3 weighted Cd and Mn K-edge EXAFS oscillations of Mn^{2+}-doped clusters with different doping concentrations. The black, red, blue and green line represent the Cd K-edge signals of Mn^{2+}-doped clusters with $x_{\mathrm{Mn}} = 0\,\%$, $4\,\%$, $7\,\%$ and $10\,\%$, while the violet lines represents the Mn K-edge in Mn^{2+}-doped clusters with $x_{\mathrm{Co}} = 10\,\%$. (b) depicts the magnitude $|\chi(R)|$ of the Fourier-transformed EXAFS spectra shown in (a). [211]

To extract quantitative structural measures, the EXAFS signal can be described with the EXAFS equation, which sums up over the different coordination shells (i) around the

Table 5.3: Bond lengths as extracted from the quantitative analysis of the Cd and Mn K-edge EXAFS spectra. The Co-Se bond length is estimated from the shift in the Fourier-transformed $|\chi(R)|$. For the analysis the coordination number is always fixed to 3, which is in contrast to the observation that the Co^{2+} ions are embedded on tetrahedrally coordinated lattice sites, as evident from the shape of the MCD spectrum. Note that this difference in the coordination number between 3 and 4 for the fit only influences the χ amplitude, while extracted bond lengths determined by the shape of χ are not affected.

Sample	Concentration	Cd-Se Cd K-edge	Mn-Se Mn K-edge	Co-Se Co K-edge
$(CdSe)_{13}$	–	2.61 Å	–	–
Mn:$(CdSe)_{13}$	$x_{Mn} = 4\,\%$	2.60 Å	–	–
Mn:$(CdSe)_{13}$	$x_{Mn} = 7\,\%$	2.60 Å	–	–
Mn:$(CdSe)_{13}$	$x_{Mn} = 10\,\%$	2.60 Å	2.56 Å	–
Co:$(CdSe)_{13}$	$x_{Co} = 4\,\%$	2.61 Å	–	–
Co:$(CdSe)_{13}$	$x_{Co} = 7\,\%$	2.61 Å	–	–
Co:$(CdSe)_{13}$	$x_{Co} = 10\,\%$	2.60 Å	–	≈ 2.38 Å

absorbing atom [210]:

$$\chi(k_{PE}) = \sum_i \frac{N_{coi} f_{scat_i}(k_{PE}) e^{-2{k_{PE}}^2 \sigma^2_{N_i}}}{k_{PE} {R_{a_i}}^2} \sin[2k_{PE}R_{ai} + \delta_{scat}(k_{PE})] \tag{5.4}$$

Herein N_{coi} denotes the coordination number of a specific shell i, R_a the distance to the neighboring atoms (i.e. the bond length for the first shell), σ^2_N is the mean - square disorder among the neighboring atoms and f_{scat} and δ_{scat} are the scattering amplitude and phase shift, respectively. While the signals of different shells interfere with each other, a Fourier transformation is able to separate the coordinations shells, becoming apparent as isolated peaks in the Fourier-transformed amplitude $|\chi(R)|$. As the $(CdSe)_{13}$ clusters do not exhibit a higher order of crystallinity, the amplitude of the Fourier-transformed $|\chi(R)|$ simply contains one peak corresponding to the Cd-Se or Mn-Se bond length, respectively (compare Figure 5.11b). The peak position in the R space corresponds to the bond length, but is shifted according to δ_{scat} (compare Equation 5.4), which depends on the atomic number Z and can be assumed to be constant for all measurements presented here, as the nearest neighbors consist of Se in all cases. Table 5.3 lists bond lengths as extracted from fitting $|\chi(R)|$ to Equation 5.4. While the Cd-Se bond length is not significantly affected in case of doping, the Mn-Se bonds are shortened by 2 % compared to the other bonds in the clusters.

Figure 5.12 depicts the magnitude of the Fourier-transformed $|\chi(R)|$ of the Cd K-edge in Co^{2+}-doped $(CdSe)_{13}$ clusters (corresponding bond lengths are listed in Table 5.3), which do not differ strongly from the Mn^{2+}-doped clusters. In strong contrast to this,

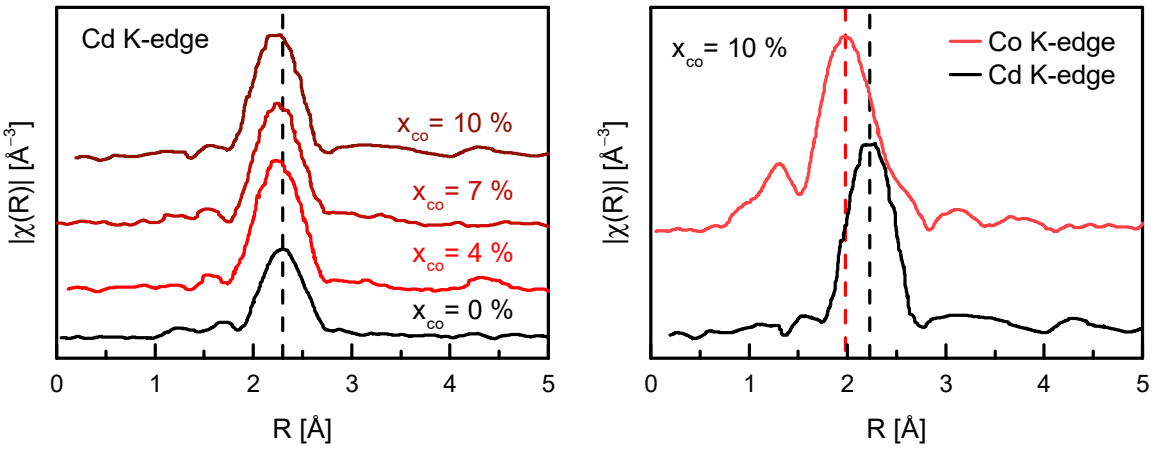

Figure 5.12: EXAFS characterization of Co^{2+}-doped $(CdSe)_{13}$. (a) depicts the Fourier-transformed $|\chi(R)|$ of the Cd K-edge in Co^{2+}-doped $(CdSe)_{13}$ MSCs with different doping concentrations between 0 % to 10 %, while in (b) the Fourier-transformed $|\chi(R)|$ signals of the Cd and the Co K-edges are compared for clusters with $x_{Co} = 10\,\%$.

the Co-K edge is significantly shifted in the R-space as compared to the Cd-K edge. As outlined above, the shift between the peak position in the R-space and the real bond length can be assumed to be constant, so that the Co-Se bond length can be roughly estimated based on the displacement of 0.22 Å to the peak of the Cd K-edge, representing the Cd-Se bond length of 2.6 Å. The Co-Se bond length can thus be estimated to be about 2.38 Å. This value exhibits nice agreement with the range extracted from the energetic position of the $^4A_2 \rightarrow {}^4T_1(P)$ transition (2.393 Å to 2.409 Å), validating the optical approach to extract structural measures presented here. Together, both characterization techniques represent an unambiguous proof of significantly shortened bond lengths in $(CdSe)_{13}$ due to the replacement of single Cd^{2+} ions by Co^{2+}. Interestingly, while the Mn-Se bonds are only shortened by about 2 % with respect to the Cd-Se bonds, this deviation is more than four times greater ($\approx 9\,\%$) in case of Co^{2+} doping.

It is conceivable, that this significant deviation in the structure generates an instability of the clusters, representing a possible origin for the unexpected dependence of the magneto-optical response of the band-edge with Co^{2+} concentration.

5.2 Anomalous Strong Bandgap Shift with Temperature in Nanoclusters

As in most semiconductors the majority of optical properties is conditioned by the characteristics of their crystal lattice, it is expected that the reduced size of the MSCs influences their optical behavior. The fundamental electronic structure, as revealed in the absorption or emission spectrum, directly derives from the atomic lattice. Besides an increase of the bandgap due to the quantization energy, the reduced size in MSCs allows the observation of magneto-optically active and inactive transitions of the exciton fine structure, as has been previously discussed [31].

The crystal lattice also determines the phonon dispersion, which, defines the impact of thermal energy on the electronic structure via electron-phonon coupling, becoming apparent in the temperature dependence of the bandgap. The fundamental bandgap operates as a fingerprint for semiconductors, determining their electrical and optical properties and therefore defining their possible applications. For most semiconductors - including silicon, the base material for modern electronics, as well as most group IV, II-VI and III-V materials (with the exception of lead salts and perovskite materials) - the bandgap decreases monotonically with increasing temperature, known to result from a superposition of electron-phonon interactions and the thermal lattice expansion. As both factors scale with the occupation number of the involved phonon modes [77, 95], the temperature dependent shift of the bandgap depends on the phonon dispersion, which directly results from the lattice, i.e. the rigidity of the bonds and the crystal structure of the material.

In $(CdSe)_{13}$ MSCs most of the lattice sites can be considered as surface with varying number of coordinating atoms and thus number of bonds (compare Figure 5.7). This suggests alteration of the temperature dependence of the bandgap. In this chapter it is shown that the fundamental bandgap in $(CdSe)_{13}$ exhibits an anomalous strong dependence on temperature compared to most bulk materials and conventional quantum dots (either colloidal or epitaxial). The temperature dependent shift is monitored via different techniques in undoped as well as doped MSCs to avoid misinterpretation related to the different peaks of the fine structure, and interpreted within a thermodynamical approach.

5.2.1 Temperature Dependent Absorption and Stokes Shift in $(CdSe)_{13}$

Figure 5.13 depicts temperature dependent absorption measurements of undoped $(CdSe)_{13}$ clusters. With increasing temperature the collective of absorption peaks shifts to lower

energies additionally affected by broadening. Comparison between cryogenic and room temperature reveals a shift for the dominant maximum of about 160 meV. This value is nearly twice as big as what is usually observed in bulk CdSe [202]. The band edge absorption below 4.0 eV results from a superposition of several fine structure peaks of the $1S_{3/2}1S_e$ transition as outlined above. In order to eliminate a mix-up between these peaks as the origin of the observed anomalous strong temperature dependence of the bandgap, additional experimental approaches to monitor the bandgap are performed.

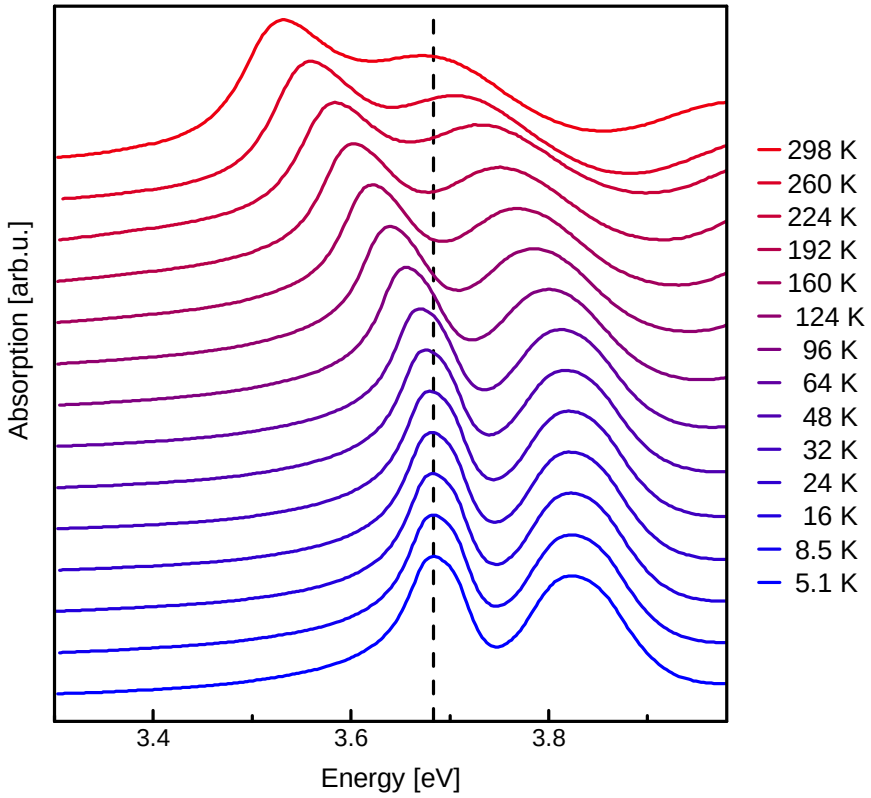

Figure 5.13: Temperature dependent absorption of undoped $(CdSe)_{13}$ MSCs between 5 K and 298 K.

Figure 5.14a depicts the time-integrated PL spectrum of undoped $(CdSe)_{13}$ clusters at cryogenic temperatures, presenting a broad emission at around 3 eV and a narrow bandgap emission at around 3.63 eV, which highlights the good quality of the prepared clusters. The broad emission might be caused by defects, e.g. unsaturated surface atoms, whose dangling bonds are known to introduce mid gap states [212]. Upon increasing the spectral resolution the band edge emission reveals at least three different peaks at 3.64 eV, 3.66 eV and a shoulder at 3.69 eV, compare Figure 5.14b. In order to distinguish the origin of these peaks, the transient PL signal was examined by means of a Streak camera, allowing simultaneous characterization of the time dependence of all peaks. A Streak image of the band edge feature with the intensity plotted in a logarithmic scale is depicted in Figure 5.14c, exhibiting an intense short component with lifetimes in the dimension of the time

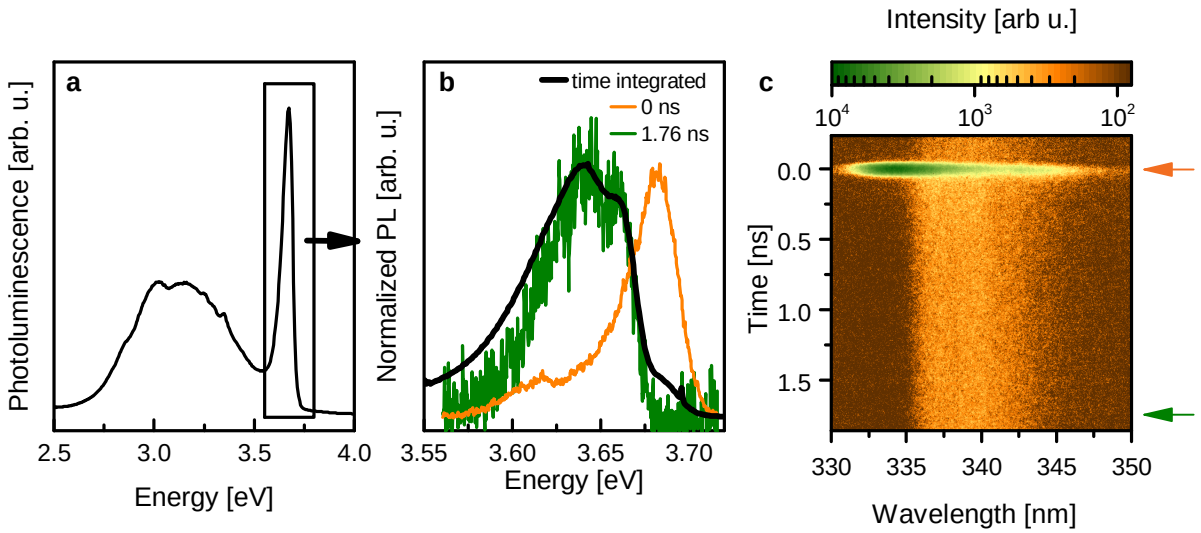

Figure 5.14: Time-integrated and time-dependent PL spectra of undoped $(CdSe)_{13}$.(a) depicts the time-integrated PL (excited at 270 nm and 30 μW with a frequency tripled Ti:Sapphire laser at 8 K). In (b) a high-resolution time-integrated spectrum is compared to the short (orange) and long component (green) of the transient PL signal after 100 fs excitation, as extracted from the Streak image shown in panel (c) (both excited with a 270 nm frequency tripled Ti:Sapphire laser with 3 μW at 8 K).

resolution (< 10 ps), accompanied by a weak long component, which lifetime exceeds the 2 ns window of the Streak camera. Since the slow component is still visible at the end of the 13 ns pulse (depicted at negative times at the top of the Streak image), its lifetime can be estimated to be > 10 ns, limited by the Ti:Sapphire repetition rate.

Time traces shown in Figure 5.14b taken right after the laser excitation at 0 ns (orange arrow in Figure 5.14c) and at the end of the Streak window after ≈ 1.76 ns (green arrow) show that both components, the long as well as the short one, consist of two distinguishable peaks. Comparison with the time integrated PL spectrum (compare Figure 5.14b) indicates that the slow components causes the two main peaks in the time integrated spectrum, while the short components accounts for the small shoulders at around 3.62 eV and 3.69 eV.

Comparison between the absorption and the short-term emission, depicted in Figure 5.15b reveals that the short components most likely represent the two lowest fine structure states of the $1S_{3/2}1S_e$, i. e. the $\pm 1^L$ and 0^L state. Absorption and emission are fit with two and five Gaussian fits, respectively, applying identical widths and similar peak positions varying by less than 10 meV (corresponding to 1 nm deviation for the wavelength). Here, the absorption fine structure is fit to five instead of four peaks (including a transition related to the ± 2 state), as the shoulder on the high energy site of the first absorption feature reveals an additional contribution between 3.65 eV and 3.75 eV. Increased optical activity of the formally forbidden ± 2 states has been observed either due to magnetic

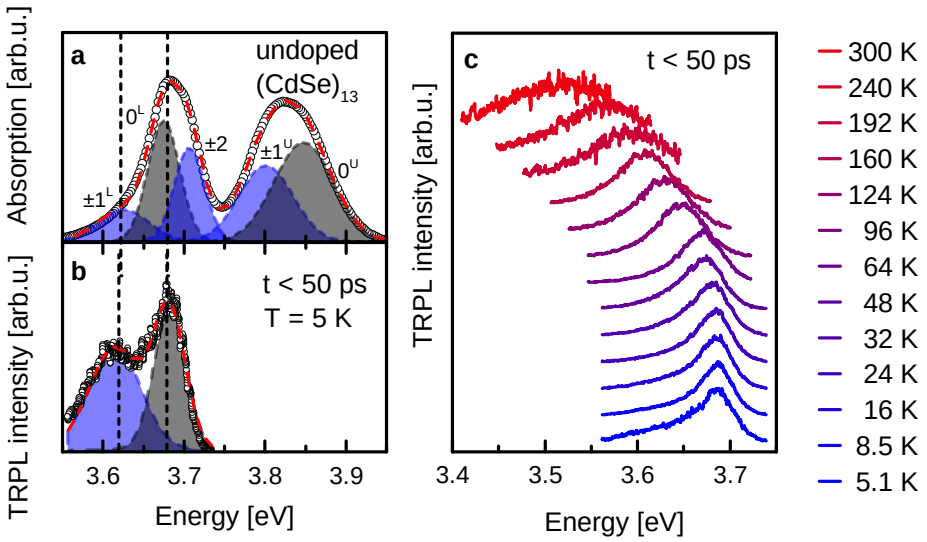

Figure 5.15: Temperature dependent TRPL characterization of undoped $(CdSe)_{13}$. (a) and (b) compare the absorption at cryogenic temperatures (taken from Figure 5.13) and a time -resolved PL spectra integrated within the first 50 ps after laser excitation from a Streak image (excited with a 270 nm frequency tripled Ti:Sapphire laser with 3 μW at 5 K). Absorption and emission spectra are fit with five and two Gaussian fits, respectively, attributed to the fine structure of the $1S_{3/2}1S_e$ excitonic transition, applying identical widths and peak positions within the experimental resolution (1 nm, corresponding to about 10 meV). (c) depicts the temperature dependent shift of the short component (< 50 ps) of the transient PL spectra, as extracted from Streak images (excited with 20 μW). Note that the spectra in panel (b) and (c) are taken at different days on freshly prepared samples.

field induced mixing with bright states [106, 107, 213, 214] or through exchange coupling with surface dangling bonds [107, 215] and may thus be conceivable in $(CdSe)_{13}$ clusters.

Coinciding in energy for absorption and short-term emission, the two energetically lowest transitions ($\pm1^L$ and 0^L) exhibit quasi no Stokes shift. This is in contrast to what is known for conventional QDs, where the fine structure cannot be resolved and which exhibit a non-resonant (i.e. excitation far above the band edge) Stokes shift of 100 meV in QDs approaching diameters below 2 nm [106, 108, 109, 216]. Although the impact of the different influences is still under discussion [109, 216], it is widely accepted that the energy shift between emission and absorption in these systems results from an interplay of the band edge fine structure, the influence of optical and acoustic phonons and the size distribution. In conventional size distributed QD ensembles the peak position in PL for non-resonant excitation is determined by the largest crystals in the ensemble, as the absorption *far above the band edge* (where the laser is absorbed) scales with the number of states, which is proportional to the crystal volume [217]. The *excitonic band edge absorption* on the other hand is supposed to follow the size distribution [106] (recent observations suggest a linear increase of the band edge absorption with size [218]), evoking

a shift between the mean energy of emission and absorption. However, due to the specific nature of the clusters consisting of a discrete number of 26 atoms, our measurements are not significantly affected by broadening due to size distribution. Simultaneously, the strong quantum confinement allows spectral differentiation between the individual fine structure states.

In conventional QDs the energetically lowest, optically forbidden ±2 state dominates the emission, while the absorption is centered at the mean position of the optically active states, and no un-shifted short term luminescence is recorded due to an efficient energy transfer to the ±2 ground states. A possible explanation for the extraordinary appearance of the unshifted fine structure peaks in time resolved PL compared to absorption in case of $(CdSe)_{13}$ MSCs may be provided by an inversed order of the fine structure states, suggesting that the third peak in energy is related to the ±2 dark state. An inverted order of the fine structure has previously been proposed for small, anisotropic crystals [219].

Identification of the short component as being related to the $\pm 1^L$ and 0^L states of the fine structure provides the base for tracing the temperature dependence of the bandgap via transient PL spectroscopy, which is depicted in Figure 5.15c. Although exhibiting increasing signal-to-noise ratios due to decreasing intensities, the 0^L transition can be traced up to room temperature. Between room and cryogenic temperatures the signal shifts by about 160 meV, which is similar to the temperature dependence observed via absorption.

5.2.2 Bandgap Shift in Mn^{2+}-Doped $(CdSe)_{13}$ with Temperature

Doping with transition metals provides an alternative experimental access to the electronic structure of the MSC: The *sp-d* exchange interactions between the band charge carriers and the spins of the transition metals introduce pronounced magneto-optical responses, which allow precise determination of the energetic position of the energetically lowest $\pm 1^L$ transition in Mn:$(CdSe)_{13}$ (compare Section 4.1.3). Figure 5.16a depicts the temperature dependence of the MCD signal for Mn^{2+}-doped clusters with $x_{Mn} = 2\,\%$. Exceeding the intrinsic Zeeman splitting by more than an order of magnitude, the *sp-d* exchange interactions in Mn^{2+}-doped clusters strongly increase the magneto-optical response of individual transitions compared to undoped $(CdSe)_{13}$, thus allowing to trace the bandgap shift all the way up to room temperature. As the sign reversal of the MCD signal precisely marks the $\pm 1^L$ transition, it can be unambiguously traced precluding any confusion between the different fine structure states. Comparison between cryogenic and room temperature signals reveals a shift of about 190 meV, which even exceeds the

shift observed in undoped $(CdSe)_{13}$. A similar shift ($\approx$ 165 meV for the first absorption maximum) is revealed in the absorption of the same sample (compare Figure 5.16b), indicating that the 0^L transition being the dominant absorption peak shifts parallel to the magneto-optically active $\pm1^L$ transition.

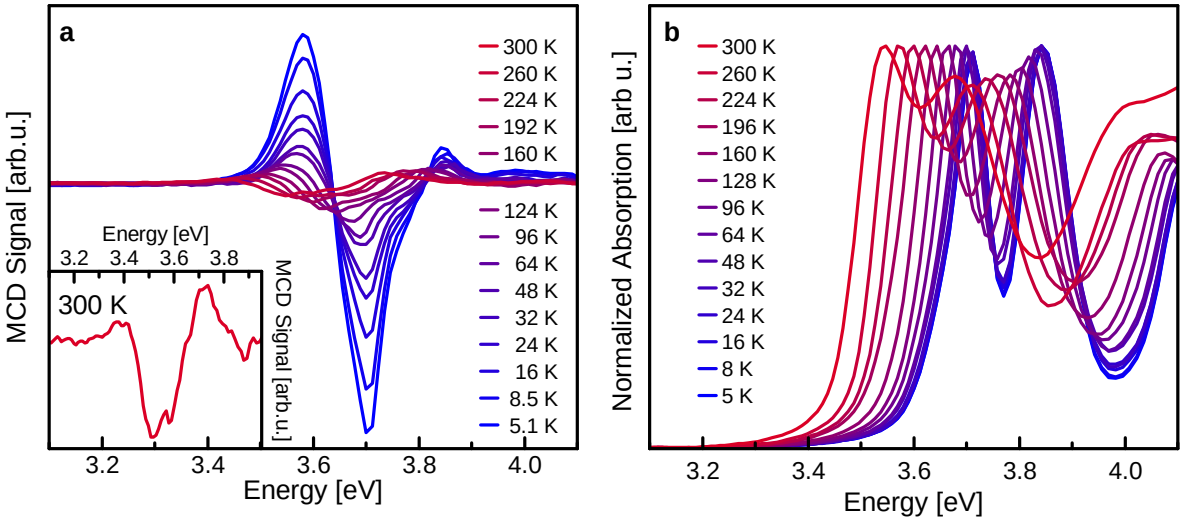

Figure 5.16: Temperature dependence of the bandgap in Mn^{2+}-doped clusters. (a) depicts MCD spectra of Mn^{2+}-doped $(CdSe)_{13}$ with $x_{Mn} = 2\,\%$ between 5 K and 300 K at 1.6 T, allowing tracking of the $\pm1^L$ transition. The inset shows the room temperature signal. (b) depicts the corresponding absorption spectra (collected with the MCD setup).

In addition to the magneto-optical activity the partial replacement of cations by Mn^{2+} also changes the emission, introducing a characteristic orange luminescence originated by the Mn^{2+} internal $^4T_1 \rightarrow {}^6A_1$ transition, which is excited by an energy transfer from the band edge. Monitoring the intensity of this emission using PLE spectroscopy represents an additional approach to the band edge electronic structure.

The development of PLE spectra with temperature is shown in Figure 5.17. Similar to absorption the PLE spectra exhibit a superposition of the various peaks of the fine structure, but with significantly deviating shape. The 4 K spectrum exhibits a maximum at around 3.69 eV accompanied by a low energy shoulder at 3.63 eV, most likely corresponding to the 0^L and $\pm1^L$ transitions, respectively. In contrast to the absorption spectrum, PLE in addition reveals a distinct peak at 3.75 eV, i.e., in the spectral region where the ±2 state is hypothesized. The broad maximum at around 3.88 eV may be attributed to a superposition of the $\pm1^U$ and 0^U states. While the intensities of the various peaks in absorption only depend on the oscillator strengths of the corresponding transitions, the intensity of the PLE peaks also includes the efficiency of the energy transfer from the absorbing states to the emissive Mn^{2+} ions. Although the precise mechanism of the energy transfer from the band charge carriers to the Mn^{2+} is still under debate, it is widely accepted to be

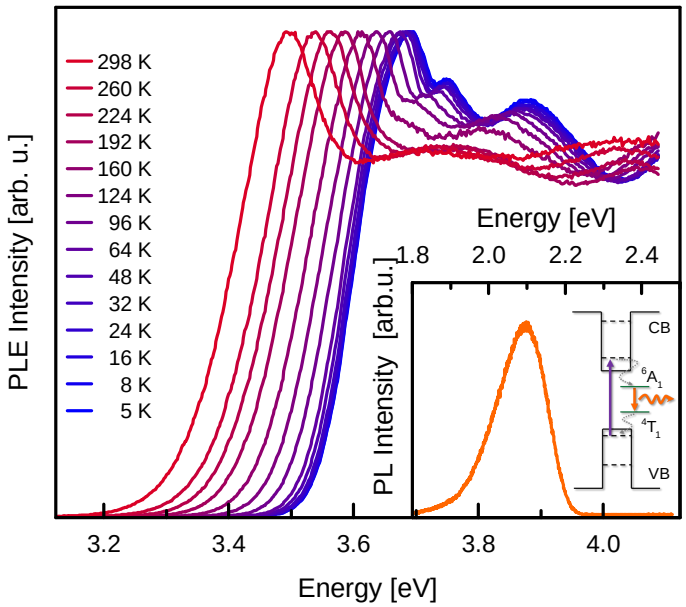

Figure 5.17: PLE spectra of Mn^{2+}-doped clusters with $x_{Mn} = 2\,\%$ probed at the Mn^{2+} internal ligand field transition at 2.1 eV between 5 K and 300 K. The energy axis is shifted by 26 meV to higher energies to compensate aging of the sample. The inset exhibits the time-integrated PL spectrum in the region of interest, revealing the corresponding Mn^{2+} transition, and a scheme representing the energy transfer from the band states.

spin-dependent [26, 220–223]. Deviations between the shape of both spectra may thus indicate differences in the energy transfer from the individual fine structure states to the Mn^{2+} cations.

Although the dominant PLE peak exhibits a shoulder at the low energy side that dissolves with increasing temperature, it can be tracked up to room temperature. Similarly to the MCD signal PLE spectroscopy reveals an energy shift of about 200 meV between 5 K and 300 K. Together, the MCD and PLE characteristics of Mn^{2+}-doped $(CdSe)_{13}$ confirm the anomalous temperature dependence of the band edge observed in undoped $(CdSe)_{13}$, eliminating a mix-up between different fine structure transitions as origin of the observed anomalous strong bandgap shift.

5.2.3 Thermodynamic Interpretation of the Enhanced Temperature Dependence

For the evaluation of the temperature dependence, the band edge in undoped as well as Mn^{2+}-doped MSCs as determined with different experimental approaches are compared in Figure 5.18. The peak position of the 0^L transition in undoped $(CdSe)_{13}$ is extracted via Gaussian fits either from absorption or from the short component of the transient

PL (integrated over the first 50 ps). For the magnetically doped Mn:$(CdSe)_{13}$ clusters the energetic position of the $\pm 1^L$ transition is taken as the energetically lowest zero crossing in the MCD signal and the 0^L is extracted from Gaussian fits to the PLE and absorption measurements, respectively. The entity of transitions in both undoped as well as magnetically doped clusters exhibits significantly enhanced slopes for the energy shift with temperature above 80 K by more than a factor of two compared to bulk CdSe (grey dashed line), leading to extraordinary large total values for the energy shift between cryogenic and room temperature between 152 meV to 200 meV.

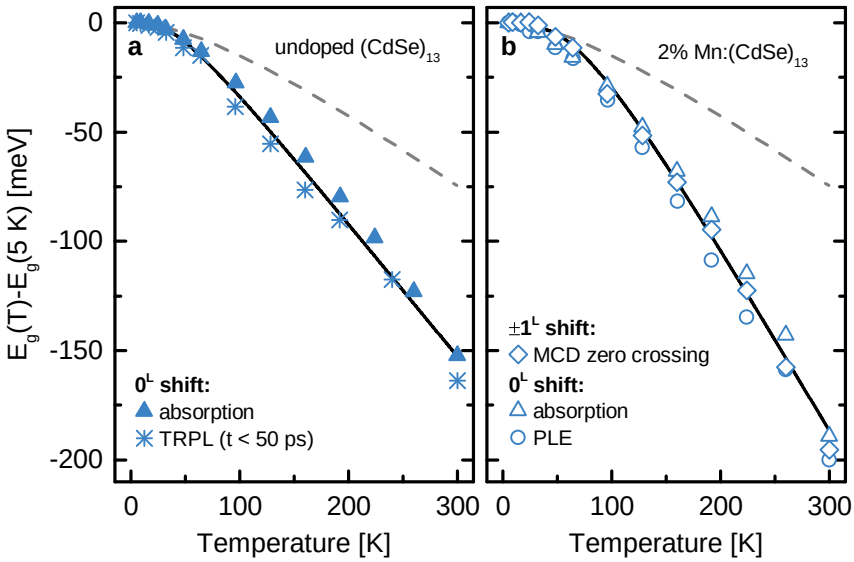

Figure 5.18: Anomalous strong bandgap shift with temperature in MSCs. Comparison of the energy shift with temperature for different transitions from cryogenic to room temperature for (a) undoped and (b) Mn^{2+}-doped clusters, as extracted with different experimental approaches. Grey lines in both panels represent reference data for bulk CdSe [89]. Black solid lines depict fits of both data sets to O'Donnels equations.

Comparison to the temperature dependence of the bandgap for various other semiconductors (compare Figure 5.19a) reveals that the magnitude of the temperature dependent shift observed in $(CdSe)_{13}$ MSCs drastically exceeds the bandgap shift in most common semiconductors of group IV elements and III-V and II-VI compounds (traces are taken from [94]). In conventional QDs, including both epitaxial and colloidal ones, the temperature dependent shift of the band edge transition is either found to be equal to [224] or even slightly decreased compared to the bulk behavior. Figure 5.19b depicts the temperature dependent shift of the $1S_{3/2}1S_e$ transition for various colloidal CdSe QDs from literature (all sources are based on absorption measurements). All samples, although possessing diverse surface coverings like inorganic shells or organic ligands, exhibit very similiar temperature traces of the band edge, not exceeding a total shift of 100 meV between cryogenic and room temperature, which is in stark contrast to what is observed in MSCs. In order to rule out synthetic factors specific for our preparation process like incorporated impurities

during synthesis or the amine-based ligands as a origin of the anomalous temperature dependence, Dr. Jiwoong Yang in addition prepared own batches of CdSe QDs, covered either with amine-ligands or with an anorganic ZnS shell, respectively. Both samples totally match the temperature dependences observed in literature, as can be seen in Figure 5.19. In contrast to that, Mn:$(ZnSe)_{13}$ (data taken from Figure 4.15) exhibits a similar anomalous strong temperature dependent bandgap shift as the CdSe based MSCs, as can be seen from the position of the MCD zero crossing illustrated in Figure 5.19. This clearly underlines that the observed anomalous temperature dependence of the bandgap is not restricted to a specific material system, but instead correlated to the specific structure of the MSCs.

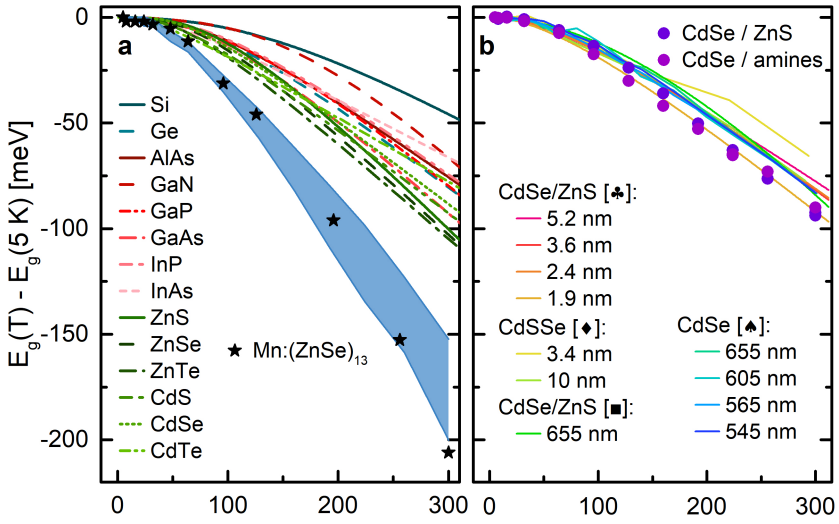

Figure 5.19: Temperature dependence of the bandgap of MSCs compared to bulk and conventional colloidal quantum dots. (a) compares the temperature dependence of the band edge transition in undoped as well as doped $(CdSe)_{13}$ (all data inside the light blue area) to the most important group IV, III-V and II-VI semiconductors (data sets are plotted using the parameters and parameterization in [94]). In addition the shift of the $\pm 1^L$ transition in Mn:$(ZnSe)_{13}$ as extracted from the zero crossing of MCD spectra (data in Figure 4.15) are shown for comparison. In (b) the temperature dependent shifts of the bandgap for various CdSe based QDs (determined exclusively via the shift of the absorption peak) are compared from literature (references are indicated by symbols: ♣-[216], ♦-[224], ■-[225], ♠-[226]). In addition two CdSe QDs batches prepared under similar conditions with both ZnS shell and covered with amines similarly as the MSCs are shown.

While the temperature dependence of the bandgap in bulk semiconductors is widely accepted as a cumulative effect of the thermal lattice expansion and electron-phonon interactions [76], both scaling with the occupation number of the phonons [77, 95], additional aspects have to be considered in case of strongly quantum confined MSCs. First, those include changes in the Coulomb or confinement energy with temperature [224, 226, 227]. The confinement energy which can be approximated from the band edge difference be-

tween $(CdSe)_{13}$ and bulk to 1.8 eV in the clusters, is expected to change due to the lattice dilatation. Considering the bulk lattice expansion at room temperature ($2.5 \times 10^{-6}\,K^{-1}$ to $4.3 \times 10^{-6}\,K^{-1}$ [202]), it can be assumed that this effect reduces the energy by less than 3 meV between 100 K to 300 K, which is far not sufficient to explain the observed behavior. Second, changes in the effective mass may also alter the confinement energy, even if the idea of an effective mass approaches its limit in a structure consisting of 26 atoms. Since the effective mass is expected to decrease slightly with increasing temperature [224, 226, 228], this effect is expected to increase the confinement energy resulting in a reduced redshift with temperature, which is in contrast to our observations Last, due to the enhanced electron and hole wave function overlap the Coulomb energy scaling with $1/a_{QD}$ (with the QD radius a_{QD}) is enhanced [105]. As the Coulomb energy depends on the dielectric constant varying with temperature from 9.17 to 9.96 between 100 K and 300 K in CdSe [202], the Coulomb energy decreases by about 5 % in the same temperature range, which implies a reduced redshift in contrast to our observations. The effects of quantum confinement and Coulomb interactions considered above can thus be excluded as the main origin for the observed anomalous strong temperature dependence.

In a thermodynamical context the fundamental bandgap in bulk semiconductors can be understood as the formation energy of an electron-hole pair, more precisely it equals the standard Gibb's energy of the equilibrium equation $0 \rightarrow e + h$ [77, 229]. Thus, the temperature dependent slope $\frac{dE_g}{dT}$ can be interpreted as the formation entropy ΔS_{e-h} of this electron-hole pair at a given temperature T. To quantify ΔS_{e-h} in the $(CdSe)_{13}$ clusters the temperature dependent traces of the bandgap are fitted to a semi-empirical oscillation model [77]. From bulk semiconductors it is known that the two qualitatively different factors causing the temperature dependence, i.e. the lattice dilatation and the electron-phonon coupling, are both proportional to the averaged occupation number of the different phonon modes and can be described with semi-empirical expressions based on Bose-Einstein terms [95]. In order to minimize the number of fitting parameters, the temperature dependence of the $(CdSe)_{13}$ bandgap was evaluated applying the single-oscillator model of O'Donnel & Chen [77], which neglects any phonon dispersion:

$$E_g(T) - E_g(5\,K) = -\frac{2S_{fit}\langle\hbar\omega\rangle}{\exp(\langle\hbar\omega\rangle/k_B T) - 1} \tag{5.5}$$

Herein $\langle\hbar\omega\rangle$ denotes the average phonon energy and S_{fit} is a dimensionless coupling constant proportional to the high temperature limit of ΔS_{e-h}. Fitting of the data in Figure 5.18 (black lines) reveals enhanced S_{fit} values of 3.6 and 5.0 for undoped and doped $(CdSe)_{13}$ clusters, respectively, compared to $S_{fit} = 2.5 \pm 0.4$ for bulk CdSe (averaged among six literature sources [89]). This trend of enhanced S_{fit} is confirmed by the eval-

uation of a total number of 14 data sets, including MCD, PLE, absorption and time resolved photoluminescence (TRPL) data of $(CdSe)_{13}$ doped with different doping concentrations (samples used in Chapter 4.1). Those reveal a mean S_{fit} of 4.4 ± 0.6 and $\langle \hbar\omega \rangle$ of $15.0 \pm 3.7\,\mathrm{meV}$ (compare Table 5.4). Since S_{fit} is proportional to $\Delta S_{\mathrm{e-h}}$ in the linear regime above approx. $100\,\mathrm{K}$ ($\Delta S_{\mathrm{e-h}}(T \to \infty) = -2 S_{\mathrm{fit}} k_{\mathrm{B}} T$ [77]), those findings can directly be ascribed to a 75 % increase of the electron-hole pair formation entropy in $(CdSe)_{13}$ MSCs as compared to bulk.

To obtain a physical understanding of $\Delta S_{\mathrm{e-h}}$ and how it depends on the phonon modes, it is helpful to interpret the electron-phonon coexistence as vibrational states perturbed by electronic states [79, 230]. The excitation of an electron-hole pair, i.e. the lifting of an electron from a bonding state in the valence band into an antibonding state in the conduction band, weakens the bonds and thus changes the individual phonon energies ($\hbar\omega \to \hbar\omega'$). As the thermal occupation of the individual phonon modes depends on the corresponding phonon energies, the phonon occupation can be assumed to change upon optical excitation. The exciton formation entropy directly results from the change of the occupation of the phonon modes due to optical excitation and can be expressed as $\Delta S_{\mathrm{e-h}} = -k_{\mathrm{B}} \sum_{phononmodes} \ln(\frac{\hbar\omega'}{\hbar\omega})$, assuming a harmonic oscillator [79]. The anomalous temperature dependence of the bandgap found in $(CdSe)_{13}$ can thus be directly correlated to the influence of optical excitation on the phonon modes.

Table 5.4: Statistics on the anomalous bandgap shift in $(CdSe)_{13}$ MSCs, summarizing the total bandgap shift between cryogenic and room temperature and the resulting fitting parameters for various doped and undoped samples.

Experimental approach	Mn^{2+} concentration	$E_{\mathrm{g}}(5\,\mathrm{K})$-$E_{\mathrm{g}}(300\,\mathrm{K})$[meV]	S_{fit}	$\langle \hbar\omega \rangle$ [meV]
MCD	2 %	195	5.2	16.9
	4 %	160	3.4	9.8
	6 %	162	4.8	20.9
	8 %	150	4.0	15.7
	10 %	156	3.6	11.0
PLE	2 %	200	4.9	13.2
	4 %	160	5.4	16.0
	6 %	162	5.1	19.1
absorption	0 %	152	3.8	16.6
	2 %	189	5.0	18.3
	6 %	164	4.4	14.9
	8 %	169	4.3	11.8
	10 %	156	4.5	18.2
TRPL	0 %	158	3.8	7.8
mean		166 ± 16	4.4 ± 0.6	15.0 ± 3.7

This influence, which appears to be fundamentally different as compared to bulk materials or conventional QDs, can be visualized within the bond charge model [231], which represents the bonds assuming an effective charge Z_b per bond. Upon excitation of an electron from the mostly-bonding valence to the mostly non-bonding conduction band the bond charge is weakened by the electron charge distributed among the N_b bonds in the crystal. This in a first approximation causes the phonon modes to change according to [79]:

$$\left(\frac{\hbar\omega'}{\hbar\omega}\right)^2 = 1 - \frac{e}{N_\mathrm{b} Z_\mathrm{b}} \tag{5.6}$$

According to that the difference between bulk semiconductors or QDs and MSCs may be originated by two impacts both resulting from the structure of the clusters.

First, the extraordinary high number of surface atoms is supposed to cause a reduction in the phonon energies especially for acoustic phonon modes. This has been observed in small semiconductor QDs and attributed to the surface region of the lattice [110, 232]. It is plausible that phonon modes with reduced energy may be stronger affected by an optically excited electron-hole pair. Thus, reduced phonon energies in $(CdSe)_{13}$ compared to their bulk counterparts may imply an increase of the exciton formation entropy. In addition, each $(CdSe)_{13}$ cluster is supposed to be capped with 13 oleylamine ligands [160], which transfer a total charge of 1.43 e to the MSCs according to DFT calculations [66]. Being collected in the predominantly anti-bonding conduction bands, this charges may reduce the bond charge and additionally weaken the bonds, which also implies a reduction of the phonon energies. However, as the single oscillator model used here neglects any phonon dispersion and thus does not allow accurate extraction of $\langle\hbar\omega\rangle$, a change in the phonon energies in $(CdSe)_{13}$ compared to bulk cannot be extracted from the fitting parameters ($\langle\hbar\omega\rangle = 15.8 \pm 4.4$ meV for $(CdSe)_{13}$ compared to 16.7 ± 4.8 meV for bulk CdSe).

A second impact, which has to be considered in MSCs, is the small number of bonds, among which the optically excited charge is distributed. Depending on the controversially discussed specific lattice structure [66] (compare Figure 5.7) the number of bonds in a single cluster varies between 40 and 52, whereas bulk materials or even conventional colloidal QDs own a huge multitude of hundreds to thousands of bonds. Upon optical excitation, the bond charge is supposed to be drastically reduced introducing a strong decrease of the phonon energy ($\hbar\omega \rightarrow \hbar\omega'$), which implies a large exciton formation entropy. Note that due to the small volume the excitation of one single electron hole pair implies a photo generated charge carrier density in the range of $10^{21}\,\mathrm{cm}^{-3}$, which corresponds to the regime of particularly high optical pumping in conventional semiconductors.

Taken both together, the anomalous temperature dependence of the bandgap observed in $(CdSe)_{13}$ MSCs, which is in strong contrast to the majority of semiconductors, most

likely represents a direct consequence of the reduced lattice structure, precisely the high number of surface atoms and the minimized number of bonds in a single $(CdSe)_{13}$ cluster. The remarkable strong bandgap shift is thus attributed to mainly arise from the optical excitation, which is intended to serve as the probe for the bandgap.

Chapter 6

Magnetic Exchange Interactions in Wave Function Engineered CdSe/Mn:CdS Hetero-Nanoplatelets

Two-dimensional semiconductors with thicknesses down to a few nanometers represent key elements in modern, industrial-relevant micro- and optoelectronics. Built by molecular beam epitaxy or metal-organic vapor phase epitaxy on crystalline substrates, these so-called quantum wells exhibit extraordinary optical and electrical properties, like a stepwise density of states and size-tunable energy states, which triggered the development of new device types whith increased performance - including laser diodes, infra-red detectors and high-performance transistors [233, 234].

Only recently, advances in colloidal chemistry allow the solution based synthesis of free standing two-dimensional nanocrystals, which, depending on the synthesis route, are denoted as nanoribbons [29, 57, 58], nanosheets [161], nanodiscs [235] or nanoplatelets (NPs) [40–43]. The latter can be synthesized exhibiting uniform thicknesses corresponding to a discrete number of monolayers (monolayer (ML)) and lateral dimensions of a few tens up to hundreds of nm. They combine high ensemble color purities [236] and short fluorescence lifetimes [35] with a distinct 2D electronic structure, large absorption cross sections [237] and a minimal Stokes shift [238]. In contrast to epitaxial quantum wells colloidal NPs combine structural flexibility with the possibility to be manipulated with solution-based transfer processes on e.g., flexible substrates. This evokes increasing interest for applications in tomorrow's electronic- and optoelectronic devices like light emitting diodes [239–241] or lasing applications [242–244].

Lately developed chemical approaches like the colloidal atomic layer deposition (c-ALD) [45] allows the preparation of complex, heterostructured NPs such as core/shell

[45, 46] or core/crown [47, 48] architectures. These heterostructures do not only provide the opportunity to boost the luminescence quantum yield as the shell prevents the exciton from non-radiative recombination via surface defects, but moreover enable precise tuning of the band alignment and thus of the wave function distribution between the core and shell or crown, to achieve various configurations like type I [245], quasi type II [48, 246] or type II [247, 248] heterostructures.

Beyond that, c-ALD offers the possibility to introduce impurity atoms into colloidal NPs [32, 49], which is so far not possible during the synthesis of the core. Only Mn^{2+}-doped CdSe nanoribbons, which are built out of Mn:$(CdSe)_{13}$ clusters, represent an exception. Those are dopable in the cluster stage, but exhibit a fixed thickness of $\approx 1.4\,\mathrm{nm}$ related to the cluster size [37]. Incorporation of transition metal ions into the shell of NPs creates a new class of DMS materials, which combines a precisely tunable 2D electronic structure with magnetic functionalities, originated by the magnetic exchange interactions between the dopants and the spins of the charge carriers. In contrast to DMS QDs, the two-dimensional electronic structure, in which the *hh*-X, *lh*-X and *so*-X transitions are spectrally separated, allows to selectively address individual excitonic states with well-defined hole characters.

Up to now confirmation of the magnetic exchange interactions in literature is only provided by magneto-PL in multi-shell CdSe/Mn:CdS/CdS NPs [32]. This technique offers information about the energetically lowest transition and thus does not allow distinction between the contribution of localized states and free carriers in the conduction and valence band, respectively [49]. In contrast to PL, the absorption-based technique of MCD enables a direct investigation of the exchange interactions between the magnetic dopants and the conduction or valence band charge carriers for different excitonic transitions.

Following the proof of *sp-d* exchange interactions with free band charge carriers, this chapter demonstrates, how the variation of the core and the shell thickness and composition tunes the *s-d* and *p-d* exchange interactions by means of wave function engineering in shell-doped CdSe(/MnS)/Mn:CdS core/shell NPs. In addition, the sensitivity for excitonic transitions provided by MCD is utilized in combination with effective mass wave function calculations to analyze the excited state electronic structure in these novel materials.

6.1 *sp-d* Exchange Interactions in Shell-Doped Nanoplatelets

Delikanli *et al.* demonstrated that the luminescent state in CdSe/Mn:CdS/CdS NPs exhibits magnetic exchange interaction with the Mn^{2+}-dopants [32], as the polarization of the PL in an external magnetic field followed the magnetization of the Mn^{2+} ions. In [49] it was hypothesized that the observed luminescence is related rather to a defect state localized at the core/shell interface than to free carriers of the semiconductors conduction and valence band, respectively. To verify the existence of direct *s-d* and *p-d* exchange interactions, similar samples were investigated via MCD. The samples used for this study were prepared by Dr. Savas Delikanli in the group of Prof. Hilmi Volkan Demir at the Nanyang Technological University in Singapore and the Bilkent University in Ankara, Turkey. Aiming at the manipulation of either the *s-d* or *p-d* exchange interactions, two different sets of samples are prepared. The first one (set I) consists of an undoped CdSe core of 2 ML or 3 ML thickness surrounded by either 6 ML or 8 ML Mn^{2+}-doped CdS (3 or 4 ML on each side). The second set (set II) is composed of samples with a 2 ML CdSe core coated with 2 ML MnS interlayer (one on each side) and additional 6 to 10 ML (3 to 5 ML on each side) of Mn^{2+}-doped CdS.

6.1.1 Verification of *sp-d* Exchange Interactions

Figure 6.1b compares the MCD signal of (2) CdSe/(8) Mn:CdS NPs (see Table 3.1 for the notation) at 5 K and 1.6 T with undoped samples of the same architecture ((2) CdSe/(8) CdS). While the Mn^{2+}-doped sample exhibits a bunch of transitions up to 3 eV, none of them can be resolved in the signal of its undoped counterpart. An $\mathscr{A}$-type MCD feature, as expected from a transition with a degenerated excited state, typically exhibits a deviated-Gaussian line shape. Here the MCD zero crossing coincides with the corresponding peak position in absorption. The shape of the feature reflects the sign of the Zeeman splitting, i.e. for a negative splitting a maximum is followed by a minimum in energy and vice versa. Comparison to the absorption of the doped sample (compare Figure 6.1a) reveals that the two energetically lowest features coincide with the two dominant absorption peaks, which are commonly attributed to the *hh*-X and *lh*-X excitonic transition in literature [35, 36]. For clarity, all transitions in this chapter are denominated according to the involved electron and hole states (e_1hh_1-X and e_1lh_1-X for the band edge *hh*-X and *lh*-X transitions).

Although including some uncertainties the corresponding Zeeman splitting for the e_1hh_1-X transition can be estimated to be in the range of -1.0 ± 0.5 meV by fitting Gaus-

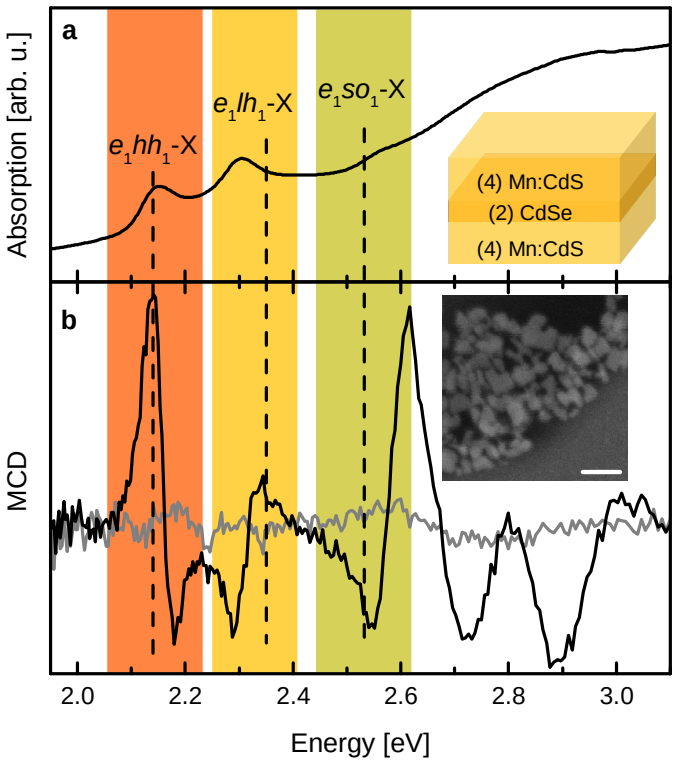

Figure 6.1: Absorption (a) and MCD (b) spectra of (2) CdSe/(8) Mn:CdS NPs at 5 K. The MCD spectrum (black) is measured at 1.6 T and compared to an undoped reference sample (grey) with equal architecture ((2) CdSe/(8) CdS). Spectral regions of the e_1hh_1-X, e_1lh_1-X and e_1so_1-X transition are highlighted in orange, yellow and olive, respectively, while dashed lines represent the calculated transition energies. The insets depict a sheme of the sample (top) and a SEM image of the NPs deposited on a silicon substrate (bottom, scale bar is 50 nm). Note that absorption and MCD spectra are measured on different quartz glass samples prepared from the same dispersion.

sian peaks to the absorption. The splitting of the e_1lh_1-X exhibits an opposite sign with a ratio between the e_1lh_1-X and e_1hh_1-X splitting of -0.54 ± 0.08. The third transition at about 2.6 eV exhibits a negative sign of the giant Zeeman splitting.

In bulk zinc blende DMS (and also in anisotropic systems like quantum wells with their predominant axis aligned parallel to the external magnetic field), the e_1hh_1-X is known to split according to $\Delta E_{\mathrm{Zhh}} = x_{\mathrm{eff}}(\gamma_{\mathrm{hh}} N_0\beta - \gamma_{\mathrm{e}} N_0\alpha)\,\langle S_{\mathrm{z}}\rangle$, exhibiting a negative splitting for all values of γ_{hh} and γ_{e}, as both exchange coupling constants usually exhibit opposite signs ($N_0\alpha = 0.22$ eV and $N_0\beta = -1.8$ eV for Mn^{2+} in CdS [8]). Note that for shell-doped NPs γ_{e}, γ_{hh}, γ_{lh} and γ_{so} correspond to the integrated wave function probability density of the electron, *hh*, *lh* and *so* in the shell, respectively. For the MCD measurements the NPs are prepared between two quarz glass substrates, where their orientation cannot be directly determined. However, after preparation of the same dispersion on a silicon substrate, SEM images reveal that the majority of the platelets is oriented parallel to the substrate (compare lower inset in Figure 6.1b). As the substrate is placed perpendicular

to the direction of the magnetic field, this implies that for most NPs the field is oriented parallel to the quantization axis of the NPs ($\vec{B} \parallel \vec{q}$). The negative sign of the e_1hh_1-X splitting, together with the absence of a magneto-optical response for the undoped NPs, unambiguously proves *sp-d* exchange coupling interactions between the Mn^{2+} spin ensemble and the conduction and valence band charge carriers.

For lh excitonic transitions the situation is more complex. In zinc blende bulk DMS materials the e_1lh_1-X giant Zeeman splitting is described by $\Delta E_{\mathrm{Zlh}} = x_{\mathrm{eff}}(\gamma_{\mathrm{lh}}\frac{N_0\beta}{3} + \gamma_{\mathrm{e}}N_0\alpha)\langle S_{\mathrm{z}}\rangle$ and the exchange coupling components of the hole and electron partly compensate each other. This leads to a small negative splitting in bulk zinc blende DMS [138, 139, 249], which can be inverted in sign in case of an anisotropic perturbation [142] e.g. through a wurtzite lattice structure [147, 148], lattice strain [149] or a quantization axis [37]. The observed positive splitting of the e_1lh_1-X in the NPs may thus be originated by a combination of the strong quantization and potential strain in the nominally zinc blende structured Mn:CdS shell.

The giant Zeeman splitting of the e_1so_1-X in bulk DMS follows $\Delta E_{\mathrm{Zso}} = x_{\mathrm{eff}}(-\gamma_{\mathrm{so}}\frac{N_0\beta}{3} + \gamma_{\mathrm{e}}N_0\alpha)\langle S_{\mathrm{z}}\rangle$, so that the electron and hole exchange coupling components amplify each other towards a positive sign [140, 148]. Since this is not expected to alter in case of an uniaxial perturbation in direction of the magnetic field, the e_1so_1-X splitting in the NPs is expected to exhibit the opposite sign as compared to the e_1hh_1-X. This is the case for the third transition at $\approx 2.6\,\mathrm{eV}$. Hence, the sign of the magneto-optical response represents a strong evidence for the assignment of this transition as the e_1so_1-X transition.

6.1.2 Double Potential Quantum Well Wave Function Calculations

In order to verify the assignment of the three energetically lowest transitions, the expected transition energies are calculated assuming a two-step potential well.

Numerical implementation of the calculations were done in part by Dr. Pedro L. Hernández-Martínez in the Group of Prof. Hilmi Volkan Demir and partly by Severin Lorenz in the group of Prof. Gerd Bacher. Quantization energies as well as the hole and the electron envelope functions were obtained solving the stationary Schrödinger equation for a two-step double potential well, assuming an effective mass approximation in analogy to the approach presented in [32]. The parameters used in the calculations are given in Table 6.1. The potential height of the hetero-interface results from the conduction (ΔU_{CB}) and valence band (ΔU_{VB}) offsets between CdSe and CdS (assumed as bulk values), respectively, and is defined to be infinity outside the NP. Note that the band offsets for

the conduction and valence band both differ between different literature sources, from −0.3 eV to 0.3 eV for the former [250–253] and from 0.4 eV to 0.8 eV for the latter [252, 254, 255]. Effective masses for the electron, *hh* and *lh* (m_e, m_{hh} and m_{lh}) in the different materials are taken from the Luttinger-Kohn parameters estimated in [35] for CdSe and CdS NPs, while the *so* masses m_{so} are taken from [256]. The potential step used for the *so* hole results from the valence band offset between CdSe and CdS reduced by the difference between the corresponding spin-orbit split-off energies Δ_{so}.

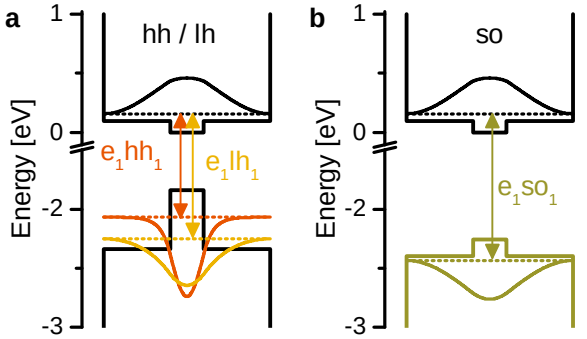

Figure 6.2: Transition energies (dashed lines) and wave function probability distributions calculated assuming a double quantum well potential. (a) depicts the $n = 1$ electron, hh_1 (orange) and lh_1 (yellow) states and (b) the so_1 state (olive). Corresponding transitions are highlighted with colored arrows (note that in this representation the exciton binding energy is not included).

Figure 6.2 depicts the relevant potential wells as well as the resulting energy levels and the probability functions for the energetically lowest ($n = 1$) electron, hh_1, lh_1 and so_1 states. While the electron is delocalized among the whole NP thickness, the hh_1 and lh_1 are largely confined within the NP core, although due to the smaller mass the lh_1 is

Table 6.1: Parameters used for the calculation of the transition energies and wave function probability functions. A ML thickness d_{ML} of 0.35 nm has been assumed for all materials. Calculated excitonic transition energies are corrected for an exciton binding energy of $E_{exc} = 88$ meV for all *hh* transitions and $E_{exc} = 61$ meV for the *lh* and *so* transitions, as determined for CdSe NPs in [35]. For MnS the parameters of ZnS were used from [257].

	CdSe	CdS	MnS
m_e	$0.18\,m_0$[35]	$0.31\,m_0$[35]	$0.28\,m_0$[257]
m_{hh}	$0.89\,m_0$[35]	$0.95\,m_0$[35]	$1.7\,m_0$[257]
m_{lh}	$0.194\,m_0$[35]	$0.227\,m_0$[35]	$0.23\,m_0$[257]
m_{so}	$0.286\,m_0$[256]	$0.331\,m_0$[256]	–
ΔU_{CB}	–	0.1 eV	0.8 eV
ΔU_{VB}	–	0.5 eV	0.96 eV
Δ_{so}	0.4 eV	0.07 eV	–
$E_g(T = 4\,K)$	1.84 eV	∼ 2.41 eV	3.6 eV[256]

more delocalized into the shell as the hh_1 state. The so_1 hole on the other hand is only weakly confined within the core. The calculated transition energies are depicted in Figure 6.1 as dashed lines, coinciding qualitatively with the three energetically lowest transitions (marked by the MCD zero crossings). The energies are corrected by an exciton binding energy of 88 meV for the e_1hh_1-X and 61 meV for the e_1lh_1-X and e_1so_1-X consistent with the values determined in [35]. This in combination with the sign of the giant Zeeman splitting allows the assignment of the feature at 2.6 eV to the e_1so_1-X transition.

The calculated wave function distributions also give valuable insights into the overlap integrals γ_{e}, γ_{hh}, γ_{lh} and γ_{so}. While the electron is delocalized along the whole NP thickness, the hole ground states are partly confined within the core. This suggests that by changing the core and shell thickness, the various hole wave function overlaps with the shell can be manipulated, influencing the *p-d* exchange interactions, which is addressed in Section 6.4.

6.2 Electronic Structure of Excited States in Core/Shell Nanoplatelets

Although several works address the electronic structure of colloidal NPs [258–260], up to now calculations of transition energies and the assignment of experimentally observed features have been mainly restricted to the two energetically lowest transitions, the hh-X_1 and lh-X_1, which have been first identified by Ithurria *et al.* [35, 236]. In wurtzite CdSe NPs the third absorption peak in energy was assigned to the first excited heavy hole state (e_2hh_2-X) [36], while in zinc blende CdSe NPs the third peak has been attributed to the e_1so_1-X transition [100]. The latter assignment is affirmed by the sign of the giant Zeeman splitting observed in this work.

Besides the hole ground state excitonic transitions (e_1hh_1-X, e_1lh_1-X and e_1so_1-X), the MCD signal reveals a bunch of excited state transitions above 2.6 eV (compare Figure 6.1). These features cannot be resolved in the absorption spectrum, which represents a superposition of the excitonic transitions with inter-band absorption of free carriers and a scattering tail. This highlights the possibility to investigate the electronic structure of transition metal doped materials by MCD. The sign of the Zeeman splitting can give additional insights into the hole character of an observed transition. As outlined above, any feature related to a hh state is expected to exhibit a negative splitting, while any transition with positive giant Zeeman splitting is anticipated to involve either a lh or a so state.

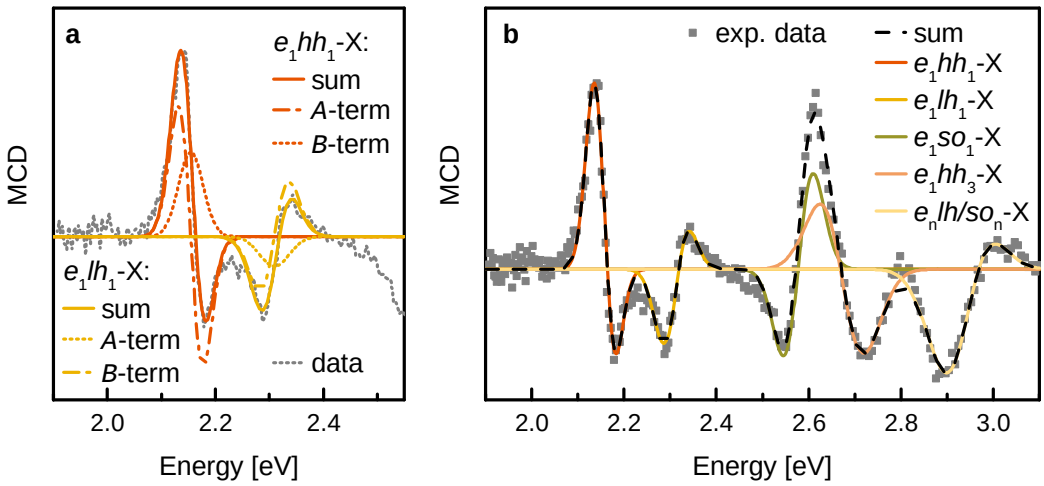

Figure 6.3: Simulation of the MCD signal. (a) depicts a simulation of the energetically lowest e_1hh_1-X and e_1lh_1-X MCD signal together with the involved $\mathscr{A}$- and $\mathscr{B}$-term contributions according to Equation 6.2. In (b) the whole MCD signal up to 3.1 eV is fitted with five asymmetric features. Simulated MCD features are depicted in colored lines while a dashed black line represents the sum of all peaks. The parameters for the fits are given in Table 6.2.

In order to unravel the number and energetic position of the excited states, the whole MCD spectrum up to 3.1 eV is simulated. As apparent from the shape of the MCD signal, most of the contributing features account for an asymmetric MCD signal, which cannot be described with a simple, deviated-Gaussian function as used for pure $\mathscr{A}$-terms. In general, any MCD signal can be described with Equation 6.1 [261–263].

$$I_{\mathrm{MCD}} \propto \left[\mathscr{A}_1\left(-\frac{\partial f(E)}{\partial E}\right) + \left(\mathscr{B}_0 + \frac{\mathscr{C}_0}{k_{\mathrm{B}}T}\right) f(E)\right] \tag{6.1}$$

Herein the MCD parameters $\mathscr{A}_1$, $\mathscr{B}_0$ and $\mathscr{C}_0$ describe the contributions of the derivative-shaped $\mathscr{A}$-term and the band-shaped $\mathscr{B}$- and $\mathscr{C}$-terms. $f(E)$ describes the band shape of an absorption band, which can be assumed to be Gaussian in case of excitonic transitions ($f(E) = \exp\left(-\frac{(E-E_0)^2}{\sigma^2}\right)$). The $\mathscr{A}$-term directly originates from the Zeeman splitting of a transition, in which either the ground or the excited state is degenerated, splitting the absorption bands of σ^- and σ^+ light with respect to each other in energy. The $\mathscr{C}$-term arises from a thermal redistribution of the population of the degenerated ground state of a transition and its absorption-like MCD contribution is expected to decrease rapidly with increasing temperature. As in the NP the ground state is non-degenerated, a $\mathscr{C}$-term is not expected. In accordance to that, the asymmetry of the different MCD transitions does not decrease with increasing temperature, as visible comparing e.g., the e_1hh_1-X feature in the 5 K and 48 K spectra in Figure 6.5. The $\mathscr{B}$-term arises from a magnetic field induced mixing between the ground or excited state with other states close in energy, which

results in a redistribution of the degree of σ^+ and σ^- character between the neighboring transitions. In case of the NPs a $\mathscr{B}$-term may arise from a mixing between the different neighboring states, i.e., the e_1hh_1-X and e_1lh_1-X transitions. Thus, the asymmetric MCD features are fitted with Equation 6.2, chosen so that $\mathscr{A}_{\mathrm{max}}$ and $\mathscr{B}_{\mathrm{max}}$ denote the maximal amplitudes of the contributive $\mathscr{A}$- and $\mathscr{B}$-terms, respectively.

$$I_{\mathrm{MCD}} = \mathscr{A}_{\mathrm{max}} \frac{\sigma\sqrt{e}}{\sqrt{2}} \left(-\frac{\partial f(E)}{\partial E} \right) + \mathscr{B}_{\mathrm{max}} \cdot f(E) \tag{6.2}$$

Simulated MCD features for the hh-X_1 and lh-X_1 transitions as well as the corresponding $\mathscr{A}$- and $\mathscr{B}$-terms are depicted in Figure 6.3 (parameters are listed in Table 6.2). Besides the $\mathscr{A}$-term, whose sign corresponds to the sign of the Zeeman splitting, both transitions exhibit a significant $\mathscr{B}$-term, representing the origin of the asymmetry of the MCD signal. As expected for a $\mathscr{B}$-term, the features of the e_1hh_1-X and the e_1lh_1-X exhibit the opposite sign [262], revealing the coupling between both transitions. According to theory, the maximum contributions of the different terms to the MCD signal scale as [262]:

$$\mathscr{A}_{\mathrm{max}} : \mathscr{B}_{\mathrm{max}} = \frac{1}{2\sqrt{\ln 2}\sigma} : \frac{1}{\Delta E_{\mathrm{tran}}} \tag{6.3}$$

Herein $2\sqrt{\ln 2}\sigma$ denotes the full width at half maximum of the absorption of a transition (54 meV and 64 meV for the e_1hh_1-X and e_1lh_1-X transitions according to the fits, respectively) and ΔE_{tran} is the energy spacing between the two transitions (i.e., 154 meV between the e_1hh_1-X and e_1lh_1-X). With the parameters given in Table 6.2, this accounts for a $\frac{\mathscr{A}_{\mathrm{max}}}{\mathscr{B}_{\mathrm{max}}}$ ratio of 2.9 and 2.4 for the e_1hh_1-X and e_1lh_1-X, which matches in magnitude with the experimentally observed ratios of 1.5 and 1.8, respectively.

Figure 6.3 shows the fully simulated MCD spectrum up to 3.1 eV containing in total five transitions. According to the theoretical considerations above, the features exhibiting a negative Zeeman splitting at 2.68 eV (indicated by the negative sign of $\mathscr{A}_{\mathrm{max}}$) can be assigned as the hh excitonic transition e_1hh_3-X, while the sign of Zeeman splitting for the fifth transition (denominated as $e_{\mathrm{n}}h_{\mathrm{n}}$-X) indicates contributions of either a so or lh.

Table 6.2: Fitting parameters used to simulate the MCD signal up to 3.1 eV according to Equation 6.2.

	transition energy E_{c} [meV]	width 2σ [meV]	$\mathscr{A}_{\mathrm{max}}$ [10^{-4}]	$\mathscr{B}_{\mathrm{max}}$ [10^{-4}]
e_1hh_1-X	2.155	33	−3.99	2.58
e_1lh_1-X	2.309	38	1.67	−0.91
e_1so_1-X	2.578	45	2.79	0.23
e_1hh_3-X	2.675	66	−2.27	−0.48
$e_{\mathrm{n}}h_{\mathrm{n}}$-X	2.934	73	1.76	2.02

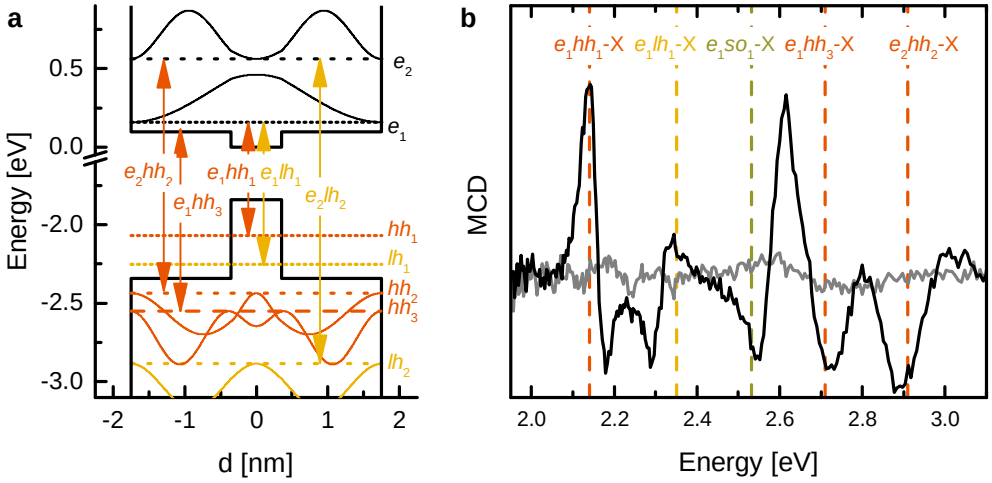

Figure 6.4: Excited states in CdSe/Mn:CdS NPs. In (a) the energy levels and envelope wave function distribution densities of the ground and excited electron states (black) and of the excited *hh* and *lh* states with $n = 2$ and $n = 3$ are shown, resulting from two-step quantum well calculations with the parameters given in Table 6.1. In (b) the MCD signal of the (2) CdSe/(8) Mn:CdS NPs is compared to an undoped reference. The corresponding transition energies (including an exciton binding energy of 88 meV for transitions involving a *hh* state and 61 meV for transitions with *lh* or *so* states) are depicted in (b) as dashed lines.

To identify these transitions, the theoretical energies of transitions involving excited hole states are calculated based on the effective mass approximation for the two-step potential well. Figure 6.4a depicts the wave function probability densities of the *hh* and *lh* excited states ($n \geqq 2$) and the corresponding energies. In addition, arrows highlight the optically allowed electron - hole transitions resulting from the quantum well envelop function selection rules [96], which predefine that only transitions with $\Delta n = 0, 2, 4...$ between the involved electron and hole states are allowed. The transition energies involving excited *hh* (e_1hh_3-X and e_2hh_2-X) are represented as dashed lines in Figure 6.4 (reduced by the exciton binding energy of 88 meV), while all excited state transitions involving a *lh* are above 3.1 eV. Note the calculated energies of the electron and *lh* excited states may be overestimated due to the non-parabolicities of the conduction and *lh* band [264–266]. The calculated energy of the e_1hh_3-X transition nicely fits the observed energy, allowing - in combination with the sign of the Zeeman splitting - a clear assignment of this feature. Although the e_1hh_3-X with $\Delta n = 2$ is expected to exhibit decreased oscillator strength compared to the e_2hh_2-X, the latter is calculated to be much higher in energy. A similar sequence of transitions (e_1hh_1-X, e_1lh_1-X, e_1hh_3-X) has been assigned in CdTe/CdMnTe quantum wells [267]. For the transition at 2.93 eV the positive sign of the Zeeman splitting indicates a contribution of a *lh* or *so* hole. However, the observed transition matches with the transition energy calculated for the e_2hh_2-X. Thus, the transition at 2.93 eV cannot be unambiguously assigned.

6.3 Magneto-Optical Properties at Elevated Temperatures

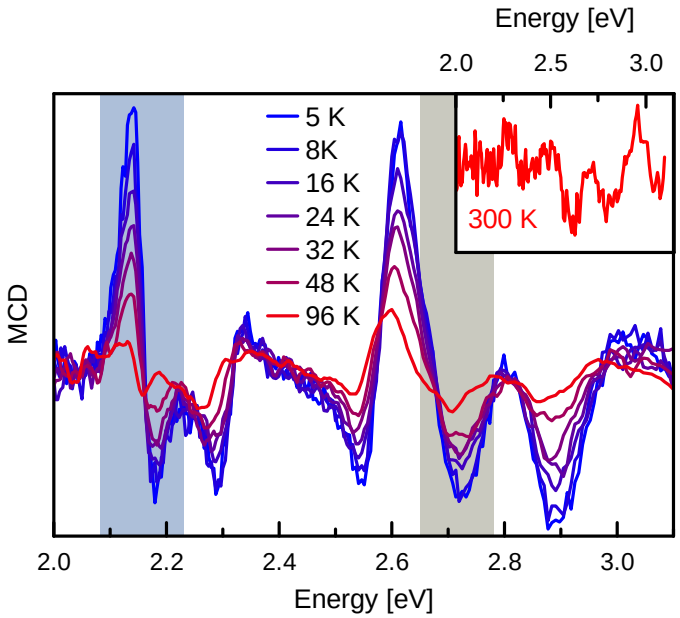

Figure 6.5: Temperature dependence of the MCD signal for the (2) CdSe/(8) Mn:CdS NPs, measured at 1.6 T. The inset depicts the room temperature magneto-optical response. The energetic range of the e_1hh_1-X and e_1hh_3-X transitions are highlighted in blue and grey, respectively.

The way temperature influences the magneto-optical response gives additional insights about its origin. While the intrinsic Zeeman splitting is known to be more or less constant between cryogenic and room temperature [129], the giant Zeeman splitting generated by the *sp-d* exchange interactions scales with the degree of orientation of the Mn^{2+} spins along the external magnetic field, which is strongly influenced by the thermal energy as decribed by the Brillouin function. Figure 6.5 depicts the magneto-optical response of the (2) CdSe/(8) Mn:CdS sample at 1.6 T between 5 K and 96 K. The signal rapidly decreases with increasing temperature as expected for the giant Zeeman splitting. The temperature dependence of the MCD signal thus represents a strong evidence for the observation of *sp-d* exchange interactions. Simultaneously, the whole spectrum experiences a shift towards lower energies as common for semiconductor bandgaps [76].

Figure 6.6 depicts the temperature dependent decrease of the MCD amplitude for the e_1hh_1-X as well as the e_1hh_3-X. As the MCD signal and thus also the amplitude (A_{MCD}) result from a superposition of a component arising from the giant Zeeman splitting and a contribution from the intrinsic Zeeman splitting, the temperature dependent decay can be described with Equation 6.4, in which $A_{\mathrm{MCD}}^{\mathrm{int}}$ and $A_{\mathrm{MCD}}^{\mathrm{sp-d}}$ denote the intrinsic and sp-d exchange coupling contribution, respectively, and $\widehat{A_{\mathrm{MCD}}^{\mathrm{sp-d}}}$ the hypothetical maximum of

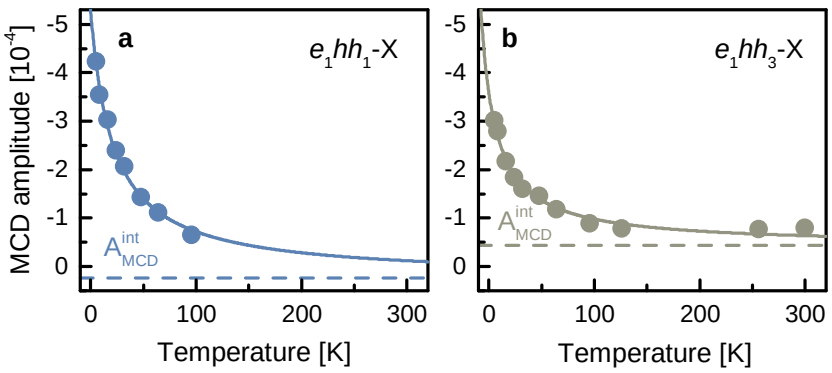

Figure 6.6: Decay of the MCD amplitude for the e_1hh_1-X (a) and e_1hh_3-X (b). Lines represent the Brillouin fits according to Equation 6.4 and dashed lines indicate the MCD contribution from the intrinsic Zeeman splitting. The MCD amplitude is taken as the mean value from the minimum and maximum amplitude of the e_1hh_1-X and the minimum amplitude of the e_1hh_3-X transition. Note that a negative amplitude corresponds to negative Zeeman splitting.

A^{sp-d}_{MCD} in case that all Mn^{2+} were perfectly aligned ($T = 0\,K$ or $B = \infty$). Note that a negative A_{MCD} corresponds to a negative ΔE_Z.

$$A_{MCD} = A^{int}_{MCD} + A^{sp-d}_{MCD} = A^{int}_{MCD} + \widehat{A^{sp-d}_{MCD}} \cdot B_S\left(\frac{g_{Mn}\mu_B SB}{k_B(T+T_{AF})}\right) \tag{6.4}$$

Fitting parameters can be found in Table 6.3. The amplitudes of both transitions can be fitted with the very same Brillouin function (using the same T_{AF} value of 21 K), but weighted with different $\widehat{A^{sp-d}_{MCD}}$ and varying intrinsic contributions A^{int}_{MCD}. This highlights that the MCD signal at low temperatures to the most extend ($\left|\frac{A^{int}_{MCD}}{A_{MCD}}\right| < 17\,\%$ at 5 K for both transitions) arises from the *sp-d* exchange interactions between the band charge carriers and the magnetic moments of the dopants.

Table 6.3: Fitting parameters used to describe the MCD amplitude of the e_1hh_1-X and e_1hh_3-X.

	$\widehat{A^{sp-d}_{MCD}}$ $[10^{-4}]$	$A^{sp-d}_{MCD}(5\,K)$ $[10^{-4}]$	A^{int}_{MCD} $[10^{-4}]$
e_1hh_1-X	−45.7	−4.4	0.24
e_1hh_3-X	−26.1	−2.53	−0.43

At elevated temperatures the MCD signal of the band edge transition vanishes below the signal-to-noise ratio (above 100 K), while the signal related to the excited hole transitions persists up to room temperature (see inset in Figure 6.5). The fits reveal that this behavior originates from a difference in sign of the intrinsic contribution of the Zeeman splitting being positive for the e_1hh_1-X and negative for the e_1hh_3-X transition. It is known that in CdSe the intrinsic Zeeman splitting exhibits the opposite sign as compared to the giant Zeeman effect ($g_{int} = 1$ to 1.4 in CdSe [129, 130]), while in Mn:CdS both

effects have the same sign ($g_{\text{int}} = -1$ to -1.3 in CdS, as estimated from [131]). Because of their architecture, a mixture between both values is expected in the NPs according to the electron and hole wave function distribution between the core and the shell. While both transitions involve the same electron state (e_1), the corresponding hole state changes from hh_1 to hh_3. The different sign of the intrinsic contribution to the Zeeman splitting may thus be originated by a redistribution of the hh wave function from the CdSe core to the CdS shell when going from $n = 1$ to $n = 3$. This is confirmed by the calculated wave function overlap with the shell (estimated by integration of the probability density function over the CdS shell), which increases from 0.24 for the hh_1 ground state to 0.89 and 0.93 for the hh_2 and hh_3 states, respectively.

6.4 Manipulation of the *sp-d* Exchange Interactions via Wave Function Engineering

In the previous sections, direct *sp-d* exchange interactions have been verified for a multitude of excitonic transitions, which could be identified and assigned according to double potential well wave function calculations. Based on these findings, the architectural degrees of freedom provided by the c-ALD synthesis route are exploited to selectively tune either the *s-d* or *p-d* exchange interactions. For this purpose the core and shell thicknesses as well as the composition are modified in order to influence the wave function distribution and thus the overlap with the magnetic dopants.

6.4.1 Manipulation of the *p-d* Exchange Interaction

A first sample series (set I) concentrates on the exchange interactions between the hole states and the Mn^{2+}-dopants. Since the valence band exchange coupling constant $N_0\beta$ excels the conduction band constant $N_0\alpha$ by more than a factor of five, the magneto-optical response is mainly determined by the hole wave function overlap with the doped shell. Since in the CdSe/CdS core/shell hetero-NPs the hh and lh ground states are mainly confined in the core, while the excited states are delocalized into the shell (compare Figure 6.4a), the ground and excited hole states can be addressed selectively. Figure 6.7 depicts the room temperature absorption and the PL spectra of all samples of sample set I. While the dominant absorption peaks distinguishing the transition energies of the e_1hh_1-X and the e_1lh_1-X transition only slightly shift with decreasing shell thickness (red and blue curve), they do exhibit a distinct redshift upon increase of the core thickness (green and blue curve).

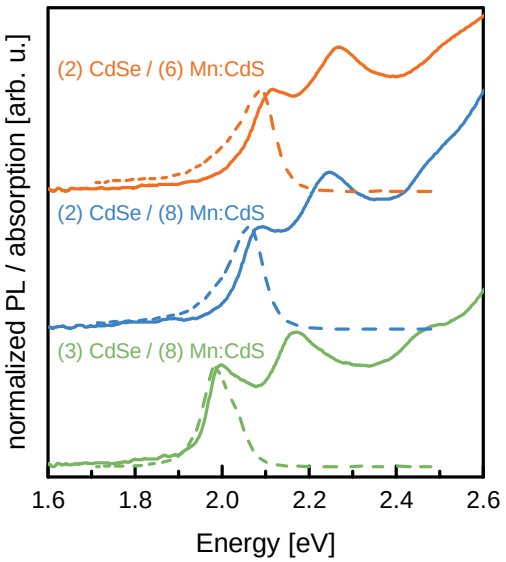

Figure 6.7: Room temperature absorption (solid lines) and PL spectra (dashed lines) of core/shell NP samples with different CdSe core and Mn:CdS shell thicknesses: (3) CdSe/(8) Mn:CdS in green, (2) CdSe/(8) Mn:CdS in blue and (2) CdSe/(6) Mn:CdS in light red.

The influence of the architectural changes on the electronic structure becomes more apparent in the cryogenic MCD spectra. Figure 6.8a depicts the 5 K MCD signals at 1.6 T of NPs with 2 ML CdSe core and 6 ML or 8 ML Mn:CdS shell, respectively. Decreasing the shell thickness shifts the transitions involving excited hole states towards higher energies, while the ground state transitions (especially the e_1hh_1-X and the e_1lh_1-X) are neither affected in energy nor in MCD intensity. These observations are reproduced by the wave function calculations (shown in panel b), illustrating that the ground hh_1 state is expected to be hardly influenced by the shell thickness, while the excited state ($n = 3$) shifts to higher energies in case that the shell thickness is reduced. The wave function overlap for the hh_1 state with the doped shell (given by the probability density), which is decisive for the strength of the *p-d* exchange interaction, is only slightly affected by the shell thickness (compare panel c). This is different in case of the so_1 state, whose wave function overlap with the shell can be calculated to decrease with decreasing shell thickness (compare Figure 6.8c). This is revealed in the experimental data, as no pronounced positive $\mathscr{A}$-term MCD feature is visible at around 2.6 eV for the e_1so_1-X transition in (2) CdSe/(6) Mn:CdS NPs.

The ground state transitions (e_1hh_1-X and e_1lh_1-X) on the other hand can be manipulated modifying the core thickness, as demonstrated in Figure 6.9. In case the core thickness increases, the ground state transitions significantly shift to the red and exhibit strongly decreased MCD amplitudes, while the excited hole transitions reveal only minor changes in both energetic position and intensity. The strong decrease in the magneto-

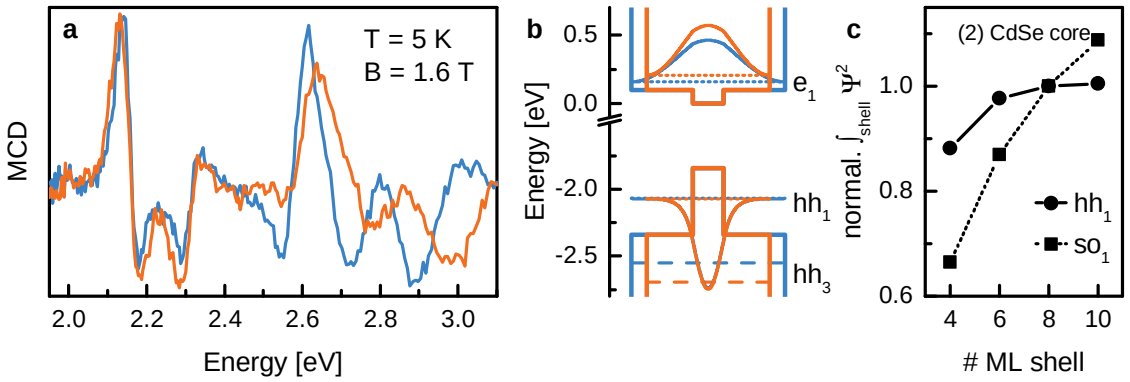

Figure 6.8: Excited state engineering in core/shell NPs. (a) compares the MCD signal of (2) CdSe/(8) Mn:CdS (blue) and (2) CdSe/(6) Mn:CdS (light red) NPs at 5 K and 1.6 T. (b) depicts the electron and hh_1 ground state wave function probability densities as well as ground state (dotted lines) and the hh_3 excited state (dashed lines) energies for the two corresponding NP architectures. In (c) the wave function overlap (i.e., the integrated probability density) for the Mn^{2+}-doped shell is calculated for the hh_1 and so_1 ground state in NPs with 2 ML core and different shell thicknesses, normalized to the value for the (2) CdSe/(8) Mn:CdS sample.

optical response of the band edge transition is due to the decreasing overlap of the hh_1 wave function with the doped region, as apparent from the effective mass calculations shown in panels b and c. The wave function overlap with the shell can be calculated to decrease by $\approx 50\,\%$ from 0.24 to 0.12 for the ground state hh_1, while especially the $n = 3$ excited state, which is widely delocalized among the whole NP, is not affected to the same degree (compare Figure 6.9c).

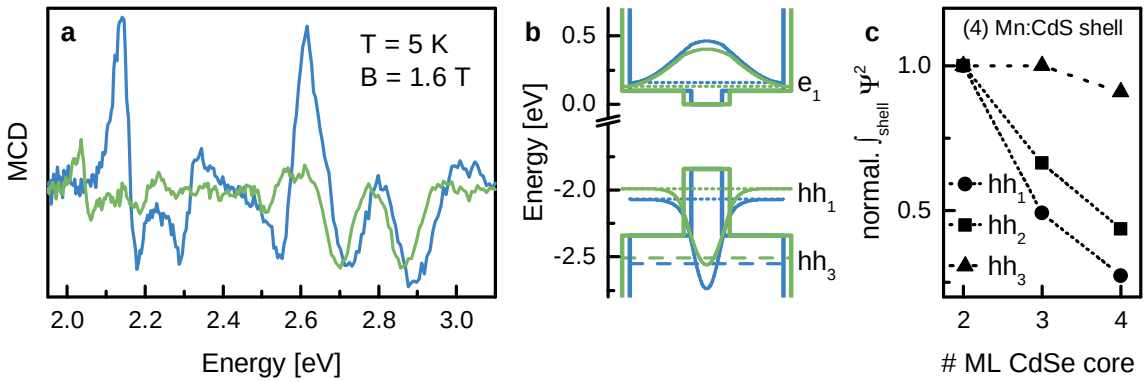

Figure 6.9: Ground state engineering in core/shell NPs. In (a) the 5 K MCD signals of (2) CdSe/(8) Mn:CdS (blue) and (3) CdSe/(8) Mn:CdS (green) at 1.6 T are compared. In (b) the calculated wave function probability densities of the electron and the hh ground states in the corresponding architectures are depicted together with the ground state (dotted lines) and hh_3 (dashed lines) energies. (c) compares the wave function overlap with the Mn^{2+}-doped shell for the ground and excited ($n = 2$ and $n = 3$) hh states in NPs with 2 ML core and different shell thicknesses normalized to the (2) CdSe/(8) Mn:CdS sample.

The CdSe/Mn:CdS core/shell hetero-NPs thus represent a material platform which allows to selectively tune the *p-d* exchange interactions of either the excited hole states by changing the shell thickness or to modify the ground hole state transition via core thickness engineering. However, as the hole exchange coupling interactions significantly exceed the electron contributions and the electron is delocalized among the whole structure, independent of the specific architecture, the *s-d* interactions of the conduction band charge carriers cannot be selectively addressed within these structures.

6.4.2 Manipulation of the *s-d* Interaction

In order to manipulate the *s-d* exchange interaction, the NPs architecture was modified by including an additional MnS interlayer between the core and the shell, which allows to confine the *hh* wave function within the undoped CdSe core. Since MnS, whose bandgap can be extrapolated from CdMnSe to be around 3.6 eV at cryogenic temperatures [88], is epitaxially grown onto the cubic CdSe core via c-ALD, and expected to be formed in zinc blende crystal structure. So-called β-MnS by itself represents a metastable salt [268–270], in which the paramagnetic Mn^{2+} magnetic moments are expected to arrange in an anti-ferromagnetic orientation below a Neel temperature of about 100 K [271].

Figure 6.10 depicts MCD spectra of the samples sharing the same (2) CdSe/(2) MnS core/interlayer structure, but different Mn:CdS shell thicknesses. All optical transitions are shifted towards higher energies in comparison to the NPs of set I due to the increased quantization caused by the high MnS bandgap. With increasing Mn:CdS shell thickness the MCD intensity decreases, while the band edge transition exhibits a small shift to lower energies. Wave function calculations (see panel b) reveal that the MnS interlayer successfully confines the hh_1 state in the undoped core, so that mainly the electron wave function distribution is affected by changes in the Mn:CdS shell thickness. The extracted wave function overlap of the electron and hole with the Mn^{2+}-doped CdS shell on the one hand and the MnS interlayer on the other hand indicates that with increasing shell thickness the electron is redistributed from the interlayer to the shell. Thus, as the MCD intensity decreases with increasing thickness, this suggests that the portion of magneto-optically active Mn^{2+} ions in the interlayer is higher compared to the Mn:CdS shell with $x_{\mathrm{Mn}} = 1.2\,\%$. This allows to conclude that the Mn^{2+} spins in the MnS interlayer in part behave paramagnetic without being antiferromagnetically coupled.

Altogether, it has been demonstrated that by modifying the structural architecture of shell-doped CdSe/Mn:CdS NPs by including a MnS shell, the *s-d* exchange coupling interactions can be tuned, confining the hole into the undoped shell. Without the MnS interlayer, the magneto-optical response related to the *p-d* exchange coupling can be tuned

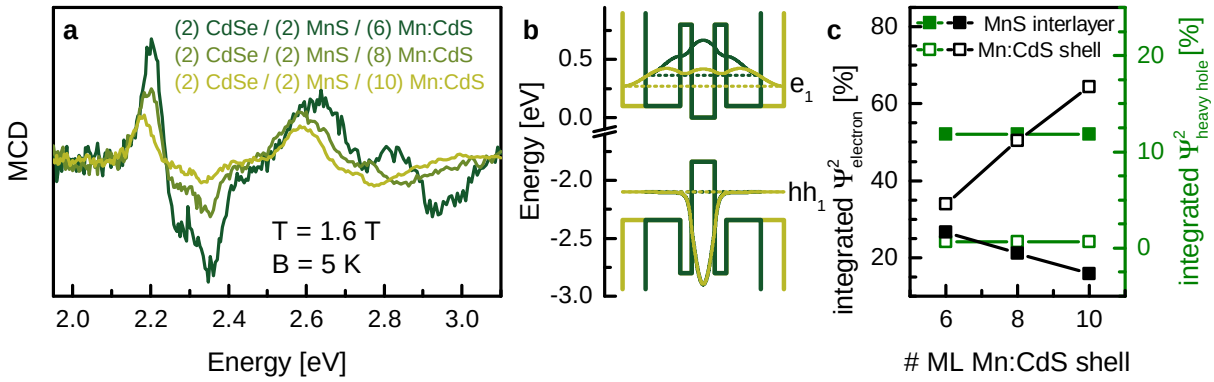

Figure 6.10: *s-d* exchange interaction engineering. (a) MCD signal at 5 K and 1.6 T of NPs with 2 ML CdSe core, 2 ML MnS interlayer and 6 to 10 ML Mn:CdS shell. (b) depicts the energy states and probability density functions of the *hh* and electron ground states in NPs with (2) CdSe/(2) MnS core/interlayer and 6 ML or 8 ML Mn:CdS shell thickness, respectively. The corresponding wave function overlaps (i.e. the integrated probability densities) of the electron (black) and *hh* (green) ground states with the interlayer (filled squares) and the shell (open squares) are shown in (c).

by variation of the CdSe core or Mn:CdS shell thickness. In addition, MCD spectroscopy of the DMS NPs enabled a valuable insight into the excited state electronic structure, which allowed the identification and assignment of a bunch of several higher excitonic states.

Chapter 7

Current-Induced Magnetism in a Colloidal Quantum Dot Device

Electrical control over the magnetization in a material represents the central functionality in lots of today's information processing technologies. Different approaches have been developed to address and manipulate the magnetic properties of metals or semiconductors in electrical devices. Those include current driven processes like spin-polarized currents in random access memories [272, 273] or spin-orbit torques in systems with reduced symmetry [274, 275]. Electric field induced phenomena [276] have been exploited in metallic ferromagnets [277, 278] via electric-field mediated control of the charge carrier concentration in magnetic semiconductors [279, 280] or via coupling of magnetic and electrical properties in multiferroica [281].

However, although these approaches provide the basis for modern lifestyle electronics, they are mostly restricted to thin-film devices prepared by vacuum growth techniques. For next generation electronics, recent developments in the performance of solution-based devices highlight the opportunities offered by solution-processed materials [17, 282] like colloidally synthesized nanostructures [15, 16]. Since the first demonstration of magnetic doping in colloidal nanostructures [19, 20] and proof of *sp-d* exchange interactions in these materials [21, 22], growing research interest in colloidal DMS nanostructures has opened the door for the discovery of several new and fascinating phenomena. Combining strongly increased *sp-d* exchange interactions due to the high dielectric and geometrical quantum confinement with possibilities to be processed in solution - e.g., via spin-coating, printing or spraying even on flexible substrates - these materials represent a promising material class for the development of tomorrow's information processing technologies.

In DMS QDs, few examples demonstrate optical control of the magnetic properties, like charge-controlled magnetism in colloidal Mn:ZnO QDs via optically generated electrons

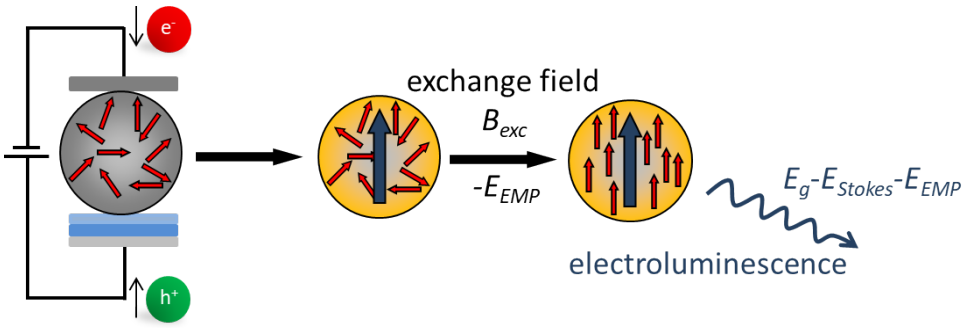

Figure 7.1: Idea of electrically induced magnetism. In the device, the charge carriers are injected via the metal cathode and the ITO anode in combination with the hole injection and transport layers, respectively. Due to the exchange interactions the spins of the Mn^{2+}-dopants align along the magnetic exchange field of the exciton.

[25], photo-induced magnetization in Cu:ZnSe/CdSe QDs [27] or laser induced spontaneous magnetization in Mn:CdSe QDs [23]. The latter, often referred to as excitonic magnetic polaron (EMP), where the spins of the Mn^{2+} ensemble are aligned along the magnetic exchange field of the photo-excited exciton and built an overall magnetization in the QD volume, could be observed even up to room temperature [23]. Although EMPs have been studied in both epitaxial [81–83] as well as colloidal [23, 80, 84] QDs for more than 20 years leading to a profound understanding of the phenomenon, electrical generation of an EMP has not been demonstrated up to now.

Here, a novel approach is presented to induce magnetization by electrical charge carrier injection in Mn^{2+}-doped CdSe/CdS QDs (compare Figure 7.1). For this purpose, the DMS QDs are embedded as active material into a light emitting device structure, which enables charge carrier injection under applied voltage. The electrically injected electrons and holes exhibit *sp-d* exchange coupling with the Mn^{2+} spins, forcing a parallel alignment of the whole spin ensemble of the dopants. This creates an electrically triggered magnetization in the QDs.

As the energetically favorable arrangement of the Mn^{2+} spins lowers the exciton emission energy by the polaron energy E_{EMP}, the polaron formation can be tracked via the EL of the device: With increasing temperature the thermal energy counteracts the ordering force of the exciton, and the degree of orientation among the Mn^{2+} ion spins as well as E_{EMP} decrease, which cause an increase of the excitonic emission energy. This anomalous temperature behavior of the bandgap emission is contradictory to the usually observed Varshni shift. Its observation in EL thus provides a distinct signature of an electrically induced magnetization in the Mn:CdSe/CdS QD device.

The synthesis of the particles used for the device preparation as well as their basic optical characterization have been conducted by Dr. Charles Barrows (doped QDs)

and Christian Erickson (undoped reference) in the group of Prof. Daniel Gamelin at the University of Washington in Seattle, United States.

7.1 Optical Properties of Mn:CdSe/CdS Giant Shell Quantum Dots

For the demonstration of electrically induced EMP formation, magnetically doped Mn:CdSe/CdS giant shell particles were synthesized via diffusion doping. In order to ensure that the band edge governs the emission, particles were realized with a total size of $13.7 \pm 1.2\,\mathrm{nm}$ ($\approx 6\,\mathrm{nm}$ Mn:CdSe core), such that the $1S_{3/2}1S_e$ transition is lower in energy compared to the Mn^{2+} internal $^4T_1 \rightarrow {}^6A_1$ transition. The giant shell consisting of 13 ML CdS is expected to increase the quantum yield of the particles [283] and to improve the device performance [154, 155].

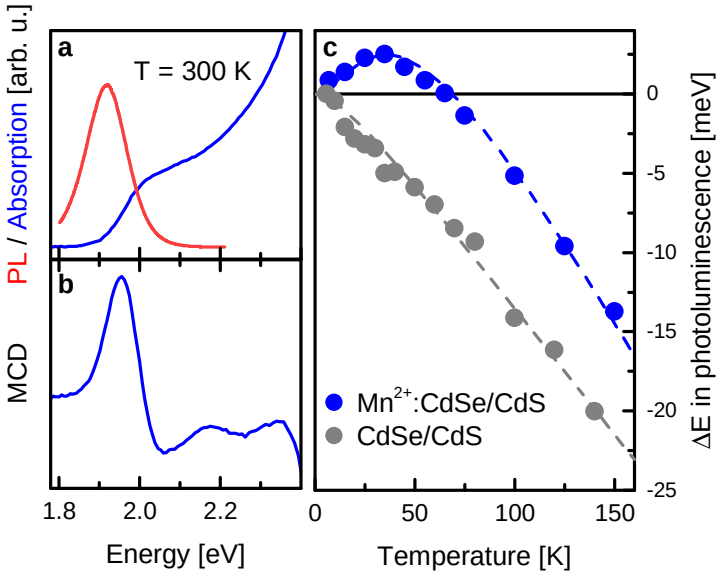

Figure 7.2: (a) and (b) depict the room temperature absorption, PL and MCD spectra (at 1.5 T) of the EMP QDs in a toluene dispersion. In (c) the temperature dependent PL energy revealing an anomalous temperature dependence below 40 K is compared to the dependence for undoped CdSe/CdS reference particles in a device.

Figure 7.2a and b depict the room temperature absorption, PL and MCD spectra of the magnetically doped particles in a toluene dispersion (determined at 1.5 T in an Aviv 40DS spectropolarimeter, all data measured by Dr. Charles Barrows in Seattle). Both absorption edge and PL emission are below 2.1 eV, the typically observed energy for the $^4T_1 \rightarrow {}^6A_1$ transition. The MCD signal exhibiting a pronounced $\mathscr{A}$-feature for the $1S_{3/2}1S_e$ transition reveals an effective g-factor of -7 ± 1. Assuming the *sp-d* exchange coupling of

a *hh*-X bulk transition ($\Delta E_Z \propto (N_0\alpha - N_0\beta)$), which is appropriate for QDs of this size [136], the concentration of magneto-optically active Mn^{2+} ions (i.e. x_{eff}) can be estimated as $1.8 \pm 0.3\,\%$.

In order to exclude that the EMP formation is prohibited by the device environment, i.e., the crosslinker or the hole injection and transport layers, temperature dependent PL measurements are performed on the Mn:CdSe/CdS QDs already embedded in a device structure. Figure 7.2c depicts the temperature dependent shift of the PL transition energies of the doped QDs in comparison to undoped reference particles. The undoped samples consist of a 4 nm CdSe core and a CdS shell with 4.5 nm thickness. The Mn^{2+}-doped QDs show an anomalous blueshift of the PL emission up to 40 K, which is not visible for the undoped reference exhibiting the commonly observed Varshni shift [76].

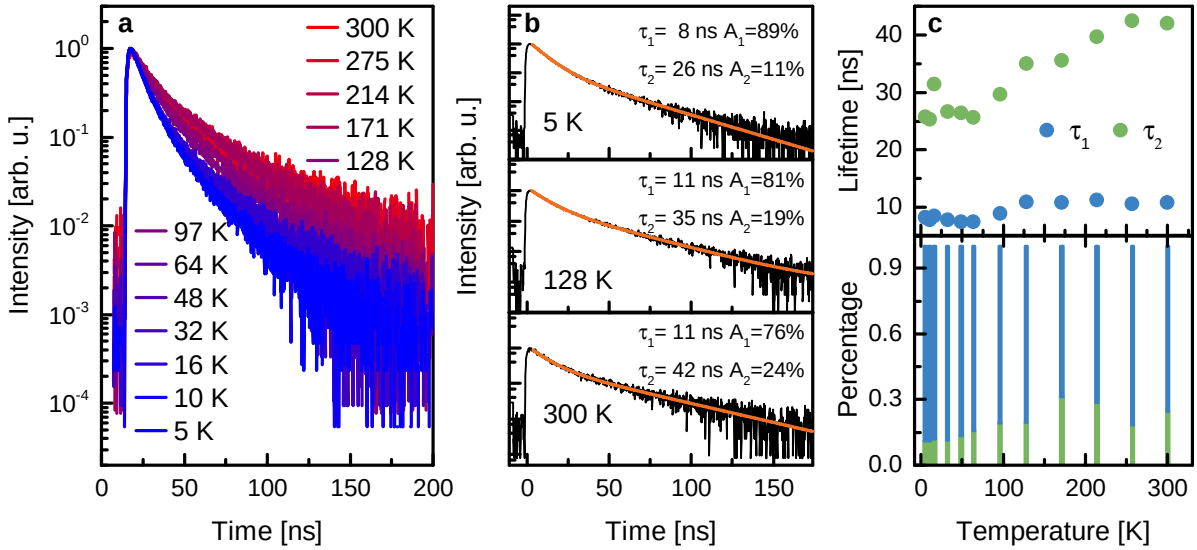

Figure 7.3: Time resolved PL of the EMP QDs. (a) visualizes time traces of the PL at temperatures between 5 K and 300 K. The dynamics are well described with biexponential fits, as shown in panel (b) for 5 K, 127 K and 300 K (fitting parameters are given in the graphs). In (c), the extracted lifetimes (top) and corresponding ratios (bottom) of the short (blue) and long (green) components are recapped for all temperatures.

In principle a blueshift of the emission energy with increasing temperature could also arise from a thermal repopulation between the different fine structure states of the $1S_{3/2}1S_e$ exciton. In case the fine structure splitting exceeds the thermal energy, the energetically lowest and optically forbidden ± 2 state is occupied and visible in PL at low temperatures, while with increasing temperature the $\pm 1^L$ state, which is higher in energy, becomes occupied. However, the fine structure splitting for QDs of this size can be extrapolated as < 0.6 meV [106, 284], suggesting that the bright state is populated even at cryogenic temperatures.

Valuable clues about the nature of emissive states in colloidal QDs - including possible

contribution of dark states - can be gathered from the PL dynamics and their temperature dependence. Figure 7.3a exhibits PL decays of the Mn:CdSe/CdS QDs at temperatures between 5 K to 300 K (obtained with an APD setup with 405 nm excitation wavelength). As commonly observed in CdSe/CdS core/shell structures, the luminescence lifetimes are found to increase with temperature, which can be attributed to the thermally activated redistribution of the electron wave function into the CdS shell, reducing the electron-hole wave function overlap and thus the oscillator strength [151, 285]. The PL decays can be well described with bi-exponential fits with a short component of lifetimes between 8 ns and 11 ns and a longer one with several tens of ns, increasing with temperature, as depicted in panel b and c.

The observed time-resolved PL is not fully consistent with what is expected for neutral excitons in QDs of this size. While in small CdSe QDs, where the dark-bright splitting of the $1S_{3/2}1S_e$ fine structure exceeds the thermal energy, lifetimes of several 100 ns up to μs are observed at cryogenic temperatures [107, 284, 286], for QDs with diameter > 6 nm cryogenic lifetimes of a few tens up to a hundred ns are expected [284]. Shortened cryogenic lifetimes in the range of $\approx$ 20 ns have been observed in colloidal DMS QDs exhibiting EMP formation, and were attributed to a field induced mixing between the dark and bright state by the magnetic exchange field of the EMP [84]. On the other hand, CdSe/CdS giant shell QDs often exhibit recombination of negatively charged excitons, so-called trions, which are characterized by lifetimes of $\approx$ 10 ns [285, 287–289]. As we observe a bi-exponential-decay, it is most likely that in the Mn:CdSe/CdS QDs a mixture between neutral (longer lifetime $>$ 24 ns) and charged excitons ($\approx$ 10 ns component) is present. According to literature, charged excitons are expected in QDs with shell thicknesses above 4 nm to 5 nm [289], and thus the simultaneous observation of neutral and charged excitons appears reasonable in our particles containing a $\approx$ 4 nm CdS shell.

However, as both components are significantly shorter as expected for an optically forbidden recombination, emission from a dark state can be excluded. The observed anomalous temperature development of the emission energy can thus be interpreted as an evidence of laser induced EMP formation in the DMS particles [23]. At cryogenic temperatures, the emission energy is reduced by the polaron energy of the optically induced EMP. With increasing temperatures up to 40 K, the polaron energy decreases, which causes the shift towards higher energies evident in Figure 7.2. At higher temperatures, the shift of the luminescence energy is dominated by the temperature dependent decrease of the bandgap.

7.2 Room Temperature Device Performance

Figure 7.4a depicts a scheme of the device structure utilized to electrically inject charge carriers into the DMS QDs. The layer arrangement is inspired by state-of-the-art solid-state light emitting diodes based on colloidal QDs [170], so-called QD-LEDs, but with the aim to keep the design as simple as possible. The transparent electrode enabling light extraction is represented by an ITO covered glass substrate. In the device, hole injection from the ITO into the active QDs is promoted by PEDOT:PSS and poly-TPD as hole transport and injection layers, while the electrons are provided directly by the silver top electrode (compare energy level diagram in Figure 7.4). The active QD layer is in addition cross-linked with EDT to increase its robustness, although such treatment is unusual for emissive devices such as QD-LEDs [16, 110, 173]. For convenience, no electron transport or injection layers such as ZnO are embedded.

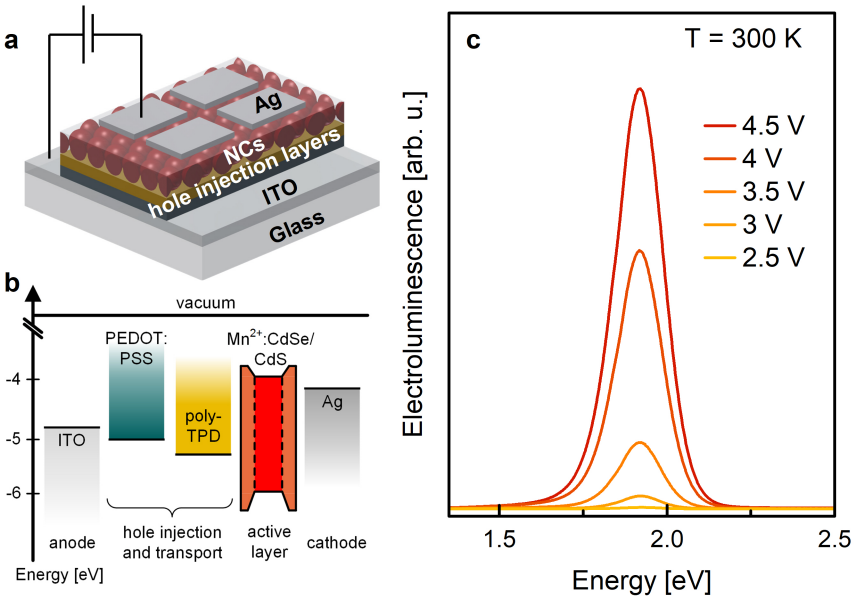

Figure 7.4: Light emitting device based on magnetically doped giant shell QDs. (a) depicts a scheme illustrating the layer assembly in the device. In (b) the corresponding energy levels for the crucial bands are shown as a flat-band energy level diagram. Values are adapted from literature [171]. In (c), room temperature EL spectra at different applied voltages are shown.

Upon application of voltages above 3 V the device emits in the red (compare Figure 7.4c). This evidences successful electron and hole injection into the DMS QDs, which represents the basis for an electrically induced EMP. The EL intensity increases with increasing voltage. The luminescence is comparable to the PL in line width and emission energy and does not significantly shift with increasing voltage. The absence of any further luminescence peaks, e. g., related to recombination in supplementary layers, ensures that all light emitted in the device originates from the QDs.

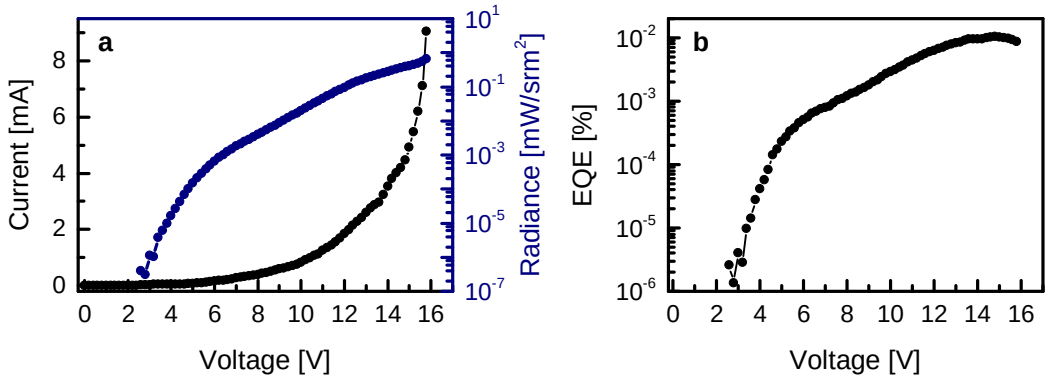

Figure 7.5: (a) Current-voltage characteristics as well as the radiance of a Mn:CdSe/CdS QD device. (b) depicts the corresponding external quantum efficiency (EQE) curve. Note that the EQE measurements have been conducted several months after the EL characterization. Electro-optical figures of merit have been obtained with the help of Svenja Wepfer in the Junior Research Group of Dr. Ekaterina Nannen.

Figure 7.5 depicts the current-voltage characteristics and the external quantum efficiency (EQE) of the EMP device. All figures of merit for the QD-LED have been determined with the help of the Junior Research Group of Dr. Ekaterina Nannen. The opto-electric characterization has been conducted with a Keithley 2601 source meter in combination with a calibrated Si-photodiode (818-UV from Newport). The magnetically doped QD-LED exhibits a non-linear IV curve as expected for a device with an asymmetric layer structure. The QD device emits luminescence starting at $\approx 3\,\mathrm{V}$, which increases in intensity with increasing voltage/current up to $0.65\,\mathrm{mW/srm^2}$. Based on the luminescence and the current, the EQE is extracted, revealing a maximum efficiency of 0.01 %. This performance is comparable to literature values of undoped QD-LED devices with similar design [172], although the EMP device exhibits an active layer treated with EDT. Even though the EMP device is not optimized regarding the "turn-on" bias, luminescence or EQE, its perfomance is comparable to established QD-LEDs, providing the basis for the observation of an electrically induced EMP.

7.3 Evidence of Electrically Induced Excitonic Magnetic Polarons

Following the establishment of Mn:CdSe/CdS QDs as active material in a QD-LED, the realization of temperature dependent EL measurements between cryogenic and room temperature represent a nontrivial task. This challenge was addressed with a home-built sample holder, allowing device integration into a helium cryostate (see Methods and Materials for details).

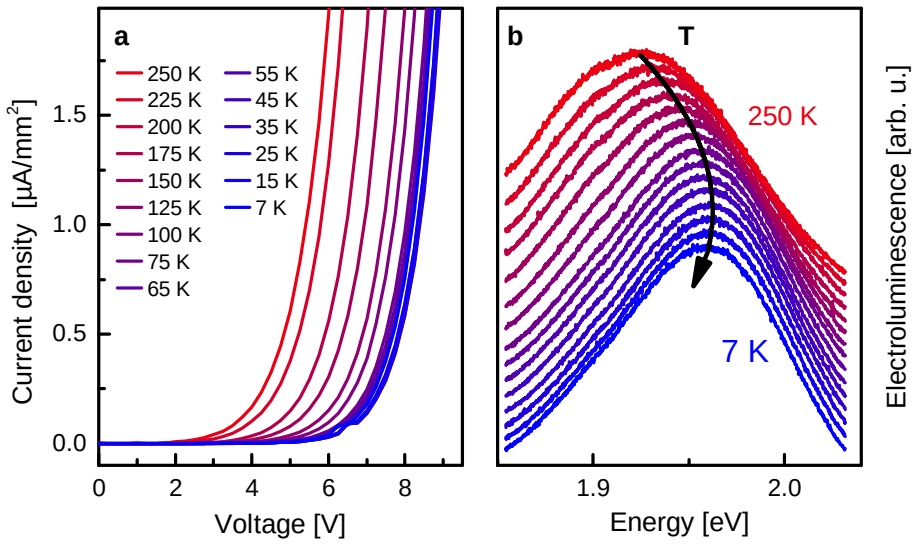

Figure 7.6: Temperature dependent EL measurements of the Mn:CdSe/CdS QD device. Current-voltage characteristic (a) and EL spectra at a constant current of 0.5 mA (b) at different temperatures between 7 K and 250 K. EL spectra are normalized and shifted along the intensity-axis for clarity.

Figure 7.6a depicts the current-voltage characteristics of the EMP device at different temperatures between 7 K and 250 K. The device exhibits stable IV curves throughout the whole temperature range, revealing a shift in the turn-on voltage above 60 K, which may be attributed to the increasing electrical conductivity of the organic layers with temperature [290].

The electrical stability of the EMP device provides the basis for the collection of temperature dependent EL spectra. The intensities of the EL spectra measured at constant currents but different temperatures do not vary by more than a factor of 2.5 in the temperature range considered. This indicates that the QD-LED does not exhibit significant degeneration during the measurements, e.g. caused by the variation of temperature or the extensive operating times necessary to conduct a whole temperature series.

Normalized EL spectra at a constant current of 0.5 mA are shown in Figure 7.6b (shifted along the intensity axis for clarity). Below 40 K the EL in similarity to the PL exhibits a blueshift with increasing temperature, which indicates the existence of an electrically induced EMP in the device. The slight asymmetry revealed in the shape of the EL is attributed to a slow component of the polaron formation, causing a shoulder at the low energy side [80]. Note that the blueshift in EL might in principle also originate from the Quantum-confined Stark effect (QCSE), depending on the applied voltage, which changes with temperature at a constant current. However, in the temperature regime of interest (i.e., 7 K to 75 K) the voltage at constant current does not shift by

more than 0.5 V, as can be seen in Figure 7.6a. The emission energy shift arising from the QCSE can thus be estimated to account for less than 0.5 meV [291] and can be neglected in explaining the anomalous temperature shift of the EL signal in the EMP device.

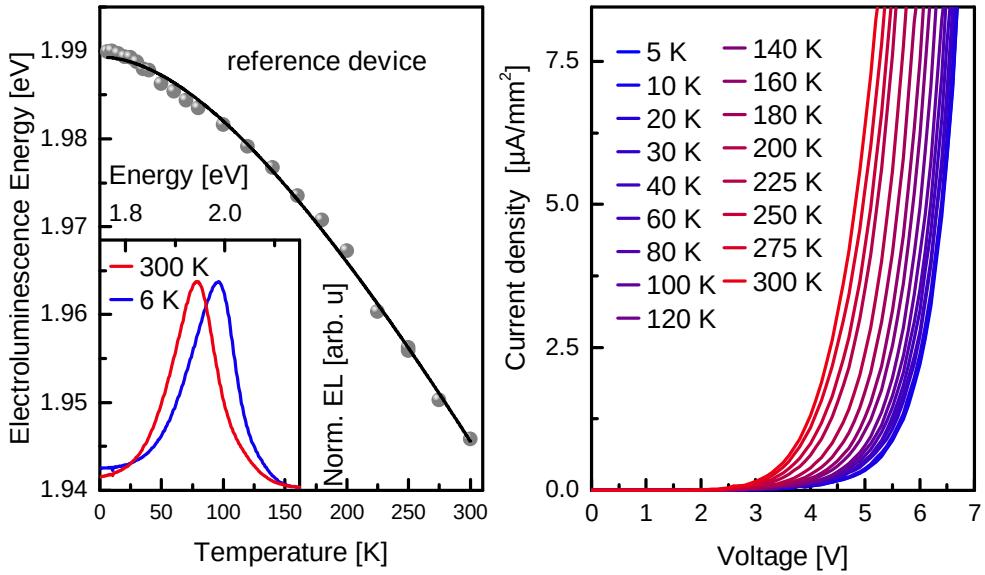

Figure 7.7: Temperature dependent behavior of a reference device with undoped CdSe/CdS giant shell NPs. (a) illustrates the temperature dependent shift of the EL peak energy. The inset compares normalized EL spectra at 6 K and 300 K. The parameters for the Varshni-fit (black line) are $\alpha_V = 2.9 \times 10^{-4}$ eV K^{-1} and $\beta_V = 299$ K. (b) depicts the temperature dependent current-voltage characteristics of the device.

A reference device, prepared with undoped CdSe/CdS giant shell QDs (4 nm core surrounded by 4.5 nm shell, PL shown in Figure 7.2d), exhibits no anomalous temperature behavior. Its EL emission peak energy monotonically shifts red with increasing temperature following the shift observed in PL, as depicted in Figure 7.7. Temperature dependent current-voltage characteristics (panel b) reveal non-linear IV-curves, which shift towards lower turn-on voltages with increasing temperatures as observed for the EMP device. This evidences that the reference device in principle underlies similar temperature induced effects on e.g., the layer conductivities as the EMP device. This underlines that the anomalous temperature behavior observed for the latter is indeed originated by the magnetic doping in the QDs, i.e., it is caused by the EMP formation. This work thus represents a first demonstration of electrically triggered magnetization in a colloidal QD device.

7.4 Polaron Energy and Exchange Field of the Magnetic Polaron

As the polaron energy in magnetically doped Mn:CdSe/CdS QDs is directly reflected in the emission peak energy, the relevant figures of merit of the electrically induced EMP can be deduced from the temperature dependent EL spectra. In undoped colloidal QDs the emission energy E_{emission} follows the absorption energy E_{abs} of the $1S_{3/2}1S_e$ band edge transition lowered by a Stokes shift E_{Stokes}. The Stokes shift, which can be assumed as temperature independent for weakly confined nanocrystals [108, 109], originates from a superposition of the fine structure, inhomogeneous broadening due to the size distribution and the contribution of phonons [106, 109]. In particles exhibiting EMP formation, the emission energy is further reduced by the polaron energy E_{EMP}:

$$E_{\mathrm{emission}}(T) = E_{\mathrm{abs}}(T) - E_{\mathrm{Stokes}} - E_{\mathrm{EMP}}(T) \tag{7.1}$$

The polaron energy E_{EMP} itself is determined by intrinsic properties of the magnetically doped QDs, i.e., the maximum energy gain $E_{\mathrm{EMP}}^{\mathrm{sat}}$ in case the entity of embedded Mn^{2+} ions is aligned parallel to each other, the strength of the magnetic exchange field B_{exc} generated by the exciton (or the hole in case of trions) and the temperature. While $E_{\mathrm{EMP}}^{\mathrm{sat}}$ scales with the concentration of magneto-optically active Mn^{2+} ions x_{eff}, B_{exc} depends on the exciton volume as resulting from the quantization (compare Section 2.4.5).

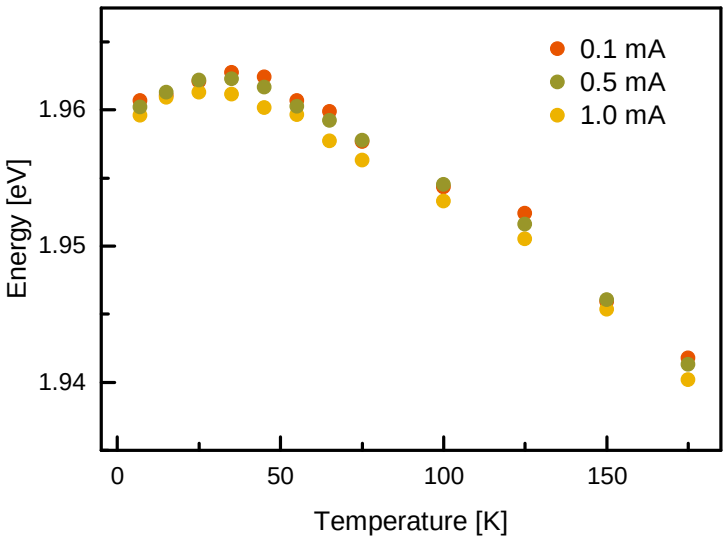

Figure 7.8: Temperature dependent emission energy in EL at different currents.

Extracted $1S_{3/2}1S_e$ peak positions of EL spectra collected at different applied currents are summarized in Figure 7.8. At all currents an anomalous blueshift in the low temperature regime can be found. Above a certain current density, the emission energies at similar

temperatures decrease, and the temperature of the maximum EL energy shifts from 40 K to 25 K for 1 mA. Note that the turning point of the anomalous temperature behavior represents the strength of the polaron formation. The red-shift of the luminescence with increasing current can be either caused by an increasing number of trions contributing to the luminescence, which are known to exhibit a reduced emission energy [285, 288], or due to increasing Joule heating through the electrical current [292]. The existence of charged excitons has been observed in QD-LEDs with unbalanced carrier injection [16]. Thus, for further analysis the spectra determined at a current of 0.5 mA are consulted, combining no detectable decrease of the turn-over temperature with superior signal-to-noise ratios as compared to the lower current data.

Figure 7.9 depicts the EL peak energies measured at a current of 0.5 mA in comparison to the $1S_{3/2}1S_e$ transition energy as determined from absorption. The temperature dependent absorption can be described using Varshnis equation with $\alpha_V = 2.3 \times 10^{-4}\,\mathrm{eV\,K^{-1}}$ and $\beta_V = 47\,\mathrm{K}$. Above 150 K both EL emission and absorption exhibit the same negative slope, which allows the determination of a temperature-independent Stokes shift of $E_{\mathrm{Stokes}} = 32\,\mathrm{meV}$, comparable to Mn:CdSe EMP QDs [80]. According to Equation 7.1 the polaron energy then results from the difference between the absorption Varshni fit reduced by the Stokes shift (visualized by the red line in Figure 7.9) and the EL energy data points.

The extracted polaron energies are plotted against the inverse temperature in Figure 7.9b and can be fitted with Equation 7.2.

$$E_{\mathrm{EMP}} = E_{\mathrm{EMP}}^{\mathrm{sat}} B_S \left(\frac{g_{\mathrm{Mn}} \mu_B S B_{\mathrm{exc}}}{k_B T} \right) \tag{7.2}$$

Herein, the Brillouin function describes the interplay of the magnetic exchange field B_{exc} and the thermal energy. Note that no T_{AF} appears, as antiferromagnetically coupled pairs are assumed to be broken by the high magnetic exchange fields [80]. Based on this fit, a saturation polaron energy of $E_{\mathrm{EMP}}^{\mathrm{sat}} = 14\,\mathrm{meV}$ and a magnetic exchange field of $B_{\mathrm{exc}} = 17\,\mathrm{T}$ can be extracted for the electrically induced polaron in the EMP device.

As elaborated above, the existence of charged excitons cannot be excluded in the Mn:CdSe/CdS QDs. In contrast to a neutral exciton, the exchange interaction of a trion is restricted to the *p-d* component, as both electrons exhibit opposite spins compensating each other. Nevertheless, as $N_0\beta$ strongly exceeds $N_0\alpha$, the exchange coupling for a trion is expected to be only slightly reduced by 15 % compared to a neutral exciton. In current driven devices, the quantity of charged excitons is expected to increase due to unbalanced charge injection [16]. Thus it is assumed, that $E_{\mathrm{EMP}}^{\mathrm{sat}}$ and B_{exc} mainly arise from charged excitons, i.e. only the hole contributes to the exchange coupling. Note that this assumption

is widely spread even for optically induced EMPs [23, 84, 293], usually justified as $N_0\beta$ exceeds $N_0\alpha$ by more than a factor of 5 [8].

In order to compare the electrically induced magnetic exchange field in the Mn:CdSe/CdS core/shell particles to B_{exc} values given in literature for optically excited EMPs in Mn:CdSe QDs, it is useful to extract an effective excitonic radius, i.e. the radius of a CdSe QD exhibiting the same band edge energy. Based on the cryogenic absorption energy of the $1S_{3/2}1S_e$ transition of $\approx 2\,\mathrm{eV}$, the effective exciton radius can be extracted as $\approx 3.6\,\mathrm{nm}$ [34], which implies an inverse exciton volume of $V_{\mathrm{ex}}^{-1} \approx 5 \times 10^{-3}\,\mathrm{nm}^{-3}$. Based on the relation between B_{exc} and V_{ex}^{-1} given in [23], an optically excited magnetic exchange field of 25 T for an exciton and 21 T for a trion can be extrapolated for the Mn:CdSe/CdS QDs, which is in very good agreement with the value achieved electrically.

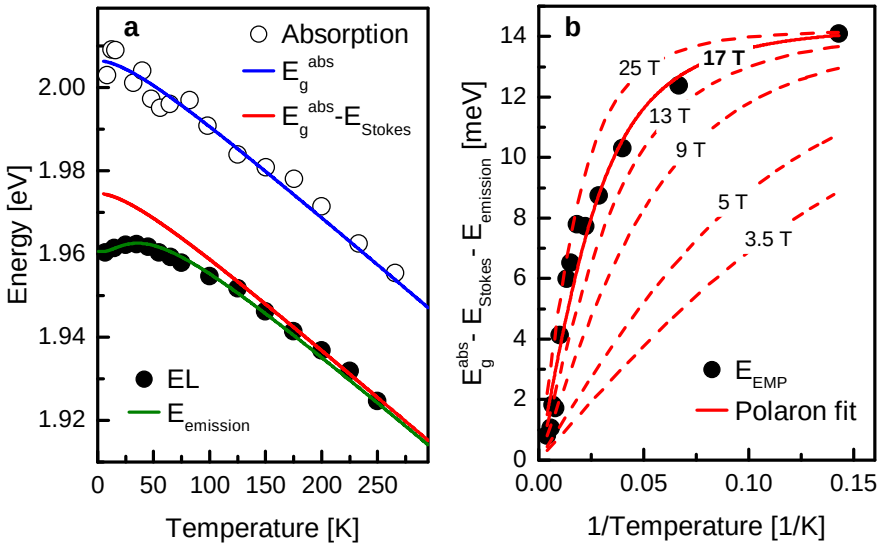

Figure 7.9: Extraction of the polaron energy and magnetic exchange field in the Mn:CdSe/CdS device. In (a) the peak energies in EL are shown together with the absorption of the excitonic transition for temperatures between 7 K to 250 K. The absorption is fit with the Varshni equation (blue line). The polaron energy results from the difference between this fit reduced by a temperature invariant Stokes shift of 32 meV (shown in red) and the data points. A fit to Equation 7.1 is indicated in green. (b) depicts the temperature dependent polaron energies. Symbols depict experimental data, while red lines indicate fits with different magnetic exchange fields.

Even though smaller than record values in colloidal [23] or specific type-II self-assembled QDs [294], the electrically induced magnetic exchange field observed in the EMP device still exceeds fields observed in most epitaxial DMS QDs ($< 3.5\,\mathrm{T}$) [83, 293]. Causing magnetic saturation at low temperatures, the exchange field of 17 T generates an electrically induced polaron energy, which exceeds the thermal energy even up to 65 K.

This work clearly proves that EMP formation in a solid-state device can be electrically triggered. It represents the first demonstration of an electrically induced EMP in

any DMS QDs (colloidal and epitaxial) and moreover the first evidence of electrically addressed magnetization in colloidal nanocrystals. Although in this proof-of-principle device the magnetization is randomly oriented among different particles, further development of the device design may open up various possibilities. As it has been recently shown that a small magnetic field is sufficient to align the EMP in colloidal QDs along a predefined axis [80], introduction of a small local magnetic field, i.e. by a tiny ferromagnetic electrode, is expected to trigger an overall net magnetization among the whole device. In addition, the introduction of an isolating interlayer, either on the cathode or anode side, creates a memory device, which is supposed to yield stable electrically gated magnetism - the next step towards spintronic devices based on colloidal DMS QD. The demonstration of electrically addressed magnetization underlines the unique potential offered by magnetically doped colloidal nanocrystals.

Chapter 8

Summary

In this thesis, the possibilities provided by the colloidal synthesis of diluted magnetic semiconductor (DMS) nanostructures are exploited intending a fundamental understanding of their magneto-optical functionality in the limit of ultimate quantum confinement, and the evaluation of the device perspectives of these novel nanocrystals. Via variation of the nanocrystal size from highly anisotropic nanoplatelets (NPs) to strongly confined spherical magic sized clusters (MSCs), access to the *sp-d* exchange interactions of magnetic ions with both two-dimensional states with strictly defined hole character and the fine structure states of a zero-dimensional electronic structure in the strong confinement regime is gained. In addition, a first proof-of-principle device based on solution-processed DMS quantum dots (QDs) is developed, which demonstrates the ability to electrically trigger a magnetic alignment of the spin sublattice in Mn:CdSe/CdS QDs.

Doping with transition metals (TM) or alloying with isovalent Zn atoms in $(CdSe)_{13}$ allows to investigate the impact of the replacement of one or more of the 26 atoms in MSCs. In Mn^{2+}-doped clusters it can be shown, that the giant magneto-optical activity can be digitally controlled via doping with either one or two Mn^{2+} ions, implying a *Digital Doping* in DMS MSCs. By comparing simulated ratios for clusters containing zero, one and two dopants among a concentration series with extracted values from light desorption/ionization time-of-flight mass spectrometry (LDI-TOF MS), the existence of clusters with three or more dopants can be excluded. The magnitude of the giant Zeeman splitting, as extracted from magnetic circular dichroism (MCD) measurements, is found to follow the ratio of monodoped clusters among a concentration series. This evidences that only clusters containing single dopants contribute to the magneto-optical response, while bidoped clusters are magnetically inactive due to an antiferromagnetic coupling between the Mn^{2+} dopants. In temperature dependent studies the magneto-optical response can be traced up to room temperature, which highlights Mn:$(CdSe)_{13}$ as promising material for

the implementation in future solotronic devices. In case of alloying of the MSCs between $(CdSe)_{13}$ and $(ZnSe)_{13}$, the successful synthesis of undoped clusters is verified by means of LDI-TOF MS measurements. A first evidence of the incorporation of Mn^{2+} ions into the alloy clusters is presented by the room temperature absorption and photoluminescence excitation (PLE) spectra: The PLE signal of the Mn^{2+} internal ligand field transition follows the shape of the absorption, evidencing energy transfer from the band edge to the dopants. Final proof of the magneto-optically active incorporation of the dopants into the clusters, i.e., the successful integration of three different types of cations in a structure consisting in total of only 26 atoms, can be provided via their magneto-optical response, revealing clear fingerprints of *sp-d* exchange interactions. The magnetically doped alloy clusters thus represent a member of the DMS family, whose magneto-optical response can be shifted even up to the high UV range of the spectrum due to the strong quantum confinement in $Mn:(ZnSe)_{13}$. Simulating ensemble MCD spectra a decrease in the MCD amplitude for alloy clusters compared to their pure $Mn:(CdSe)_{13}$ and $Mn:(ZnSe)_{13}$ counterparts can be traced back to the fact that the MCD signals of clusters, differing in the number of Zn atoms by only one or two, partly cancel out each other.

In addition, the impact of the reduced size and the distinct lattice structure of the MSCs on structure related properties is investigated, including the influence on the temperature dependent bandgap shift as well as the structural ability to respond to doping with a foreign atom. Magneto-optical characterization of the band edge transition reveals *sp-d* exchange interactions between band charge carriers and the Co^{2+} ions, evidencing the successful incorporation of Co^{2+} into the $(CdSe)_{13}$ clusters. Based on this, an optical approach is presented allowing an experimental insight into the clusters' lattice structure, i.e., the direct environment of the dopant ions. Room temperature absorption spectra of the Co^{2+} internal ligand field transition exhibit the typical three-fold split spin-orbit fine structure, which indicates Co^{2+} incorporation on a tetrahedrally coordinated lattice site. MCD spectra of this transition at cryogenic temperatures are shifted with respect to conventional Co^{2+}-doped QDs, which is ascribed to significantly shortened Co-anion bond lengths. This shortening can be verified with the aid of extendend X-ray absorption fine structure (EXAFS) measurements.

On the other hand, the impact of the small size with only 26 atoms - whose crystal structure cannot be captured within the formalism used for bulk - on the temperature dependence of the bandgap is studied. For different types of clusters, including undoped $(CdSe)_{13}$, and Mn^{2+}-doped $(CdSe)_{13}$ and $(ZnSe)_{13}$ clusters, the energy shift of the band edge transitions between cryogenic and room temperature is found to be nearly twice as big as in their bulk counterparts. This observation is verified by different optical approaches, including absorption, time-resolved photoluminescence (PL), PLE and MCD

measurements, ensuring the transition energy is monitored for a specific fine structure state. The anomalous strong band shrinkage with temperature is interpreted within a thermodynamic model and traced back to an enhanced exciton formation entropy. This is hypothesized to derive from the strong influence of an optically excited charge carrier pair distributed among the small number of bonds in the $(CdSe)_{13}$ clusters. This process may be assisted by the negative charge transferred from the surrounding organic ligands and the high amount of surface atoms, both expected to decrease the phonon energies.

In magnetically doped colloidal NPs, the synthetic degrees of freedom are used to examine changes in the *sp-d* exchange interactions caused by variations in NPs thickness on an atomic layer scale. Using MCD spectroscopy, clear evidence of *sp-d* exchange interactions between the band charge carriers and the Mn^{2+}-dopants is found in shell-doped CdSe/Mn:CdS NPs. A combination of wave function calculations with a fitting procedure of the excited state MCD signal allows to identify and assign various transitions including ground and excited heavy hole (hh), light hole (lh) and spin-orbit split-off hole (so) states. Thus, Mn^{2+}-doping is shown to enable a valuable insight into the electronic structure of this novel material class. The synthetic degrees of freedom provided by colloidal atomic layer deposition (c-ALD) are used to selectively tune the *s-d* or *p-d* interactions of different transitions. By variation of either the core or the shell thickness in CdSe/Mn:CdS NPs, the magneto-optical response related to either the ground or excited hole states can be manipulated. Upon introduction of an additional MnS interlayer, the ground hh state can be successfully confined in the core, allowing to tune the electron exchange interaction via variation of the Mn:CdS shell thickness.

In order to take the step from materials to devices, the incorporation of colloidal DMS nanostructures into an electrically driven device is demonstrated. For this purpose Mn:CdSe/CdS particles are embedded as active material in a light emitting diode (LED), allowing injection of electrons and holes into the QDs. Temperature dependent electroluminescence (EL) studies are successfully realized and found to exhibit a clear anomalous temperature dependence of the luminescence energy, which represents a fingerprint of the formation of excitonic magnetic polarons (EMPs). This demonstrates that the device allows electrically triggering magnetization in the DMS QDs. Comparison to the temperature dependent absorption allows the extraction of the polaron exchange field and energy, the latter found to excell the thermal energy up to a temperature of 65 K. These findings emphasize the great potential offered by the fascinating material class of magnetically-doped colloidal nanostructures in the field of semiconductor spintronics.

Bibliography

[1] Moore, G. "Cramming More Components onto Integrated Circuits" *Electronics* 38(8), 114–117 (**1965**).

[2] Wolf, S. A. "Spintronics: A Spin-Based Electronics Vision for the Future" *Science* 294(5546), 1488–1495 (**2001**).

[3] Žutić, I., Fabian, J. & Das Sarma, S. "Spintronics: Fundamentals and applications" *Rev. Mod. Phys.* 76(2), 323–410 (**2004**).

[4] Worschech, L., Schmidt, T., Forchel, A., Slobodskyy, T., Schmidt, G. & Molenkamp, L. W. "Optical polarization of semimagnetic CdSe quantum dots with low manganese content" *Semicond. Sci. Technol.* 23(11), 114018 (**2008**).

[5] Binasch, G., Grünberg, P., Saurenbach, F. & Zinn, W. "Enhanced magnetoresistance in layered magnetic structures with antiferromagnetic interlayer exchange" *Phys. Rev. B* 39(7), 4828–4830 (**1989**).

[6] Baibich, M. N., Broto, J. M., Fert, A., Van Dau, F. N., Petroff, F., Etienne, P., Creuzet, G., Friederich, A. & Chazelas, J. "Giant Magnetoresistance of (001)Fe/(001)Cr Magnetic Superlattices" *Phys. Rev. Lett.* 61(21), 2472–2475 (**1988**).

[7] Ohno, H. "Making Nonmagnetic Semiconductors Ferromagnetic" *Science* 281(5379), 951–956 (**1998**).

[8] Gaj, J. & Kossut, J. *Introduction to the Physics of Diluted Magnetic Semiconductors* (Springer, Berlin, Heidelberg, **2011**).

[9] Furdyna, J. K. & Kossut, J. *Diluted Magnetic Semiconductors* vol. 25. *Semiconductors and Semimetals* (Academic Press, Inc., San Diego, **1988**).

[10] Bryan, J. D. & Gamelin, D. R. "Doped Semiconductor Nanocrystals: Synthesis, Characterization, Physical Properties, and Applications" *Progress in Inorganic Chemistry* 54, 47–126 (**2005**).

[11] Beaulac, R., Archer, P. I., Ochsenbein, S. T. & Gamelin, D. R. "Mn^{2+}-Doped CdSe Quantum Dots: New Inorganic Materials for Spin-Electronics and Spin-Photonics" *Adv. Funct. Mater.* 18(24), 3873–3891 (**2008**).

[12] Klimov, V. I. *Nanocrystal Quantum Dots* (CRC Press, Boca Raton, **2010**).

[13] Fainblat, R., Barrows, C. J. & Gamelin, D. R. "Single Magnetic Impurities in Colloidal Quantum Dots and Magic-Size Clusters" *Chemistry of Materials* 29(19), 8023–8036 (**2017**).

[14] Pradhan, N., Das Adhikari, S., Nag, A. & Sarma, D. D. "Luminescence, Plasmonic, and Magnetic Properties of Doped Semiconductor Nanocrystals" *Angew. Chemie - Int. Ed.* 56(25), 7038–7054 (**2017**).

[15] Kovalenko, M. V., Manna, L., Cabot, A., Hens, Z., Talapin, D. V., Kagan, C. R., Klimov, V. I., Rogach, A. L., Reiss, P., Milliron, D. J., Guyot-Sionnest, P., Konstantatos, G., Parak, W. J., Hyeon, T., Korgel, B. A., Murray, C. B. & Heiss, W. "Prospects of Nanoscience with Nanocrystals" *ACS Nano* 9(2), 1012–1057 (**2015**).

[16] Pietryga, J. M., Park, Y.-S., Lim, J., Fidler, A. F., Bae, W. K., Brovelli, S. & Klimov, V. I. "Spectroscopic and Device Aspects of Nanocrystal Quantum Dots" *Chem. Rev.* 116(18), 10513–10622 (**2016**).

[17] Rim, Y. S., Bae, S.-H., Chen, H., De Marco, N. & Yang, Y. "Recent Progress in Materials and Devices toward Printable and Flexible Sensors" *Adv. Mater.* 28(22), 4415–4440 (**2016**).

[18] Huang, Y., Li, W., Qin, M., Zhou, H., Zhang, X., Li, F. & Song, Y. "Printable Functional Chips Based on Nanoparticle Assembly" *Small* 13(4), 1503339 (**2017**).

[19] Bhargava, R. N., Gallagher, D., Hong, X. & Nurmikko, A. "Optical Properties of Manganese-Doped Nanocrystals of ZnS" *Phys. Rev. Lett.* 72(3), 416–419 (**1994**).

[20] Suyver, J. F., Wuister, S. F., Kelly, J. J. & Meijerink, A. "Luminescence of nanocrystalline ZnSe:Mn^{2+}" *Phys. Chem. Chem. Phys.* 2(23), 5445–5448 (**2000**).

[21] Hoffman, D. M., Meyer, B. K., Ekimov, A. I., Merkulov, I. A., Efros, Al. L., Rosen, M., Couino, G., Gacoin, T. & Boilot, J. P. "Giant internal magnetic fields in Mn doped nanocrystal quantum dots" *Solid State Commun.* 114(10), 547–550 (**2000**).

[22] Norris, D. J., Yao, N., Charnock, F. T. & Kennedy, T. A. "High-Quality Manganese-Doped ZnSe Nanocrystals" *Nano Lett.* 1(1), 3–7 (**2001**).

[23] Beaulac, R., Schneider, L., Archer, P. I., Bacher, G. & Gamelin, D. R. "Light-Induced Spontaneous Magnetization in Doped Colloidal Quantum Dots." *Science* 325(5943), 973–6 (**2009**).

[24] Bussian, D. A., Crooker, S. A., Yin, M., Brynda, M., Efros, Al. L. & Klimov, V. I. "Tunable magnetic exchange interactions in manganese-doped inverted core-shell ZnSe-CdSe nanocrystals." *Nat. Mater.* 8(1), 35–40 (**2009**).

[25] Ochsenbein, S. T., Feng, Y., Whitaker, K. M., Badaeva, E., Liu, W. K., Li, X. & Gamelin, D. R. "Charge-controlled magnetism in colloidal doped semiconductor nanocrystals." *Nat. Nanotechnol.* 4(10), 681–687 (**2009**).

[26] Viswanatha, R., Pietryga, J., Klimov, V. I. & Crooker, S. A. "Spin-Polarized Mn^{2+} Emission from Mn-Doped Colloidal Nanocrystals" *Phys. Rev. Lett.* 107(6), 067402 (**2011**).

[27] Pandey, A., Brovelli, S., Viswanatha, R., Li, L., Pietryga, J. M., Klimov, V. I. & Crooker, S. A. "Long-lived photoinduced magnetization in copper-doped ZnSe–CdSe core–shell nanocrystals" *Nat. Nanotechnol.* 7(12), 792–797 (**2012**).

[28] Rice, W. D., Liu, W., Baker, T. A., Sinitsyn, N. A., Klimov, V. I. & Crooker, S. A. "Revealing giant internal magnetic fields due to spin fluctuations in magnetically doped colloidal nanocrystals" *Nat. Nanotechnol.* 11(2), 137–142 (**2016**).

[29] Yu, J. H., Liu, X., Kweon, K. E., Joo, J., Park, J., Ko, K.-T., Lee, D. W., Shen, S., Tivakornsasithorn, K., Son, J. S., Park, J.-H., Kim, Y.-W., Hwang, G. S., Dobrowolska, M., Furdyna, J. K. & Hyeon, T. "Giant Zeeman splitting in nucleation-controlled doped CdSe:Mn^{2+} quantum nanoribbons" *Nat. Mater.* 9(1), 47–53 (**2010**).

[30] Vlaskin, V. A., Barrows, C. J., Erickson, C. S. & Gamelin, D. R. "Nanocrystal Diffusion Doping" *J. Am. Chem. Soc.* 135(38), 14380–14389 (**2013**).

[31] Yang, J., Fainblat, R., Kwon, S. G., Muckel, F., Yu, J. H., Terlinden, H., Kim, B. H., Iavarone, D., Choi, M. K., Kim, I. Y., Park, I., Hong, H.-K., Lee, J., Son, J. S., Lee, Z., Kang, K., Hwang, S.-J., Bacher, G. & Hyeon, T. "Route to the Smallest Doped Semiconductor: Mn^{2+}-Doped $(CdSe)_{13}$ Clusters" *J. Am. Chem. Soc.* 137(40), 12776–12779 (**2015**).

[32] Delikanli, S., Akgul, M. Z., Murphy, J. R., Barman, B., Tsai, Y., Scrace, T., Zhang, P., Bozok, B., Hernández-Martínez, P. L., Christodoulides, J., Cartwright, A. N., Petrou, A. & Demir, H. V. "Mn^{2+}-Doped CdSe/CdS Core/Multishell Colloidal Quantum Wells Enabling Tunable Carrier-Dopant Exchange Interactions" *ACS Nano* 9(12), 12473–12479 (**2015**).

[33] Ekimov, A. I., Hache, F., Schanne-Klein, M. C., Ricard, D., Flytzanis, C., Kudryavtsev, I. A., Yazeva, T. V., Rodina, A. V. & Efros, Al. L. "Absorption and intensity-dependent photoluminescence measurements on CdSe quantum dots: assignment of the first electronic transitions" *J. Opt. Soc. Am. B* 10(1), 100–107 (**1993**).

[34] Norris, D. & Bawendi, M. "Measurement and assignment of the size-dependent optical spectrum in CdSe quantum dots." *Phys. Rev. B* 53(24), 16338–16346 (**1996**).

[35] Ithurria, S., Tessier, M. D., Mahler, B., Lobo, R. P. S. M., Dubertret, B. & Efros, Al. L. "Colloidal nanoplatelets with two-dimensional electronic structure" *Nat. Mater.* 10(12), 936–941 (**2011**).

[36] Liu, Y.-H., Wayman, V. L., Gibbons, P. C., Loomis, R. A. & Buhro, W. E. "Origin of High Photoluminescence Efficiencies in CdSe Quantum Belts" *Nano Lett.* 10(1), 352–357 (**2010**).

[37] Fainblat, R., Frohleiks, J., Muckel, F., Yu, J. H., Yang, J., Hyeon, T. & Bacher, G. "Quantum Confinement-Controlled Exchange Coupling in Manganese(II)-Doped CdSe Two-Dimensional Quantum Well Nanoribbons" *Nano Lett.* 12(10), 5311–5317 (**2012**).

[38] Fainblat, R., Muckel, F., Barrows, C. J., Vlaskin, V. A., Gamelin, D. R. & Bacher, G. "Valence-Band Mixing Effects in the Upper-Excited-State Magneto-Optical Re-

sponses of Colloidal Mn^{2+}-Doped CdSe Quantum Dots" *ACS Nano* 8(12), 12669–12675 (**2014**).

[39] Vlaskin, V. A., Beaulac, R. & Gamelin, D. R. "Dopant-Carrier Magnetic Exchange Coupling in Colloidal Inverted Core/Shell Semiconductor Nanocrystals" *Nano Letters* 9(12), 4376–4382 (**2009**).

[40] Bouet, C., Tessier, M. D., Ithurria, S., Mahler, B., Nadal, B. & Dubertret, B. "Flat Colloidal Semiconductor Nanoplatelets" *Chem. Mater.* 25(8), 1262–1271 (**2013**).

[41] Wang, F., Wang, Y., Liu, Y.-H., Morrison, P. J., Loomis, R. A. & Buhro, W. E. "Two-Dimensional Semiconductor Nanocrystals: Properties, Templated Formation, and Magic-Size Nanocluster Intermediates" *Acc. Chem. Res.* 48(1), 13–21 (**2015**).

[42] Lhuillier, E., Pedetti, S., Ithurria, S., Nadal, B., Heuclin, H. & Dubertret, B. "Two-Dimensional Colloidal Metal Chalcogenides Semiconductors: Synthesis, Spectroscopy, and Applications" *Acc. Chem. Res.* 48(1), 22–30 (**2015**).

[43] Nasilowski, M., Mahler, B., Lhuillier, E., Ithurria, S. & Dubertret, B. "Two-Dimensional Colloidal Nanocrystals" *Chem. Rev.* 116(18), 10934–10982 (**2016**).

[44] Kormilina, T. K., Cherevkov, S. A., Fedorov, A. V. & Baranov, A. V. "Cadmium Chalcogenide Nano-Heteroplatelets: Creating Advanced Nanostructured Materials by Shell Growth, Substitution, and Attachment" *Small* 13(41), 1702300 (**2017**).

[45] Ithurria, S. & Talapin, D. V. "Colloidal Atomic Layer Deposition (c-ALD) using Self-Limiting Reactions at Nanocrystal Surface Coupled to Phase Transfer between Polar and Nonpolar Media" *J. Am. Chem. Soc.* 134(45), 18585–18590 (**2012**).

[46] Thomson, J. W., Nagashima, K., Macdonald, P. M. & Ozin, G. A. "From Sulfur-Amine Solutions to Metal Sulfide Nanocrystals: Peering into the Oleylamine-Sulfur Black Box" *J. Am. Chem. Soc.* 133(13), 5036–5041 (**2011**).

[47] Tessier, M. D., Spinicelli, P., Dupont, D., Patriarche, G., Ithurria, S. & Dubertret, B. "Efficient Exciton Concentrators Built from Colloidal Core/Crown CdSe/CdS Semiconductor Nanoplatelets" *Nano Letters* 14(1), 207–213 (**2014**).

[48] Prudnikau, A., Chuvilin, A. & Artemyev, M. "CdSe-CdS Nanoheteroplatelets with Efficient Photoexcitation of Central CdSe Region through Epitaxially Grown CdS Wings" *J. Am. Chem. Soc.* 135(39), 14476–14479 (**2013**).

[49] Murphy, J. R., Delikanli, S., Scrace, T., Zhang, P., Norden, T., Thomay, T., Cartwright, A. N., Demir, H. V. & Petrou, A. "Time-resolved photoluminescence study of CdSe/CdMnS/CdS core/multi-shell nanoplatelets" *Appl. Phys. Lett.* 108(24), 242406 (**2016**).

[50] Erwin, S. C., Zu, L., Haftel, M. I., Efros, Al. L., Kennedy, T. A. & Norris, D. J. "Doping semiconductor nanocrystals." *Nature* 436(7047), 91–4 (**2005**).

[51] Norris, D. J., Efros, Al. L. & Erwin, S. C. "Doped Nanocrystals" *Science* 319(5871), 1776–1779 (**2008**).

[52] Kasuya, A., Sivamohan, R., Barnakov, Y. A., Dmitruk, I. M., Nirasawa, T., Romanyuk, V. R., Kumar, V., Mamykin, S. V., Tohji, K., Jeyadevan, B., Shinoda,

K., Kudo, T., Terasaki, O., Liu, Z., Belosludov, R. V., Sundararajan, V. & Kawazoe, Y. "Ultra-stable nanoparticles of CdSe revealed from mass spectrometry" *Nat. Mater.* 3(2), 99–102 (**2004**).

[53] Kudera, S., Zanella, M., Giannini, C., Rizzo, A., Li, Y., Gigli, G., Cingolani, R., Ciccarella, G., Spahl, W., Parak, W. J. & Manna, L. "Sequential Growth of Magic-Size CdSe Nanocrystals" *Adv. Mater.* 19(4), 548–552 (**2007**).

[54] Wang, Y., Liu, Y.-H., Zhang, Y., Wang, F., Kowalski, P. J., Rohrs, H. W., Loomis, R. A., Gross, M. L. & Buhro, W. E. "Isolation of the Magic-Size CdSe Nanoclusters $[(CdSe)_{13}$(n-octylamine)$_{13}]$ and $[(CdSe)_{13}$(oleylamine)$_{13}]$" *Angew. Chemie - Int. Ed.* 51(25), 6154–6157 (**2012**).

[55] Gary, D. C., Terban, M. W., Billinge, S. J. L. & Cossairt, B. M. "Two-Step Nucleation and Growth of InP Quantum Dots via Magic-Sized Cluster Intermediates" *Chem. Mater.* 27(4), 1432–1441 (**2015**).

[56] Wang, Y., Zhou, Y., Zhang, Y. & Buhro, W. E. "Magic-Size II-VI Nanoclusters as Synthons for Flat Colloidal Nanocrystals" *Inorg. Chem.* 54(3), 1165–1177 (**2015**).

[57] Joo, J., Son, J. S., Kwon, S. G., Yu, J. H. & Hyeon, T. "Low-temperature solution-phase synthesis of quantum well structured CdSe nanoribbons." *J. Am. Chem. Soc.* 128(17), 5632–3 (**2006**).

[58] Liu, Y.-H., Wang, F., Wang, Y., Gibbons, P. C. & Buhro, W. E. "Lamellar Assembly of Cadmium Selenide Nanoclusters into Quantum Belts" *J. Am. Chem. Soc.* 133(42), 17005–17013 (**2011**).

[59] Yang, J., Muckel, F., Baek, W., Fainblat, R., Chang, H., Bacher, G. & Hyeon, T. "Chemical Synthesis, Doping, and Transformation of Magic-Sized Semiconductor Alloy Nanoclusters" *J. Am. Chem. Soc.* 139(19), 6761–6770 (**2017**).

[60] Gaj, J., Planel, R. & Fishman, G. "Relation of magneto-optical properties of free excitons to spin alignment of Mn^{2+} ions in $Cd_{1-x}Mn_xTe$" *Solid State Commun.* 29(5), 435–438 (**1979**).

[61] Larson, B., Hass, K., Ehrenreich, H. & Carlsson, A. "Exchange mechanisms in diluted magnetic semiconductors" *Solid State Commun.* 56(4), 347–350 (**1985**).

[62] Koenraad, P. M. & Flatté, M. E. "Single dopants in semiconductors." *Nat. Mater.* 10(2), 91–100 (**2011**).

[63] Fernández Rossier, J. "Single-atom devices: Quantum engineering" *Nat. Mater.* 12(6), 480–481 (**2013**).

[64] Del Ben, M., Havenith, R. W. A., Broer, R. & Stener, M. "Density Functional Study on the Morphology and Photoabsorption of CdSe Nanoclusters" *J. Phys. Chem. C* 115(34), 16782–16796 (**2011**).

[65] Yang, P., Tretiak, S. & Ivanov, S. "Influence of Surfactants and Charges on CdSe Quantum Dots" *J. Clust. Sci.* 22(3), 405–431 (**2011**).

[66] Azpiroz, J. M., Matxain, J. M., Infante, I., Lopez, X. & Ugalde, J. M. "A DFT/TDDFT study on the optoelectronic properties of the amine-capped magic $(CdSe)_{13}$ nanocluster." *Phys. Chem. Chem. Phys.* 15(26), 10996–11005 (**2013**).

[67] Gao, Y., Zhou, B., Kang, S.-G., Xin, M., Yang, P., Dai, X., Wang, Z. & Zhou, R. "Effect of ligands on the characteristics of $(CdSe)_{13}$ quantum dots" *RSC Adv.* 4(52), 27146–27151 (**2014**).

[68] Cui, Y., Lou, Z., Wang, X., Yu, S. & Yang, M. "A study of optical absorption of cysteine-capped CdSe nanoclusters using first-principles calculations" *Phys. Chem. Chem. Phys.* 17(14), 9222–9230 (**2015**).

[69] Sun, J., Zheng, X., He, H., Chen, X., Dong, B. & Fei, R. "Theoretical study of ligand and solvent effects on optical properties and stabilities of CdSe nanoclusters" *J. Mol. Struct.* 1114, 123–131 (**2016**).

[70] Figgis, B. & Hitchman, M. A. *Ligand Field Theory and Its Applications* (Wiley, New York, **2000**).

[71] Archer, P. I., Santangelo, S. A. & Gamelin, D. R. "Inorganic Cluster Syntheses of TM^{2+}-Doped Quantum Dots (CdSe, CdS, CdSe/CdS): Physical Property Dependence on Dopant Locale" *J. Am. Chem. Soc.* 129(31), 9808–9818 (**2007**).

[72] Radovanovic, P. V. & Gamelin, D. R. "Electronic Absorption Spectroscopy of Cobalt Ions in Diluted Magnetic Semiconductor Quantum Dots: Demonstration of an Isocrystalline Core/Shell Synthetic Method" *J. Am. Chem. Soc.* 123(49), 12207–12214 (**2001**).

[73] Eichhöfer, A., Lan, Y., Mereacre, V., Bodenstein, T. & Weigend, F. "Slow Magnetic Relaxation in Trigonal-Planar Mononuclear Fe(II) and Co(II) Bis(trimethylsilyl)amido Complexes-A Comparative Study" *Inorg. Chem.* 53(4), 1962–1974 (**2014**).

[74] Pittala, S., Mortelliti, M. J., Kato, F. & Kittilstved, K. R. "Substitution of Co^{2+} ions into CdS-based molecular clusters" *Chem. Commun.* 51(51), 17096–17099 (**1709**).

[75] Santangelo, S. A., Hinds, E. A., Vlaskin, V. A., Archer, P. I. & Gamelin, D. R. "Bimodal Bond-Length Distributions in Cobalt-Doped CdSe, ZnSe, and $Cd_{1-x}Zn_xSe$ Quantum Dots" *J. Am. Chem. Soc.* 129(13), 3973–3978 (**2007**).

[76] Varshni, Y. "Temperature dependence of the energy gap in semiconductors" *Physica* 34(1), 149–154 (**1967**).

[77] O'Donnell, K. P. & Chen, X. "Temperature dependence of semiconductor band gaps" *Appl. Phys. Lett.* 58(25), 2924–2926 (**1991**).

[78] Van Vechten, J. A. & Wautelet, M. "Variation of semiconductor band gaps with lattice temperature and with carrier temperature when these are not equal" *Phys. Rev. B* 23(10), 5543–5550 (**1981**).

[79] Heine, V. & Van Vechten, J. A. "Effect of electron-hole pairs on phonon frequencies in Si related to temperature dependence of band gaps" *Phys. Rev. B* 13(4), 1622–1626 (**1976**).

[80] Nelson, H. D., Bradshaw, L. R., Barrows, C. J., Vlaskin, V. A. & Gamelin, D. R. "Picosecond Dynamics of Excitonic Magnetic Polarons in Colloidal Diffusion-Doped $Cd_{1-x}Mn_xSe$ Quantum Dots" *ACS Nano* 9(11), 11177–11191 (**2015**).

[81] Oka, Y., Shen, J., Takabayashi, K., Takahashi, N., Mitsu, H., Souma, I. & Pittini, R. "Dynamics of excitonic magnetic polarons in nanostructure diluted magnetic semiconductors" *J. Lumin.* 83-84, 83–89 (**1999**).

[82] Seufert, J., Bacher, G., Scheibner, M., Forchel, A., Lee, S., Dobrowolska, M. & Furdyna, J. K. "Dynamical Spin Response in Semimagnetic Quantum Dots" *Phys. Rev. Lett.* 88(2), 027402 (**2002**).

[83] Kłopotowski, Ł., Cywiński, Ł., Wojnar, P., Voliotis, V., Fronc, K., Kazimierczuk, T., Golnik, A., Ravaro, M., Grousson, R., Karczewski, G. & Wojtowicz, T. "Magnetic polaron formation and exciton spin relaxation in single $Cd_{1-x}Mn_xTe$ quantum dots" *Phys. Rev. B* 83(8), 081306 (**2011**).

[84] Rice, W. D., Liu, W., Pinchetti, V., Yakovlev, D. R., Klimov, V. I. & Crooker, S. A. "Direct Measurements of Magnetic Polarons in $Cd_{1-x}Mn_xSe$ Nanocrystals from Resonant Photoluminescence" *Nano Lett.* 17(5), 3068–3075 (**2017**).

[85] Phillips, J. C. & Van Vechten, J. A. "Dielectric Classification of Crystal Structures, Ionization Potentials, and Band Structures" *Phys. Rev. Lett.* 22(14), 705–708 (**1969**).

[86] Wepfer, S. Courtesy of Svenja Wepfer. **2017**

[87] Adachi, S. *Properties of Group-IV, III-V and II-VI Semiconductors* (John Wiley & Sons, Chichester, UK, **2005**).

[88] Furdyna, J. K. "Diluted magnetic semiconductors" *J. Appl. Phys.* 64(4), R29–R64 (**1988**).

[89] Hernández-Calderón, I. "Optical properties and electronic structure of wide band gap II-VI semiconductors" in *II-VI Semiconductor Matererials and their Applications* (Tamargo, M.) chap. 4 (Taylor and Francis, New York, **2002**).

[90] Pajaczkowska, A. "Physicochemical properties and crystal growth of $A^{II}B^{VI}$-MnB^{VI} systems" *Prog. Cryst. Growth Charact.* 1(3), 289–326 (**1978**).

[91] Rockett, A. *The Materials Science of Semiconductors* (Springer, Boston, US, **2008**).

[92] Vegard, L. "Die Konstitution der Mischkristalle und die Raumfüllung der Atome" *Zeitschrift für Phys.* 5(1), 17–26 (**1921**).

[93] Van Vechten, J. A. & Bergstresser, T. K. "Electronic Structures of Semiconductor Alloys" *Phys. Rev. B* 1(8), 3351–3358 (**1970**).

[94] Pässler, R. "Dispersion-related description of temperature dependencies of band gaps in semiconductors" *Phys. Rev. B* 66(8), 085201 (**2002**).

[95] Pässler, R. "Moderate phonon dispersion shown by the temperature dependence of fundamental band gaps of various elemental and binary semiconductors including wide-band gap materials" *J. Appl. Phys.* 88(5), 2570–2577 (**2000**).

[96] Davies, J. H. *The Physics of Low-Dimensional Semiconductors* (Cambridge University Press, Cambridge, **1997**).

[97] Schäfer, W. & Wegener, M. *Semiconductor Optics and Transport Phenomena* (Springer Berlin Heidelberg, Berlin, Heidelberg, **2002**).

[98] Ralph, H. "The electronic absorption edge in layer type crystals" *Solid State Commun.* 3(10), 303–306 (**1965**).

[99] Bugajski, M. & Regiński, K. "Optical properties of semiconductor quantum wells" *Opto-Electr. Rev.* 3/4(4), 83–100 (**1996**).

[100] Scott, R., Heckmann, J., Prudnikau, A. V., Antanovich, A., Mikhailov, A., Owschimikow, N., Artemyev, M., Climente, J. I., Woggon, U., Grosse, N. B. & Achtstein, A. W. "Directed emission of CdSe nanoplatelets originating from strongly anisotropic 2D electronic structure" *Nat. Nanotechnol.* 12(12), 1155–1160 (**2017**).

[101] Van Kesteren, H. W., Cosman, E. C., Greidanus, F. J. A. M., Dawson, P., Moore, K. J. & Foxon, C. T. "Optically Detected Magnetic Resonance Study of a Type-II GaAs-AlAs Multiple Quantum Well" *Phys. Rev. Lett.* 61(1), 129–132 (**1988**).

[102] Van Kesteren, H. W., Cosman, E. C., van der Poel, W. A. J. A. & Foxon, C. T. "Fine structure of excitons in type-II GaAs/AlAs quantum wells" *Phys. Rev. B* 41(8), 5283–5292 (**1990**).

[103] Blackwood, E., Snelling, M. J., Harley, R. T., Andrews, S. R. & Foxon, C. T. B. "Exchange interaction of excitons in GaAs heterostructures" *Phys. Rev. B* 50(19), 14246–14254 (**1994**).

[104] Gammon, D., Snow, E. S., Shanabrook, B. V., Katzer, D. S. & Park, D. "Fine Structure Splitting in the Optical Spectra of Single GaAs Quantum Dots" *Phys. Rev. Lett.* 76(16), 3005–3008 (**1996**).

[105] Brus, L. "Electronic wave functions in semiconductor clusters: experiment and theory" *J. Phys. Chem.* 90(12), 2555–2560 (**1986**).

[106] Efros, Al. L., Rosen, M., Kuno, M., Nirmal, M., Norris, D. & Bawendi, M. "Band-edge exciton in quantum dots of semiconductors with a degenerate valence band: Dark and bright exciton states" *Phys. Rev. B* 54(7), 4843–4856 (**1996**).

[107] Crooker, S. A., Barrick, T., Hollingsworth, J. A. & Klimov, V. I. "Multiple temperature regimes of radiative decay in CdSe nanocrystal quantum dots: Intrinsic limits to the dark-exciton lifetime" *Appl. Phys. Lett.* 82(17), 2793–2795 (**2003**).

[108] Kuno, M., Lee, J. K., Dabbousi, B. O., Mikulec, F. V. & Bawendi, M. G. "The band edge luminescence of surface modified CdSe nanocrystallites: Probing the luminescing state" *J. Chem. Phys.* 106(23), 9869–9882 (**1997**).

[109] Liptay, T. J., Marshall, L. F., Rao, P. S., Ram, R. J. & Bawendi, M. G. "Anomalous Stokes shift in CdSe nanocrystals" *Phys. Rev. B* 76(15), 155314 (**2007**).

[110] Bozyigit, D., Yazdani, N., Yarema, M., Yarema, O., Lin, W. M. M., Volk, S., Vuttivorakulchai, K., Luisier, M., Juranyi, F. & Wood, V. "Soft surfaces of nanomaterials enable strong phonon interactions" *Nature* 531(7596), 618–622 (**2016**).

[111] Nguyen, K. A., Day, P. N. & Pachter, R. "Understanding structural and optical properties of nanoscale CdSe magic-size quantum dots: Insight from computational prediction" *J. Phys. Chem. C* 114(39), 16197–16209 (**2010**).

[112] Harrison, W. A. *Electronic Structure and the Properties of Solids: The Physics of Chemical Bonds* (W.H. Freeman and Company, San Francisco, **1980**).

[113] Lorenz, S. personal communication. **2017**

[114] Bethe, H. "Termaufspaltung in Kristallen" *Ann. Phys.* 395(2), 133–208 (**1929**).

[115] Eyring, H., Walter, J. & Kimball, G. E. *Quantum Chemistry* (Wiley, New York, **1944**).

[116] Lancashire, R. L. *Tanabe-Sugano diagrams via spreadsheets* Department of Chemistry, University of West Indies, Jamaica. `http://wwwchem.uwimona.edu.jm/courses/Tanabe-Sugano/TSspread.html` (07/24/2017).

[117] Fano, U. & Racah, G. *Irreducible tensorial sets* (Academic Press, Oxford, **1959**).

[118] Tanabe, Y. & Sugano, S. "On the absorption spectra of complex ions. I" *J. Phys. Soc. Japan* 9(5), 753–766 (**1954**).

[119] Langer, D. W. & Richter, H. J. "Zero-Phonon Lines and Phonon Coupling of ZnSe:Mn and CdS:Mn" *Phys. Rev.* 146(2), 554–557 (**1966**).

[120] Dreyhsig, J. & Litzenburger, B. "Nature of optical transitions in the charge-transfer region of ZnS:Co and ZnSe:Co." *Phys. Rev. B* 54(15), 10516–10524 (**1996**).

[121] Langer, J. M. & Baranowski, J. M. "Optical Properties of Transition Metal Impurities in CdSe. I. Crystal-Field Spectra" *Phys. Status Solidi* 44(1), 155–166 (**1971**).

[122] Pappalardo, R. & Dietz, R. E. "Absorption Spectra of Transition Ions in CdS Crystals" *Phys. Rev.* 123(4), 1188–1203 (**1961**).

[123] Weakliem, H. A. "Optical Spectra of Ni^{2+}, Co^{2+}, and Cu^{2+} in Tetrahedral Sites in Crystals" *J. Chem. Phys.* 36(8), 2117–2140 (**1962**).

[124] Boulanger, D., Parrot, R. & Cherfi, Z. "Cluster model for radiative transition probabilities of d^5 ions in tetrahedralsymmetry: Case of Mn^{2+} in the common cation series ZnS, ZnSe, and ZnTe" *Phys. Rev. B* 70(7), 075209 (**2004**).

[125] Schwartz, D. A., Norberg, N. S., Nguyen, Q. P., Parker, J. M. & Gamelin, D. R. "Magnetic Quantum Dots: Synthesis, Spectroscopy, and Magnetism of Co^{2+}- and Ni^{2+}-Doped ZnO Nanocrystals" *J. Am. Chem. Soc.* 125(43), 13205–13218 (**2003**).

[126] Norberg, N. S., Parks, G. L., Salley, G. M. & Gamelin, D. R. "Giant Excitonic Zeeman Splittings in Colloidal Co^{2+}-doped ZnSe Quantum Dots" *J. Am. Chem. Soc.* 128(6), 13195–13203 (**2006**).

[127] Archer, P. I., Santangelo, S. A. & Gamelin, D. R. "Direct Observation of sp-d Exchange Interactions in Colloidal Mn^{2+}- and Co^{2+}-Doped CdSe Quantum Dots." *Nano Lett.* 7(4), 1037–1043 (**2007**).

[128] Luttinger, J. M. "Quantum Theory of Cyclotron Resonance in Semiconductors-General Theory" *Phys. Rev.* 102(4), 1030–1041 (**1956**).

[129] Barrows, C. J., Fainblat, R. & Gamelin, D. R. "Excitonic Zeeman splittings in colloidal CdSe quantum dots doped with single magnetic impurities" *J. Mater. Chem. C* 5, 5232–5238 (**2017**).

[130] Kuno, M., Nirmal, M., Bawendi, M. G., Efros, Al. L. & Rosen, M. "Magnetic circular dichroism study of CdSe quantum dots" *J. Chem. Phys.* 108(10), 4242–4247 (**1998**).

[131] Taguchi, S., Ishizumi, A., Tayagaki, T. & Kanemitsu, Y. "Mn-Mn couplings in Mn-doped CdS nanocrystals studied by magnetic circular dichroism spectroscopy" *Appl. Phys. Lett.* 94(17), 173101 (**2009**).

[132] Gennser, U., Liu, X. C., Vu, T. Q., Heiman, D., Fries, T., Shapira, Y., Demianiuk, M. & Twardowski, A. "Exchange energies, bound magnetic polarons, and magnetization in CdSe:Co and CdS:Co" *Phys. Rev. B* 51(15), 9606–9611 (**1995**).

[133] Larson, B. E., Hass, K. C., Ehrenreich, H. & Carlsson, A. E. "Theory of exchange interactions and chemical trends in diluted magnetic semiconductors" *Phys. Rev. B* 37(8), 4137–4154 (**1988**).

[134] Gaj, J. "Semimagnetic Semiconductors" in *Comprehensive Semiconductor Science and Technology - Vol. 2: Physics and Fundamental Theory* (Bhattacharya, B., Fornari, R. & Kamimura, H.) 95–124 (Elsevier, **2011**).

[135] Bhattacharjee, A., Fishman, G. & Coqblin, B. "Virtual bound state model for the exchange interaction in semimagnetic semiconductors such as $Cd_{1-x}Mn_xTe$" *Phys. B+C* 117-118, 449–451 (**1983**).

[136] Beaulac, R., Feng, Y., May, J., Badaeva, E., Gamelin, D. & Li, X. "Orbital pathways for Mn^{2+}-carrier sp-d exchange in diluted magnetic semiconductor quantum dots" *Phys. Rev. B* 84(19), 195324 (**2011**).

[137] Lee, Y., Ramdas, A. & Aggarwal, R. "Energy gap, excitonic, and "internal" Mn^{2+} optical transition in Mn-based II-VI diluted magnetic semiconductors" *Phys. Rev. B* 38(15), 10600–10610 (**1988**).

[138] Twardowski, A., Dietl, T. & Demianiuk, M. "The study of the s-d type exchange interaction in $Zn_{1-x}Mn_xSe$ mixed crystals" *Solid State Commun.* 48(10), 845–848 (**1983**).

[139] Twardowski, A., Swiderski, P., von Ortenberg, M. & Pauthenet, R. "Magnetoabsorption and magnetization of $Zn_{1-x}Mn_xTe$ mixed crystals" *Solid State Commun.* 50(6), 509–513 (**1984**).

[140] Twardowski, A., Pokita, E. & Gaj, J. A. "Valence band spin-orbit splitting in CdTe and $Cd_{1-x}Mn_xTe$ and giant zeeman effect in the Γ7 band of $Cd_{1-x}Mn_xTe$" *Solid State Commun.* 36(11), 927–930 (**1980**).

[141] Kuhn-Heinrich, B., Ossau, W., Bangert, E., Waag, A. & Landwehr, G. "Zeeman pattern of semimagnetic (CdMn)Te/(CdMg)Te quantum wells in inplane magnetic fields" *Solid State Commun.* 91(6), 413–418 (**1994**).

[142] Kuhn-Heinrich, B. *Magneto-optische Untersuchungen semimagnetischer Schichtstruckturen auf der Basis von $Cd_{1-x}Mn_xTe$* PhD thesis (Julius-Maximilian Universität, Würzburg, **1995**).

[143] Bhattacharjee, A. K. "Confinement-induced reduction of the effective exchange parameters in semimagnetic semiconductor nanostructures" *Phys. Rev. B* 58(23), 15660–15665 (**1998**).

[144] Mackh, G., Ossau, W., Waag, A. & Landwehr, G. "Effect of the reduction of dimensionality on the exchange parameters in semimagnetic semiconductors" *Phys. Rev. B* 54(8), R5227–R5230 (**1996**).

[145] Schimpf, A. M. & Gamelin, D. R. "Thermal Tuning and Inversion of Excitonic Zeeman Splittings in Colloidal Doped CdSe Quantum Dots" *J. Phys. Chem. Lett.* 3(10), 1264–1268 (**2012**).

[146] Merkulov, I., Yakovlev, D., Keller, A., Ossau, W., Geurts, J., Waag, A., Landwehr, G., Karczewski, G., Wojtowicz, T. & Kossut, J. "Kinetic Exchange between the Conduction Band Electrons and Magnetic Ions in Quantum-Confined Structures" *Phys. Rev. Lett.* 83(7), 1431–1434 (**1999**).

[147] Aggarwal, R. L., Jasperson, S. N., Stankiewicz, J., Shapira, Y., Foner, S., Khazai, B. & Wold, A. "Magnetoreflectance at the band edge in $Cd_{1-x}Mn_xSe$" *Phys. Rev. B* 28(12), 6907–6913 (**1983**).

[148] Arciszewska, M. & Nawrocki, M. "Determination of the band structure parameters of $Cd_{0.95}Mn_{0.05}Se$ from magnetoabsorption measurements" *J. Phys. Chem. Solids* 47(3), 309–314 (**1986**).

[149] Yu, W. Y., Twardowski, A., Fu, L. P., Petrou, A. & Jonker, B. T. "Magnetoanisotropy in $Zn_{1-x}Mn_xSe$ strained epilayers" *Phys. Rev. B* 51(15), 9722–9727 (**1995**).

[150] Kavokin, K. V., Merkulov, I. A., Yakovlev, D. R., Ossau, W. & Landwehr, G. "Exciton localization in semimagnetic semiconductors probed by magnetic polarons" *Phys. Rev. B* 60(24), 16499–16505 (**1999**).

[151] Christodoulou, S., Vaccaro, G., Pinchetti, V., De Donato, F., Grim, J. Q., Casu, A., Genovese, A., Vicidomini, G., Diaspro, A., Brovelli, S., Manna, L. & Moreels, I. "Synthesis of highly luminescent wurtzite CdSe/CdS giant-shell nanocrystals using a fast continuous injection route" *J. Mater. Chem. C* 2, 3439–3447 (**2014**).

[152] Chen, Y., Vela, J., Htoon, H., Casson, J. L., Werder, D. J., Bussian, D. A., Klimov, V. I. & Hollingsworth, J. A. ""Giant" Multishell CdSe Nanocrystal Quantum Dots with Suppressed Blinking" *J. Am. Chem. Soc.* 130(15), 5026–5027 (**2008**).

[153] Mahler, B., Spinicelli, P., Buil, S., Quelin, X., Hermier, J.-P. & Dubertret, B. "Towards non-blinking colloidal quantum dots" *Nat. Mater.* 7(8), 659–664 (**2008**).

[154] Lim, J., Jeong, B. G., Park, M., Kim, J. K., Pietryga, J. M., Park, Y. S., Klimov, V. I., Lee, C., Lee, D. C. & Bae, W. K. "Influence of Shell Thickness on the Performance of Light-Emitting Devices based on $CdSe/Zn_{1-x}Cd_xS$ Core/Shell Heterostructured Quantum Dots" *Adv. Mater.* 26(47), 8034–8040 (**2014**).

[155] Pal, B. N., Ghosh, Y., Brovelli, S., Laocharoensuk, R., Klimov, V. I., Hollingsworth, J. A. & Htoon, H. "'Giant' CdSe/CdS Core/Shell Nanocrystal Quantum Dots As Efficient Electroluminescent Materials: Strong Influence of Shell Thickness on Light-Emitting Diode Performance" *Nano Lett.* 12(1), 331–336 (**2012**).

[156] Barrows, C. J., Chakraborty, P., Kornowske, L. M. & Gamelin, D. R. "Tuning Equilibrium Compositions in Colloidal $Cd_{1-x}Mn_xSe$ Nanocrystals Using Diffusion Doping and Cation Exchange" *ACS Nano* 10(1), 910–918 (**2016**).

[157] Muckel, F., Barrows, C. J., Graf, A., Schmitz, A., Erickson, C. S., Gamelin, D. R. & Bacher, G. "Current-Induced Magnetic Polarons in a Colloidal Quantum-Dot Device" *Nano Letters* 17(8), 4768–4773 (**2017**).

[158] Qu, L. & Peng, X. "Control of Photoluminescence Properties of CdSe Nanocrystals in Growth." *J. Am. Chem. Soc.* 124(9), 2049–2055 (**2002**).

[159] Coropceanu, I. & Bawendi, M. G. "Core/Shell Quantum Dot Based Luminescent Solar Concentrators with Reduced Reabsorption and Enhanced Efficiency" *Nano Lett.* 14(7), 4097–4101 (**2014**).

[160] Wang, Y., Liu, Y.-H., Zhang, Y., Kowalski, P. J., Rohrs, H. W. & Buhro, W. E. "Preparation of Primary Amine Derivatives of the Magic-Size Nanocluster $(CdSe)_{13}$" *Inorg. Chem.* 52(6), 2933–2938 (**2013**).

[161] Son, J. S., Wen, X.-D., Joo, J., Chae, J., Baek, S., Park, K., Kim, J. H., An, K., Yu, J. H., Kwon, S. G., Choi, S.-H., Wang, Z., Kim, Y.-W., Kuk, Y., Hoffmann, R. & Hyeon, T. "Large-Scale Soft Colloidal Template Synthesis of 1.4 nm Thick CdSe Nanosheets" *Angew. Chemie - Int. Ed.* 48(37), 6861–6864 (**2009**).

[162] Wang, Y., Zhang, Y., Wang, F., Giblin, D. E., Hoy, J., Rohrs, H. W., Loomis, R. A. & Buhro, W. E. "The Magic-Size Nanocluster $(CdSe)_{34}$ as a Low-Temperature Nucleant for Cadmium Selenide Nanocrystals; Room-Temperature Growth of Crystalline Quantum Platelets" *Chem. Mater.* 26(7), 2233–2243 (**2014**).

[163] Riedinger, A., Ott, F. D., Mule, A., Mazzotti, S., Knüsel, P. N., Kress, S. J., Prins, F., Erwin, S. C. & Norris, D. J. "An intrinsic growth instability in isotropic materials leads to quasi-two-dimensional nanoplatelets" *Nat. Mater.* 16(7), 743–748 (**2017**).

[164] Hines, M. A. & Guyot-Sionnest, P. "Synthesis and Characterization of Strongly Luminescing ZnS-Capped CdSe Nanocrystals" *J. Phys. Chem.* 100(2), 468–471 (**1996**).

[165] Fainblat, R. *Spin-Spin-Wechselwirkung an magnetisch dotierten kolloidalen Halbleiter-Nanostrukturen* PhD thesis (Universität Duisburg-Essen, **2015**).

[166] Gefahrstoffinformationssystem der Deutschen Gesetzlichen Unfallversicherung. *GESTIS-Stoffdatenbank*

[167] Guzelturk, B., Erdem, O., Olutas, M., Kelestemur, Y. & Demir, H. V. "Stacking in Colloidal Nanoplatelets: Tuning Excitonic Properties" *ACS Nano* 8(12), 12524–12533 (**2014**).

[168] Jana, S., Phan, T. N. T., Bouet, C., Tessier, M. D., Davidson, P., Dubertret, B. & Abécassis, B. "Stacking and Colloidal Stability of CdSe Nanoplatelets" *Langmuir* 31(38), 10532–10539 (**2015**).

[169] Guzelturk, B., Olutas, M., Delikanli, S., Kelestemur, Y., Erdem, O. & Demir, H. V. "Nonradiative energy transfer in colloidal CdSe nanoplatelet films." *Nanoscale* 7(6), 2545–2551 (**2015**).

[170] Shang, Y. & Ning, Z. "Colloidal quantum dots surface and device structure engineering for high performance light emitting diodes" *Natl. Sci. Rev.* 4(2), 170–183 (**2017**).

[171] Dai, X., Zhang, Z., Jin, Y., Niu, Y., Cao, H., Liang, X., Chen, L., Wang, J. & Peng, X. "Solution-processed, high-performance light-emitting diodes based on quantum dots" *Nature* 515(7525), 96–99 (**2014**).

[172] Shirasaki, Y., Supran, G. J., Bawendi, M. G. & Bulović, V. "Emergence of colloidal quantum-dot light-emitting technologies" *Nat. Photonics* 7(1), 13–23 (**2012**).

[173] Choi, J. J., Lim, Y.-F., Santiago-Berrios, M. B., Oh, M., Hyun, B.-R., Sun, L., Bartnik, A. C., Goedhart, A., Malliaras, G. G., Abruña, H. D., Wise, F. W. & Hanrath, T. "PbSe Nanocrystal Excitonic Solar Cells" *Nano Lett.* 9(11), 3749–3755 (**2009**).

[174] Piepho, S. B. & Schatz, P. N. *Group Theory in Spectroscopy with Applications to Magnetic Circular Dichroism* (Wiley, New York, **1983**).

[175] Mason, W. R. *A Practical Guide to Magnetic Circular Dichroism Spectroscopy* (John Wiley & Sons, Inc., Hoboken, NJ, USA, **2007**).

[176] Hohage, P. E. *Dynamik, Transport und Manipulation kohärenter Spinzustände in Halbleiter- Hybridsystemen* PhD thesis (Universität Duisburg-Essen, **2012**).

[177] Shapira, Y., Foner, S., Ridgley, D. H., Dwight, K. & Wold, A. "Technical saturation and magnetization steps in diluted magnetic semiconductors: Predictions and observations" *Phys. Rev. B* 30(7), 4021–4023 (**1984**).

[178] Gaj, J. A., Grieshaber, W., Bodin-Deshayes, C., Cibert, J., Feuillet, G., Merle d'Aubigné, Y. & Wasiela, A. "Magneto-optical study of interface mixing in the CdTe-(Cd,Mn)Te system" *Phys. Rev. B* 50(8), 5512–5527 (**1994**).

[179] Fatah, J. M., Piorek, T., Harrison, P., Stirner, T. & Hagston, W. E. "Numerical simulation of antiferromagnetic spin-pairing effects in diluted magnetic semiconductors and enhanced paramagnetism at interfaces" *Phys. Rev. B* 49(15), 10341–10344 (**1994**).

[180] Kobak, J., Smoleński, T., Goryca, M., Papaj, M., Gietka, K., Bogucki, A., Koperski, M., Rousset, J.-G., Suffczyński, J., Janik, E., Nawrocki, M., Golnik, A., Kossacki, P. & Pacuski, W. "Designing quantum dots for solotronics" *Nat. Commun.* 5, 3191 (**2014**).

[181] Fainblat, R., Barrows, C. J., Hopmann, E., Siebeneicher, S., Vlaskin, V. A., Gamelin, D. R. & Bacher, G. "Giant Excitonic Exchange Splittings at Zero Field

in Single Colloidal CdSe Quantum Dots Doped with Individual Mn^{2+} Impurities" *Nano Lett.* 16(10), 6371–6377 (**2016**).

[182] *Springer Handbook of Condensed Matter and Materials Data* (Martienssen, W. & Warlimont, H.) (Springer Verlag, Berlin Heidelberg, **2005**).

[183] Park, K. M., Bae, Y. J., Ahn, S. H. & Kim, M. S. "A Simple Method for Quantification of Peptides and Proteins by Matrix-Assisted Laser Desorption Ionization Mass Spectrometry" *Anal. Chem.* 84(23), 10332–10337 (**2012**).

[184] Park, K. M., Moon, J. H., Kim, K. P., Lee, S. H. & Kim, M. S. "Relative Quantification in Imaging of a Peptide on a Mouse Brain Tissue by Matrix-Assisted Laser Desorption Ionization" *Anal. Chem.* 86(10), 5131–5135 (**2014**).

[185] Heiman, D., Shapira, Y., Foner, S., Khazai, B., Kershaw, R., Dwight, K. & Wold, A. "Exchange energy, magnetization, and Raman scattering of (Cd,Mn)Se" *Phys. Rev. B* 29(10), 5634–5640 (**1984**).

[186] Keller, D., Yakovlev, D. R., König, B., Ossau, W., Gruber, T., Waag, A., Molenkamp, L. W. & Scherbakov, A. V. "Heating of the magnetic ion system in (Zn, Mn)Se/(Zn, Be)Se semimagnetic quantum wells by means of photoexcitation" *Phys. Rev. B* 65(3), 035313 (**2001**).

[187] König, B., Merkulov, I. A., Yakovlev, D. R., Ossau, W., Ryabchenko, S. M., Kutrowski, M., Wojtowicz, T., Karczewski, G. & Kossut, J. "Energy transfer from photocarriers into the magnetic ion system mediated by a two-dimensional electron gas in (Cd,Mn)Te/(Cd, Mg)Te quantum wells" 61(24), 870–882 (**2000**).

[188] Kneip, M., Yakovlev, D., Bayer, M., Maksimov, A., Tartakovskii, I., Keller, D., Ossau, W., Molenkamp, L. & Waag, A. "Spin-lattice relaxation of Mn ions in ZnMnSe/ZnBeSe quantum wells measured under pulsed photoexcitation" *Phys. Rev. B* 73(4), 045305 (**2006**).

[189] Kneip, M., Yakovlev, D., Bayer, M., Maksimov, A., Tartakovskii, I., Keller, D., Ossau, W., Molenkamp, L. & Waag, A. "Direct energy transfer from photocarriers to Mn-ion system in II-VI diluted-magnetic-semiconductor quantum wells" *Phys. Rev. B* 73(3), 035306 (**2006**).

[190] Gui, Y. S., Becker, C. R., Liu, J., König, M., Daumer, V., Kiselev, M. N., Buhmann, H. & Molenkamp, L. W. "Current heating of a magnetic two-dimensional electron gas in $Hg_{1-x}Mn_xTe/Hg_{0.3}Cd_{0.7}Te$ quantum wells" *Phys. Rev. B* 70(19), 195328 (**2004**).

[191] Besombes, L., Léger, Y., Maingault, L., Ferrand, D., Mariette, H. & Cibert, J. "Probing the Spin State of a Single Magnetic Ion in an Individual Quantum Dot" *Phys. Rev. Lett.* 93(20), 207403 (**2004**).

[192] Lifshitz, E., Vaxenburg, R., Maikov, G. I., Rubin-Brusilovski, A., Yanover, D., Tilchin, J. & Sashchiuk, A. "The Influence of Alloy Composition on the Electronic Properties of IV-VI Core/Shell Colloidal Heterostructures" *Isr. J. Chem.* 52(11-12), 1037–1052 (**2012**).

[193] Lim, B., Yu, T. & Xia, Y. "Shaping a bright future for platinum-based alloy electrocatalysts" *Angew. Chemie - Int. Ed.* 49(51), 9819–9820 (**2010**).

[194] Regulacio, M. D. & Han, M.-Y. "Composition-Tunable Alloyed Semiconductor Nanocrystals" *Acc. Chem. Res.* 43(5), 621–630 (**2010**).

[195] Ferrando, R., Jellinek, J. & Johnston, R. L. "Nanoalloys: From Theory to Applications of Alloy Clusters and Nanoparticles" *Chem. Rev.* 108(3), 845–910 (**2008**).

[196] Zhang, B., Zheng, X., Voznyy, O., Comin, R., Bajdich, M., Garcia-Melchor, M., Han, L., Xu, J., Liu, M., Zheng, L., Garcia de Arquer, F. P., Dinh, C. T., Fan, F., Yuan, M., Yassitepe, E., Chen, N., Regier, T., Liu, P., Li, Y., De Luna, P., Janmohamed, A., Xin, H. L., Yang, H., Vojvodic, A. & Sargent, E. H. "Homogeneously dispersed multimetal oxygen-evolving catalysts" *Science* 352(6283), 333–337 (**2016**).

[197] Sun, S., Murray, C. B., Weller, D., Folks, L. & Moser, A. "Monodisperse FePt Nanoparticles and Ferromagnetic FePt Nanocrystal Superlattices" *Science* 287(5460), 1989–1992 (**2000**).

[198] Muckel, F., Yang, J., Lorenz, S., Baek, W., Chang, H., Hyeon, T., Bacher, G. & Fainblat, R. "Digital Doping in Magic-Sized CdSe Clusters" *ACS Nano* 10(7), 7135–7141 (**2016**).

[199] Kim, Y. D., Klein, M. V., Ren, S. F., Chang, Y. C., Luo, H., Samarth, N. & Furdyna, J. K. "Optical properties of zinc-blende CdSe and $Zn_xCd_{1-x}Se$ films grown on GaAs" *Phys. Rev. B* 49(11), 7262–7270 (**1994**).

[200] Lunz, U., Kuhn, J., Goschenhofer, F., Schüssler, U., Einfeldt, S., Becker, C. R. & Landwehr, G. "Temperature dependence of the energy gap of zinc-blende CdSe and $Cd_{1-x}Zn_xSe$ epitaxial layers" *J. Appl. Phys.* 80(12), 6861–6863 (**1996**).

[201] Islam, R. & Rao, D. "Optical constants of polycrystalline ZnSe CdSe alloy films" *Opt. Mater. (Amst).* 7(1-2), 47–50 (**1997**).

[202] Madelung, O., Rössler, U. & Schulz, M. *II-VI and I-VII Compounds; Semimagnetic Compounds* New Series (Madelung, O., Rössler, U. & Schulz, M.) (Springer-Verlag, Berlin/Heidelberg, **1999**).

[203] Shannon, R. D. "Revised Effective Ionic Radii and Systematic Studies of Interatomic Distances in Halides and Chalcogenides" *Acta Crystallogr. Sect. A* 32(5), 751–767 (**1976**).

[204] Baranowski, J. M., Allen, J. W. & Pearson, G. L. "Crystal-Field Spectra of $3d^n$ Impurities in II-VI and III-V Compound Semiconductors" *Phys. Rev.* 160(3), 627–632 (**1967**).

[205] Cantalupo, S. A., Lum, J. S., Buzzeo, M. C., Moore, C., DiPasquale, A. G., Rheingold, A. L. & Doerrer, L. H. "Three-coordinate late transition metal fluorinated alkoxide complexes" *Dalt. Trans.* 39(2), 374–383 (**2010**).

[206] Dance, I. G. "Synthesis, Crystal Structure, and Properties of the hexa(μ-benzenethiolato)tetra(benzenethiolatocobaltate(II)) Dianion, the Prototype Cobalt(II)-Thiolate Molecular Cluster" *J. Am. Chem. Soc.* 101(21), 6264–6273 (**1979**).

[207] Pittala, S. & Kittilstved, K. R. "Cation Exchange in Small ZnS and CdS Molecular Analogues" *Inorg. Chem.* 54(12), 5757–5767 (**2015**).

[208] Lever, A. B. P., Walker, I. M., McCarthy, P. J., Mertes, K. B., Jircitano, A. & Sheldon, R. "Crystallographic and Spectroscopic Studies of Low-Symmetry Nickel(II) Complexes Possessing Long Nickel-Nitrogen Bonds" *Inorg. Chem* 22, 2252–2258 (**1983**).

[209] Hauser, A. "Intersystem crossing in the $[Fe(ptz)_6](BF_4)_2$ spin crossover system (ptz = 1-propyltetrazole)" *J. Chem. Phys.* 94(4), 2741–2748 (**1991**).

[210] Newville, M. "Fundamentals of XAFS" *Rev. Mineral. Geochemistry* 78(1), 33–74 (**2014**).

[211] Yang, J. personal communication. **2016**

[212] Houtepen, A. J., Hens, Z., Owen, J. S. & Infante, I. "On the Origin of Surface Traps in Colloidal II–VI Semiconductor Nanocrystals" *Chem. Mater.* 29(2), 752–761 (**2017**).

[213] Furis, M., Hollingsworth, J. A., Klimov, V. I. & Crooker, S. A. "Time- and Polarization-Resolved Optical Spectroscopy of Colloidal CdSe Nanocrystal Quantum Dots in High Magnetic Fields" *J. Phys. Chem. B* 109(32), 15332–15338 (**2005**).

[214] Johnston-Halperin, E., Awschalom, D. D., Crooker, S. A., Efros, Al. L., Rosen, M., Peng, X. & Alivisatos, A. P. "Spin spectroscopy of dark excitons in CdSe quantum dots to 60 T" *Phys. Rev. B* 63(20), 205309 (**2001**).

[215] Biadala, L., Shornikova, E. V., Rodina, A. V., Yakovlev, D. R., Siebers, B., Aubert, T., Nasilowski, M., Hens, Z., Dubertret, B., Efros, Al. L. & Bayer, M. "Magnetic polaron on dangling-bond spins in CdSe colloidal nanocrystals" *Nat. Nanotechnol.* 12(6), 569–574 (**2017**).

[216] Joshi, A., Narsingi, K. Y., Manasreh, M. O., Davis, E. A. & Weaver, B. D. "Temperature dependence of the band gap of colloidal CdSe/ZnS core/shell nanocrystals embedded into an ultraviolet curable resin" *Appl. Phys. Lett.* 89(13), 89–92 (**2006**).

[217] Efros, Al. L. & Efros, A. L. "Interband absorption of light in a semiconductor sphere" *Sov. Phys. Semicond. Ussr* 16(7), 772–775 (**1982**).

[218] Leatherdale, C. A., Woo, W.-K., Mikulec, F. V. & Bawendi, M. G. "On the Absorption Cross Section of CdSe Nanocrystal Quantum Dots" *J. Phys. Chem. B* 106(31), 7619–7622 (**2002**).

[219] Moreels, I., Rainò, G., Gomes, R., Hens, Z., Stöferle, T. & Mahrt, R. F. "Band-Edge Exciton Fine Structure of Small, Nearly Spherical Colloidal CdSe/ZnS Quantum Dots" *ACS Nano* 5(10), 8033–8039 (**2011**).

[220] Chernenko, A. V., Brichkin, A. S., Sobolev, N. A. & Carmo, M. C. "Mechanisms of manganese-assisted non-radiative recombination in Cd(Mn)Se/Zn(Mn)Se quantum dots" *J. Phys. Condens. Matter* 22(35), 355306 (**2010**).

[221] Chernenko, A., Dorozhkin, P., Kulakovskii, V., Brichkin, A., Ivanov, S. & Toropov, A. "Auger recombination of excitons in semimagnetic quantum dot structure in a magnetic field" *Phys. Rev. B* 72(4), 045302 (**2005**).

[222] Abramishvili, V., Komarov, A., Ryabchenko, S. & Semenov, Y. "Magnetic-field affected luminescence of Mn^{2+} ions in $Zn_{1-x}Mn_xSe$ compounds under resonance excitation of excitons" *Solid State Commun.* 78(12), 1069–1072 (**1991**).

[223] Nawrocki, M., Rubo, Y. G., Lascaray, J. P. & Coquillat, D. "Suppression of the Auger recombination due to spin polarization of excess carriers and Mn^{2+} ions in the semimagnetic semiconductor $Cd_{0.95}Mn_{0.05}S$" *Phys. Rev. B* 52(4), R2241–R2244 (**1995**).

[224] Nomura, S. & Kobayashi, T. "Exciton–LO-phonon couplings in spherical semiconductor microcrystallites" *Phys. Rev. B* 45(3), 1305–1316 (**1992**).

[225] Korsunska, N. E., Dybiec, M., Zhukov, L., Ostapenko, S. & Zhukov, T. "Reversible and non-reversible photo-enhanced luminescence in CdSe/ZnS quantum dots" *Semicond. Sci. Technol.* 20(8), 876–881 (**2005**).

[226] Liptay, T. J. & Ram, R. J. "Temperature dependence of the exciton transition in semiconductor quantum dots" *Appl. Phys. Lett.* 89(22), 223132 (**2006**).

[227] Olkhovets, A., Hsu, R.-C., Lipovskii, A. & Wise, F. "Size-Dependent Temperature Variation of the Energy Gap in Lead-Salt Quantum Dots" *Phys. Rev. Lett.* 81(16), 3539–3542 (**1998**).

[228] Stradling, R. A. & Wood, R. A. "The temperature dependence of the band-edge effective masses of InSb, InAs and GaAs as deduced from magnetophonon magnetoresistance measurements" *J. Phys. C: Solid State Phys.* 3(5), L94–L99 (**1970**).

[229] Thurmond, C. D. "The Standard Thermodynamic Functions for the Formation of Electrons and Holes in Ge, Si, GaAs, and GaP" *J. Electrochem. Soc.* 122(8), 1133–1141 (**1975**).

[230] Brooks, H. "Theory of the Electrical Properties of Germanium and Silicon" *Adv. Electron. Electron Phys.* 7, 85–182 (**1955**).

[231] Phillips, J. C. "Covalent Bond in Crystals. I. Elements of a Structural Theory" *Phys. Rev.* 166(3), 832–838 (**1968**).

[232] Kelley, A. M. "Electron–Phonon Coupling in CdSe Nanocrystals from an Atomistic Phonon Model" *ACS Nano* 5(6), 5254–5262 (**2011**).

[233] *Intersubband Transitions in Quantum Wells: Physics and Devices* (Springer US, Boston, MA, **1998**).

[234] Nag, B. R. *Physics of Quantum Well Devices* (Kluwer Academic Publishers, Dordrecht, **2002**).

[235] Li, Z. & Peng, X. "Size/Shape-Controlled Synthesis of Colloidal CdSe Quantum Disks: Ligand and Temperature Effects" *J. Am. Chem. Soc.* 133(17), 6578–6586 (**2011**).

[236] Ithurria, S. & Dubertret, B. "Quasi 2D Colloidal CdSe Platelets with Thicknesses Controlled at the Atomic Level" *J. Am. Chem. Soc.* 130(49), 16504–16505 (**2008**).

[237] Yeltik, A., Delikanli, S., Olutas, M., Kelestemur, Y., Guzelturk, B. & Demir, H. V. "Experimental Determination of the Absorption Cross-Section and Molar Extinction Coefficient of Colloidal CdSe Nanoplatelets" *J. Phys. Chem. C* 119(47), 26768–26775 (**2015**).

[238] Tessier, M. D., Javaux, C., Maksimovic, I., Loriette, V. & Dubertret, B. "Spectroscopy of Single CdSe Nanoplatelets" *ACS Nano* 6(8), 6751–6758 (**2012**).

[239] Zhang, F., Wang, S., Wang, L., Lin, Q., Shen, H., Cao, W., Yang, C., Wang, H., Yu, L., Du, Z., Xue, J. & Li, L. S. "Super Color Purity Green Quantum Dot Light-Emitting Diodes by Using CdSe/CdS Nanoplatelets" *Nanoscale* 8, 12182–12188 (**2016**).

[240] Fan, F., Kanjanaboos, P., Saravanapavanantham, M., Beauregard, E., Ingram, G., Yassitepe, E., Adachi, M. M., Voznyy, O., Johnston, A. K., Walters, G., Kim, G. H., Lu, Z. H. & Sargent, E. H. "Colloidal $CdSe_{1-x}S_x$ Nanoplatelets with Narrow and Continuously-Tunable Electroluminescence" *Nano Lett.* 15(7), 4611–4615 (**2015**).

[241] Chen, Z., Nadal, B., Mahler, B., Aubin, H. & Dubertret, B. "Quasi-2D Colloidal Semiconductor Nanoplatelets for Narrow Electroluminescence" *Adv. Funct. Mater.* 24, 295–302 (**2014**).

[242] She, C., Fedin, I., Dolzhnikov, D. S., Demortière, A., Schaller, R. D., Pelton, M. & Talapin, D. V. "Low-Threshold Stimulated Emission Using Colloidal Quantum Wells" *Nano Lett.* 14(5), 2772–2777 (**2014**).

[243] Guzelturk, B., Kelestemur, Y., Olutas, M., Delikanli, S. & Demir, H. V. "Amplified Spontaneous Emission and Lasing in Colloidal Nanoplatelets" *ACS Nano* 8(7), 6599–6605 (**2014**).

[244] Grim, J. Q., Christodoulou, S., Di Stasio, F., Krahne, R., Cingolani, R., Manna, L. & Moreels, I. "Continuous-wave biexciton lasing at room temperature using solution-processed quantum wells" *Nat. Nanotechnol.* 9(11), 891–895 (**2014**).

[245] Delikanli, S., Guzelturk, B., Hernández-Martínez, P. L., Erdem, T., Kelestemur, Y., Olutas, M., Akgul, M. Z. & Demir, H. V. "Continuously Tunable Emission in Inverted Type-I CdS/CdSe Core/Crown Semiconductor Nanoplatelets" *Adv. Funct. Mater.* 25(27), 4282–4289 (**2015**).

[246] Mahler, B., Nadal, B., Bouet, C., Patriarche, G. & Dubertret, B. "Core/shell Colloidal Semiconductor Nanoplatelets" *J. Am. Chem. Soc.* 134(45), 18591–18598 (**2012**).

[247] Pedetti, S., Ithurria, S., Heuclin, H., Patriarche, G. & Dubertret, B. "Type-II CdSe/CdTe Core/Crown Semiconductor Nanoplatelets" *J. Am. Chem. Soc.* 136(46), 16430–16438 (**2014**).

[248] Kelestemur, Y., Olutas, M., Delikanli, S., Guzelturk, B., Akgul, M. Z. & Demir, H. V. "Type-II Colloidal Quantum Wells: CdSe/CdTe Core/Crown Heteronanoplatelets" *J. Phys. Chem. C* 119(4), 2177–2185 (**2015**).

[249] Gaj, J. A., Ginter, J. & Gałazka, R. R. "Exchange Interaction of Manganese $3d^5$ States with Band Electrons in $Cd_{1-x}Mn_xTe$" *Phys. Status Solidi* 89(2), 655–662 (**1978**).

[250] Trager-Cowan, C., Parbrook, P. J., Henderson, B. & O'Donnell, K. P. "Band alignments in Zn(Cd)S(Se) strained layer superlattices" *Semicond. Sci. Technol.* 7(4), 536–541 (**1992**).

[251] O'Donnell, K., Parbrook, P., Yang, F., Chen, X., Irvine, D., Trager-Cowan, C., Henderson, B., Wright, P. & Cockayne, B. "The optical properties of wide bandgap binary II–VI superlattices" *J. Cryst. Growth* 117(1-4), 497–500 (**1992**).

[252] Nethercot, A. H. "Prediction of Fermi Energies and Photoelectric Thresholds Based on Electronegativity Concepts" *Phys. Rev. Lett.* 33(18), 1088–1091 (**1974**).

[253] Peng, X., Schlamp, M. C., Kadavanich, A. V. & Alivisatos, A. P. "Epitaxial Growth of Highly Luminescent CdSe/CdS Core/Shell Nanocrystals with Photostability and Electronic Accessibility" *J. Am. Chem. Soc.* 119(30), 7019–7029 (**1997**).

[254] Pandey, A. & Guyot-Sionnest, P. "Intraband spectroscopy and band offsets of colloidal II-VI core/shell structures" *J. Chem. Phys.* 127(10), 104710 (**2007**).

[255] Steiner, D., Dorfs, D., Banin, U., Della Sala, F., Manna, L. & Millo, O. "Determination of Band Offsets in Heterostructured Colloidal Nanorods Using Scanning Tunneling Spectroscopy" *Nano Lett.* 8(9), 2954–2958 (**2008**).

[256] Deguchi, D., Sato, K., Kino, H. & Kotani, T. "Accurate energy bands calculated by the hybrid quasiparticle self-consistent GW method implemented in the ecalj package" *Jpn. J. Appl. Phys.* 55(5), 051201 (**2016**).

[257] Wang, C. S. & Klein, B. M. "First-principles electronic structure of Si, Ge, GaP, GaAs, ZnS, and ZnSe. I. Self-consistent energy bands, charge densities, and effective masses" *Phys. Rev. B* 24(6), 3393–3416 (**1981**).

[258] Benchamekh, R., Gippius, N. A., Even, J., Nestoklon, M. O., Jancu, J.-M., Ithurria, S., Dubertret, B., Efros, Al. L. & Voisin, P. "Tight-binding calculations of image-charge effects in colloidal nanoscale platelets of CdSe" *Phys. Rev. B* 89(3), 035307 (**2014**).

[259] Bose, S., Song, Z., Fan, W. J. & Zhang, D. H. "Effect of lateral size and thickness on the electronic structure and optical properties of quasi two-dimensional CdSe and CdS nanoplatelets" *J. Appl. Phys.* 119(14), 143107 (**2016**).

[260] Achtstein, A. W., Schliwa, A., Prudnikau, A., Hardzei, M., Artemyev, M. V., Thomsen, C. & Woggon, U. "Electronic Structure and Exciton–Phonon Interaction in Two-Dimensional Colloidal CdSe Nanosheets" *Nano Lett.* 12(6), 3151–3157 (**2012**).

[261] Stephens, P. J. "Magnetic Circular Dichroism" *Annu. Rev. Phys. Chem.* 25(1), 201–232 (**1974**).

[262] Stephens, P. J. "Magnetic Circular Dichroism" *Adv. Chem. Phys.* 35, 197–264 (**1976**).

[263] Andersson, L. A. "Magnetic Circular Dichroism" in *Encycl. Spectrosc. Spectrom.* (Lindon, J. C., Tranter, G. E. & Koppenaal, D. W.) 3rd Edition (Academic Press, Oxford, United Kingdom, **2017**).

[264] Haldar, S., Dixit, V. K., Vashisht, G., Khamari, S. K., Porwal, S., Sharma, T. K. & Oak, S. M. "Effect of carrier confinement on effective mass of excitons and estimation of ultralow disorder in $Al_xGa_{1-x}As$/GaAs quantum wells by magneto-photoluminescence" *Sci. Rep.* 7(1), 4905 (**2017**).

[265] Nelson, D. F., Miller, R. C. & Kleinman, D. A. "Band nonparabolicity effects in semiconductor quantum wells" *Phys. Rev. B* 35(14), 7770–7773 (**1987**).

[266] Kotera, N. "Energy dependence of electron effective mass and effect of wave function confinement in a nanoscale $In_{0.53}Ga_{0.47}As/In_{0.52}Al_{0.48}As$ quantum well" *J. Appl. Phys.* 113(23), 234314 (**2013**).

[267] Waslela, A., Peyla, P., Merle D'Aubigné, Y., Nicholls, J. E., Ashenford, D. E. & Lunn, B. "Magneto-optical study of $CdTe/Cd_{1-x}Mn_xTe$ mutliple quantum wells with low potential barriers" *Semicond. Sci. Technol.* 7(4), 571–577 (**1992**).

[268] Kim, D. S., Lee, J. Y., Na, C. W., Yoon, S. W., Kim, S. Y., Park, J., Jo, Y. & Jung, M.-h. "Synthesis and Photoluminescence of Cd-doped α-MnS Nanowires" *J. Phys. Chem. B* 110(37), 18262–18266 (**2006**).

[269] Goede, O., Heimbrodt, W. & Weinhold, V. "Luminescence and Excitation Spectroscopy of MnS Thin Films" *Phys. Status Solidi* 136(1), K49–K54 (**1986**).

[270] Fan, D., Yang, X., Wang, H., Zhang, Y. & Yan, H. "Photoluminescence of MnS thin film prepared by chemical bath deposition" *Physica B* 337(1-4), 165–169 (**2003**).

[271] Demper, M., Heimbrodt, W., Bradford, C. & Prior, K. A. "Optical measurements of field-induced phenomena of the magnetic phase transition in quasi 2D MnS layers grown by MBE" *J. Nanoparticle Res.* 13(11), 5635–5640 (**2011**).

[272] Myers, E. B., Ralph, D. C., Katine, J. A., Louie, R. N. & Buhrman, R. A. "Current-Induced Switching of Domains in Magnetic Multilayer Devices" *Science* 285(5429), 867–870 (**1999**).

[273] Ikeda, S., Sato, H., Yamanouchi, M., Gan, H., Miura, K., Mizunuma, K., Kanai, S., Fukami, S., Matsukura, F., Kasai, N. & Ohno, H. "Recent Progress of Perpendicular Anisotropy Magnetic Tunnel Junctions for Nonvolatile VLSI" *SPIN* 02(03), 1240003 (**2012**).

[274] Chernyshov, A., Overby, M., Liu, X., Furdyna, J. K., Lyanda-Geller, Y. & Rokhinson, L. P. "Evidence for reversible control of magnetization in a ferromagnetic material by means of spin–orbit magnetic field" *Nat. Phys.* 5(9), 656–659 (**2009**).

[275] Mihai Miron, I., Gaudin, G., Auffret, S., Rodmacq, B., Schuhl, A., Pizzini, S., Vogel, J. & Gambardella, P. "Current-driven spin torque induced by the Rashba effect in a ferromagnetic metal layer" *Nat. Mater.* 9(3), 230–234 (**2010**).

[276] Matsukura, F., Tokura, Y. & Ohno, H. "Control of magnetism by electric fields" *Nat. Nanotechnol.* 10(3), 209–220 (**2015**).

[277] Maruyama, T., Shiota, Y., Nozaki, T., Ohta, K., Toda, N., Mizuguchi, M., Tulapurkar, A. A., Shinjo, T., Shiraishi, M., Mizukami, S., Ando, Y. & Suzuki, Y. "Large voltage-induced magnetic anisotropy change in a few atomic layers of iron" *Nat. Nanotechnol.* 4(3), 158–161 (**2009**).

[278] Chiba, D., Fukami, S., Shimamura, K., Ishiwata, N., Kobayashi, K. & Ono, T. "Electrical control of the ferromagnetic phase transition in cobalt at room temperature" *Nat. Mater.* 10(11), 853–856 (**2011**).

[279] Ohno, H., Chiba, D., Matsukura, F., Omiya, T., Abe, E., Dietl, T., Ohno, Y. & Ohtani, K. "Electric-field control of ferromagnetism" *Nature* 408(6815), 944–946 (**2000**).

[280] Sawicki, M., Chiba, D., Korbecka, A., Nishitani, Y., Majewski, J. A., Matsukura, F., Dietl, T. & Ohno, H. "Experimental probing of the interplay between ferromagnetism and localization in (Ga, Mn)As" *Nat. Phys.* 6(1), 22–25 (**2010**).

[281] Tokunaga, Y., Taguchi, Y., Arima, T.-H. & Tokura, Y. "Electric-field-induced generation and reversal of ferromagnetic moment in ferrites" *Nat. Phys.* 8(11), 838–844 (**2012**).

[282] Magliulo, M., Mulla, M. Y., Singh, M., Macchia, E., Tiwari, A., Torsi, L. & Manoli, K. "Printable and flexible electronics: from TFTs to bioelectronic devices" *J. Mater. Chem. C* 3(48), 12347–12363 (**2015**).

[283] Hollingsworth, J. A. "Heterostructuring Nanocrystal Quantum Dots Toward Intentional Suppression of Blinking and Auger Recombination" *Chem. Mater.* 25(8), 1318–1331 (**2013**).

[284] de Mello Donegá, C., Bode, M. & Meijerink, A. "Size- and temperature-dependence of exciton lifetimes in CdSe quantum dots" *Phys. Rev. B* 74(8), 085320 (**2006**).

[285] Javaux, C., Mahler, B., Dubertret, B., Shabaev, A., Rodina, A. V., Efros, Al. L., Yakovlev, D. R., Liu, F., Bayer, M., Camps, G., Biadala, L., Buil, S., Quelin, X. & Hermier, J.-P. "Thermal activation of non-radiative Auger recombination in charged colloidal nanocrystals." *Nat. Nanotechnol.* 8(3), 206–212 (**2013**).

[286] Labeau, O., Tamarat, P. & Lounis, B. "Temperature Dependence of the Luminescence Lifetime of Single CdSe/ZnS Quantum Dots" *Phys. Rev. Lett.* 90(25), 257404 (**2003**).

[287] Spinicelli, P., Buil, S., Quélin, X., Mahler, B., Dubertret, B. & Hermier, J. P. "Bright and Grey States in CdSe-CdS Nanocrystals Exhibiting Strongly Reduced Blinking" *Phys. Rev. Lett.* 102(13), 136801 (**2009**).

[288] Feng, D., Yakovlev, D. R., Pavlov, V. V., Rodina, A. V., Shornikova, E. V., Mund, J. & Bayer, M. "Dynamic Evolution from Negative to Positive Photocharging in Colloidal CdS Quantum Dots" *Nano Lett.* 17(5), 2844–2851 (**2017**).

[289] Liu, F., Biadala, L., Rodina, A. V., Yakovlev, D. R., Dunker, D., Javaux, C., Hermier, J. P., Efros, Al. L., Dubertret, B. & Bayer, M. "Spin dynamics of negatively charged excitons in CdSe/CdS colloidal nanocrystals" *Phys. Rev. B* 88(3), 035302 (**2013**).

[290] Nardes, A. M., Kemerink, M., Janssen, R. A. J., Bastiaansen, J. A. M., Kiggen, N. M. M., Langeveld, B. M. W., van Breemen, A. J. J. M. & de Kok, M. M. "Microscopic Understanding of the Anisotropic Conductivity of PEDOT:PSS Thin Films" *Adv. Mater.* 19(9), 1196–1200 (**2007**).

[291] Shirasaki, Y., Supran, G. J., Tisdale, W. A. & Bulović, V. "Origin of Efficiency Roll-Off in Colloidal Quantum-Dot Light-Emitting Diodes" *Phys. Rev. Lett.* 110(21), 217403 (**2013**).

[292] Tessler, N. "Efficient Near-Infrared Polymer Nanocrystal Light-Emitting Diodes" *Science* 295(5559), 1506–1508 (**2002**).

[293] Maksimov, A. A., Bacher, G., McDonald, A., Kulakovskii, V. D., Forchel, A., Becker, C. R., Landwehr, G. & Molenkamp, L. W. "Magnetic polarons in a single diluted magnetic semiconductor quantum dot" *Phys. Rev. B* 62(12), R7767–R7770 (**2000**).

[294] Barman, B., Oszwałdowski, R., Schweidenback, L., Russ, A. H., Pientka, J. M., Tsai, Y., Chou, W.-C., Fan, W. C., Murphy, J. R., Cartwright, A. N., Sellers, I. R., Petukhov, A. G., Žutić, I., McCombe, B. D. & Petrou, A. "Time-resolved magnetophotoluminescence studies of magnetic polaron dynamics in type-II quantum dots" *Phys. Rev. B* 92(3), 035430 (**2015**).

Acknowledgement

At this point I want to thank those people, who - with their advice, help and support - made the years of my PhD an instructive, valuable and wonderful periode of my life.

First of all I want to express my gratitude to my adviser Prof. Dr. rer. nat Gerd Bacher for his continuous guidance, motivation and willingness to help. He gave me the possibility and resources to grow and work in an environment of abundant support and trust. Besides his scientific attitude I especially acknowledge his joy and enthusiasm about his profession. It was a pleasure working with you. And many thanks for all the proofreading.

I would like to thank Prof. Dr. Paul Koenraad for his kind willingness to take the part of the second reviewer, and for a very nice and diverting lunch break in Santa Fe.

My very special thanks go to my international collaborators around the world. As someone doing spectroscopy without any access to sample preparation, all outcome of this thesis is based on the excellent and exceptional nanocrystals they provided. I want to thank Prof. Taeghwan Hyeon from the Seoul National University for the great cooperation and the motivating support. Thanks to Dr. Jiwoong Yang for the preparation of clusters with incomparable quality and the very fruitful and productive cooperation. I want to express gratitude to Prof. Daniel Gamelin from the University of Washington in Seattle, for his great support, very instructive discussions and for sharing his infectious enthusiasm about science, especially DMS QDs. Thanks to Charly (Dr. Charles Barrows) for all the beautiful nanocrystals, for being such a lovely host during my stay in Seattle and the piano concerts given during his visit in the WET (after “sweets time”). I am grateful to Prof. Volkan Demir from the Nanyang Technological University Signapore and the Bilkent University in Turkey, for the valuable discussions and beneficial collaboration. Within his group I thank Dr. Savas Delikanli for the preparation of extraordinary platelets and his willingness to share helpful advices about nanoparticle solution processing.

I owe particular thanks to those, who generously offered to scarify many hours of their time to help me get rid of quite a few linguistic mistakes. Thank you, Alex, Elke, Sevi and Ulrike.

My gratitude goes to all technicians at the WET: Thanks to Horst Watzel, to Udo Rau for the repairing of many high vacuum pumps, to Nicole Stracke for introducing me to the cleanroom in the very early days and to Helmut Lebeau for great technological support and encouraging words at the right time. Special thanks goes to Petra Merker for providing indispensable support, sometimes through the additional admonition needed.

My very special thanks goes to the whole WET working group. Thank you for your support, the willingness to help, the great working atmosphere, for the lots of fun we had and the terrific memories. I had a splendid time during my PhD thanks to all of you. Thanks Katja for introducing and integrating me to the WET at the very beginning. I am grateful to Olli for helping me out with the Streak camera so many times and to Wolf for stimulating discussions. Thanks Ulrike, Domme and Bilge, for sweets and coffee, the maintenance of an inviting kitchen and for always welcoming me on my search for distraction. Thank you Ulrike, also for proofreading. I want to express gratitude to Dr. Rachel Fainblat; I very much benefit from what I learned from you, either techniques, methods or working attitude.

I am deeply grateful to all students I had the pleasure to work with. Many of the results in this thesis were achieved based on your efforts. I thank Thomas for introducing me to ligand field theory and Arthur for his commitment to determine a single temperature dependent absorption. Warm thanks goes to Julia and Tamara, who did not give up hope whether struggling with green clusters or intractable nanoplatelets. You did great jobs. I want to thank Alex for his belief in and great work for our "Polarönchen", for never ever refusing any of my requests for help, and of course for health care in the form of vitamin C supply.

Thank you Sevi, for giving me the opportunity of working together with you, and for all your inestimable input (including cluster measurements, wave function calculations, nice three-dimensional *3d* orbitals,...). It was a real pleasure to do science with you and I learned a lot. I will definitively miss this.

I want to express my gratitude to Svenja Wepfer, who remained steadfastly at my side throughout my graduate time. Many thanks for clarifying conversations with salad and wine, after which any problem or question seemed a bit smaller. Without your great support during a certain time, I might not even have started the project of becoming a doctor. Thanks also for training me how to produce QD-LEDs, many answers to technological questions, the EQE measurements and fancy lattice structure drawings.

Great thanks go to my friends, both in Duisburg as well as Solingen. Thanks to those (Lisa, Ulrike, Sandra, Svenja and others) who made me really feel at home in Duisburg, including healthy and delicious warm meals when times were busy. Thanks goes to the

"Solinger Partyb*" for providing a space allowing me to stand back from trouble at all times. Thank you Susi, for always supporting me, even though I might have seemed insane to you sometimes. Finally I want to express my gratitude to my family: My parents, who always allayed any doubts, who moreover encouraged us to achieve whatever we desire, as well as to my brother Alex for continuously pointing out the amusing aspects of life.

List of Figures

List of Tables